Development of Optical Imaging of Metabolism for Monitoring and Predicting Drug Efficacy

By

Alexandra Jule Walsh

Dissertation

Submitted to the Faculty of the

Graduate School of Vanderbilt University

in partial fulfillment of the requirements

for the degree of

DOCTOR OF PHILOSOPHY

in

Biomedical Engineering

May, 2015

Nashville, Tennessee

Approved:

Melissa C. Skala, Ph.D.
Rebecca S. Cook, Ph.D.
Anita Mahadevan-Jansen, Ph.D.
H. Charles Manning, Ph.D.
Jamey Young, Ph.D.

ACKNOWLEDGEMENTS

First, I would like to thank my adviser, Dr. Skala. Her expertise in fluorescence lifetime imaging and optical technologies was instrumental to the success of my project. In addition, she helped me develop research skills, technical writing skills, presentations, and grant writing skills. Additionally, I would like to thank each member of my committee. Dr. Cook taught me about the biology of breast cancer and provided invaluable cell lines and reagents necessary for my experiments. In addition, she taught animal procedures and the organoid generation protocol that became major aspects of my research. Dr. Mahadevan-Jansen has advised me throughout my project, with research direction, presentation skills, and career counseling. Dr. Manning provided expertise with FDG-PET imaging that was crucial for Chapter 4. Dr. Young has provided expertise on cellular metabolism and helped shaped my research direction particularly at the beginning of my project.

Next, I would like to thank my collaborators and peers without whom this work would have taken much longer. I would like to thank Dr. Sanders and Connie Nixon for providing the patient samples which allowed the feasibility studies in human tissues. Additionally, I am thankful for Dr. Arteaga's guidance and helpful comments on all our manuscripts, and the use of the HR6 cell line developed in his laboratory. I would also like to thank the other members of Dr. Skala's lab and all the Biophotonics Lab students who provided comradery and research assistance. Additionally, many undergraduates, including Matt Sunderman, Alec Lafontant, Michael Schultis, Miranda Kunz, and Andy Lee, helped with cell culture, imaging experiments, and data analysis.

I would like to thank the funding sources that provided the equipment and supplies necessary for this project, including NIH/NCI (NIH R00-CA142888, R01-CA185747), DOD BCRP (DOD-BC121998), the Mary Kay Foundation (067-14), the American Society for Laser

Surgery and Medicine, and the NCI Breast Cancer SPORE (P50-CA098131). Additionally, I am appreciative for the funding sources, NSF (DGE-0909667) and Vanderbilt Provost Fellowship, that supported my living expenses and allowed me to work on my degree full time. Experiments were performed in part through the use of the VUMC Cell Imaging Shared Resource (supported by NIH grants CA68485, DK20593, DK58404, HD15052, DK59637 and EY08126). Flow Cytometry experiments were performed in the VUMC Flow Cytometry Shared Resource. The VUMC Flow Cytometry Shared Resource is supported by the Vanderbilt Ingram Cancer Center (P30 CA68485) and the Vanderbilt Digestive Disease Research Center (DK058404).

Finally, I would like to thank my family and friends for all of their unending support over the last five years. My parents and sisters are particularly supportive and I appreciate all their encouragement and understanding. Lastly, I would like to thank Huy, my fiancé, for his patience, understanding, and support both as I have finished my dissertation and as I have prepared for the next stage of my career.

TABLE OF CONTENTS

Chapter

4. OPTICAL METABOLIC IMAGING IDENTIFIES BREAST CANCER GLYCOLYTIC LEVELS, SUBTYPES, AND EARLY TREATMENT RESPONSE 63

Appendix

LIST OF TABLES

LIST OF FIGURES

CHAPTER 1

Introduction

1.1 Motivation

Each year, an estimated 300,000 new cases of breast cancer are diagnosed (1). Fortunately, many new molecularly specific, effective treatments are available for these patients. However, clinical selections of the most efficacious drug regimen for an individual breast tumor remain rather arbitrary, based on static measurements of the presence or absence of several biomarkers, including the estrogen receptor (**ER**) and the human epidermal growth factor receptor 2 (**HER2**) in the diagnostic biopsy. Furthermore, therapy effectiveness is most commonly determined by tumor size regression, or growth in the case of ineffective treatments. Therefore, treatments may not be identified as ineffective until weeks or months after treatment is initiated. Due to the heterogeneity of tumor genotype and phenotype, sub-populations of cells, innately within the original tumor or arising as a result of treatment, can cause therapy relapse (2). A technology capable of quickly and accurately predicting and monitoring therapy effectiveness is imperative for guiding therapeutic decisions, especially as additional drugs are approved for clinical use.

This dissertation develops a light-based technology, optical metabolic imaging (**OMI**), for monitoring metabolism changes due to anti-cancer therapy and for predicting tumor response to anti-cancer therapy. Current methods, such as palpation, fluorodeoxyglucose positron emission tomography (**FDG-PET**), magnetic resonance imaging (**MRI**), and ultra-sound size measurements to assess therapeutic response lack the resolution and/or sensitivity to provide accurate measures of response (3-7). OMI measures the fluorescence intensity and lifetime of intrinsic cellular metabolism coenzymes, nicotinamide adenine dinucleotide (**NADH**) and flavin adenine dinucleotide (**FAD**), which provide a robust measure of cellular metabolism (8, 9).

Furthermore, OMI is high-resolution and non-invasive, which allows longitudinal studies of tumor heterogeneity.

Preliminary (Appendix C) and early studies (Chapters 3-4) demonstrated the unique sensitivity of OMI to drug-induced metabolism changes. Therefore, an organoid-based platform was developed to enable high-throughput screening of drug response. Organoids are macrosuspensions derived from primary tumors and contain all the innate cells and microenvironment of the tumor (10, 11). Therefore, organoids are an attractive, relevant platform to test drug response. The second part of this dissertation (Chapters 5-6, Appendices 4-5) characterizes OMI in excised tissues and organoids, and robustly validates an organoid-OMI screen for predicting drug response for breast cancer patients.

1.2 Specific Aims

The objectives of this dissertation are to fully characterize OMI endpoints and OMI analysis, develop OMI for monitoring anti-cancer drug-induced cellular metabolism changes *in vivo*, and demonstrate feasibility of an organoid-OMI technology for clinical translation.

Aim 1: Characterize subpopulation analysis of OMI data to quantify heterogeneous cell populations. Tumor heterogeneity contributes to therapy resistance; and this aim develops OMI analysis techniques to identify and quantify heterogeneity within OMI data. Subpopulation analysis (**SPA**) techniques were developed to quantify heterogeneous cell populations within OMI data. OMI-SPA was characterized by simulation experiments and validated with cell co-culture experiments. Generic simulation experiments characterized the relationships between sample size, data standard deviation, and subpopulation mean separation distance required for OMI-SPA to identify subpopulations.

Aim 2: Determine the sensitivity of OMI to breast cancer subtypes and therapeutic response *in vitro* and validate OMI measures of response in human breast cancer xenografts *in vivo*. OMI endpoints, redox ratio, mean NADH lifetime, and mean FAD lifetime, were analyzed across a panel of breast cancer cells, including ER+, HER2+, and triple negative, and validated with assays of cellular metabolism. Responsive and resistant cells were treated with the clinically used HER2-inhibitor trastuzumab, to determine OMI sensitivity to therapeutic response. Additionally, OMI variables were analyzed to assess statistical correlation or independence with other OMI variables and biochemical assays of cellular metabolism. *In vivo* OMI was also performed on xenograft models of HER2 overexpressing breast cancers responsive, resistant, and partially responsive to the HER2 inhibitor, trastuzumab. *In vivo* OMI endpoints of response were compared to current clinical measures (FDG-PET). Tumor size and immunohistochemical (**IHC**) endpoints (proliferation, cell death) served as gold standards of drug response.

Aim 3: Characterize OMI endpoints in excised tissues. There are many challenges to *in vivo* OMI measurements. However, freshly excised or frozen tissues are more accessible, can be obtained during routine medical procedures, and enable OMI technologies to be implemented remotely. This aim compares OMI endpoints of tissue *in vivo*, excised tissue over 48hr, and flash-frozen and thawed tissues, in order to determine if excised or frozen tissues can be used when *in vivo* experiments are not feasible.

Aim 4: Validate organoid-OMI measured tumor response with *in vivo* OMI in human breast cancer xenografts and compare organoid-OMI measured tumor response with measures of response in human breast cancers. Organoid culture of primary human tumor tissue is an attractive platform for testing and predicting drug response. Organoids contain all the original cells and microenvironment of the original tumor and therefore, may respond to treatments in a similar manner. In this aim, organoids were generated from two xenograft models of breast cancer, one responsive and one resistant to trastuzumab. The organoids were treated with a panel of anti-cancer drugs and imaged over a 72hr time course. Organoid response to the drugs was assessed from the OMI index, a combination variable of individual OMI endpoints. Organoid-OMI response was compared to *in vivo* drug response of the breast cancer xenografts, as measured by changes in tumor size, and to gold standard IHC. Heterogeneity of drug response was assessed by subpopulation analysis of the OMI index. Additionally, feasibility for growing organoids from primary, human breast tumor biopsies was demonstrated. Organoids were generated from six primary human tumors and were treated with clinically relevant anti-cancer drugs. OMI was performed on the organoids over a 72hr time course and OMI data was analyzed to identify heterogeneity in response. OMI measured response was compared to measurements of cell death and proliferation within the organoids after 72hr of drug treatment.

1.3 Dissertation Outline

This dissertation has been organized in the following manner:

Chapter 1 is the introduction and provides the motivation behind the research and outlines the specific aims that are addressed. Chapter 1 also includes a brief summary of the chapters.

Chapter 2 provides background information on breast cancer and breast cancer treatment strategies, cellular metabolism, and optical technologies. In particular, fluorescence lifetime imaging is discussed.

Chapter 3 reports and fully characterizes the subpopulation analysis technique developed for identifying heterogeneity in cell populations of OMI data. This work presents specific and generalized simulation experiments to demonstrate the limits of the subpopulation analysis technique. Additionally, the technique is tested on experimental data of two co-culture cells lines. This work was published in 2015 in *Biomedical Optics Express* (12).

Chapter 4 contains the cell line and *in vivo* OMI experiments which characterized the OMI technology and demonstrated different metabolic profiles in trastuzumab responsive and resistant cells upon treatment with trastuzumab. First, this chapter provides the results of a cyanide experiment which validate the imaging of NADH and FAD, two co-enzymes of metabolism. This chapter also reports the basal OMI endpoints of a panel of cell lines. Finally, this chapter explores changes in OMI endpoints when responsive and resistant cells are exposed to the anti-HER2 antibody, trastuzumab. *In vivo* xenograft experiments of three different models confirm the cell line results. Furthermore, FDG-PET was performed on a parallel cohort of mice to directly compare OMI measured drug response with a clinically used technology. This work was published in 2013 in *Cancer Research* (13).

Chapter 5 demonstrates the stability of OMI endpoints in freshly excised and frozen tissues. Performed on the hamster cheek pouch model, this work quantifies the timeline for obtaining OMI measurements in freshly excised tissues before significant changes in metabolism occur. This work was published in 2012 in the *Journal of Biomedical Optics* (14).

Chapter 6 reports the OMI-organoid experiment results. First, OMI-organoid drug response was tested in two xenograft models and the OMI-predicted drug response correlated with *in vivo* tumor growth. Next, feasibility with organoid generation and OMI-measurements was shown for 6 different primary human breast cancer samples. This work also demonstrates the utility of single-cell analysis and sub-population modeling techniques to identify heterogeneity in cellular metabolism following drug treatment. This work was published in 2014 in *Cancer Research* (15).

Chapter 7 provides a summary of the major results and objectives of this dissertation. The impact of this research is also discussed and several future directions are recommended. Finally, Chapter 7 also contains a discussion of this work's contribution to the field and societal impact.

Appendix A contains supplementary tables and figures for Chapter 3.

Appendix B contains supplementary tables and figures for Chapter 4.

Appendix C reports a preliminary study in which the optical redox ratio was explored in ER and HER2 overexpressing breast cancer cell lines. In this study, the NADH and FAD fluorescence was obtained on a confocal fluorescence microscope. This work was published in 2012 in *Biomedical Optics Express* (16).

Appendix D contains the image analysis protocol that was developed to automatically segment NADH and FAD autofluorescence images into individual nucleus, cytoplasm, and cell regions. This enabled fast processing of OMI data sets and heterogeneity analysis of single-cell data. This work was published in 2014 as an *SPIE Proceedings* paper (17).

Appendix E explores the use of frozen tissues to generate organoids. These experiments compare two different freezing protocols, flash freezing in liquid nitrogen and slow freezing in DMSO, for the preservation of bulk tissues for subsequent thawing, organoid generation, and OMI measures of drug response. This work is currently in preparation for publication.

Appendix F reports changes in collagen content and organization due to trastuzumab treatment in two xenograft models, one resistant and one responsive to trastuzumab. Collagen can be imaged with second harmonic generation imaging which provides high resolution images of collagen fibers which can be quantitatively assessed for collagen density and alignment. This work was published in 2015 in *Journal of Biomedical Optics* (18).

1.4 References

1. Breast Cancer. National Institutes of Health, 2009.
2. Sharma SV, Settleman J. Oncogene addiction: setting the stage for molecularly targeted cancer therapy. Genes & development. 2007;21(24):3214-31.
3. Shah C, Miller TW, Wyatt SK, McKinley ET, Olivares MG, Sanchez V, Nolting DD, Buck JR, Zhao P, Ansari MS, Baldwin RM, Gore JC, Schiff R, Arteaga CL, Manning HC. Imaging biomarkers predict response to anti-HER2 (ErbB2) therapy in preclinical models of breast cancer. Clin Cancer Res. 2009;15(14):4712-21.
4. Brown RS, Wahl RL. Overexpression of Glut-1 glucose transporter in human breast cancer. An immunohistochemical study. Cancer. 1993;72(10):2979-85.
5. Basu S, Chen W, Tchou J, Mavi A, Cermik T, Czerniecki B, Schnall M, Alavi A. Comparison of triple-negative and estrogen receptor-positive/progesterone receptor-positive/HER2-negative breast carcinoma using quantitative fluorine-18 fluorodeoxyglucose/positron emission tomography imaging parameters: a potentially useful method for disease characterization. Cancer. 2008;112(5):995-1000.
6. Jacobs MA, Ouwerkerk R, Wolff AC, Gabrielson E, Warzecha H, Jeter S, Bluemke DA, Wahl R, Stearns V. Monitoring of neoadjuvant chemotherapy using multiparametric, (23)Na sodium MR, and multimodality (PET/CT/MRI) imaging in locally advanced breast cancer. Breast cancer research and treatment. 2011;128(1):119-26.
7. Mankoff DA, Dunnwald LD, L. K., Doot RK, Specht JM, Gralow JR, Ellis GK, Livingston RB, Linden HM, Gadi VK, Kurland BF, Schubert EK, Muzi M. PET Tumor Metabolism in Locally Advanced Breast Cancer Patients Undergoing Neoadjuvant Chemotherapy: Value of Static versus Kinetic Measures of Fluorodeoxyglucose Uptake. Clinical Cancer Research. 2011;17(8):2400-9.
8. Chance B, Schoener B, Oshino R, Itshak F, Nakase Y. Oxidation-reduction ratio studies of mitochondria in freeze-trapped samples. NADH and flavoprotein fluorescence signals. J Biol Chem. 1979;254(11):4764-71.
9. Georgakoudi I, Quinn KP. Optical imaging using endogenous contrast to assess metabolic state. Annu Rev Biomed Eng. 2012;14:351-67.
10. Campbell JJ, Davidenko N, Caffarel MM, Cameron RE, Watson CJ. A multifunctional 3D co-culture system for studies of mammary tissue morphogenesis and stem cell biology. PloS one. 2011;6(9):e25661.
11. Straussman R, Morikawa T, Shee K, Barzily-Rokni M, Qian ZR, Du J, Davis A, Mongare MM, Gould J, Frederick DT, Cooper ZA, Chapman PB, Solit DB, Ribas A, Lo RS, Flaherty KT, Ogino S, Wargo JA, Golub TR. Tumour micro-environment elicits innate resistance to RAF inhibitors through HGF secretion. Nature. 2012;487(7408):500-4.

12. Walsh AJ, Skala MC. Optical metabolic imaging quantifies heterogeneous cell populations. Biomedical optics express. 2015;6(2):559-73.

13. Walsh AJ, Cook RS, Manning HC, Hicks DJ, Lafontant A, Arteaga CL, Skala MC. Optical metabolic imaging identifies glycolytic levels, subtypes, and early-treatment response in breast cancer. Cancer Res. 2013;73(20):6164-74.

14. Walsh AJ, Poole KM, Duvall CL, Skala MC. Ex vivo optical metabolic measurements from cultured tissue reflect in vivo tissue status. Journal of biomedical optics. 2012;17(11):116015.

15. Walsh AJ, Cook RS, Sanders ME, Aurisicchio L, Ciliberto G, Arteaga CL, Skala MC. Quantitative optical imaging of primary tumor organoid metabolism predicts drug response in breast cancer. Cancer Res. 2014;74(18):5184-94.

16. Walsh A, Cook RS, Rexer B, Arteaga CL, Skala MC. Optical imaging of metabolism in HER2 overexpressing breast cancer cells. Biomedical optics express. 2012;3(1):75-85.

17. Walsh AJ, Skala MC. An automated image processing routine for segmentation of cell cytoplasms in high-resolution autofluorescence images. SPIE Proceedings. 2014;8948(56).

18. Walsh AJ, Cook RS, Lee JH, Arteaga CL, Skala MC. Collagen density and alignment in responsive and resistant trastuzumab-treated breast cancer xenografts. Journal of biomedical optics. 2015;20(2):26004.

CHAPTER 2

Background

2.1 Clinical Problem: Treatment Selection in Breast Cancer

Introduction

Each year, approximately 300,000 new cases of breast cancer are discovered and approximately 40,000 women die from breast cancer (1). While primary breast cancer tumors are usually painless and have relatively few major complications, the tumors can metastasize and travel throughout the body, causing malignant tumors in essential organs which can result in death. The probability of death from breast cancer varies widely across patients with differing tumor size, estrogen receptor status, and age of diagnosis (2). Breast cancer treatment and prognosis are greatly correlated with tumor expression of certain receptors, such as the estrogen receptor (ER) and the human epidermal growth factor receptor 2 (HER2).

Due to the wide range of genetic mutations and phenotypes present in cancers, a host of drugs are available and in development for targeted therapeutic action. Yet, few biomarkers exist to direct drug selection. Often, patients are prescribed a fixed drug regimen and tumor response (based on tumor size) is determined weeks or months after treatment begins. Clinical treatment decisions and pre-clinical drug development studies would greatly benefit from the development of robust biomarkers of tumor response.

Risk Factors

Breast cancer can occur in both genders; however, it is more prevalent in women than men (3). Genetic, hormonal, and dietary factors are thought to contribute to the likelihood of the development of breast cancer (4). Additional risk factors include age, ethnicity, and environmental factors, such as exposure to radiation (1).

Breast cancer can be caused by genetic mutations. Five to ten percent of all women with breast cancer have a mutation of the BRCA-1 and BRCA-2 genes (5). Individuals with either but not both mutations do not have an increased incidence of breast cancer (5). The estimated lifetime risk of developing breast cancer for women with both mutations is estimated between 40-85% (5).

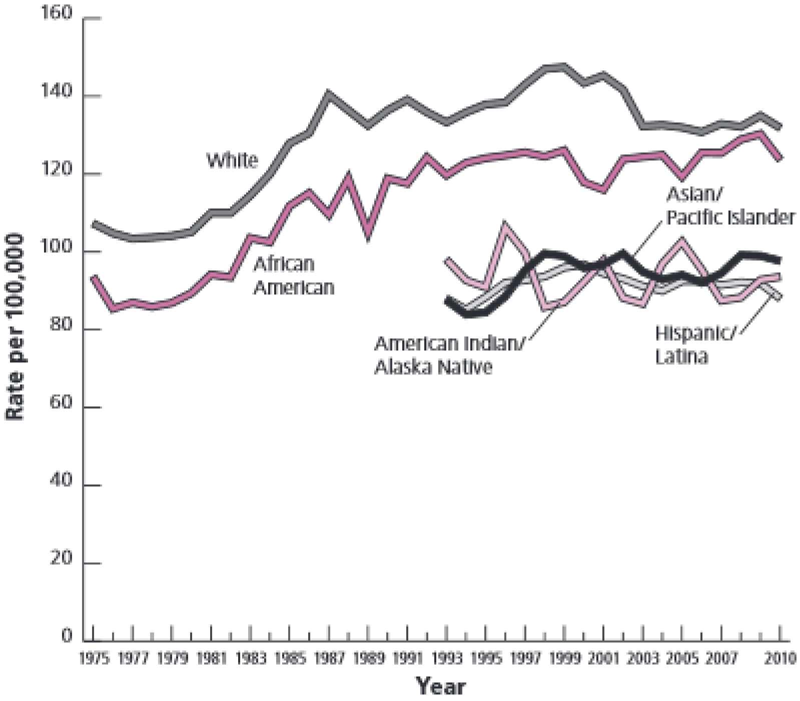

Figure 2.1: Breast Cancer Incidence. Incidence of American women with breast cancer across five ethnic groups: whites, Hispanics, African Americans, Asians/Pacific Islanders, and American Indians/Alaskan Natives (1).

Breast cancer incidence and mortality rates are linked with ethnicity (Fig. 2.1). According to reports from the National Cancer Institute, white American women have the highest incidence of breast cancer. However, African-American women have the highest mortality rates from breast cancer. Incidence and mortality of breast cancer is lowest in Hispanics, Asians/Pacific Islanders, and American Indians/Alaskan Natives (1).

Diagnosis

The diagnostic process for breast cancer has evolved to include many procedures and imaging modalities. The initial suspicious lump is generally discovered by the patient or doctor during a physical examination (3). Symptoms of breast cancer include presence of a lump or thickening of the breast, change in the size or shape of the breast, changes in the skin of the breast, and fluid discharge (6). Usually the lump is painless, but on retrospect, the patient may remember mild discomfort from the area (3).

Several imaging modalities are used to detect lumps in the breast that are too small to be found in a physical exam. A mammogram is an x-ray image of the breast tissue which can show lumps and calcified tissues (6). Due to increased rates of survival and treatment outcomes with early cancer detection, women over 40 are encouraged to annual mammogram screenings for breast cancer (1). An ultrasound can be used to determine whether the lump is solid or fluid filled (6). MRI images are also used to distinguish normal breast tissue from benign lesions (6).

Fine needle aspiration and core needle biopsy procedures extract cells of suspicious lumps for histological analysis. In fine-needle aspiration, a needle is used to extract a small amount of liquid from the cyst or lump to determine the pathology of the suspicious lesion (3). Fine-needle aspiration is performed on large tumors and fluid filled tumors. A core needle biopsy is used to extract cells of lesions for histological analysis (3). Open surgical biopsy can also be performed if the lump is too small for the needle biopsies or if the needle biopsies are inconclusive (3).

Histopathology of the biopsied tissue provides characterization of the tumor and guides therapy selection. Pathologists inspect the cells for the presence of abnormal or cancerous cells. The biopsied cells are also stained for expression of ER and HER2 to determine if the patient is eligible for targeted therapies.

Common Breast Cancers

A carcinoma is a malignant tumor derived from epithelial cells (3). In breast tissue, epithelial cells line the ducts, acini, or lobules which are the locations where breast cancer can develop (3). When examined microscopically, cancer cells exhibit changes within the cell different from normal epithelial cells (3). When viewed macroscopically, the changes within the cells cause alterations in the arrangement of cells in relation to each other leading to the tumor appearance (3). Breast cancer can be divided into two main categories: *in situ* carcinoma (Fig. 2.2) and invasive carcinoma (Fig. 2.3). *In situ* carcinoma is where the proliferating, malignant cells are confined by the basement membrane surrounding the ducts. Between 1 and 5% of breast cancer cases are independent *in situ* carcinoma (4). Invasive carcinomas are cases where the proliferating cells invade the breast stroma and tissue spaces (3).

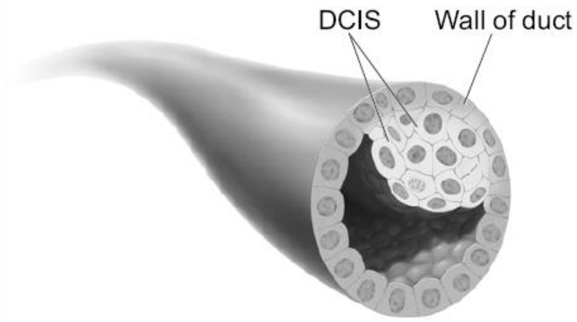

Figure 2.2: **Carcinoma *In Situ***. In ductal carcinoma *in situ*, diseased tumor cells are confined by the duct (6).

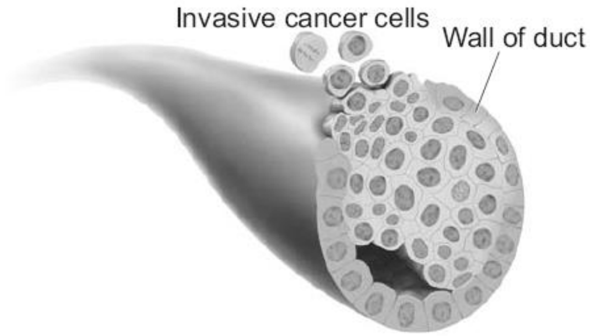

Figure 2.3: Invasive Carcinoma. Invasive carcinoma cells outgrow the duct and spread into the surrounding tissue (6).

2.2 Role of Receptors in Breast Cancer

Estrogen Receptor (ER)

The estrogen receptor (ER) has several functions in breast cancer tumors. The ER can act as a transcription factor. In this pathway, estrogen binds to the ER causing it to phosphorylate, which dissociates several attached proteins such as heat shock protein 90 (HSP-90), resulting in an ER with a different conformation in an active form (7). The activated ER binds with other factors, co-activators or co-repressors, in the nucleus to moderate gene transcription (7). ER can also activate non-genomic pathways in the cytoplasm. In one example, the activated ER activates the mitogen-activated protein kinase pathway (MAPK) which increases cellular metabolism and promotes cell growth (7). Hormonal therapies, such as tamoxifen, bind ER without activating it, reducing the oncogenic effects of ER signaling.

Human Epidermal Growth Factor Receptor 2 (HER2)

HER2 is overexpressed in approximately 30% of primary breast cancer tumors and is associated with more aggressive tumors, increased recurrence, and poor patient outcomes (8). HER2 is commonly expressed in breast tissue, including non-cancerous cells; thus, overexpression beyond the basal expression of normal tissue is clinically monitored. Breast tumors are tested for HER2 overexpression by fluorescence *in situ* hybridization which labels copies of the HER2 gene with fluorescence tags (9). The HER2 pathway is thought to activate PI3K, a major driver of cellular metabolism (Fig. 2.4). HER2 inhibitors prolong survival in responsive patients by impairing the oncogenic effects of HER2 signaling (10).

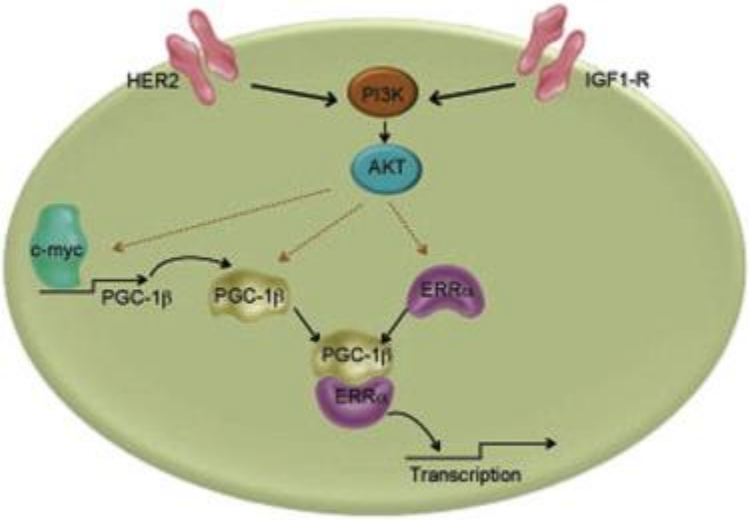

Figure 2.4: HER2 and PI3K Pathway. HER2 pathway activation activates PI3K and AKT (11).

2.3 Current Breast Cancer Treatments

Treatments for breast cancer include surgical intervention, chemotherapy, radiation, and targeted therapeutics. Often, breast cancer treatment involves a multimodal approach, using several different therapies to combat different aspects of the disease. Age, menopausal state, disease stage, histology, and receptor expression influence the selection of therapy to optimize treatment to each specific cancer.

Traditionally, mastectomy was the most common surgical intervention and treatment of breast cancers (12). Mastectomy was preferred because other surgical interventions, such as lumpectomies, had a high recurrence, 25-50% while only 1-2% of mastectomy patients had recurrence; however lumpectomy procedures have greatly improved (12). Surgical management for malignant breast cancers is frequently paired with radiation therapy, chemotherapy, and targeted therapies. During surgery, lymph nodes are removed and dissected to determine whether metastases from the breast cancer tumors have migrated to the lymph nodes and throughout the body.

The treatment of inoperable late-stage or inflammatory breast cancer is a similar multimodal approach. A biopsy first provides histology of the breast cancer revealing ER status, progesterone receptor status, and HER2 status. Radiation, hormonal, and chemotherapy treatments are attempted initially (13). Upon favorable prognosis with the initial therapy, surgery may be performed (13). Stage IV, recurrent, and metastatic breast cancer is combated with a variety of surgical, radiation, and hormonal therapies.

In addition to surgical interventions, chemotherapy and radiation therapy are often utilized to combat breast cancer. Radiation therapy uses high-energy electromagnetic radiation to kill cancer cells. Radiation therapy is often used in conjunction with breast conserving surgeries, lumpectomy, because this combination has the same outcomes as mastectomy (14, 15). Systemic chemotherapy may also be used to target local and metastatic breast cancer. Chemotherapy is often used in combination with other agents, additional chemotherapy drugs, hormonal agents, or targeted drugs.

Targeted Breast Cancer Therapies

Recent breast cancer research has focused on therapeutic agents targeting specific pathways within the cancerous cell. Breast cancers expressing ER are often treated with tamoxifen, an ER antagonist. Breast tumors which overexpress HER2 display more aggressive cancer progression (8). Trastuzumab and lapatinib, two therapeutic agents that inhibit HER2, prolong survival in patients with HER2-overexpressing breast cancers.

Recent studies have proven that tamoxifen is an effective hormonal drug for the systemic treatment of breast cancer (16). Tamoxifen prevents estrogen from binding to breast cancer cells, preventing the activation of ER. An analysis of 80,273 women in 71 trials of tamoxifen found that after five years, the death rate by breast cancer was reduced by 31% (16). In this trial, worse outcomes were associated with ER-negative receptor status and a longer duration of treatment (16). Current recommendations are that tamoxifen treatment be terminated after five years due to the development of tamoxifen resistant tumors (17, 18). Tamoxifen can be an advantageous anti-cancer agent for breast cancer cases of ER-positive tumors. Currently several aromatase inhibitors are in clinical trials as possible alternatives to tamoxifen (13).

Breast cancers that overexpress HER2 are treated with HER2 inhibitors such trastuzumab and lapatinib. A high concentration of HER2 receptors expressed by breast cancer cells is associated with increased tumor progression and metastases (9). Trastuzumab is a monoclonal antibody that binds HER2, while lapatinib is a small molecular inhibitor which binds both HER2 and the epridermal growth factor receptor. Both trastuzumab and lapatinib prolong survival in patients with HER2 overexpressing breast cancers (19-21). Trastuzmab specifically binds to the extracellular domain of HER2 and prevents activation of the intracellular HER2 tyrosine kinase. Furthermore, trastuzumab has additional mechanisms of action, including blockade of HER2 dimerization, increased HER2 endocytosis and degradation, and induction of antibody-dependent cellular cytotoxicity (ADCC) (22, 23). Trastuzumab induces cytostatic effects by arresting the cell cycle in the G1 phase and inhibits signaling involved in cell survival (24, 25). Lapatinib is a small molecule inhibitor which binds HER2 and prevents the formation of activated HER2 dimers, preventing the activation of the HER2 cascade and reducing the oncogenic effects of HER2 signaling (19).

Due to the importance of choosing the correct treatment for breast cancer patients, tumor biopsies are screened for hormone receptors. Currently, malignancy, ER, and HER2 expression is determined by histology staining and fluorescence *in situ* hybridization (FISH) of the biopsy specimen. Treatment plans are determined based on the stage and size of the tumor and presence or absence of ER and HER2.

2.4 Tumor Heterogeneity and Resistance

Another factor influencing treatment decisions and ultimately limiting the clinical outcome of breast cancers is resistance to chemotherapy and targeted therapies. Only 57% of patients with ER-positive breast cancers respond to tamoxifen therapy (26). Similarly, approximately one-third of breast tumors that overexpress HER2 do not respond to trastuzumab and lapatinib therapy (21), and about 40% of patients do not respond to paclitaxel, a chemotherapy (27). Resistance to therapies can be innate or acquired.

Drug resistance by tumors may arise from subpopulations of cancer cells within the tumor that are resistant to the given treatment (28, 29). These subpopulations of cells are inherent to tumors due to the highly mutagenic nature of cancer (28). In this model, individual cells with differing genotypes can arise within tumors and lead to sub-populations of cells that express different oncogenic transformations, possibly respond differently to therapies, and can repopulate the tumor (Fig. 2.5). However, recent research has demonstrated varying behaviors among tumors with identical genes, suggesting that cancer cell behavior is influenced by more than just genetic mutations (30). Novel therapeutics are in development to overcome clinical resistance to these therapeutic inhibitors (10). Early identification of the tumors that will respond to targeted therapies versus those that are resistant, will expedite clinical decisions regarding course of treatment, and will improve the clinical outcomes of breast cancer patients.

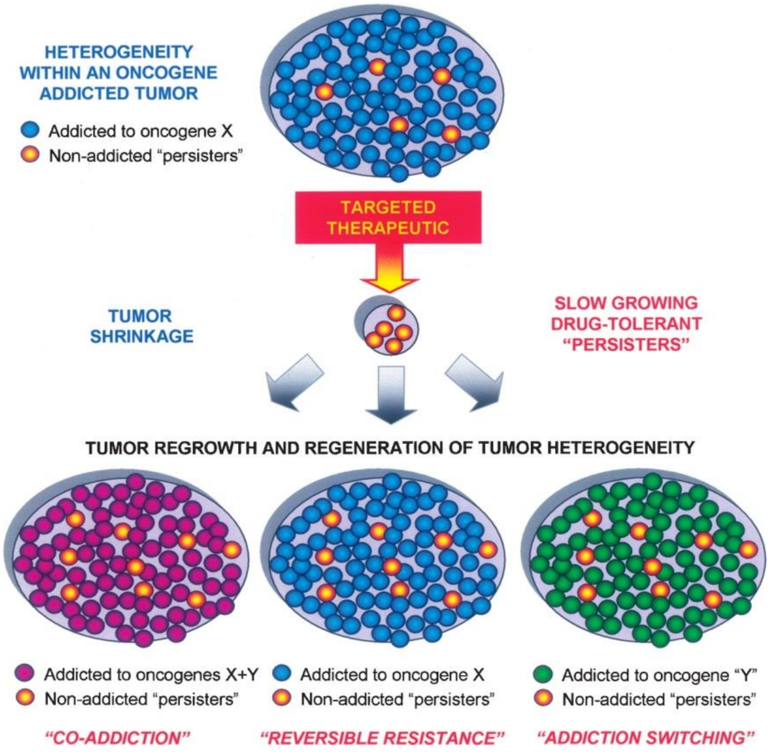

Figure 2.5. Theories of tumor heterogeneity. (29)

Alternative Treatment Options for Resistant Tumors

If a tumor is resistant to traditional therapies, patient treatment can be tailored to improve clinical outcome. For example, the patient can receive more aggressive surgical intervention and experimental drugs and drug combinations. Many new drugs, including HER3, mTOR, and PI3K inhibitors, are in development to overcome therapy resistance (31-39).

In HER2 overexpressing cancers, possible mechanisms to overcome trastuzumab resistance include inhibition of down-stream effectors of HER2 that may be activated, even in the absence of HER2 signaling. For example, HER2 signaling activates PI3K/Akt/mTOR, which regulates cellular glucose metabolism (31). In a tumor with HER2-overexpression, mutations within the PI3K signaling pathway can allow continued PI3K activation even when HER2 is inhibited by trastuzumab or lapatinib (31, 33, 37). In this way, a heterogeneous tumor may contain subpopulations of tumor cells with varying levels of response to HER2 inhibition. Indeed, efforts to overcome HER2 inhibitor resistance include combined therapy of HER2 inhibitors with PI3K inhibitors (31, 37). Combined treatment to target HER2 and PI3K may increase therapy efficacy and decrease tumor recurrence. Similarly, HER3 can dimerize with HER2 to produce similar signaling effects within cells; therefore, HER3 inhibitors are being explored for combined treatment with trastuzumab (31).

2.5 Cellular Metabolism

Introduction to Cellular Metabolism

Cellular metabolism encompasses the biochemical processes within a cell which generate energy. Typically, these processes are broadly categorized into aerobic and anaerobic respiration. In mammalian cells, anaerobic respiration includes glycolysis, the breakdown of glucose into pyruvate, which occurs without oxygen in the cytoplasm. Aerobic respiration includes oxidative phosphorylation, the citric acid cycle, and the electron transport chain. These processes occur in the mitochondria and require oxygen. Nicotinamide adenine dinucleotide (NADH) and flavin adenine dinucleotide (FAD) are coenzymes that serve as electron carriers during cellular metabolism processes (Fig. 2.6) (40).

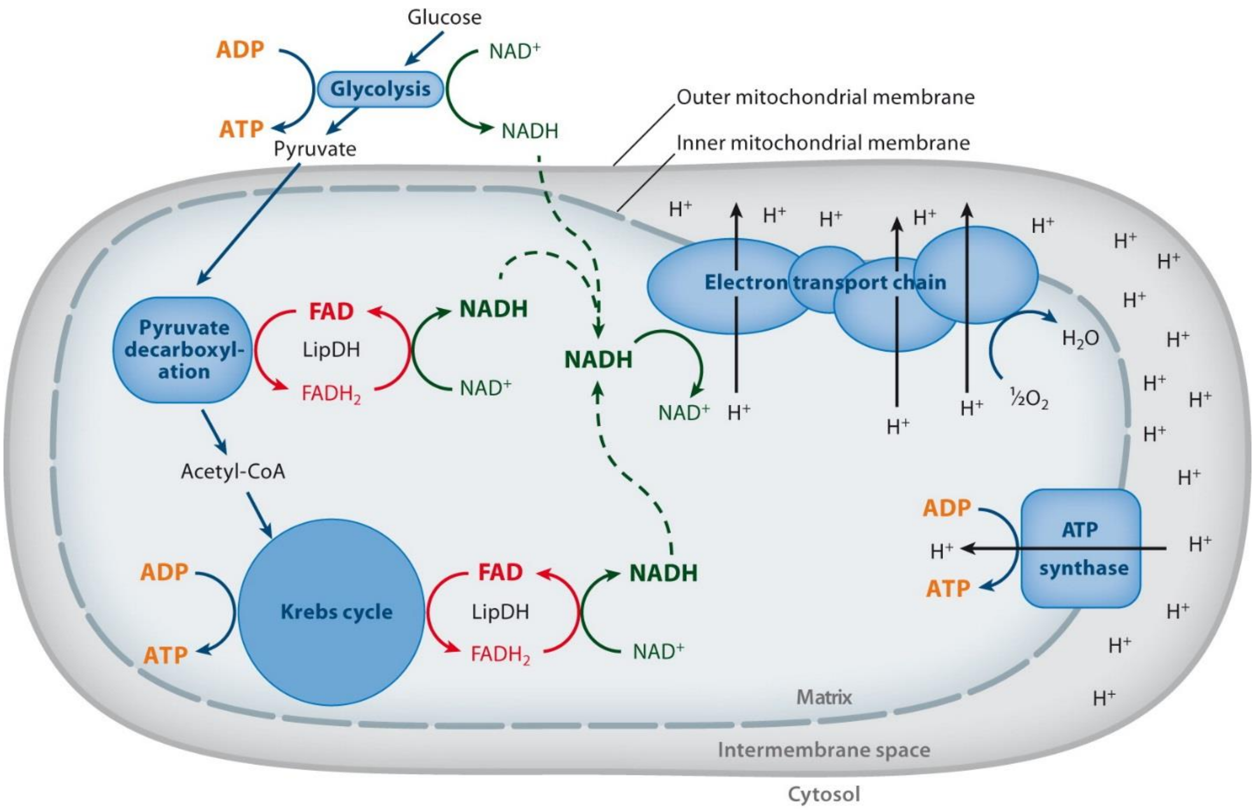

Figure 2.6: Cellular respiration and the roles of NADH and FAD.

Motivation for Using Cellular Metabolism as a Measure of Tumor Response to Therapy

Cancer cells often exhibit abnormal cellular metabolism. Unlike normal cells that rely on oxidative phosphorylation to generate ATP, or that use glycolysis under anaerobic conditions, cancer cells often generate ATP through aerobic glycolysis (41). This observation is generally expressed as the Warburg effect. Interestingly, oncogenic protein signaling in breast cancer cells often drives metabolism processes.

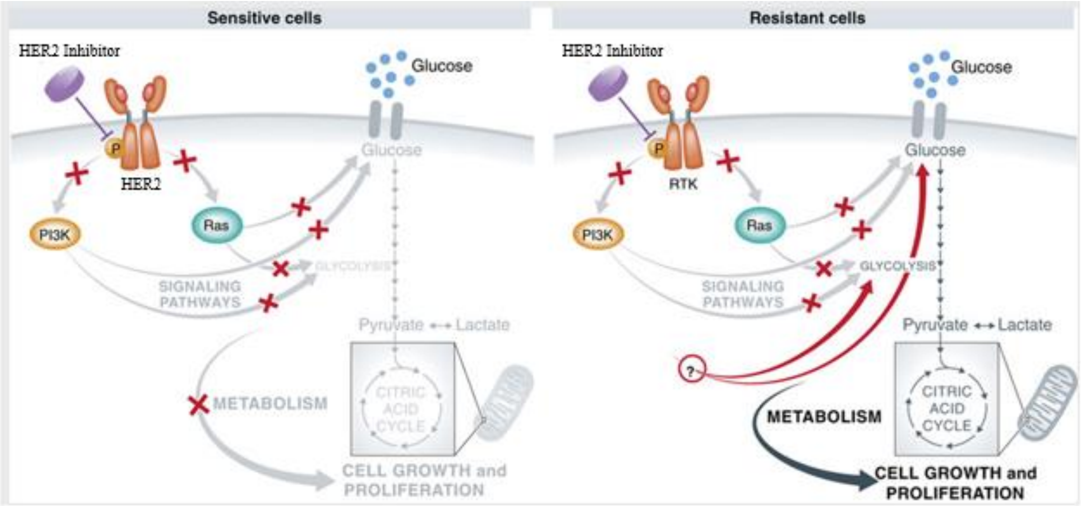

Figure 2.7: Role of HER2 in cellular metabolism. HER2 activation pathway and effect on cellular metabolism through PI3K in anti-HER2 drug sensitive and resistant cells. (42)

Many up-regulated oncogenes, including ER and HER2, directly affect or activate down-stream regulators of cellular metabolism pathways. ER regulates gene expression of glucose transporter proteins and proteins involved in oxidative phosphorylation and the citric acid cycle such as isocitrate dehydrogenase which actively reduces NAD^+ to NADH (43-46). HER2 mediates metabolism through signaling of the PI3K/AKT/mTOR pathway which directs transcription of glycolytic enzymes (47, 48). In mouse models of HER2 overexpressing breast cancer, trastuzumab and lapatinib inhibited PI3K activity and decreased glucose uptake (Fig. 2.7) (32, 34, 36, 42).

Furthermore, drug resistant cancers often display abnormal utilization of cellular metabolism pathways. Resistance to therapeutic agents, including the HER2 inhibitors lapatinib and trastuzumab, activates hypoxia signaling in the presence of adequate oxygen, consistent with the activation of aerobic glycolysis. Furthermore, PI3K pathway activation, which is a major driver of aerobic glycolysis, is often elevated in trastuzumab- or lapatinib-resistant breast cancer cells (32, 37, 49, 50). Possible mechanisms of trastuzumab resistance include metabolic activation by proteins outside of the PI3K/AKT/mTOR pathway (Fig. 2.7) and continued activation of

PI3K/AKT/mTOR despite HER2 inhibition (31, 32, 35, 49, 51). Therefore, cellular metabolism may be a powerful reporter of cellular malignancy and therapeutic efficacy due to the direct relationships between oncogene driven PI3K/AKT/mTOR activation and inhibition by anti-cancer drugs.

Metabolism Imaging Modalities

Current methods to monitor cellular metabolism and assess therapy response include immuno-histochemical (**IHC**) assessment of metabolic regulators, fluorodeoxyglucose positron emission tomography (**FDG-PET**), diffuse optical tomography (**DOT**), and metabolic flux analyses (37, 52-56). FDG-PET and IHC endpoints have been evaluated clinically as biomarkers of response (52, 55, 57-61). Evidence of metabolism-based contrast for tumor response to targeted inhibitors was demonstrated with the use of FDG-PET, which is capable of detecting areas of high glucose uptake, such as is seen in many solid tumors (62). A preliminary study of lapatinib-treated breast cancers showed changes in cellular metabolism, as measured by FDG-PET, after 1 month of lapatinib treatment (60). Yet, these currently available technologies provide only low resolution images and cannot resolve sub-populations of cells that may cause therapy relapse. FDG-PET and other technologies that monitor therapy response are limited to the evaluation of the single regimen received by the patient, and cannot predict a more efficacious treatment regimen if non-response is detected. Given the high cost and limitations of these procedures, it is unlikely that these will be adopted as standard of care, underscoring the need for more efficient, accurate, and cost-effective methods of identifying receptor expression and therapeutic response.

2.6 Fluorescence Lifetime Imaging

Fluorescence

Particular molecules, called fluorophores, are capable of emitting a photon of longer wavelength when excited by a photon of an optimal energy. This phenomenon is illustrated in the Joblonski diagram (Fig. 2.8). Several biomolecules are natural fluorophores, including collagen, tryptophan, NADH, FAD, and elastin. These fluorophores are often referred to as 'auto-fluorescent' because the addition of fluorescent dyes or antibodies is not required for imaging contrast.

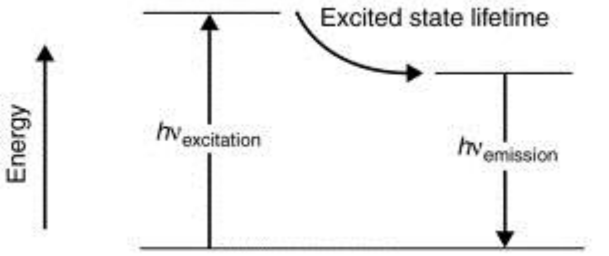

Figure 2.8: Jablonski Diagram of Fluorescence. When a fluorophore is excited by a photon ($h\upsilon_{excitation}$), the fluorophore enters an excited state. Sometime later, the fluorophore returns to ground state and emits a photon ($h\upsilon_{emission}$) (63).

Multiphoton Fluorescence

Multi-photon fluorescence microscopy uses the additive effect of two photons with one-half the energy necessary to excite the fluorophore (Fig. 2.9). The localized focus point of the excitation beam and negligent probability of two-photon excitation occurring outside the focal point of the beam, allows single pixel illumination and wide-field emission collection to increase depth-resolution and signal-to-noise ratio of weak fluorophores (Fig. 2.9) (64). In addition, multi-photon excitation wavelengths are double that of single photon fluorescence. This shifts the excitation of NADH and FAD into the near infrared (NIR) optical window where light absorption by tissue constituents is minimized (Fig. 2.10).

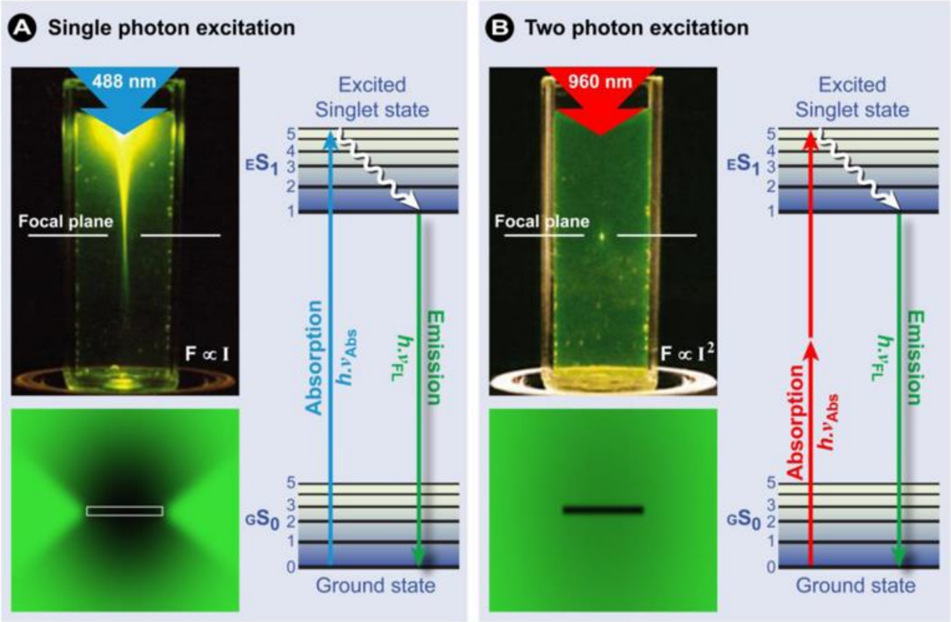

Figure 2.9: Multiphoton fluorescence. Focal point of single photon (A) and two photon (B) fluorescence (65).

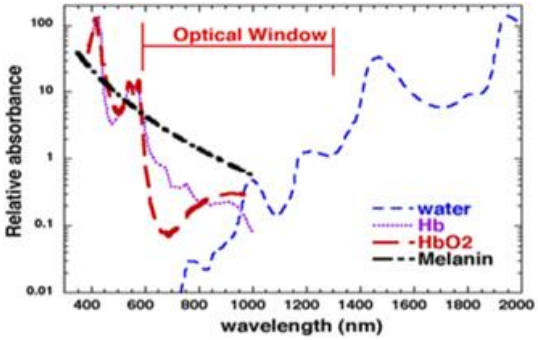

Figure 2.10: Relative absorbance of tissue constituents. Deeper tissue penetration is achieved by using excitation light in the NIR optical window (66).

Fluorescence Lifetime Imaging

Fluorescence lifetime imaging (FLIM) measures the average time a fluorophore is excited, or the time between an excitation photon absorption and emission photon. Fluorescence lifetime values report differences in the conformation and binding of the fluorophore as well as microenvironment changes, including pH, temperature, and proximity to quenchers such as free oxygen (64). A fluorescence decay curve plots the intensity of fluorescence of a region or pixel over time following excitation and is a cumulative recording of multiple events (Fig. 2.11). Fluorescence lifetime decays can be modeled as an exponential decay, or as a multi-exponential decay in the case of multiple lifetimes present in the sample (Fig. 2.11). Fluorescence lifetimes can be measured by time correlated single photon counting (TCSPC). TCSPC electronics time individual fluorescence events and generate fluorescence decay curves with repeated observations. TCSPC is the optimal fluorescence lifetime imaging technique for high accuracy of lifetime measurements and the low light levels observed with endogenous fluorophores (64).

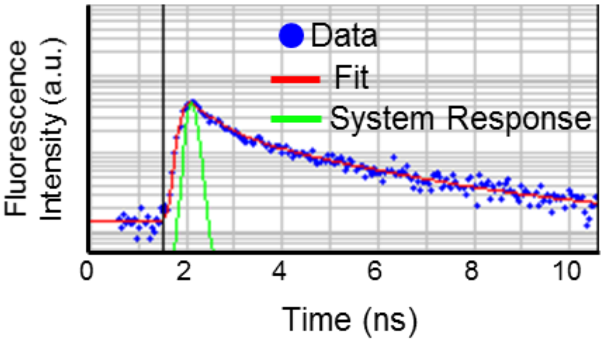

Figure 2.11: Fluorescence lifetime decay curve. After deconvolving the system response, decay data is modeled as an exponential decay to extract lifetime parameters, $I(t) = \alpha_1 exp^{-t/\tau_1} + \alpha_2 exp^{-t/\tau_2} + C$, where I(t) is the fluorescence intensity at time t after the excitation pulse, α_1 and α_2 are the weighted contributions of the short and long lifetime components $(\alpha_1 + \alpha_2) = 1$ and τ_1 and τ_2 are the short and long lifetime components, respectively, and C accounts for background light.

The fluorescence lifetimes of NADH and FAD are affected by the fluorophore microenvironment, with influencing factors including local oxygen levels, temperature, pH, fluorophore confirmation, and protein binding (64, 67). Fluorescence lifetime values remain fairly unexplored as reporters of cellular metabolism; however, exploratory studies have observed differences in NADH lifetime values in malignant and pre-malignant tissues (68, 69). Typically, in tissues, NADH and FAD molecules exist in two configurations, either unbound (free in solution) or protein-bound (67, 70). The fluorescence lifetime of protein-bound FAD and free NADH is short due to dynamic quenching of the adenine moiety (67, 70, 71). Therefore, the free FAD and protein-bound NADH have longer lifetimes.

Optical Imaging of Metabolism

Dynamic profiles of cellular metabolism can be obtained with optical metabolic imaging (OMI). OMI probes the endogenous fluorescence properties of two coenzymes involved in metabolism, reduced nicotinamide adenine dinucleotide (NAD(P)H) and flavin adenine dinucleotide (FAD). Optical imaging is an ideal modality for probing chemical specificity and molecular contrast within tissues, including auto-fluorescence imaging of NADH and FAD, which allows quantitative measurements of cellular metabolism. In oxidative phosphorylation, NADH is oxidized to NAD+ and FAD is reduced to $FADH_2$ (Fig. 2.12). In glycolysis, NAD+ is reduced to NADH (Fig. 2.12). Because fluorescence intensity is proportional to fluorophore concentration, the optical redox ratio (NADH fluorescence intensity divided by FAD fluorescence intensity) represents relative amounts of glycolysis and oxidative phosphorylation within a cell (72).

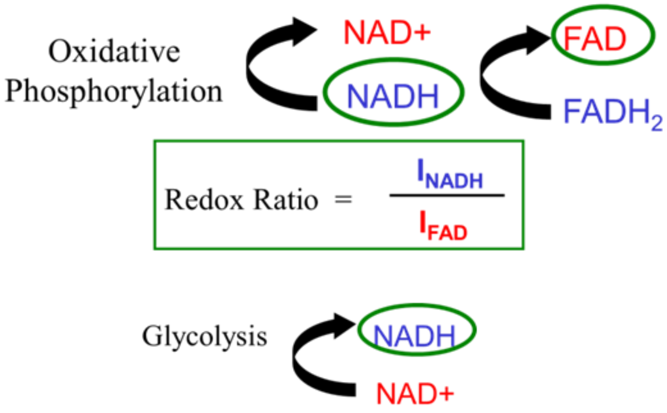

Figure 2.12: Optical redox ratio. The optical redox ratio is the relative intensity of cellular NADH fluorescence to FAD fluorescence.

The optical redox ratio is a proven method of probing cellular metabolism and has been used to differentiate cancerous from non-cancerous tissues in a variety of models including oral and breast cancer (69, 72-77). Ostrander et al. showed the optical redox ratio is sensitive to ER expression in breast cancer cell cultures and that treatment with tamoxifen decreased the redox ratio of those cells that were responsive to tamoxifen, but not those that lacked the estrogen receptor (77). The optical redox ratio is used to examine changes in cellular metabolism due to receptor expression and cellular response to targeted therapies.

The fluorescence lifetimes report changes in the microenvironment of NAD(P)H and FAD and are especially sensitive to the binding state of the fluorophore, as well as local temperature, pH, and proximity to quenchers such as molecular oxygen (64). Both NAD(P)H and FAD fluorescence lifetimes can be either short or long, depending on the binding state of NAD(P)H and FAD (free or bound to an enzyme complex) (67, 70). Previous studies have shown that OMI endpoints are sensitive to metabolism differences between cancer subtypes (78-80). Additionally, the OMI endpoints provide dynamic readouts of cellular metabolism and detect pre-malignant transformations within tissues (68, 69), classify subtypes of breast cancer cells (78, 79), and detect response to anti-cancer drugs (80). Furthermore, fluorescence microscopy is uniquely suited to study tumor heterogeneity in cells and tissues due to the high resolution capabilities of microscopy and molecular specificity attained by probing endogenous fluorophores. For this reason, OMI endpoints are attractive biomarkers of therapeutic response because they directly report cellular function, rather than a static measure of the genetic code.

FLIM Instrumentation

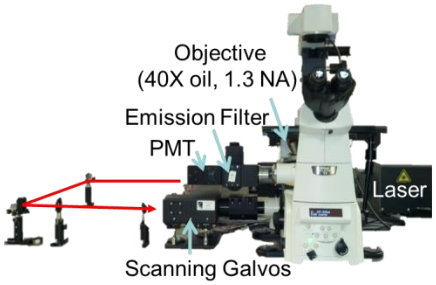

Figure 2.13: Multiphoton fluorescence microscope used to obtain NADH and FAD fluorescence lifetime images.

A custom built, commercial multi-photon fluorescence microscope (Bruker) is used to acquire NADH and FAD autofluorescence images (Fig. 2.13). In this experimental set up, a titanium: sapphire laser (Coherent Inc.) provides the excitation light and is tuned to 750 nm for excitation of NADH and 890 nm for FAD excitation. A 40X water-immersion objective (1.15 NA) or a 40X oil-immersion objective (1.3 NA) couples the excitation and emission light through an inverted microscope (TiE, Nikon). A GaAsP PMT (H7422P-40, Hamamatsu) detects emitted photons. A pre-amplifier and TCSPC electronics (SPC-150 card) enable fluorescence lifetime imaging.

Selection of Imaging Parameters

Imaging parameters were optimized for excitation of NADH and FAD. Excitation wavelengths and emission filters were chosen to ensure adequate isolation of NADH and FAD fluorescence. The peak excitation wavelength for NADH is near 350 nm and emission spans 400-500 nm (Fig. 7) (81). FAD excitation peak is near 450 nm. FAD emission spans 500-600 nm (Fig. 2.14) (81). For multiphoton excitation, NADH is excited at 750 nm and FAD is excited at 890 nm. Emission between 400-480 nm is collected for NADH, with the assumption that FAD excitation at 750 nm and emission at 400-480 nm is negligible. For FAD, 500-600 nm emission light is collected. Isolation of NADH and FAD fluorescence can be verified by a cyanide experiment. Average laser power, pixel dwell time, and lifetime imaging time are optimized to ensure adequate signal for lifetime decays without damage or photobleaching of the sample. The average laser power is 7.5-7.8 mW for NADH and 8.4-8.6 mW for FAD. A pixel dwell time of 4.8 μs is used. Images of 256x256 pixels are acquired using an integration time of 60 seconds. For consistent redox ratio measurements, system parameters, including laser power, PMT voltage, and integration time are maintained across all imaging sessions.

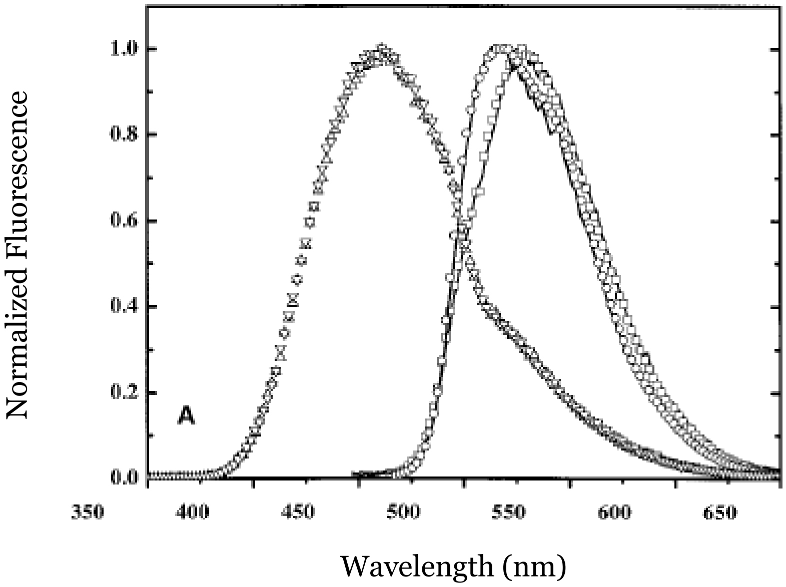

Figure 2.14. NADH and FAD Fluorescence Emission Spectra. Fluorescence emission spectra for NADH (triangle) and FAD (circle, square) (81).

2.7 Organoid Culture

Primary tumors can be cultured *ex vivo* as organoids, which contain the malignant tumor cells and the supporting cells from the tumor environment, such as fibroblasts, leukocytes, endothelial cells, and hematopoietic cells (82). Interactions between cancer cells and stromal cells have been shown to mediate therapeutic resistance in tumors (83). Therefore, organoid cultures provide an attractive platform to test cancer cell response to drugs in a relevant, "body-like" environment. Furthermore, multiple organoids can be generated from one biopsy, enabling high-throughput tests of multiple drug combinations with a small amount of tissue to identify the most effective treatment for an individual patient.

2.8 References

1. American Cancer Society. Breast Cancer Facts & Figures 2013-2014. 2013(Atlanta: American Cancer Society).
2. Schairer C, Mink PJ, Carroll L, Devesa SS. Probabilities of death from breast cancer and other causes among female breast cancer patients. Journal of the National Cancer Institute. 2004;96(17):1311-21.
3. Hoogstraten J, George W, Bloom H. Breast Cancer. Berlin: Springer-Verlag; 1989.
4. Dickson R, Lippman ME, McGuire W. Breast Cancer: Cellular and Molecular Biology. Boston: Kluwer Academic Publishers; 1988.
5. Blackwood MA, Weber BL. BRCA1 and BRCA2: from molecular genetics to clinical medicine. Journal of clinical oncology : official journal of the American Society of Clinical Oncology. 1998;16(5):1969-77.
6. Breast Cancer. National Institutes of Health, 2009.
7. Eroles P, Bosch A, Bermejo B, Lluch A. Mechanisms of resistance to hormonal treatment in breast cancer. Clin Transl Oncol. 2010;12(4):246-52.
8. Ross JS, Fletcher JA. The HER-2/neu oncogene in breast cancer: prognostic factor, predictive factor, and target for therapy. Stem Cells. 1998;16(6):413-28.
9. Freudenberg JA, Wang Q, Katsumata M, Drebin J, Nagatomo I, Greene MI. The role of HER2 in early breast cancer metastasis and the origins of resistance to HER2-targeted therapies. Exp Mol Pathol. 2009;87(1):1-11.

10. Esteva FJ, Yu DH, Hung MC, Hortobagyi GN. Molecular predictors of response to trastuzumab and lapatinib in breast cancer. Nat Rev Clin Oncol. 2010;7(2):98-107.

11. Chang CY, Kazmin D, Jasper JS, Kunder R, Zuercher WJ, McDonnell DP. The metabolic regulator ERRalpha, a downstream target of HER2/IGF-1R, as a therapeutic target in breast cancer. Cancer Cell. 2011;20(4):500-10.

12. Fonseca R, Hartmann LC, Petersen IA, Donohue JH, Crotty TB, Gisvold JJ. Ductal carcinoma in situ of the breast. Ann Intern Med. 1997;127(11):1013-22.

13. Breast Cancer Treatment. US Institutes of Health.

14. Fisher B, Anderson S, Bryant J, Margolese RG, Deutsch M, Fisher ER, Jeong JH, Wolmark N. Twenty-year follow-up of a randomized trial comparing total mastectomy, lumpectomy, and lumpectomy plus irradiation for the treatment of invasive breast cancer. The New England journal of medicine. 2002;347(16):1233-41.

15. Litiere S, Werutsky G, Fentiman IS, Rutgers E, Christiaens MR, Van Limbergen E, Baaijens MH, Bogaerts J, Bartelink H. Breast conserving therapy versus mastectomy for stage I-II breast cancer: 20 year follow-up of the EORTC 10801 phase 3 randomised trial. The Lancet Oncology. 2012;13(4):412-9.

16. Effects of chemotherapy and hormonal therapy for early breast cancer on recurrence and 15-year survival: an overview of the randomised trials. Lancet. 2005;365(9472):1687-717.

17. Tormey DC, Gray R, Falkson HC. Postchemotherapy adjuvant tamoxifen therapy beyond five years in patients with lymph node-positive breast cancer. Eastern Cooperative Oncology Group. Journal of the National Cancer Institute. 1996;88(24):1828-33.

18. Swain SM. Tamoxifen: the long and short of it. Journal of the National Cancer Institute. 1996;88(21):1510-2.

19. Burris HA, 3rd, Hurwitz HI, Dees EC, Dowlati A, Blackwell KL, O'Neil B, Marcom PK, Ellis MJ, Overmoyer B, Jones SF, Harris JL, Smith DA, Koch KM, Stead A, Mangum S, Spector NL. Phase I safety, pharmacokinetics, and clinical activity study of lapatinib (GW572016), a reversible dual inhibitor of epidermal growth factor receptor tyrosine kinases, in heavily pretreated patients with metastatic carcinomas. Journal of clinical oncology : official journal of the American Society of Clinical Oncology. 2005;23(23):5305-13.

20. Piccart-Gebhart MJ, Procter M, Leyland-Jones B, Goldhirsch A, Untch M, Smith I, Gianni L, Baselga J, Bell R, Jackisch C, Cameron D, Dowsett M, Barrios CH, Steger G, Huang CS, Andersson M, Inbar M, Lichinitser M, Lang I, Nitz U, Iwata H, Thomssen C, Lohrisch C, Suter TM, Ruschoff J, Suto T, Greatorex V, Ward C, Straehle C, McFadden E, Dolci MS, Gelber RD. Trastuzumab after adjuvant chemotherapy in HER2-positive breast cancer. The New England journal of medicine. 2005;353(16):1659-72.

21. Vogel CL, Cobleigh MA, Tripathy D, Gutheil JC, Harris LN, Fehrenbacher L, Slamon DJ, Murphy M, Novotny WF, Burchmore M, Shak S, Stewart SJ, Press M. Efficacy and safety

of trastuzumab as a single agent in first-line treatment of HER2-overexpressing metastatic breast cancer. Journal of Clinical Oncology. 2002;20(3):719-26.

22. Valabrega G, Montemurro F, Aglietta M. Trastuzumab: mechanism of action, resistance and future perspectives in HER2-overexpressing breast cancer. Annals of oncology : official journal of the European Society for Medical Oncology / ESMO. 2007;18(6):977-84.

23. Hudis CA. Trastuzumab--mechanism of action and use in clinical practice. The New England journal of medicine. 2007;357(1):39-51.

24. Mayfield S, Vaughn JP, Kute TE. DNA strand breaks and cell cycle perturbation in herceptin treated breast cancer cell lines. Breast cancer research and treatment. 2001;70(2):123-9.

25. Cuello M, Ettenberg SA, Clark AS, Keane MM, Posner RH, Nau MM, Dennis PA, Lipkowitz S. Down-regulation of the erbB-2 receptor by trastuzumab (herceptin) enhances tumor necrosis factor-related apoptosis-inducing ligand-mediated apoptosis in breast and ovarian cancer cell lines that overexpress erbB-2. Cancer Res. 2001;61(12):4892-900.

26. Chang J, Powles TJ, Allred DC, Ashley SE, Makris A, Gregory RK, Osborne CK, Dowsett M. Prediction of clinical outcome from primary tamoxifen by expression of biologic markers in breast cancer patients. Clin Cancer Res. 2000;6(2):616-21.

27. Holmes FA, Walters RS, Theriault RL, Forman AD, Newton LK, Raber MN, Buzdar AU, Frye DK, Hortobagyi GN. Phase II trial of taxol, an active drug in the treatment of metastatic breast cancer. Journal of the National Cancer Institute. 1991;83(24):1797-805.

28. Al-Hajj M, Wicha MS, Benito-Hernandez A, Morrison SJ, Clarke MF. Prospective identification of tumorigenic breast cancer cells. Proc Natl Acad Sci U S A. 2003;100(7):3983-8.

29. Sharma SV, Settleman J. Oncogene addiction: setting the stage for molecularly targeted cancer therapy. Genes & development. 2007;21(24):3214-31.

30. Kreso A, O'Brien CA, van Galen P, Gan OI, Notta F, Brown AM, Ng K, Ma J, Wienholds E, Dunant C, Pollett A, Gallinger S, McPherson J, Mullighan CG, Shibata D, Dick JE. Variable clonal repopulation dynamics influence chemotherapy response in colorectal cancer. Science. 2013;339(6119):543-8.

31. Arteaga CL, Sliwkowski MX, Osborne CK, Perez EA, Puglisi F, Gianni L. Treatment of HER2-positive breast cancer: current status and future perspectives. Nat Rev Clin Oncol. 2012;9(1):16-32.

32. Berns K, Horlings HM, Hennessy BT, Madiredjo M, Hijmans EM, Beelen K, Linn SC, Gonzalez-Angulo AM, Stemke-Hale K, Hauptmann M, Beijersbergen RL, Mills GB, van de Vijver MJ, Bernards R. A functional genetic approach identifies the PI3K pathway as a major determinant of trastuzumab resistance in breast cancer. Cancer Cell. 2007;12(4):395-402.

33. Chen FL, Xia W, Spector NL. Acquired resistance to small molecule ErbB2 tyrosine kinase inhibitors. Clin Cancer Res. 2008;14(21):6730-4.

34. Miller TW, Forbes JT, Shah C, Wyatt SK, Manning HC, Olivares MG, Sanchez V, Dugger TC, de Matos Granja N, Narasanna A, Cook RS, Kennedy JP, Lindsley CW, Arteaga CL. Inhibition of mammalian target of rapamycin is required for optimal antitumor effect of HER2 inhibitors against HER2-overexpressing cancer cells. Clin Cancer Res. 2009;15(23):7266-76.

35. Nahta R, O'Regan RM. Evolving strategies for overcoming resistance to HER2-directed therapy: targeting the PI3K/Akt/mTOR pathway. Clin Breast Cancer. 2010;10 Suppl 3:S72-8.

36. Tan M, Zhao YH, Liu H, Liu ZX, Ding Y, LeDoux SP, Wilson GL, Voellmy R, Lin YF, Lin WS, Nahta R, Liu BL, Fodstad O, Chen JQ, Wu Y, Price JE. Overcoming Trastuzumab Resistance in Breast Cancer by Targeting Dysregulated Glucose Metabolism. Cancer Res. 2011;71(13):4585-97.

37. Wang L, Zhang Q, Zhang J, Sun S, Guo H, Jia Z, Wang B, Shao Z, Wang Z, Hu X. PI3K pathway activation results in low efficacy of both trastuzumab and lapatinib. BMC Cancer. 2011;11(1):248.

38. Xia W, Bacus S, Hegde P, Husain I, Strum J, Liu L, Paulazzo G, Lyass L, Trusk P, Hill J, Harris J, Spector NL. A model of acquired autoresistance to a potent ErbB2 tyrosine kinase inhibitor and a therapeutic strategy to prevent its onset in breast cancer. Proc Natl Acad Sci U S A. 2006;103(20):7795-800.

39. Garrett JT, Olivares MG, Rinehart C, Granja-Ingram ND, Sanchez V, Chakrabarty A, Dave B, Cook RS, Pao W, McKinely E, Manning HC, Chang J, Arteaga CL. Transcriptional and posttranslational up-regulation of HER3 (ErbB3) compensates for inhibition of the HER2 tyrosine kinase. Proc Natl Acad Sci U S A. 2011;108(12):5021-6.

40. Georgakoudi I, Quinn KP. Optical imaging using endogenous contrast to assess metabolic state. Annu Rev Biomed Eng. 2012;14:351-67.

41. Warburg O. On the origin of cancer cells. Science. 1956;123(3191):309-14.

42. Locasale JW. Metabolic rewiring drives resistance to targeted cancer therapy. Mol Syst Biol. 2012;8:597.

43. Chen JQ, Brown TR, Russo J. Regulation of energy metabolism pathways by estrogens and estrogenic chemicals and potential implications in obesity associated with increased exposure to endocrine disruptors. Biochimica Et Biophysica Acta. 2009;1793(7):1128-43.

44. Cheng CM, Cohen M, Wang J, Bondy CA. Estrogen augments glucose transporter and IGF1 expression in primate cerebral cortex. FASEB J. 2001;15(6):907-15.

45. Yadav RN. Isocitrate dehydrogenase activity and its regulation by estradiol in tissues of rats of various ages. Cell Biochem Funct. 1988;6(3):197-202.

46. Pastorelli R, Carpi D, Airoldi L, Chiabrando C, Bagnati R, Fanelli R, Moverare S, Ohlsson C. Proteome analysis for the identification of in vivo estrogen-regulated proteins in bone. Proteomics. 2005;5(18):4936-45.

47. Harari D, Yarden Y. Molecular mechanisms underlying ErbB2/HER2 action in breast cancer. Oncogene. 2000;19(53):6102-14.

48. Plas DR, Thompson CB. Akt-dependent transformation: there is more to growth than just surviving. Oncogene. 2005;24(50):7435-42.

49. Engelman JA, Luo J, Cantley LC. The evolution of phosphatidylinositol 3-kinases as regulators of growth and metabolism. Nat Rev Genet. 2006;7(8):606-19.

50. Cooper C, Liu GY, Niu YL, Santos S, Murphy LC, Watson PH. Intermittent hypoxia induces proteasome-dependent down-regulation of estrogen receptor alpha in human breast carcinoma. Clin Cancer Res. 2004;10(24):8720-7.

51. Yakes FM, Chinratanalab W, Ritter CA, King W, Seelig S, Arteaga CL. Herceptin-induced inhibition of phosphatidylinositol-3 kinase and Akt Is required for antibody-mediated effects on p27, cyclin D1, and antitumor action. Cancer Res. 2002;62(14):4132-41.

52. Brown RS, Wahl RL. Overexpression of Glut-1 glucose transporter in human breast cancer. An immunohistochemical study. Cancer. 1993;72(10):2979-85.

53. Zhang D, Tai LK, Wong LL, Chiu LL, Sethi SK, Koay ES. Proteomic study reveals that proteins involved in metabolic and detoxification pathways are highly expressed in HER-2/neu-positive breast cancer. Mol Cell Proteomics. 2005;4(11):1686-96.

54. Nguyen QD, Perumal M, Waldman TA, Aboagye EO. Glucose Metabolism Measured by [F]Fluorodeoxyglucose Positron Emission Tomography Is Independent of PTEN/AKT Status in Human Colon Carcinoma Cells. Transl Oncol. 2011;4(4):241-8.

55. Shah C, Miller TW, Wyatt SK, McKinley ET, Olivares MG, Sanchez V, Nolting DD, Buck JR, Zhao P, Ansari MS, Baldwin RM, Gore JC, Schiff R, Arteaga CL, Manning HC. Imaging biomarkers predict response to anti-HER2 (ErbB2) therapy in preclinical models of breast cancer. Clin Cancer Res. 2009;15(14):4712-21.

56. Specht JM, Kurland BF, Montgomery SK, Dunnwald LK, Doot RK, Gralow JR, Ellis GK, Linden HM, Livingston RB, Allison KH, Schubert EK, Mankoff DA. Tumor Metabolism and Blood Flow as Assessed by Positron Emission Tomography Varies by Tumor Subtype in Locally Advanced Breast Cancer. Clinical Cancer Research. 2010;16(10):2803-10.

57. Basu S, Chen W, Tchou J, Mavi A, Cermik T, Czerniecki B, Schnall M, Alavi A. Comparison of triple-negative and estrogen receptor-positive/progesterone receptor-positive/HER2-negative breast carcinoma using quantitative fluorine-18 fluorodeoxyglucose/positron emission tomography imaging parameters: a potentially useful method for disease characterization. Cancer. 2008;112(5):995-1000.

58. Jacobs MA, Ouwerkerk R, Wolff AC, Gabrielson E, Warzecha H, Jeter S, Bluemke DA, Wahl R, Stearns V. Monitoring of neoadjuvant chemotherapy using multiparametric, (23)Na sodium MR, and multimodality (PET/CT/MRI) imaging in locally advanced breast cancer. Breast cancer research and treatment. 2011;128(1):119-26.

59. Mankoff DA, Dunnwald LD, L. K., Doot RK, Specht JM, Gralow JR, Ellis GK, Livingston RB, Linden HM, Gadi VK, Kurland BF, Schubert EK, Muzi M. PET Tumor Metabolism in Locally Advanced Breast Cancer Patients Undergoing Neoadjuvant Chemotherapy: Value of Static versus Kinetic Measures of Fluorodeoxyglucose Uptake. Clinical Cancer Research. 2011;17(8):2400-9.

60. Minami H, Kawada K, Murakami K, Sato T, Kojima Y, Ebi H, Mukai H, Tahara M, Shimokata K. Prospective study of positron emission tomography for evaluation of the activity of lapatinib, a dual inhibitor of the ErbB1 and ErbB2 tyrosine kinases, in patients with advanced tumors. Japanese Journal of Clinical Oncology. 2007;37(1):44-8.

61. Reilly RM, McLarty K, Fasih A, Scollard DA, Done SJ, Vines DC, Green DE, Costantini DL. (18)F-FDG Small-Animal PET/CT Differentiates Trastuzumab-Responsive from Unresponsive Human Breast Cancer Xenografts in Athymic Mice. Journal of Nuclear Medicine. 2009;50(11):1848-56.

62. Benard F, Aliaga A, Rousseau JA, Cadorette J, Croteau E, van Lier JE, Lecomte R. A small animal positron emission tomography study of the effect of chemotherapy and hormonal therapy on the uptake of 2-deoxy-2-[F-18]fluoro-D-glucose in murine models of breast cancer. Molecular Imaging and Biology. 2007;9(3):144-50.

63. Emptage NJ. Fluorescent imaging in living systems. Curr Opin Pharmacol. 2001;1(5):521-5.

64. Lakowicz J. Principles of fluorescence spectroscopy. New York: Plenum Publishers; 1999.

65. Ishikawa-Ankerhold HC, Ankerhold R, Drummen GP. Advanced fluorescence microscopy techniques--FRAP, FLIP, FLAP, FRET and FLIM. Molecules. 2012;17(4):4047-132.

66. Huang Y, Hamblin M, Chen AC-H. Low-level laser therapy: an emerging clinical paradigm. SPIE Newsroom [Internet]. 2009.

67. Lakowicz JR, Szmacinski H, Nowaczyk K, Johnson ML. Fluorescence Lifetime Imaging of Free and Protein-Bound Nadh. Proc Natl Acad Sci U S A. 1992;89(4):1271-5.

68. Skala MC, Riching KM, Bird DK, Gendron-Fitzpatrick A, Eickhoff J, Eliceiri KW, Keely PJ, Ramanujam N. In vivo multiphoton fluorescence lifetime imaging of protein-bound and free nicotinamide adenine dinucleotide in normal and precancerous epithelia. Journal of biomedical optics. 2007;12(2):024014.

69. Skala MC, Riching KM, Gendron-Fitzpatrick A, Eickhoff J, Eliceiri KW, White JG, Ramanujam N. In vivo multiphoton microscopy of NADH and FAD redox states, fluorescence lifetimes, and cellular morphology in precancerous epithelia. Proc Natl Acad Sci U S A. 2007;104(49):19494-9.

70. Tanaka F, Tamai N, Yamazaki I. Picosecond-resolved fluorescence spectra of D-amino-acid oxidase. A new fluorescent species of the coenzyme. Biochemistry. 1989;28(10):4259-62.

71. Sato K, Nishina Y, Shiga K, Tanaka F. Hydrogen-bonding dynamics of free flavins in benzene and FAD in electron-transferring flavoprotein upon excitation. J Photochem Photobiol B. 2003;70(2):67-73.

72. Chance B, Schoener B, Oshino R, Itshak F, Nakase Y. Oxidation-reduction ratio studies of mitochondria in freeze-trapped samples. NADH and flavoprotein fluorescence signals. J Biol Chem. 1979;254(11):4764-71.

73. Drezek R, Brookner C, Pavlova I, Boiko I, Malpica A, Lotan R, Follen M, Richards-Kortum R. Autofluorescence microscopy of fresh cervical-tissue sections reveals alterations in tissue biochemistry with dysplasia. Photochem Photobiol. 2001;73(6):636-41.

74. Gulledge CJ, Dewhirst MW. Tumor oxygenation: a matter of supply and demand. Anticancer Res. 1996;16(2):741-9.

75. Kirkpatrick ND, Zou C, Brewer MA, Brands WR, Drezek RA, Utzinger U. Endogenous fluorescence spectroscopy of cell suspensions for chemopreventive drug monitoring. Photochem Photobiol. 2005;81(1):125-34.

76. Mujat C, Greiner C, Baldwin A, Levitt JM, Tian F, Stucenski LA, Hunter M, Kim YL, Backman V, Feld M, Munger K, Georgakoudi I. Endogenous optical biomarkers of normal and human papillomavirus immortalized epithelial cells. Int J Cancer. 2008;122(2):363-71.

77. Ostrander JH, McMahon CM, Lem S, Millon SR, Brown JQ, Seewaldt VL, Ramanujam N. Optical redox ratio differentiates breast cancer cell lines based on estrogen receptor status. Cancer Res. 2010;70(11):4759-66.

78. Walsh A, Cook RS, Rexer B, Arteaga CL, Skala MC. Optical imaging of metabolism in HER2 overexpressing breast cancer cells. Biomedical optics express. 2012;3(1):75-85.

79. Walsh AJ, Cook RS, Manning HC, Hicks DJ, Lafontant A, Arteaga CL, Skala MC. Optical metabolic imaging identifies glycolytic levels, subtypes, and early-treatment response in breast cancer. Cancer Res. 2013;73(20):6164-74.

80. Walsh AJ, Cook RS, Sanders ME, Aurisicchio L, Ciliberto G, Arteaga CL, Skala MC. Quantitative optical imaging of primary tumor organoid metabolism predicts drug response in breast cancer. Cancer Res. 2014;74(18):5184-94.

81. Huang S, Heikal AA, Webb WW. Two-photon fluorescence spectroscopy and microscopy of NAD(P)H and flavoprotein. Biophys J. 2002;82(5):2811-25.

82. Campbell JJ, Davidenko N, Caffarel MM, Cameron RE, Watson CJ. A multifunctional 3D co-culture system for studies of mammary tissue morphogenesis and stem cell biology. PLoS One. 2011;6(9):e25661.

83. Straussman R, Morikawa T, Shee K, Barzily-Rokni M, Qian ZR, Du J, Davis A, Mongare MM, Gould J, Frederick DT, Cooper ZA, Chapman PB, Solit DB, Ribas A, Lo RS, Flaherty KT, Ogino S, Wargo JA, Golub TR. Tumour micro-environment elicits innate resistance to RAF inhibitors through HGF secretion. Nature. 2012;487(7408):500-4.

CHAPTER 3

Optical Metabolic Imaging Quantifies Heterogeneous Cell Populations

Walsh AJ, Skala MC, “Optical metabolic imaging quantifies heterogeneous cell populations,” *Biomedical Optics Express*, 2015; 6(2):559-573.

3.1 Abstract

The genetic and phenotypic heterogeneity of cancers can contribute to tumor aggressiveness, invasion, and resistance to therapy. Fluorescence imaging occupies a unique niche to investigate tumor heterogeneity due to its high resolution and molecular specificity. Here, heterogeneous populations are identified and quantified by combined optical metabolic imaging and subpopulation analysis (OMI-SPA). OMI probes the fluorescence intensities and lifetimes of metabolic enzymes in cells to provide images of cellular metabolism, and SPA models cell populations as mixed Gaussian distributions to identify cell subpopulations. In this study, OMI-SPA is characterized by simulation experiments and validated with cell experiments. To generate heterogeneous populations, two breast cancer cell lines, SKBr3 and MDA-MB-231, were co-cultured at varying proportions. OMI-SPA correctly identifies two populations with minimal mean and proportion error using the optical redox ratio (fluorescence intensity of NAD(P)H divided by the intensity of FAD), mean NAD(P)H fluorescence lifetime, and OMI index. Simulation experiments characterized the relationships between sample size, data standard deviation, and subpopulation mean separation distance required for OMI-SPA to identify subpopulations.

3.2 Introduction

Solid tumors are highly heterogeneous, both across patients and within individual tumors. Tumor heterogeneity may contribute to tumor aggression, invasion, metastases, and therapy resistance (1-3). Studies of tumor heterogeneity are challenging because traditional cell and tissue analyses require pooling of proteins, RNA, or DNA from hundreds to thousands of cells, which provides information on the protein and genetic expression of the majority of cells but may mask unique expression profiles and phenotypes of heterogeneous populations. Therefore, a technology capable of resolving cancer cell behaviors at single cell resolution is imperative for studies of tumor heterogeneity.

Breast cancers are often classified into three subtypes based on the expression or lack of expression of oncogenic proteins within the malignant cells. In particular, estrogen receptor (ER), progesterone receptor (PR), and human epidermal growth factor receptor 2 (HER2), are used to classify breast cancers and inform clinical therapy selection. Breast cancer clinical subtypes include: triple negative (not expressing any of the three receptors), ER positive (expressing ER but lacking HER2 overexpression), and HER2 overexpressing (overexpressing HER2 receptors, ER and PR may be expressed or not). Primary tumors are heterogeneous, containing subpopulations of cells with different genetic profiles and protein expression (1, 4, 5). Therapy selection is often based on the expression or lack of expression of ER and HER2 in a small sampling of cells, a biopsy. However, due to heterogeneity across large tumors and within the biopsy itself, populations of cells with different receptor expression and/or adaptations that make them resistant to therapy, may escape clinical detection (1). This suggests that different portions of a tumor may respond differently to treatment, and while therapies are selected to target the majority of cells, there may be subpopulations of malignant cells not adequately targeted. Subpopulations of cells with stem cell like behaviors may contribute to drug resistance and recurrent tumor growth (6). Cancer stem cells comprise between 3 and 35% of the number of cells within a solid breast tumor (6).

Fluorescence microscopy is uniquely suited to study tumor heterogeneity in cells and tissues due to the high resolution capabilities of microscopy and molecular specificity attained by probing fluorophores. Dynamic profiles of cellular metabolism can be obtained with optical metabolic imaging (OMI). OMI probes the endogenous fluorescence properties of two coenzymes involved in metabolism, reduced nicotinamide adenine dinucleotide (NAD(P)H) and flavin adenine dinucleotide (FAD). NAD(P)H and FAD are used in multiple metabolism processes including glycolysis and oxidative phosphorylation. The endpoints of OMI include the redox ratio, NAD(P)H fluorescence lifetime, FAD fluorescence lifetime, and a combination variable, the OMI index. The redox ratio is the intensity of NAD(P)H fluorescence relative to the intensity of FAD fluorescence and provides relative information on the global metabolism of the cell (7, 8). The redox ratio is sensitive to shifts in metabolic pathways (7, 9). The fluorescence lifetimes report changes in the microenvironment of NAD(P)H and FAD and are especially sensitive to the binding state of the fluorophore, as well as local temperature, pH, and proximity to quenchers such as molecular oxygen (10). Both NAD(P)H and FAD fluorescence lifetimes can be either short or long, depending on the binding state of NAD(P)H and FAD (free or bound to an enzyme complex) (11, 12). Previous studies have shown that OMI endpoints are sensitive to metabolism differences between cancer subtypes (9, 13, 14). Additionally, the OMI endpoints provide dynamic readouts of cellular metabolism and detect pre-malignant transformations within tissues (15, 16), classify subtypes of breast cancer cells (9, 13), and detect response to anti-cancer drugs (14).

This study describes and validates OMI subpopulation analysis (OMI-SPA) for identification and quantification of cellular heterogeneity. OMI can be performed at high resolution to allow reporting of OMI endpoints at the single-cell level. Heterogeneity of the cell population can then be assessed by subpopulation analysis (SPA). SPA uses mixed distribution Gaussian models with multiple components to fit the population density representation of the data. In this study, we used both computational simulation and co-cultured experiments to validate OMI-

SPA for identification and quantification of cellular subpopulation heterogeneity. Simulation experiments demonstrate the population characteristics required for robust SPA identification of two subpopulations. These experiments were validated by OMI-SPA of heterogeneous samples created by co-culturing two different breast cancer cell lines, a triple negative breast cancer (MDA-MB-231) and a HER2+ cell line (SKBr3) at varying proportions. These two cell lines were chosen to represent cell populations responsive (SKBr3) and resistant (MDA-MB-231) to the anti-HER2 antibody, trastuzumab. The OMI endpoints and morphology of these two cells are sufficiently different to allow computational separation and heterogeneity analysis.

3.3 Methods

3.3.1 SKBr3 and MDA-MB-231 Specific Simulations

The average and standard deviation for the experimentally measured redox ratio, NAD(P)H mean lifetime, and FAD mean lifetime for the SKBr3 cells and MDA-MB-231 cells cultured independently were determined and used to generate model data sets. A random number generator (Matlab) was used to generate a data set of repeated observations within the distributions of the OMI endpoints for a population of N cells, containing a percent SKBr3 cells and b percent MDA-MB-231 cells. N, a, and b were varied to investigate the ability of OMI-SPA to identify two populations under a range of conditions. N ranged from 25 to 1000 cells and a varied from 0 to 1 (b = 1-a, and varied from 1 to 0). These simulate data sets were then evaluated with subpopulation analysis (Methods 2.2).

3.3.2 Subpopulation Analysis (SPA)

Each cell population is modeled as a Gaussian mixture distribution model (9, 14, 17),

$f(y;\ \Phi_g) = \sum_{i=1}^{g} \pi_i \phi(y;\ \mu_i, V_i)$, where g is the number of components, $\phi(y;\ \mu_i, V_i)$ represents a normal probability density function with mean μ_i and variance V_i, and π_i is the mixing proportion. Φ_g represents the unknown parameters, (π_i, μ_i, V_i): i =1…g in a g-component model. The mixture model is fitted by maximum likelihood using the expectation maximization algorithm to determine the optimum parameters, (π, μ, V), (Matlab). In the simulation and co-culture experiments, data is modeled three times as Gaussian mixture distribution models with 1-3 components (g = 1, 2, or 3). Fit parameters for each model including the Akaiki information criteria (AIC), population means, population standard deviations, and proportions, were recorded. The AIC information criteria is a measure of model goodness of fit and is minimized in the optimal model (18). The most representative model of the data was selected as the model with the lowest AIC.

3.3.3 Cell culture

MDA-MB-231 and SKBr3 cells were grown separately in DMEM with 10% fetal bovine serum and 1% penicillin: streptomycin. Cells were plated at a density of 10^6 cells per 35-mm glass bottom petri dish (MatTek Corp.), 48 hours before imaging, in the following proportions based on cell count (Table 3.1): 100% (10^6) MDA-MB-231 cells; 70% (7×10^5) MDA-MB-231 cells and 30% (3×10^5) SKBr3 cells; 50% (5×10^5) MDA-MB-231 cells and 50% (5×10^5) SKBr3 cells; 30% (3×10^5) MDA-MB-231 cells and 70% (7×10^5) SKBr3 cells; and 100% (10^6) SKBr3 cells. Two 35-mm glass bottom petri dishes were plated per group.

3.3.4 Fluorescence lifetime instrumentation

Fluorescence lifetime imaging was performed on a custom built multi-photon microscope (Bruker), which has previously been described (9, 14, 19). Excitation and emission light are coupled through a 40X oil immersion (1.3 NA) objective of an inverted microscope (Nikon, TiE). For NAD(P)H excitation, a titanium:sapphire laser (Coherent Inc.) was tuned to 750 nm (average power 7.5-7.9 mW). For FAD excitation, the laser was tuned to 890 nm (average power 8.4-6 mW). Bandpass filters, with a 440-480 nm passband for NAD(P)H and a 500-600 nm passband for FAD, isolated emission light. A pixel dwell time of 4.8 μs was used to acquire 256x256 pixel images. Each fluorescence lifetime image was collected using time correlated single photon counting electronics (SPC-150, Becker and Hickl) and a GaAsP PMT (H7422P-40, Hamamatsu). Photon count rates were maintained above 5×10^5 for the entire 60 second image acquisition time, ensuring no photobleaching occurred and adequate signal for fluorescence lifetime decay fits.

3.3.5 Cell imaging

Cells were imaged directly through the bottom of 35mm glass-bottom petri dishes (MatTek Corp). For each dish, six representative fields of view were imaged, for a total number of ~200 cells per group. First, an NAD(P)H lifetime image was acquired, and then an FAD lifetime image was acquired from the same field of view. Sequential fields of view were separated by at least 1 field of view, 270 μm.

3.3.6 Generation of redox ratio images

A fluorescence intensity image was generated by integrating the fluorescence lifetime decay over time for each pixel in the lifetime image. The total number of NAD(P)H photons per pixel was then divided by the total number of FAD photons per pixel and used to create a redox ratio image for each field of view (Matlab, Mathworks). NAD(P)H and FAD fluorescence specific to cellular metabolism is localized in the cytoplasm and mitochondria. Therefore, the redox ratio image was thresholded to remove background and nuclear fluorescence, and the average redox ratio for each remaining cell cytoplasm was computed (ImageJ). Cells were manually segmented in ImageJ.

3.3.7 Generation of NAD(P)H and FAD lifetime images

For each pixel, the photon counts for the 9 surrounding pixels were binned (SPCImage). Fluorescence lifetime components for each pixel were computed by de-convolving a measured system response curve from urea crystals and fitting the fluorescent decay to a two component model, $I(t) = \alpha_1 \exp\left(-\frac{t}{\tau_1}\right) + \alpha_2 \exp\left(-\frac{t}{\tau_2}\right) + C$. In this model, I(t) is the fluorescence intensity at time t after the laser excitation pulse, α_1 and α_2 are the fractional contributions of the free and bound molecules (i.e. $\alpha_1 + \alpha_2 = 1$), τ_1 and τ_1 are the fluorescence lifetimes of the short and long lifetime components, and C is a constant that accounts for background light. Matrices of the lifetime components were exported as ascii files for further processing in ImageJ. The mean lifetime, $\tau_m = \alpha_1 \tau_1 + \alpha_2 \tau_2$, was computed for each pixel to create a mean lifetime image for each field of view. The NAD(P)H τ_m and FAD τ_m for each cell cytoplasm was computed and recorded. The OMI index (14) is a linear combination of mean centered redox ratio, NAD(P)H τ_m, and FAD τ_m data and can be computed per cell as follows: $OMI\ Index = \frac{RR_i}{\langle RR \rangle} + \frac{NAD(P)H\ \tau_{mi}}{\langle NAD(P)H\ \tau_m \rangle} - \frac{FAD\ \tau_{mi}}{\langle FAD\ \tau_m \rangle}$.

3.3.8 OMI-SPA Behavior Simulations

Simulation experiments were performed to model the behavior of OMI-SPA for generalized data. In the first simulation, populations of cells were generated with a normalized mean of 1 and equal proportions of the two populations. The standard deviation and distance between the means was varied from 0-1 and 0-2, respectively. In the last simulations, the mean distance was varied from 0-2, the population proportions varied from 0-1, and the standard deviation of the populations was 0.05, 0.1, 0.25, or 0.5. These normalized standard deviation values span the range typically observed in OMI data (9, 14). Simulated cell populations were generated for each mean distance, population proportion, and standard deviation at increasing sample sizes (up to 10,000) to determine the minimum sample size necessary to resolve two subpopulations ($AIC_2 < AIC_1 - 20$).

3.4 Results

3.4.1 MDA-MB-231 and SKBr3 Simulations

First, SPA was performed on simulated cell populations using experimentally determined mean and standard deviation values of the redox ratio of SKBr3 and MDA-MB-231 cells, 1.92 +/- 0.39 and 1.06 +/- 0.22, respectively. The AIC represents a model goodness of fit and is minimized in the optimal model (18). The AIC includes penalties for an increased number of model components, to account for increased fitness of models with increased components (18). The AIC for two components is less than the AIC for the single component model ($AIC_1 - AIC_2 > 0$) at large sample sizes and SKBr3 proportions less than 0.8 (Fig. 3.1a). The error of the SKBr3 redox ratio mean is greatest (>10%) at high and low proportions and low sample sizes (Fig. 3.1b). SKBr3 redox ratio mean error is minimized (<5%) at high sample sizes and proportions near 50% (Fig. 3.1b). Likewise, MDA-MB-231 mean error is maximal (>10%) at small sample sizes and low proportions, and minimized (<5%) with high sample sizes and proportions around 50% (Fig. 3.1c). The large errors of MDA-MB-231 mean values at SKBr3 population proportions greater than 0.8, correspond to data points where the two-component model fit the data less well than the single component model. The population proportion error, or the error of how many cells are attributed to each cell subpopulation, is minimal (<5%) at high sample sizes and at SBRr3 proportions less than 80% (Fig. 3.1d).

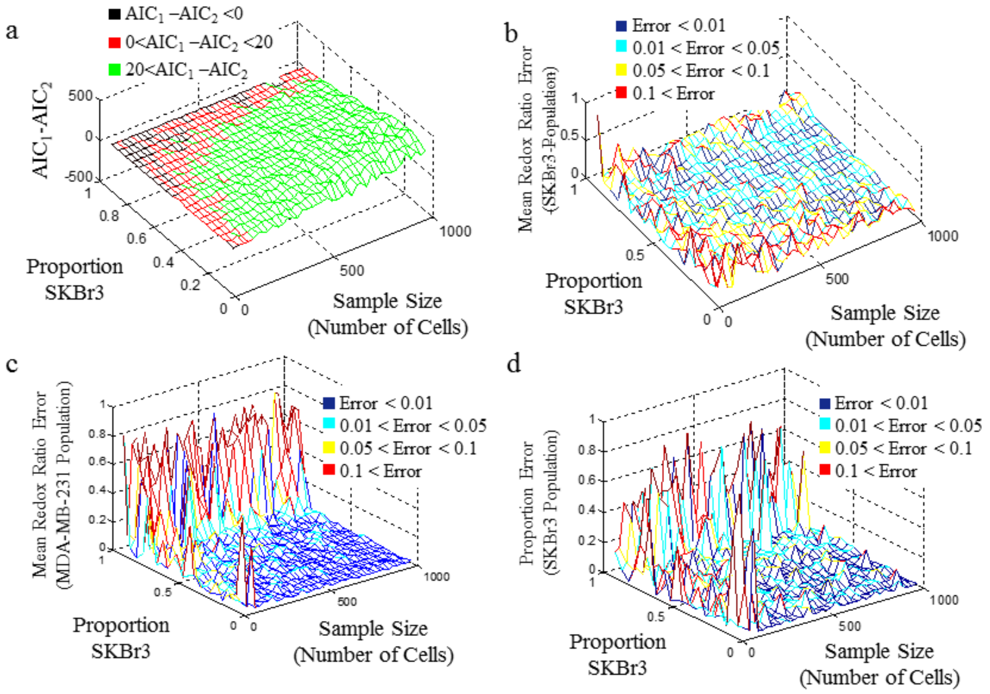

Figure 3.1. Behavior of OMI-SPA to model simulated data using the redox ratio mean and standard deviation of SKBr3 and MDA-MB-231 cells. (a) Difference in the AIC values of 1 and 2 component Gaussian models of the simulated cell populations as a function of varying sample sizes and varying proportions (0% to 100%) of SKBr3 cells. AIC_1-AIC_2 > 0 indicates two component model is a better fit than the one-component model. (b) Error of the mean redox ratio computed for the SKBr3 subpopulation, and (c) MDA-MB-231 population. (d) Error of the estimated proportion of the SKBr3 subpopulation.

Similar simulations demonstrate the ability of OMI-SPA to identify SKBr3 and MDA-MB-231 subpopulations using NAD(P)H τ_m values (Fig. 3.2). The SKBr3 cells have a mean NAD(P)H τ_m of 1.31 +/- 0.13 ns and the MDA-MB-231 cells have a mean NAD(P)H τ_m of 0.85 +/- 0.11 ns, determined from experiments. In the simulation, OMI-SPA identifies two populations in all simulated data sets with a sample size greater than 75 (Fig. 3.2a) and the error of the SKBr3 and MDA-MB-231 subpopulation means identified by the models is within 1% at sample sizes greater than 100 and proportions between 20% and 80% (Fig. 3.2b-c). Likewise, the proportion error is minimized (<5%) at sample sizes > 200 and SKBr3 proportions between 20 and 80%.

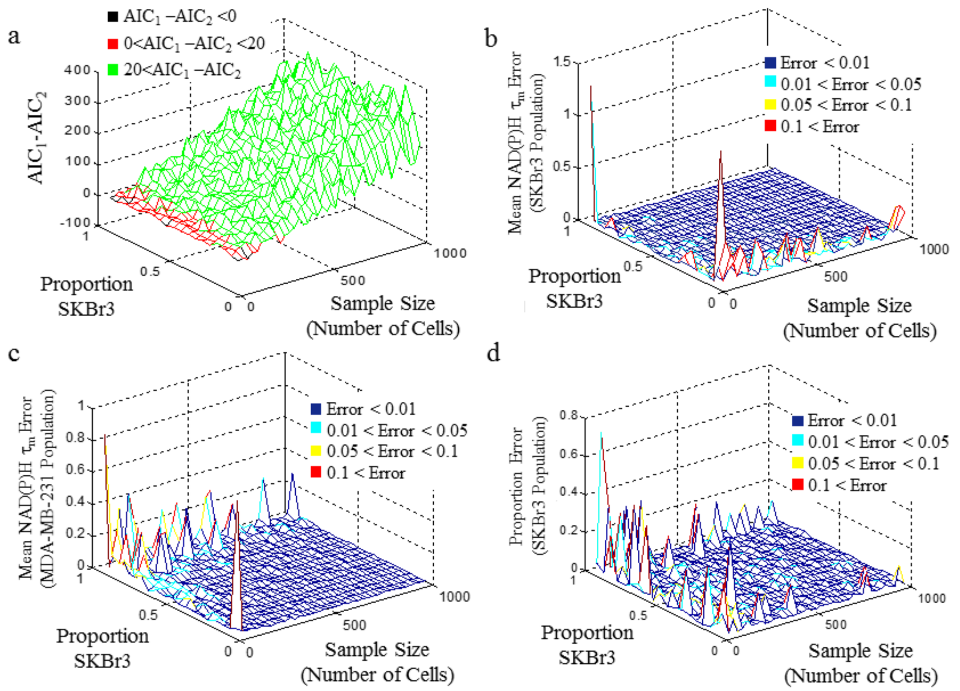

Figure 3.2. Behavior of OMI-SPA to model data simulated from the mean and standard deviations of NAD(P)H τ_m of SKBr3 and MDA-MB-231 cells. (a) Difference in the AIC values of 1 and 2 component Gaussian models of the simulated cell populations as a function of varying sample sizes and varying proportion of SKBr3 cells. (b) Error of the mean NAD(P)H τ_m computed for the SKBr3 subpopulation, and (c) MDA-MB-231 population. (d) Error of the estimated proportion of the SKBr3 subpopulation.

Finally, the simulations were repeated using the mean and standard deviations of the SKBr3 and MDA-MB-231 mean FAD lifetimes, which were experimentally measured as 1.09 +/- 0.10 ns and 1.12 +/- 0.13 ns, respectively. For most of the simulated cell populations, the two component model does not have an AIC value less than the single component fit (Fig. 3.3a). The error of the FAD lifetime values for the modeled SKBr3 and MDA-MB-231 subpopulations was within 10% of the true FAD lifetime values except at sample sizes < 100 (Fig. 3.3b-c); however, the error of the proportion of cells assigned to each subpopulation was greater than 10% at almost all sample sizes and proportions (Fig. 3.3d).

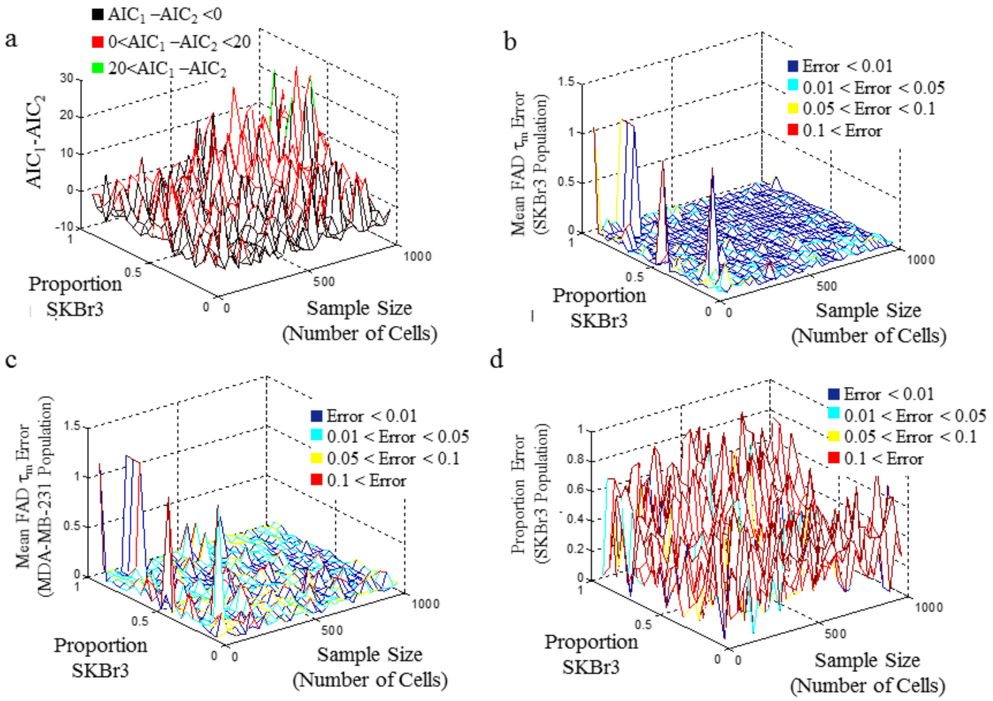

Figure 3.3. Behavior of OMI-SPA to model data simulated from the mean and standard deviations of the FAD τ_m of SKBr3 and MDA-MB-231 cells. (a) Difference in the AIC values of 1 and 2 component Gaussian models to the simulated cell populations as a function of varying sample sizes (N) and varying proportion of SKBr3 cells. (b) Error of the mean FAD τ_m computed for the SKBr3 subpopulation and (c) MDA-MB-231 population. (d) Error of the estimated proportion of the SKBr3 subpopulation.

A.4.2 MDA-MB-231 and SKBr3 co-culture experiments

High-resolution images (Fig. 3.4) demonstrate the variability of redox ratios, NAD(P)H mean lifetimes, and FAD mean lifetimes between the two cell lines. MDA-MB-231 cells have a lower redox ratio, a shorter mean NAD(P)H lifetime, and a longer mean FAD lifetime, than SKBr3 cells. The images from the co-culture experiments demonstrate heterogeneity in cellular morphology and fluorescence imaging endpoints (Fig. 3.4). The images from the co-culture experiments were examined manually and each cell designated as SKBr3 or MDA-MB-231 based on morphology. Any cells that could not be identified were excluded from the analysis. While the cells were plated at the following proportions, 30/70%, 50/50%, and 70/30%, the manual analysis verified the heterogeneity of the co-cultured experiments and reports the actual proportions of the imaged cells for each co-culture group (Table 3.1).

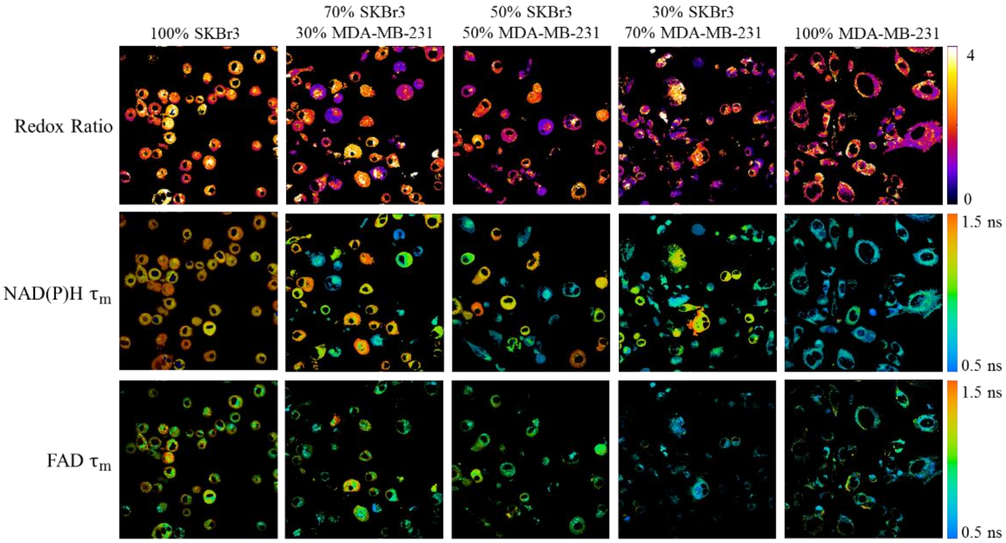

Figure 3.4. Representative OMI images of co-cultured cells. Representative images of the redox ratio (NAD(P)H/FAD), NAD(P)H mean lifetime, and FAD mean lifetime of MDA-MB-231 cells, SKBr3 cells, and mixed populations.

Table 3.1: Experimental groups for the SKBr3 and MDA-MB-231 co-culture experiments.

Experimental Group	Portion of MDA-MB-231 Cells		Portion of SKBr3 Cells	
	Plated	Observed	Plated	Observed
Group 1	0	0	1	1
Group 2	0.3	0.37	0.7	0.63
Group 3	0.5	0.60	0.5	0.40
Group 4	0.7	0.82	0.3	0.18
Group 5	1	1	0	0

OMI-SPA of the co-culture experiment reveals that the single cell data sets are modeled best by a one component Gaussian distribution model and data from the co-culture groups are best modeled by two component Gaussian distribution models. OMI-SPA of the redox ratio correctly identifies two populations in all three co-culture experiments (Fig. 3.5). The mean redox ratio values of the SKBr3 modeled populations are within 6% of the true mean redox ratio (defined as the mean redox ratio of manually classified SKBr3 cells) (Table 3.2). Likewise, the mean error of the MDA-MB-231 cells ranges is 5% or less for all co-culture experiments (Table 3.2). The error of the model-estimated proportion of each subpopulation of cells is 5% or less for all three co-culture groups (Table 3.2). The error of the standard deviations for the identified SKBr3 populations ranges from 5% for the 100% SKBr3 culture to 25% for the 30% SKBr3 culture, while the standard deviation errors for the MDA-MB-231 model redox ratios is 10% or less for all experiments (Table 3.2).

The mean redox ratio for each population of cells, SKBr3 and MDA-MB-231, was compared across all experimental groups to evaluate the stability of the redox ratio when cells are grown in different environments. The MDA-MB-231 cells grown independently of the SKBr3 cells had a mean redox ratio of 1 and a standard deviation of 0.23. The mean MDA-MB-231 redox ratio was not significantly different for any of the co-culture experiments: 0.97+/- 0.22 for 70% MDA-MB-231 cells, 0.99+/-0.2 for 50%, and 0.82 +/- 0.25 for 30%. Likewise, the redox ratio for the SKBr3 cells was similar when the cells were cultured without and with the MDA-MB-231 cells. The only statistically significant ($p<0.05$) difference in redox ratio was observed for the SKBr3 cells grown in the 30% SKBr3/70% MDA-MB-231 culture versus the 100% SkBr3 culture, 1.2+/-0.5 vs. 1.8 +/- 0.39, respectively. These results suggest that the redox ratio remains relatively stable irrespective of whether cells are grown independently or in co-culture.

Table 3.2: Mean, proportion (P), and standard deviation and % errors computed from the optimal fitting Gaussian distribution model of the co-culture experimental data.

		Population 1 (SKBr3)			Population 2 (MDA-MB-231)		
	Proportion SKBr3/ MDA-MB-231	Mean (%Error*)	P (%Error)	Std (%Error)	Mean (%Error)	P (%Error)	Std (%Error)
Redox Ratio	100%/0%	1.91 (6)	1 (0)	0.39 (5)	-	-	-
	70%/30%	2.11 (3)	0.68 (4)	0.55 (18)	0.82 (0.5)	0.32 (5)	0.23 (6)
	50%/50%	1.88 (2)	0.44 (4)	0.60 (16)	1.02 (3)	0.56 (4)	0.18 (10)
	30%/70%	2.12 (5)	0.23 (5)	0.73 (25)	1.02 (5)	0.77 (5)	0.21 (1)
	0%/100%	-	-	-	1.06 (6)	1 (0)	0.23 (6)
NAD(P)H τ_m (ns)	100%/0%	1.31 (0.1)	1 (0)	0.13 (0.3)	-	-	-
	70%/30%	1.25 (0.2)	0.65 (2)	0.11 (4)	0.83 (3)	0.35 (2)	0.11 (16)
	50%/50%	1.18 (3)	0.44 (4)	0.14 (17)	0.81 (3)	0.56 (4)	0.10 (17)
	30%/70%	1.20 (7)	0.28 (10)	0.18 (28)	0.83 (2)	0.72 (10)	0.10 (11)
	0%/100%	-	-	-	0.85 (0.1)	1 (0)	0.12 (0.2)
FAD τ_m (ns)	100%/0%	1.09 (0.1)	1 (0)	0.10 (0.3)	-	-	-
	70%/30%	1.02 (5)	0.61 (0.02)	0.09 (41)	1.19 (8)	0.39 (2)	0.15 (19)
	50%/50%	1.12 (11)	1 (0.6)	0.14 (28)	-	-	-
	30%/70%	1.03 (6)	0.18 (0.01)	0.10 (1)	1.12 (4)	0.82 (0.3)	0.12 (5)
	0%/100%	-	-	-	1.17 (0.4)	1(0)	0.13 (0.2)
OMI Index	100%/0%	1.67 (0.1)	1 (0)	0.31 (0.3)	-	-	-
	70%/30%	1.81 (0.02)	0.62 (1)	0.38 (1)	0.47 (1)	0.38 (1)	0.23 (3)
	50%/50%	1.62 (6)	0.40 (0.2)	0.47 (16)	0.49 (4)	0.60 (0.2)	0.20 (11)
	30%/70%	2.06 (2)	0.17 (1)	0.36 (20)	0.56 (0.2)	0.83 (1)	0.23 (2)
	0%/100%	-	-	-	0.54 (0.7)	1 (0)	0.21 (0.2)

* % error computed for the mean, proportion, and standard deviation of the endpoint values between the manually classified SKBr3 and MDA-MB-231 cell populations and the results of the best-fit SPA model.

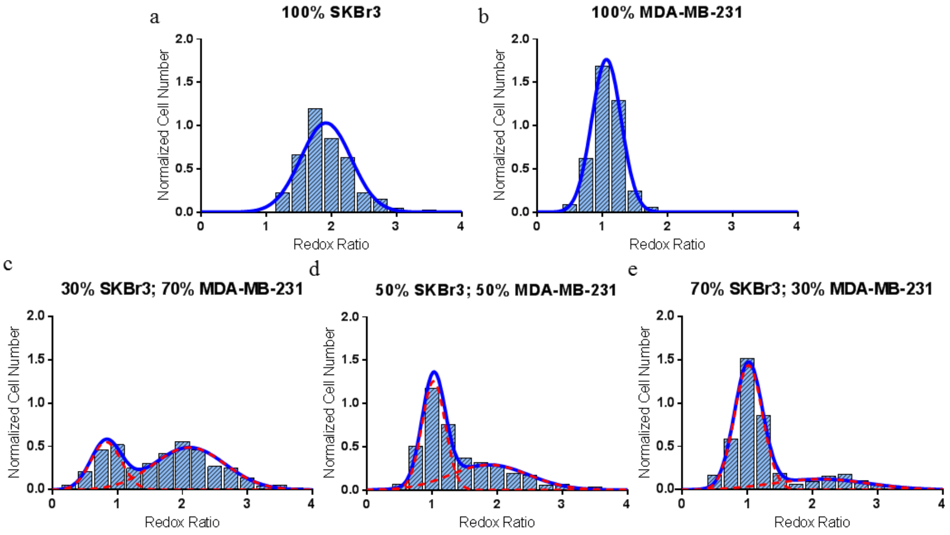

Figure 3.5. Redox ratio histograms. Histograms of redox ratios, quantified per cell, of a population of approximately 200 cells of varying percentages of MDA-MB-231 cells and SKBr3 cells measured experimentally. The solid blue line represents best mixed-model Gaussian distribution fit. The red dashed curves represent the two component contributions, if a two component model is optimal. Histograms are normalized to have a total area of 1.

The mean NAD(P)H τ_m values of the two cell lines grown independently are 1.3 ns for SKBr3 cells and 0.85 ns for the MDA-MB231 cells (Fig. 3.6a-b). SPA of the NAD(P)H τ_m data from the co-culture experiments reveals two populations for all three co-culture groups (Fig. 3.6c-e). The errors of the means of the computationally determined SKBr3 and MDA-MB-231 subpopulations are within 7% of the respective, true NAD(P)H τ_m means (Table 3.2). Likewise, the proportion of cells attributed to each population as determined computationally by the SPA models, is within 10% of the true populations and the standard deviation errors within 28% (Table 3.2). To demonstrate the cellular heterogeneity visually, the average NAD(P)H τ_m value of each cell was used to classify cells as SKBr3 or MDA-MB-231, and cells are color coded red if SKBr3 and blue if MDA-MB-231 (Fig. 3.7). An NAD(P)H τ_m cut-off value of 1.06 ns was chosen because it is equal-distance, 1.9 standard deviations, from each mean and minimized classification error. This NAD(P)H τ_m threshold value yielded an overall accuracy of 95.2% to correctly classify all cells, with 94.2% of SKBr3 cells correctly classified and 95.5% of MDA-MB-231 cells correctly classified.

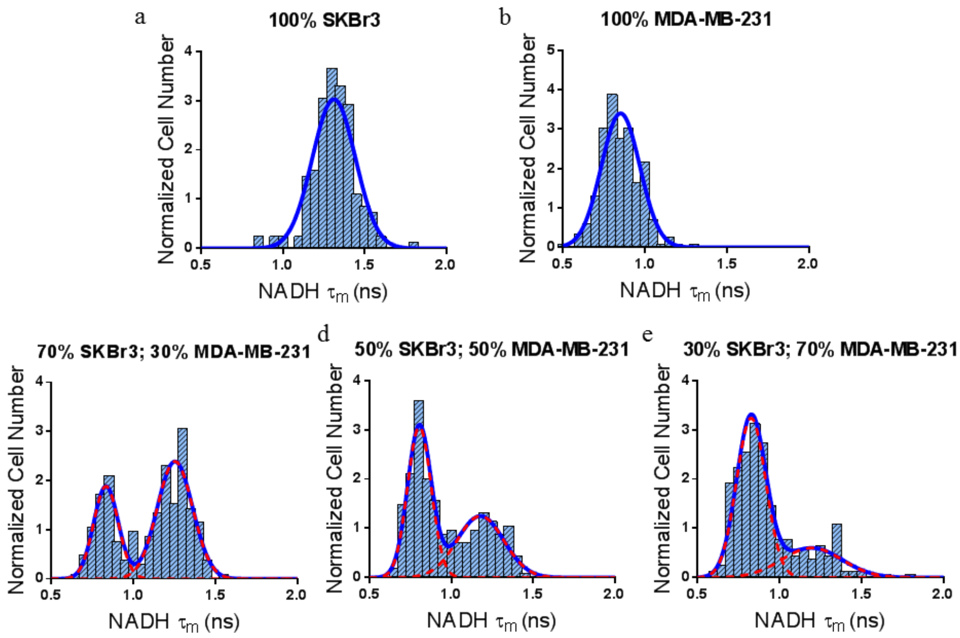

Figure 3.6. NAD(P)H τ_m histograms. Histograms of NAD(P)H τ_m from populations of approximately 200 cells of varying percentages of MDA-MB-231 cells and SKBr3 cells. The solid blue line represents the best mixed-model Gaussian distribution fit. The red dashed curves represent the two component contributions, if a two component model is optimal. Histograms are normalized to have a total area of 1.

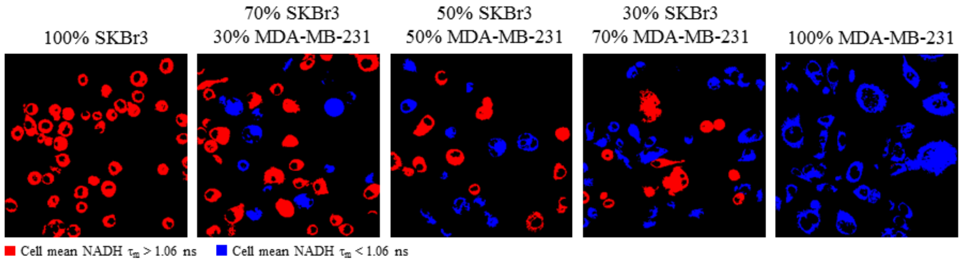

Figure 3.7. Representative color coded images. Images with cells color coded red if the cell mean NAD(P)H τ_m value is greater than 1.06 ns and blue if the NAD(P)H τ_m value is less than 1.06 ns.

SPA of the heterogeneous co-cultures is less successful at separating the two populations using the FAD τ_m (Fig. 3.8, Table 3.2). While two populations are identified in the 30/70% experiments, the model fails to identify two populations in the 50/50% group (Fig. 3.8d).

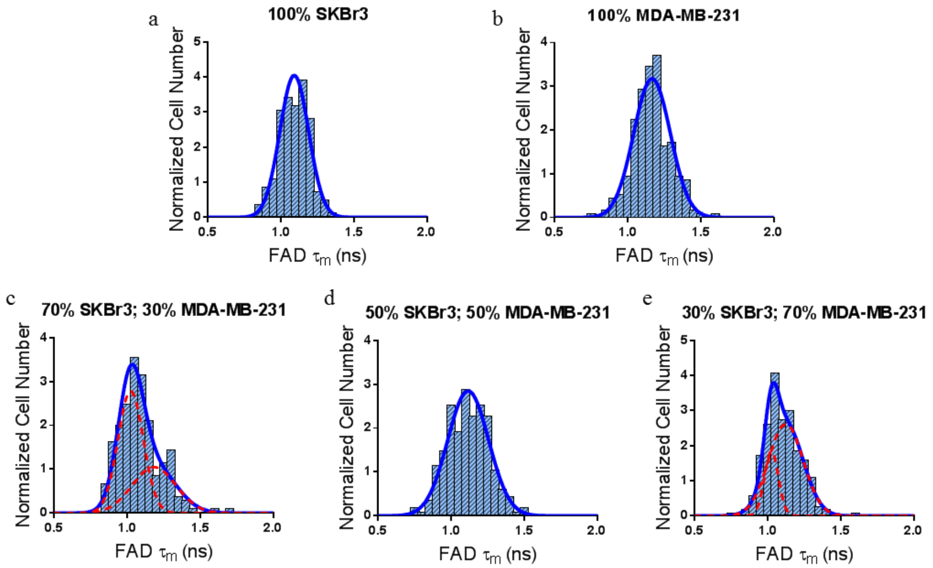

Figure 3.8 FAD τ_m histograms. Histograms of FAD τ_m from populations of approximately 200 cells of varying percentages of MDA-MB-231 cells and SKBr3 cells. The solid blue line represents the best mixed-model Gaussian distribution fit. The red dashed curves represent the two component contributions, if a two component model is optimal. Histograms are normalized to have a total area of 1.

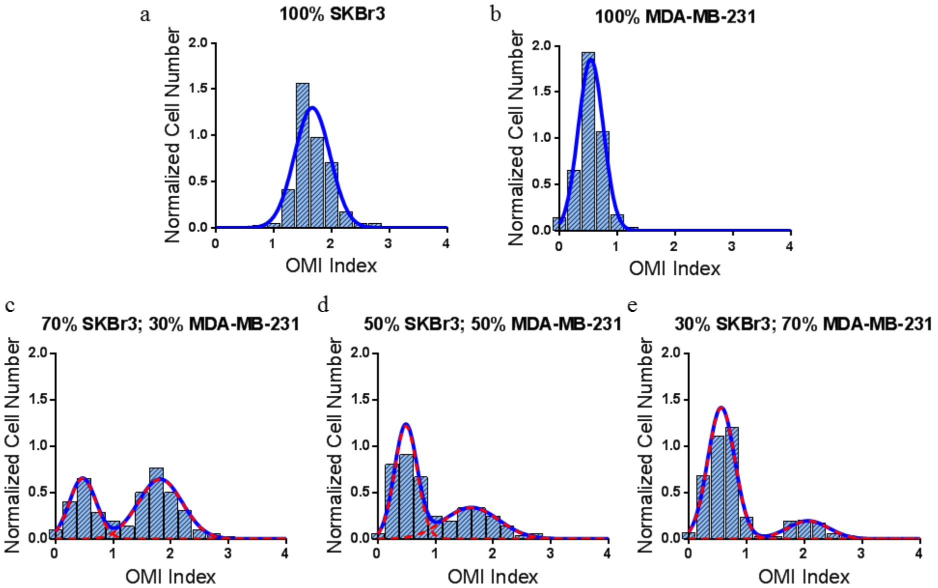

Figure 3.9 OMI index histograms. Histograms of OMI Index from populations of approximately 200 cells of varying percentages of MDA-MB-231 cells and SKBr3 cells. The solid blue line represents the best mixed-model Gaussian distribution fit. The red dashed curves represent the two component contributions, if a two component model is optimal. Histograms are normalized to have a total area of 1.

The OMI index is a linear combination of mean centered redox ratio, NAD(P)H τ_m, and FAD τ_m values computed per cell (14). The mean OMI index values for SKBr3 and MDA-MB-231 cells are 1.67 +/- 0.31 and 0.54 +/- 0.22, respectively. OMI-SPA of the OMI index for the co-culture experiments resolves a single population for the 100% SKBr3 and 100% MDA-MB-231 groups and two populations for each of the co-culture groups (Fig. 3.9). The error of the SKBr3 subpopulation OMI index means is <6% for all co-culture experiments grant (Table 3.2). The mean error for the OMI index for the modeled populations of MDA-MB-231 cells are all less than 4% (Table 3.2), and the proportions for the SKBr3 and MDA-MB-231 populations within 1% (Table 3.2). The standard deviation error for the modeled SKBr3 populations is 20% or less for all experiments and 11% or less for the MDA-MB-231 populations (Table 3.2).

3.4.3 Behavior of AIC and SPA

Simulations were performed to determine the characteristics of data sets from which two distinct subpopulations can be resolved. In the first experiments, populations of size N = 300 were generated with a random number generator and each population proportion was 0.5. All populations had a normalized mean of 1, and the distance between the means was varied from 0-2. The standard deviation of the populations varied from 0-1. For these simulations, the two component model is most representative of the data ($AIC_2<AIC_1$) at low standard deviations and at greater distances between the means (Fig. 3.10a). If a cutoff of $AIC_2<AIC_1$ is used to select the most representative model, a two component model is most representative when the standard deviation < 0.46*(distance between means) + 0.0821. However, if the difference AIC_1-AIC_2 must be greater than 5% of AIC_1, then standard deviations < 0.2563*(Distance between means) + 0.0832 describes the populations with two components that can be identified by OMI-SPA. However, even though the AIC selects a two component model for these populations, the error of the computed population mean values, standard deviations, and proportions increases with increased subpopulation standard deviation and decreased distance between the means (Fig. 3.10b-d).

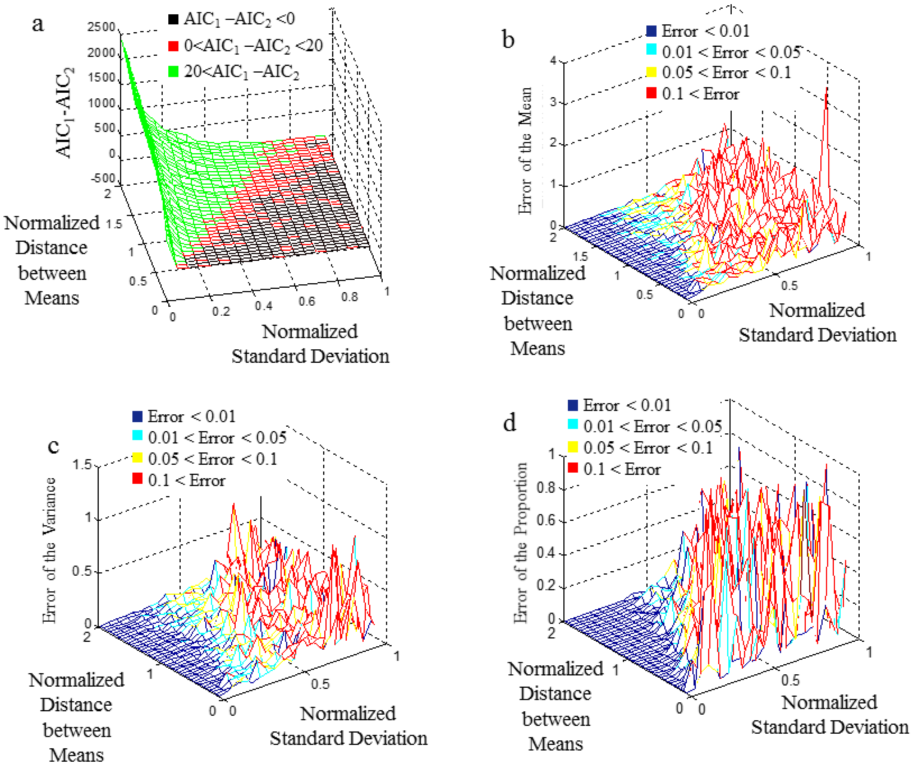

Figure 3.10. Behavior of OMI-SPA for generalized data. Simulation initial conditions include a population of size N = 300 cells, each population proportion was 0.5, and all populations had a normalized mean of 1. The distance between the means was varied from 0-2. The standard deviation of the populations varied from 0-1. (a) AIC difference for the 1 and 2 component models to fit the simulated data. (b) Error of the mean, (c) error of the variance, and (d) error of the subpopulation proportions computed for the two-component models of the simulated data.

Similar simulations were performed to determine the sample size necessary to resolve two populations of known, normalized mean distances, standard deviations, and proportions (Fig. 3.11). In Fig. 3.11, the simulations, in which the normalized distance varied from 0-2 and the proportion of each population varied from 0-1, are repeated at increasing standard deviation values (a) 0.05, (b) 0.1, (c) 0.25, and (d) 0.5. These simulations demonstrate that SPA requires a larger sample size to identify two subpopulations at smaller distances between the means (Fig. 3.11). As the standard deviation increases, an increased sample size is required to identify subpopulations.

SPA fails to identify two subpopulations within a sample size of 10,000, at low mean distances: mean distances < 0.3 for a standard deviation of 0.05, mean distances < 0.4 for a standard deviation of 0.1, mean distances < 0.6 for a standard deviation of 0.25, and mean distances < 0.8 for a standard deviation of 0.5. Additionally, SPA fails to identify two populations in data sets up to 10,000 cells, at percentages of 0 and 1, as expected for uni-modal populations. Increased sample sizes are required to identify populations of very small proportions, in the 0.02-0.12 range (Fig. 3.11c). The dashed red circle (Fig. 3.11b) and red dashed line (Fig. 3.11d) encompass measured subpopulations (9, 14) in breast cancer (see 3.5 Discussion). Altogether, these simulations on normalized data sets demonstrate the relationships between mean distance, standard deviation, population proportion, and sample size necessary to resolve two subpopulations.

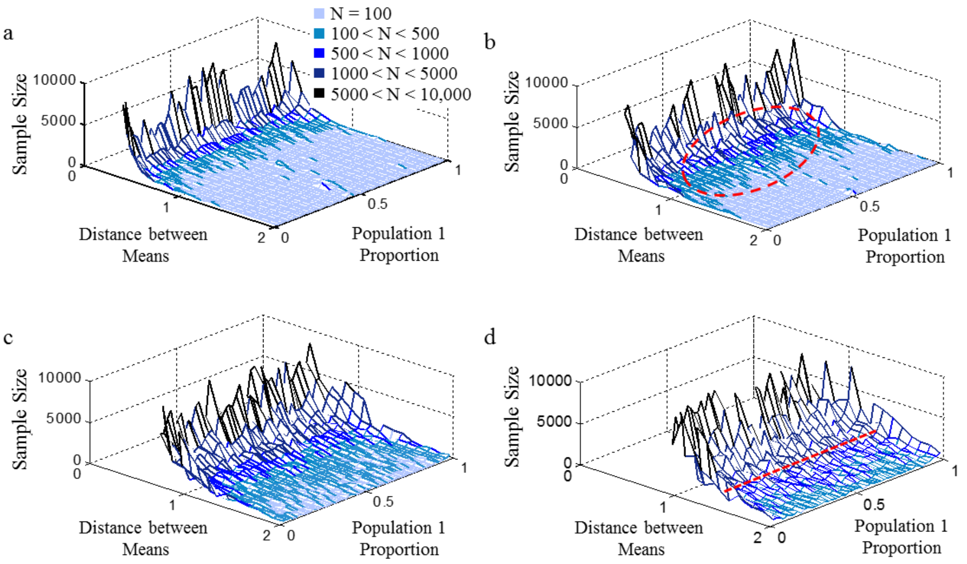

Figure 3.11. Minimum sample size for OMI-SPA for populations of varying parameters. Minimum sample size (N), if less than 10,000 cells, required to resolve two populations with minimal population mean and proportion error ($AIC_2<AIC_1-20$) at varied mean distances (0-2) and population proportions (0-1). Standard deviation of the populations was varied: (a) 0.05, (b) 0.1, (c) 0.25, and (d) 0.5. The red, dashed circle in (b) encompasses the majority of normalized OMI endpoint mean distances and proportions of subpopulations observed in patient-derived organoids. The red, dashed line (d) represents the normalized distance (1.16) and standard deviation between two HER2 positive cell lines, one responsive to trastuzumab and one resistant.

3.5. Discussion

Recent evidence suggests that tumor heterogeneity is a major source of drug resistance (1). Cancer stem cell populations may contribute to drug resistance and tumor recurrence (6). Within breast cancers, stem cells can compromise 3-35% of the tumor cells (6). Therefore, non-invasive single cell analysis technologies that can monitor changes in cellular subpopulations over time are critically needed to understand and combat drug resistance in tumors. Optical imaging of NAD(P)H and FAD is highly sensitive to metabolic differences among breast cancer subtypes (9, 14), and can be performed at high resolution for single-cell analysis. Here, we demonstrate the capabilities and limitations of OMI-SPA to quantify subpopulations of cells by co-culture and simulation experiments.

Simulations of the OMI-SPA behavior for co-cultured SKBr3 and MDA-MB-231 cells (Fig. 3.1-3) demonstrate that for these two cell lines, OMI-SPA will be able to identify the two populations, with minimal mean and proportion error, using the NAD(P)H τ_m values at population sizes greater than 50 cells and at proportions between 0.1 and 0.9 (Fig. 3.2). The normalized distance between mean redox ratios for SKBr3 and MDA-MB-231 is greater than that of NAD(P)H τ_m (0.57 vs. 0.42), but the normalized average standard deviation is twice as great for the redox ratios than NAD(P)H τ_m (0.22 vs. 0.12). Therefore, the redox ratio simulations demonstrate that OMI-SPA can resolve two populations with minimal mean and proportion error at larger sample sizes (>100 total cells) and proportions between 20 and 80% SKBr3 (Fig. 3.1). While the normalized average standard deviation of the SKBr3 and MDA-MB-231 FAD τ_m values is 0.10, the smallest of these three OMI endpoints, the normalized mean FAD τ_m distance for SKBr3 and MDA-MB-231 cells is only 0.06, and OMI-SPA is unable to identify two populations in the FAD τ_m simulations due to this small difference in means of the two populations (Fig. 3.3). This highlights the fact that OMI-SPA can identify two populations only if the two populations have sufficiently large mean separation and small standard deviations. Otherwise, OMI-SPA cannot identify both subpopulations.

Co-culture experiments of SKBr3 and MDA-MB-231 cells were performed to test OMI-SPA on experimental data. Due to the large differences in mean redox ratio and NAD(P)H τ_m, the redox ratio and NAD(P)H τ_m images of co-cultured SKBr3 and MDA-MB-231 cells appear heterogeneous (Fig. 3.4). This highlights the advantage of microscopy techniques that provide images for qualitative and quantitative assessment. Furthermore, false-coloring of the images based on the cellular NAD(P)H τ_m values visually demonstrates the presence of SKBr3 cells and MDA-MB-231 cells in the images of co-cultured cells (Fig. 3.7). OMI-SPA of the redox ratio and NAD τ_m values of the co-cultured SKBr3 and MDA-MB-231 cells identified two subpopulations with minimal error (Fig 3.5, 3.6; Table 3.2). OMI-SPA of the FAD τ_m data failed to resolve two populations in the 50%/50% co-culture experiment, which was expected from the simulation data that suggested the FAD τ_m means were too similar for OMI-SPA to distinguish (Fig. 3.8).

The OMI index is a linear combination of the redox ratio, NAD(P)H τ_m, and FAD τ_m, and provides a single optical variable that is highly sensitive to cellular metabolic changes with receptor expression and drug response in breast cancer (14). Subpopulation analysis of the OMI index of co-cultured SKBr3 and MDA-MB-231 cells identifies two subpopulations when grown at 30/70%, 50/50%, and 70/30% with minimal error in population means, standard deviations, and subpopulation proportions (Fig 3.9, Table 3.2). In comparison with the three individual OMI index constituents, the OMI index has the greatest normalized mean distance between SKBr3 and MDA-MB-231 cells, 1.02, and a normalized standard deviation, 0.24, indicating robust SPA for these two cell lines.

Generalized simulations were performed to assess the characteristics of data sets that can be accurately modeled as two subpopulations by OMI-SPA. These generalized simulations can be used to predict SPA performance for any two subpopulations by computing a subpopulation mean separation distance and standard deviation normalized to the mean of the data set. The results of these simulations (Fig. 3.10-11) demonstrate the relationships between sample size, population standard deviation, and distance between means necessary to resolve two populations. A larger standard deviation is tolerated if the distance between means is greater (Fig. 3.10) or the sample size is larger (Fig. 3.11). OMI-SPA subpopulation mean, standard deviation, and proportion errors increase with increased population standard deviation and decreased distances between means (Fig. 3.10). Cancer stem cells compromise 3-35% of the cells within a tumor (6), and the generalized OMI-SPA results (Fig. 3.11) demonstrate the capabilities of OMI-SPA to resolve these small populations provided that the stem cells have different OMI endpoints from the non-stem cell population.

The utility of OMI-SPA is to identify subpopulations of cells within unknown, heterogeneous populations. OMI-SPA has been used in xenograft and patient derived- primary tumor organoids to identify subpopulations with varied response to anti-cancer drug treatment (14). The normalized mean separation for the OMI index of trastuzumab responsive (BT474, ER+/HER2+) cells and resistant cells (HR6, ER+/HER2+) is 1.16 and the normalized OMI index standard deviation is 0.42 for responsive cells and 0.28 for resistant cells (9). The normalized simulation experiments (red dashed line; Fig. 3.11d) suggest that OMI-SPA will be able to resolve heterogeneous populations of responsive and non-responsive cells, if there are at least 500 cells in the population. Analysis of primary-tumor derived organoids with heterogeneous drug-response, identified subpopulations of cells with varied OMI index values (14). The normalized mean separation for OMI-SPA subpopulations within patient primary tumor derived organoids ranged from 0.4-1.4, population percentages ranged from 0.15-0.85, and the normalized standard deviations ranged from 0.02 to 0.36. As indicated by the red dashed circle (Fig. 3.11b), OMI-SPA can resolve these subpopulations with high mean separations with as few as 100 cells, and can resolve the majority of these subpopulations with less than 500 cells.

Heterogeneous tumors may contain more than two subpopulations and the characteristics of these subpopulations may be unknown in advance. Furthermore, the metabolism of these subpopulations may change dynamically over time and in response to stimuli. SPA, as described here, can be used to evaluate the presence of multiple subpopulations. Additionally, the simulation experiments (Fig. 3.10 and 3.11) generalize the OMI-SPA technique and show this is a robust method for populations of cells with varying OMI endpoint means and standard deviations and not limited to the two specific cell lines used in the co-culture experiments. Furthermore, one advantage of OMI is the non-invasive capabilities which enable imaging of *in vitro* samples over time to study subpopulation and individual cell dynamics. Altogether, OMI-SPA is a robust, attractive platform for evaluating and monitoring subpopulation heterogeneity.

OMI-SPA assumes that the OMI endpoints distributions for each population exhibit normality. A Wilk-Shapiro test for normality revealed that the NAD(P)H and FAD mean lifetimes of both cell lines exhibited normality but the OMI index did not for either cell line and neither did the redox ratio for the SKBr3 cells. The lack of normality of these data sets may introduce error when modeled as Gaussian curves. Even with this know error, however, the errors for the mean OMI index modeled for both cell lines and the errors for the SKBr3 redox ratio in the co-culture experiments was less than 6%, suggesting OMI-SPA performs well with these distributions represented as Gaussian curves. SPA can be improved to account for different data distributions by using additional distributions that better represent the homogenous population.

The results of this experiment demonstrate that OMI-SPA can be used to identify cancer cell subpopulations based on the OMI endpoints: redox ratio, NAD(P)H mean lifetime, FAD mean lifetime, and OMI index. Furthermore, these results characterize the relationships between sample size, standard deviation, and mean distance required for OMI-SPA to accurately describe the two populations. Our previously published analyses of cellular subpopulations within *in vivo* tumors (9) and patient-derived tumor organoids (14) also indicate that OMI-SPA can accurately identify cell subpopulations with a sample of as few as 300 cells.

3.6 Acknowledgements

We acknowledge Miranda Kunz for assistance with cell culture and imaging. Funding sources include Vanderbilt Provost Fellowship (AJW), the DOD BCRP (DOD-BC121998), the NSF (AJW; DGE-0909667), the NIH/NCI (NIH R00-CA142888, R01-CA185747), the Mary Kay Foundation (067-14), and the NCI Breast Cancer SPORE (P50-CA098131).

3.7 References

1. Fisher R, Pusztai L, Swanton C. Cancer heterogeneity: implications for targeted therapeutics. British journal of cancer. 2013;108(3):479-85.
2. Kiviet DJ, Nghe P, Walker N, Boulineau S, Sunderlikova V, Tans SJ. Stochasticity of metabolism and growth at the single-cell level. Nature. 2014;514(7522):376-9.
3. Cheung KJ, Gabrielson E, Werb Z, Ewald AJ. Collective invasion in breast cancer requires a conserved basal epithelial program. Cell. 2013;155(7):1639-51.
4. Almendro V, Cheng YK, Randles A, Itzkovitz S, Marusyk A, Ametller E, Gonzalez-Farre X, Munoz M, Russnes HG, Helland A, Rye IH, Borresen-Dale AL, Maruyama R, van Oudenaarden A, Dowsett M, Jones RL, Reis-Filho J, Gascon P, Gonen M, Michor F, Polyak K. Inference of tumor evolution during chemotherapy by computational modeling and in situ analysis of genetic and phenotypic cellular diversity. Cell reports. 2014;6(3):514-27.
5. Polyak K. Tumor Heterogeneity Confounds and Illuminates: A case for Darwinian tumor evolution. Nature medicine. 2014;20(4):344-6.

6. Visvader JE, Lindeman GJ. Cancer stem cells in solid tumours: accumulating evidence and unresolved questions. Nature Reviews Cancer. 2008;8(10):755-68.

7. Georgakoudi I, Quinn KP. Optical imaging using endogenous contrast to assess metabolic state. Annu Rev Biomed Eng. 2012;14:351-67.

8. Chance B, Schoener B, Oshino R, Itshak F, Nakase Y. Oxidation-reduction ratio studies of mitochondria in freeze-trapped samples. NADH and flavoprotein fluorescence signals. J Biol Chem. 1979;254(11):4764-71.

9. Walsh AJ, Cook RS, Manning HC, Hicks DJ, Lafontant A, Arteaga CL, Skala MC. Optical metabolic imaging identifies glycolytic levels, subtypes, and early-treatment response in breast cancer. Cancer Res. 2013;73(20):6164-74.

10. Lakowicz J. Principles of fluorescence spectroscopy. New York: Plenum Publishers; 1999.

11. Lakowicz JR, Szmacinski H, Nowaczyk K, Johnson ML. Fluorescence Lifetime Imaging of Free and Protein-Bound Nadh. Proc Natl Acad Sci U S A. 1992;89(4):1271-5.

12. Tanaka F, Tamai N, Yamazaki I. Picosecond-resolved fluorescence spectra of D-amino-acid oxidase. A new fluorescent species of the coenzyme. Biochemistry. 1989;28(10):4259-62.

13. Walsh A, Cook RS, Rexer B, Arteaga CL, Skala MC. Optical imaging of metabolism in HER2 overexpressing breast cancer cells. Biomedical optics express. 2012;3(1):75-85.

14. Walsh AJ, Cook RS, Sanders ME, Aurisicchio L, Ciliberto G, Arteaga CL, Skala MC. Quantitative optical imaging of primary tumor organoid metabolism predicts drug response in breast cancer. Cancer Res. 2014;74(18):5184-94.

15. Skala MC, Riching KM, Bird DK, Gendron-Fitzpatrick A, Eickhoff J, Eliceiri KW, Keely PJ, Ramanujam N. In vivo multiphoton fluorescence lifetime imaging of protein-bound and free nicotinamide adenine dinucleotide in normal and precancerous epithelia. Journal of biomedical optics. 2007;12(2):024014.

16. Skala MC, Riching KM, Gendron-Fitzpatrick A, Eickhoff J, Eliceiri KW, White JG, Ramanujam N. In vivo multiphoton microscopy of NADH and FAD redox states, fluorescence lifetimes, and cellular morphology in precancerous epithelia. Proc Natl Acad Sci U S A. 2007;104(49):19494-9.

17. Pan W, Lin J, Le CT. Model-based cluster analysis of microarray gene-expression data. Genome biology. 2002;3(2):RESEARCH0009.

18. Akaike H. A new look at the statistical model identification. Automatic Control, IEEE Transactions on. 1974;19(6):716-23.

19. Walsh AJ, Poole KM, Duvall CL, Skala MC. Ex vivo optical metabolic measurements from cultured tissue reflect in vivo tissue status. Journal of biomedical optics. 2012;17(11):116015.

CHAPTER 4

Optical Metabolic Imaging Identifies Breast Cancer Glycolytic Levels, Sub-Types, and Early Treatment Response

Walsh AJ, Cook RS, Manning HC, Hicks DJ, Lafontant A, Arteaga CL, Skala MC, "Optical metabolic imaging identifies breast cancer glycolytic levels, sub-types, and early treatment response," *Cancer Research*. 2013; 73(20):6164-74.

4.1 Abstract

Abnormal cellular metabolism is a hallmark of cancer, yet there is an absence of quantitative methods to dynamically image this powerful cellular function. Optical metabolic imaging (OMI) is a non-invasive, high-resolution, quantitative tool for monitoring cellular metabolism. OMI probes the fluorescence intensities and lifetimes of the autofluorescent metabolic co-enzymes reduced nicotinamide adenine dinucleotide (NADH) and flavin adenine dinucleotide (FAD). We confirm that OMI correlates with cellular glycolytic levels across a panel of human breast cell lines, using standard assays of cellular rates of glucose uptake and lactate secretion ($p<0.05$, $r=0.89$). Additionally, OMI resolves differences in the basal metabolic activity of untransformed from malignant breast cells ($p<0.05$), and between breast cancer sub-types ($p<0.05$), defined by estrogen receptor (ER) and/or HER2 expression or absence. *In vivo* OMI is sensitive to metabolic changes induced by inhibition of HER2 with the antibody trastuzumab (Herceptin) in HER2-overexpressing human breast cancer xenografts in mice. This response was confirmed with tumor growth curves and stains for Ki67 and cleaved caspase-3. OMI resolved trastuzumab-induced changes in cellular metabolism *in vivo* as early as 48 hours post-treatment ($p<0.05$), while FDG-PET did not resolve any changes with trastuzumab up to 12-days post-treatment ($p>0.05$). In addition, OMI resolved cellular sub-populations of differing response *in vivo* that are critical for investigating drug resistance mechanisms. Importantly, OMI endpoints

remained unchanged with trastuzumab-treatment in trastuzumab-resistant xenografts ($p>0.05$). OMI has significant implications for rapid cellular-level assessment of metabolic response to molecular expression and drug action, which would greatly accelerate drug development studies.

4.2 Introduction

Cellular metabolism produces energy and macromolecules necessary for cell survival. Abnormal metabolism is involved in many of the diseases that cause the greatest burden of morbidity and mortality in the developed world. Many malignant cancer cells maintain high rates of glycolysis in the presence of oxygen (1) and oncogenic transformation is linked with changes in metabolic rates. For example, the HER2 receptor tyrosine kinase, which is amplified in about 20% of invasive breast cancer, potently activates the phosphatidylinositol-3 kinase (PI3K)/Akt/mTOR pathway, a master regulator of glucose metabolism (2, 3). Patients with HER2 gene-amplified breast cancers present with more aggressive disease and generally have a poor prognosis (4). HER2 inhibitors, such as the antibody trastuzumab (Herceptin), provide substantial clinical benefits. However, the action of HER2 inhibitors is limited due to innate and acquired drug resistance (5).

Clinically and in preclinical drug development, there is a need for high-resolution, non-invasive, functional imaging tools to monitor and predict drug efficacy vs. lack of efficacy. In cancer research, the primary endpoint of drug efficacy is tumor regression. However, cellular and molecular changes precede changes in tumor size. If these molecular endpoints could be identified and measured, they would provide biomarkers predictive of drug response or drug resistance. Cellular metabolism is particularly sensitive to upstream molecular interventions, and therefore may be a powerful biomarker of early drug response. The HER2 inhibitor trastuzumab, for example, inhibits PI3K-mediated glucose metabolism (6-8). Current preclinical and clinical methodologies to assess metabolic state in tumors *in situ* include fluorodeoxyglucose-positron emission tomography (FDG-PET), immunohistochemical (IHC) assessment of levels of metabolic regulators, and metabolic flux analyses (7, 9-13). Yet each of these techniques fails to capture dynamic changes in metabolic state and poorly reflect sensitivity to drug efficacy (7, 9, 14-18).

Optical metabolic imaging (OMI) exploits the autofluorescent properties of reduced nicotinamide adenine dinucleotide (NADH) and flavin adenine dinucleotide (FAD), two metabolic co-enzymes. We use multi-photon fluorescence and time-correlated single photon counting to measure the optical redox ratio and fluorescence lifetimes of NADH and FAD in living cells and tissues. The optical redox ratio is the ratio of NADH fluorescence intensity divided by FAD fluorescence intensity (19), and provides a dynamic measure of cellular metabolism (8, 19-21). The fluorescence lifetime, the time a molecule remains in the excited state, is independent of inter- or intra- instrument variability, resolves free and bound protein configurations, and is influenced by preferred protein-binding of the molecules and proximity to quenchers (e.g. oxygen) (22). NADH and FAD each have two-component fluorescence decays. For NADH, the short lifetime (τ_1) corresponds to NADH free in solution, while the long lifetime (τ_2) corresponds to protein-bound NADH (23). Conversely, protein-bound FAD corresponds to the short lifetime, while free FAD corresponds with the long lifetime (24). The shorter fluorescence lifetimes of both protein-bound FAD and free NADH are due to dynamic quenching by the adenine moiety (22, 25). The mean fluorescence lifetime (τ_m) is the weighted average of the short and long lifetime components, $\tau_m = \alpha_1\tau_1+\alpha_2\tau_2$, where α_1 and α_2 are the fractional contributions of the short and long lifetimes, respectively.

The images acquired by OMI provide sufficient resolution and contrast to distinguish the cellular and extracellular tissue compartments, as the collagen-enriched extracellular matrix generates a strong second harmonic signal that has a lifetime and spectral emission distinct from cellular NADH and FAD (26). Resolution is adequately high to isolate single cells, allowing identification of inflammatory infiltrates in the stroma and tumor epithelia. This single cell-level resolution may be useful for identifying resistant sub-populations of cells that pre-exist in the tumor and are responsible for cancer relapse.

Because OMI is inexpensive, fast, and directly measures dynamic changes in cellular metabolism that reflect glycolysis, oxidative phosphorylation, and metabolic enzyme microenvironment interactions, we investigated the potential of OMI as a tool for monitoring metabolic response to targeted therapies in human breast cancer cells and xenografts. OMI was validated by measuring metabolic inhibition by cyanide, and by comparison with standard assays of glycolytic metabolism. The sensitivity of OMI to breast cancer sub-types was confirmed. Finally, the OMI-measured response of mouse xenograft models treated with trastuzumab was compared with FDG-PET, IHC, and tumor size measurements. This work represents a significant advancement in the tools available to study cellular metabolism and tumor response to treatment in living systems.

4.3 Materials and Methods

4.3.1 Fluorescence lifetime instrumentation

A custom built, commercial multi-photon fluorescence microscope (Prairie Technologies) was used to acquire fluorescence images. A 40X water-immersion objective (1.15 NA) or a 40X oil-immersion objective (1.3 NA) coupled the excitation and emitted light through an inverted microscope (TiE, Nikon). A titanium:sapphire laser (Coherent Inc.) was tuned to 750 nm for excitation of NADH and 890 nm for FAD excitation. The average laser power was 7.5-7.8 mW for NADH and 8.4-8.6 mW for FAD. A pixel dwell time of 4.8 μs was used. A GaAsP PMT

(H7422P-40, Hamamatsu) detected emitted photons. A 400-480 nm bandpass filter isolated NADH fluorescence. A 500 nm high pass dichroic mirror and a 500-600 nm bandpass filter isolated FAD fluorescence.

Fluorescence lifetime images were acquired using time correlated single photon counting (TCSPC) electronics (SPC-150, Becker and Hickl). TCSPC uses a fast detector PMT to measure the time between a laser pulse and fluorescence event. Each image of 256x256 pixels was acquired using an integration time of 60 seconds. No change in the photon count rate was observed, ensuring that photobleaching did not occur. The instrument response function (measured from the second harmonic generated signal of urea crystals excited at 900 nm) full width at half maximum was measured to be 260 ps. The single-component fluorescence lifetime of a fluorescent bead (Polysciences Inc.) was measured daily. The measured fluorescence lifetime of the bead was 2.1 ± 0.08 ns ($n = 18$), which is consistent with published studies (20, 27).

4.3.2 Cell culture

All cell lines were acquired from the ATCC except the HR6 cell line (28) which was provided by the Arteaga lab. The non-cancerous mammary epithelium cell line, MCF10A, was cultured in MEBM (Lonza) supplemented with cholera toxin, penicillin: streptomycin, bovine pituitary extract, hydrocortisone, insulin, and human epidermal growth factor. All malignant cell lines were grown in DMEM (Invitrogen) with 10% fetal bovine serum and 1% penicillin: streptomycin. The growth media for the HR6 cell line was further enhanced with 25 μg/ml trastuzumab (Vanderbilt Pharmacy). For fluorescence imaging, cells were plated at a density of 10^6 cells per 35 mm glass-bottom imaging dish (MatTek Corp.) 48 hours before imaging.

The MCF10A cell line was used as a daily fluorescence standard for the redox ratio, and imaged each day measurements were acquired. All other cell lines were imaged on at least two different days. A total of 18 different locations were imaged for each cell line (58 for MCF10A cells) from six different dishes (three images were acquired from each dish, see Appendix A Table A.1).

4.3.3 Cyanide experiment

NADH and FAD fluorescence lifetime images of three locations of three dishes were acquired. Media of two of the MCF10A dishes was removed and replaced with cyanide supplemented MCF10A growth media (4 mM NaCN, Sigma). The cells were allowed 5 minutes for the cyanide to react, and post-cyanide NADH and FAD fluorescence images were acquired from three unique locations from each dish.

4.3.4 Trastuzumab perturbation

The effect of HER2 inhibition by trastuzumab was tested in HER2-overexpressing cells. The cells were plated at a density of 10^6 cells per imaging dish, 48 hours before imaging. At 24 hours before imaging, the growth media was exchanged for growth media containing 25 μg/ml trastuzumab. This dose of trastuzumab, 25 μg/ml, was chosen to mimic therapeutic drug dosage in patients (29).

4.3.5 Mouse xenografts

This study was approved by the Vanderbilt University Animal Care and Use Committee and meets the National Institutes of Health guidelines for animal welfare. MDA-MB-361 cells (10^6), BT474 cells (10^8), or HR6 cells (10^8) in 100μl Matrigel were injected in the inguinal mammary fat pads of female athymic nude mice (J:NU; Jackson Laboratories). Tumors were allowed to grow to ~150mm^3. Tumor-bearing mice were treated with trastuzumab (Vanderbilt University Medical Center pharmacy) or control human IgG 10 mg/kg twice weekly for two weeks. This dose of trastuzumab was chosen to mimic therapeutic drug dosage in patients (30).

4.3.6 OMI xenograft imaging

Isoflurane-anesthetized mice were used for vital imaging, by removing the skin overlying the tumor, overlaying the tumor with a coverslip, and placing the mouse on the microscope stage. NADH and FAD fluorescence lifetime images of three different tumor locations were acquired each day. After imaging, mice were humanely euthanized while under anesthesia. Each OMI group contained 3 mice, each with 2 tumors for a total *n* of 6 tumors at each time point.

4.3.7 FDG-PET imaging

The FDG-PET protocol follows published methods (7, 31, 32). The mice were fasted overnight and allowed to acclimate to the PET facility for 1hr on a warm water pad. A single retroorbital injection of ~200 μCi (100μl) of [^{18}F]FDG was administered. Following a 40-min distribution period, 20-min static PET scans were collected on a Concorde Microsystems microPET Focus 220 (Siemens) while mice were anesthetized with isoflurane. PET images were reconstructed using the ordered subsets expectation maximization algorithm (33). FDG-uptake values were obtained by isolating the uptake of each tumor volume and correcting for the injected dose. Each FDG-PET group contained 5 mice, each with 2 tumors for a total *n* of 10 tumors.

4.3.8 Quantification of the optical redox ratio

The optical redox ratio was computed from the NADH and FAD fluorescence lifetime data. The photons detected at each pixel in an image were integrated over time to compute the sum of photons per pixel. The total number of NADH photons was divided by the total number of FAD photons at each pixel to create a redox ratio image (Matlab, MathWorks). The redox ratio image was thresholded to remove background and nuclear fluorescence and the average redox ratio for the remaining cell cytoplasms was computed. This approach has been confirmed to be consistent with redox ratios obtained with steady-state detection (8, 21).

4.3.9 Quantification of fluorescence lifetime components

For each image, a threshold was selected to eliminate background and nuclear fluorescence (SPCImage, Becker and Hickl). A binning of nine surrounding pixels was used. Then, the fluorescence lifetime components were computed for each pixel by de-convolving the measured system response and fitting the resulting exponential decay to a two-component model, $I(t) = \alpha_1 \exp^{-t/\tau_1} + \alpha_2 \exp^{-t/\tau_2} + C$, where $I(t)$ is the fluorescence intensity at time t after the laser excitation pulse, α_1 and α_2 are the fractional contributions of the short and long lifetime components, respectively (i.e. $\alpha_1 + \alpha_2 = 1$), τ_1 and τ_2 are the fluorescence lifetimes of the short and long lifetime components, and C accounts for background light. A two-component decay was used to represent the lifetimes of the free and bound configurations of NADH and FAD (20, 23, 24). The average lifetime component values and a mean fluorescence lifetime ($\tau_m = \alpha_1\tau_1 + \alpha_2\tau_2$) for each image were computed in Matlab.

4.3.10 Statistical analysis

A rank sum test of means was used to test for significant differences due to cyanide. A Bonferroni correction for multiple-comparisons was used on rank sum tests of means of the metabolic values from the panel of cell lines. A rank sum test of means was used to identify significant differences when cell lines were treated with trastuzumab and to find differences in the *in vivo* xenograft experiments. A student's t-test of means tested for significantly different FDG uptake values between control and trastuzumab-treated xenografts. For all statistical tests, an alpha significance level of 0.05 was used and the test was assumed to be two-way.

Spearman's rank correlation coefficient was used to identify correlations. Both a correlation coefficient (r) and a *P*-value were computed. An alpha level of less than 0.05 signified significance. Scatterplots of the significant correlations confirmed that the correlation was due to data trends and not a single outlier.

4.3.11 Computation of intra- and inter- cellular variation

Inter-cellular variation was visualized by histogram representation of the mean metabolic measure (optical redox ratio, NADH τ_m, or FAD τ_m) for all cells. The histogram was fit to one, two, and three component Gaussian curves to determine the number of modes within the data. The fit with the lowest Akaike information criterion (AIC) was selected to represent the probability density function of the histogram (34). Intra-cellular variation was computed as the average coefficient of variation (standard deviation divided by mean) for each cell and averaged over all cells.

4.3.12 Percentage of mitotic cells

The percentage of proliferating cells was measured by flow cytometry. Cells were plated at a density of 10^6 cells per 35 mm dish. After 48 hours, the cells were labeled with Phospho-Histone H3 (Ser10) antibody (Cell Signaling Technology) and a secondary antibody, Alexa Fluor 488 goat anti-rabbit IgG (Invitrogen) enabled detection of labeled cells by flow cytometry.

4.3.13 Glycolytic Index

Media glucose and lactate concentrations were measured using standard assay kits (Amplex® Red Glucose/Glucose Oxidase Assay Kit (Invitrogen) and L-Lactate Assay Kit (Eton Bioscience Inc.)). Concentrations of glucose and lactate in the cell growth media were determined at the time of plating (0hr) and at the time of imaging (48hr). The “glycolytic index” was computed as the moles of glucose consumed within 48hr divided by the moles of lactate produced in 48hr.

4.3.14 Histological analysis

Tumors were collected and placed in buffered formalin, paraffin embedded, sliced, and stained with H&E. Additional slides were stained for Ki-67 and cleaved caspase-3. Staining protocols were verified in positive control samples. The percentage of positively stained cells was quantified from 5 fields of view from 3 tumors in each group.

4.4 Results

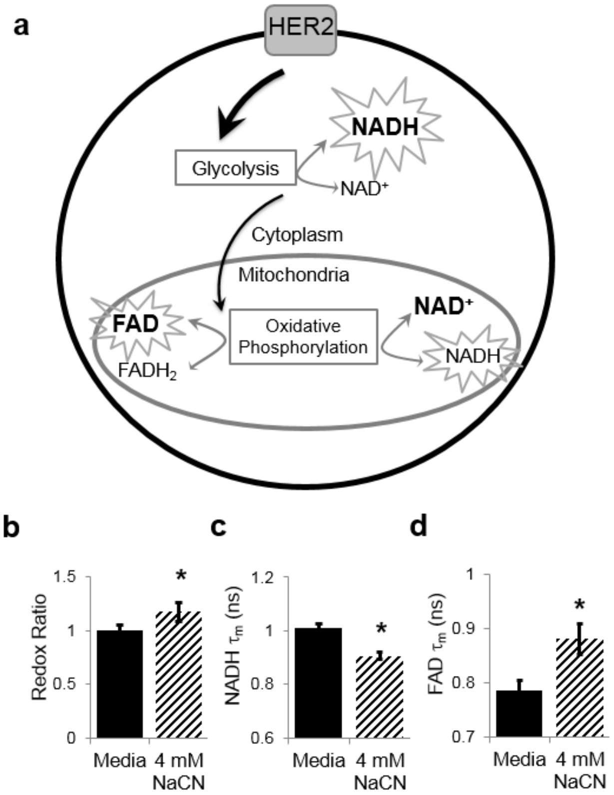

Figure 4.1 Cyanide validation experiment. Graphical representation (a) of the relationship between HER2, NADH and FAD. HER2 activation drives an increase in glycolysis, which produces NADH. The pyruvate generated in glycolysis can enter the mitochondria as a reactant in oxidative phosphorylation. Oxidative phosphorylation consumes NADH and produces FAD. A net gain of NADH relative to FAD is observed with HER2 activation due to a relative increase in glycolysis. Inhibition of HER2 by trastuzumab reduces cellular glycolysis rates resulting in a decrease of cellular NADH relative to FAD. NADH and FAD are highlighted as the fluorescent molecules in this diagram, and molecules in bold indicate the net direction of the reaction. Optical redox ratio (b), NADH τ_m (c), and FAD τ_m (d) of MCF10A (non-malignant) cells before (n=9) and after (n=6) treatment with 4 mM NaCN. τ_m is the mean lifetime ($\tau_m = \tau_1*\alpha_1 + \tau_2*\alpha_2$). *$P$ <0.05.

Figure 4.1a demonstrates the relationship between HER2 and the fluorescent molecules NADH and FAD. HER2 activation drives an increase in glycolysis, which generates NADH. The pyruvate produced in glycolysis can enter the mitochondria as a reactant in oxidative phosphorylation. Oxidative phosphorylation consumes NADH and produces FAD. A net gain of NADH relative to FAD is observed with HER2 activation due to a relative increase in glycolysis.

4.4.1 Validation

Chemical inhibition of oxidative phosphorylation affects the relative fluorescence intensities of NADH and FAD in a cell (35), so this perturbation was used to validate the optical imaging approach (Fig. 4.1b-d, Appendix A Fig. A.1). Cyanide (which disrupts the electron transport chain) induced the predicted trends[23, 27]: an increase in the optical redox ratio and a decrease in NADH τ_m. Unreported until now, FAD τ_m increased with cyanide treatment.

4.4.2 Metabolic profiling of breast cancer cells

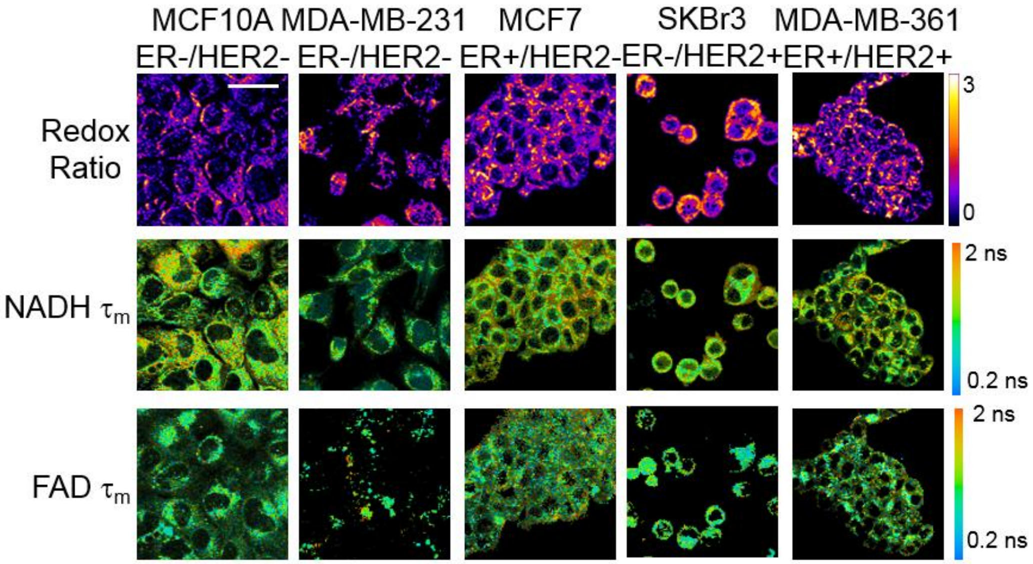

Figure 4.2 Representative OMI images. Representative images of the optical redox ratio (NADH/FAD; first row), NADH τ_m (second row), and FAD τ_m (third row) of MCF10A (non-malignant) and malignant breast cells. Scale bar represents 30 μm. The redox ratio is normalized to the mean daily MCF10A mean redox ratio as a daily fluorescence standard. τ_m is the mean lifetime ($\tau_m = \tau_1*\alpha_1 + \tau_2*\alpha_2$). The ER and HER2 status of each cell line is provided under its name.

High resolution images (Fig. 4.2) allowed visualization of cellular morphology and cell-to-cell variability of the optical redox ratio and NADH and FAD fluorescence lifetimes for human breast cell lines (Appendix A Table A.1). Cellular fluorescence localized to the cytoplasm of cells. ER+/HER2- cells displayed increased redox ratios over that seen in triple-negative cells (*P*<0.001; Fig. 3a), and the greatest redox ratios were measured in HER2 gene-amplified cells *(P*<0.001). To account for any differences in cellular proliferation rates among the cell lines and demonstrate that the redox ratio is not a reporter of cellular proliferation (Appendix A Fig. A.2a), we normalized the redox ratio to the % mitotic cells (Appendix A Fig. A.2b) and found similar trends, increased redox ratio/% mitotic cells in ER+ cells and the greatest redox ratio/% mitotic cells in HER2+ cells.

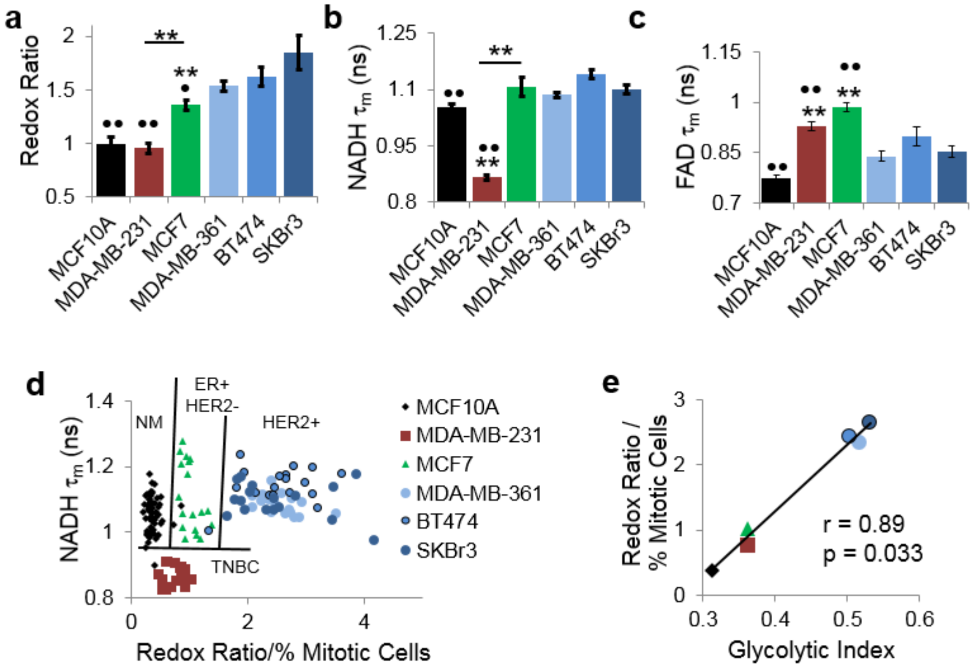

Figure 4.3 ***In vitro*** **OMI results.** (a) The optical redox ratio (mean +/- SE), (b) NADH τ_m, and (c) FAD τ_m for a panel of breast cancer cell lines. (d) A scatterplot of NADH τ_m versus redox ratio/% mitotic cells [non-malignant (NM), triple negative (TNBC)]. (h) Correlation between redox ratio/% mitotic cells and glycolytic index. Unless indicated with a line, stars (*) indicate statistically significant differences with the MCF10A (non-malignant) cells and bullets (•) indicate statistically significant differences with the HER2+ cells grouped together. ** *P* <0.001, •• *P* < 0.001. *n* = 18 for all malignant cell lines and *n* = 58 for MCF10A.

NADH τ_m of HER2+ and ER+ cells were increased over that measured in non-malignant cells (*P*<0.001; Fig. 4.3b), but were statistically similar to each other (*P*=0.5). Triple negative cells exhibited the shortest NADH τ_m. Reduced free and protein-bound NADH lifetimes (τ_1 and τ_2) were observed in the triple negative and ER+ cells (Appendix A Fig. A.3a-b). The portion of free NADH (α_1) was decreased in the HER2+ cells compared to the non-malignant cells (Appendix A Fig. A.3c). Compared to non-malignant cells, FAD τ_m was increased in all malignant cells (*P*<0.001), with the longest FAD τ_m observed in ER+/HER2- cells (*P*<0.001; Fig. 3.3c). Increased FAD τ_1 and τ_2 values, as well as a reduced α_1 (contribution of bound FAD) contributed to the increased FAD τ_m observed in the malignant cells (Appendix A Fig. A.3d-f). A scatterplot of NADH τ_m vs. redox ratio/% mitotic cells (Fig. 4.3d) allowed accurate clustering of data-points of non-malignant, triple-negative, ER+, and HER2+ cells. Scatterplots of FAD τ_m vs redox ratio and NADH τ_m vs FAD τ_m allow separation of triple negative and non-malignant cells (Appendix A Fig. A.4).

We compared OMI to cellular rates of glucose uptake and lactate secretion, or the “glycolytic index”. A Spearman's rank correlation coefficient (r) of 0.89 (*P*<0.05) defined a positive correlation between the optical redox ratio/% mitotic cells and the glycolytic index (Fig. 4.3e). Neither NADH τ_m nor FAD τ_m correlated with the glycolytic index or the redox ratio (Appendix A Table A.2).

4.4.3 Trastuzumab response *in vitro*

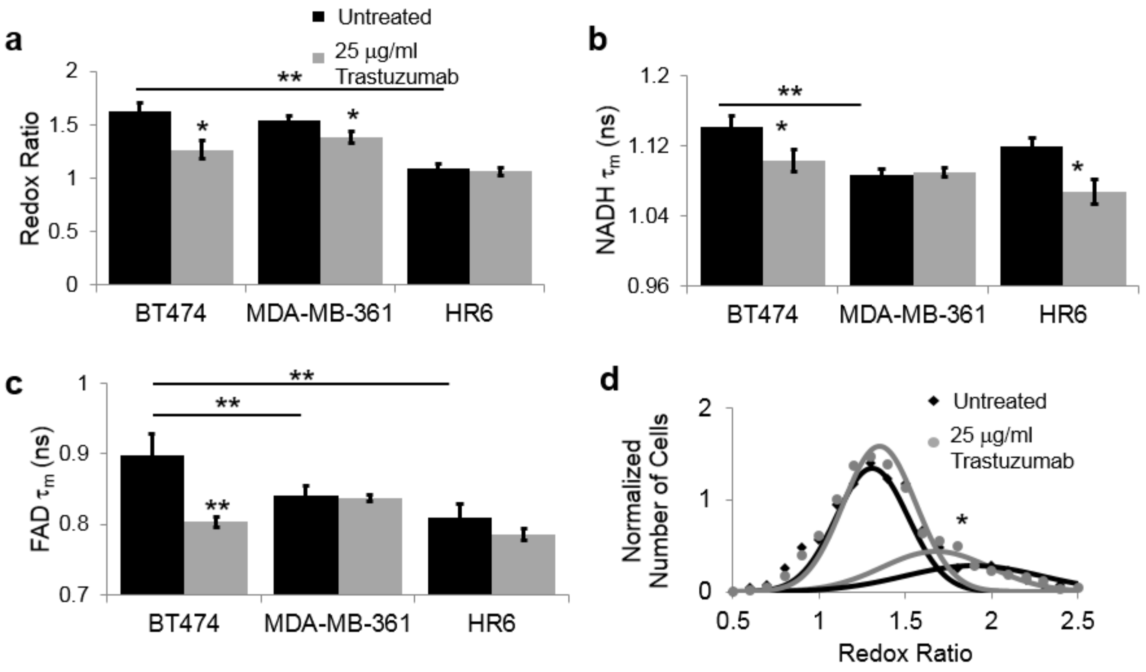

Figure 4.4 *In vitro* trastuzumab response. (a) The redox ratio (mean +/- SE) decreases with trastuzumab-treatment in responsive (BT474) and partially responsive (MDA-MB-361) cells but remains unchanged in cells with acquired resistance to trastuzumab (HR6). (b) NADH τ_m (mean +/- SE; $\tau_m = \tau_1 * \alpha_1 + \tau_2 * \alpha_2$) is shorter in trastuzumab-treated responsive cells (BT474) and cells with acquired resistance (HR6), but unchanged in cells with poor response (MDA-MB-361). (c) FAD τ_m (mean +/- SE) is shorter in trastuzumab-treated BT474 but unchanged MDA-MB-361 and HR6 cells. * indicates significance between control and treated, unless otherwise indicated. (d) Distribution density modeling (black line represents fit of untreated cell histogram, gray line represents fit of trastuzumab treated cells) of the redox ratio on a cell-by-cell basis reveals two distinct populations of MDA-MB-361 cells for the redox ratio, with 70% and 30% of cells in the majority and minority populations, respectively, for both control and treated cells. There is a significant decrease ($P<0.05$) in the mean of the minority population of treated cells (but not in the majority population), suggesting trastuzumab response in a sub-population of cells. ** $P < 0.001$, * $P < 0.05$. n = 18 images for control and treated for all cell lines.

The effect of trastuzumab on cellular metabolism was investigated in three HER2-overexpressing cell lines: BT474 cells which are responsive to trastuzumab, MDA-MB-361 cells which partially respond to trastuzumab, and HR6 cells, which were derived from a BT474 xenograft that acquired resistance to trastuzumab *in vivo* (28). The redox ratio ($P<0.05$), NADH τ_m ($P<0.05$), and FAD τ_m ($P<0.001$) of BT474 cells decreased upon trastuzumab treatment for 24 hours (Fig. 4.4a-c). Lifetime component analysis demonstrated significant increases in the portions of free NADH (α_1) and bound FAD (α_1) of BT474 cells treated with trastuzumab (Appendix A Fig. A.5). Similarly, the redox ratio of the MDA-MB-361 cells decreased ($P<0.05$) with trastuzumab treatment (Fig. 4.4a). The high resolution OMI enabled analysis of cellular heterogeneity in response to trastuzumab (Fig. 4.4d, Appendix A Fig. A.6). Distribution modeling of cellular redox ratios of MDA-MB-361 cells revealed two sub-populations characterized by differing redox ratios (Fig. 4.4d). The mean redox ratio of the first population, representing 70% of cells, showed no change (1.34 to 1.31) upon trastuzumab treatment ($P=0.07$), suggesting that trastuzumab did not affect metabolic processes in the majority of MDA-MB-361 cells. However, 30% of the cells responded to trastuzumab with a mean redox ratio that decreased from 1.89 to 1.65 ($P<0.001$).

HR6 cells are a trastuzumab-resistant BT474-derived sub-line that retains HER2 overexpression. Previous studies have shown maintenance of HER2 overexpression and PI3K/Akt signaling in trastuzumab-treated HR6 cells (28). Consistent with this observation, the redox ratio remained unchanged upon treatment with trastuzumab, as was FAD $\tau_{m.}$ NADH τ_m decreased in HR6 cells upon treatment with the antibody ($P<0.05$; Fig. 4.4a-c). An increased portion of free NADH (α_1) contributed to the decreased NADH τ_m observed in the HR6 cells (Appendix A Fig. A.5).

4.4.4 *In Vivo* Xenografts

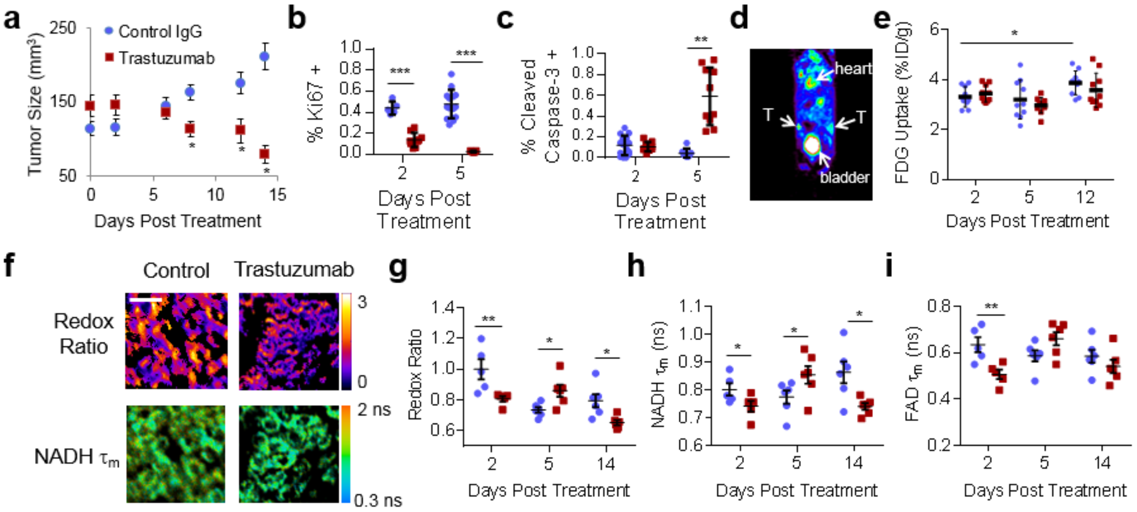

Figure 4.5 BT474 Xenograft OMI and FDG-PET. (a) BT474 tumors treated with trastuzumab (10 mg/kg, 2 x weekly) decrease in size (mean +/- SE) compared to control IgG treated tumors. Trastuzumab vs. control at each time point. (b) Ki67 staining demonstrates reduced proliferation in trastuzumab-treated tumors. (c) Cleaved caspase 3 staining demonstrates increased apoptosis in trastuzumab-treated tumors at day 5. (d) Representative FDG-PET image (T=tumor). (e) FDG uptake increases in control tumors at day 12 compared to control tumors at day 2. No significant difference in FDG uptake between trastuzumab-treated and control tumors is observed. $n = 10$. (f) Representative OMI images. Scale bar is 50 μm. (g) Decreased redox ratio, (h) NADH τ_m, and (i) FAD τ_m are observed in trastuzumab-treated tumors at 2 days post trastuzumab-treatment. * $P<0.05$, ** $P<0.01$; *** $P < 0.001$; $n = 6$ tumors.

To verify the OMI response observed in cultured cells, we performed OMI on HER2-overexpressing xenografts and compared these findings with tumor size, IHC, and FDG-PET measurements. Established BT474 xenografts treated with control IgG continued to grow throughout the course of the experiment while the trastuzumab-treated tumors decreased in size (Fig. 4.5a). IHC staining confirmed lower rates of proliferation and higher rates of apoptosis in the trastuzumab-treated group (Fig. 4.5b,c). A representative FDG-PET image displays the location of the tumors in the mammary fat near the hind limbs and demonstrates increased FDG-uptake in the tumors compared to the surrounding tissue (Fig. 4.5d). FDG-uptake increased in the control mice between days 2 and 12 post-treatment; however, no difference was observed between control and trastuzumab treated tumors at any time point (day 2, 5, or 12 post-treatment; Fig. 4.5e). OMI imaging of an identical cohort of tumors allowed cellular-level visualization of metabolism (Fig. 4.5f) and resolved metabolic differences in the redox ratio (Fig. 4.5g), NADH τ_m (Fig. 4.5h, Appendix A Fig. A.7a-c), and FAD τ_m (Fig. 4.5i, Appendix A Fig. A.7) between control and trastuzumab-responding tumors as early as 2 days after the first dose of trastuzumab.

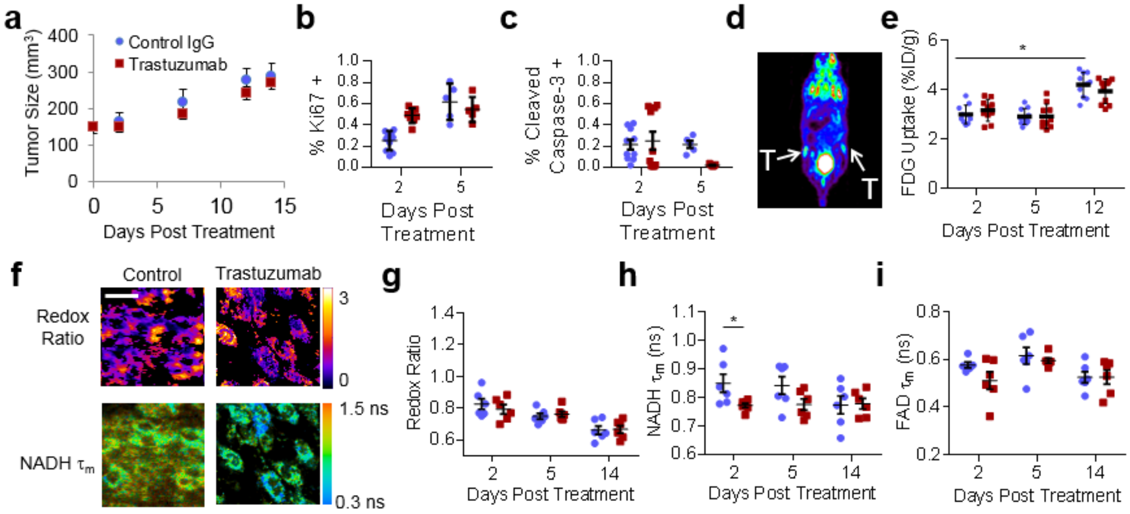

Figure 4.6 HR6 Xenograft OMI and FDG-PET. (a) HR6 tumor size (mean +/- SE) treated with trastuzumab (10 mg/kg, 2 x weekly) compared to control IgG treated tumors. (b) Ki67 staining of HR6 control IgG and trastuzumab-treated tumors. (c) Cleaved Caspase 3 staining of HR6 control IgG and trastuzumab-treated tumors. (d) Representative FDG-PET image (T=tumor). (e) FDG uptake increases in control tumors at day 12 compared to control tumors at day 2, * $P<0.05$. No significant difference in FDG uptake between trastuzumab-treated and control tumors is observed at any time. $n = 10$. (f) Representative OMI images, scale bar is 50 μm.. (g) Redox ratio, (h) NADH τ_m, and (i) FAD τ_m of control and trastuzumab-treated tumors. * $P<0.05$; n = 6 tumors.

Tumor size measurements of the HR6 xenografts showed similar growth of both control and trastuzumab-treated HR6 tumors (Fig. 4.6a). IHC confirmed that the trastuzumab-treated HR6 tumors retain proliferative capabilities and express similar rates of apoptosis compared to control treated tumors (Fig. 4.6b,c). A representative FDG-PET image of the HR6 tumors shows increased FDG-uptake by the tumor compared to the surrounding tissue (Fig. 4.6d). No change in FDG-PET was observed between control and trastuzumab-treated tumors at any time point; however, the FDG-uptake was increased in the control mice at 12 days compared to 2 days (Fig. 4.6e). No difference was observed in the redox ratio between control and treated HR6 tumors at any time point (Fig. 4.6f,g). NADH τ_m decreased in the HR6 treated tumors relative to controls at 2 days post treatment, but was similar to controls at days 5 and 14 (Fig. 4.6h, Appendix A Fig. A.8). No change in FAD τ_m was observed at any time point (Fig. 4.6i, Appendix A Fig. A.8).

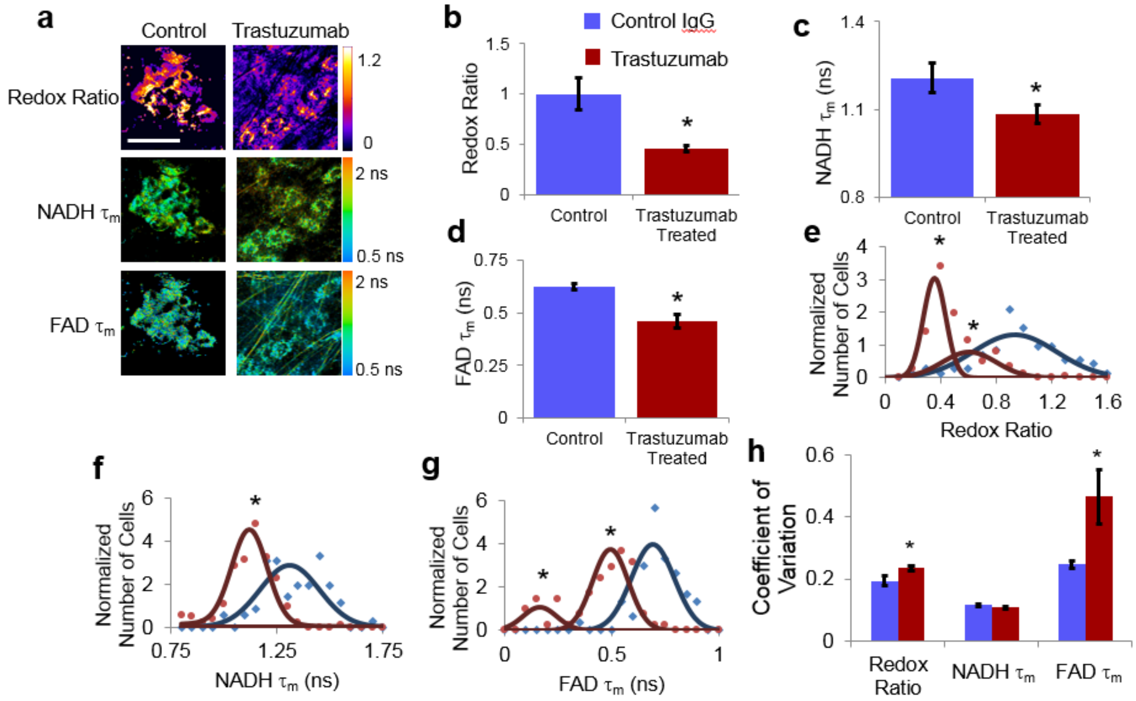

Figure 4.7 MDA-MB-231 Xenograft OMI. (a) Representative images of the optical redox ratio (first row), NADH τ_m (second row), and FAD τ_m (third row) of control and trastuzumab-treated (10 μg/kg; 48 hours) MDA-MB-361 mouse xenograft tumors. Scale bar is 50 μm. (b) Redox ratio, (c) NADH τ_m and (d) FAD τ_m mean +/- SE for control and trastuzumab-treated tumors evaluated on a per-image basis. (e) Redox ratio, (f) NADH τ_m and (g) FAD τ_m distribution density modeling of single-cell analysis in control and trastuzumab-treated tumors. (e-g) Distribution density modeling reveals two distinct populations of trastuzumab-treated cells for the redox ratio (e, maroon line) and FAD τ_m (g, maroon line) measurements, indicating heterogeneous cellular metabolic response to treatment. All control populations (e-g; blue lines) and the trastuzumab-treated NADH τ_m population (f, maroon line) are uni-modal. (h) The increased coefficient of variation in the redox ratio and FAD τ_m of the trastuzumab treated xenografts indicates increased intra-cellular variation in metabolism. * $P < 0.05$

The redox ratio ($P<0.05$), NADH τ_m ($P<0.05$), and FAD τ_m ($P<0.05$) decreased in trastuzumab-treated MDA-MB-361 xenografts as compared to IgG-treated controls (Fig. 4.7a-d;

Appendix A Fig. A.9) 2 days after treatment. Modeling of the optical redox ratio and FAD τ_m values on a cell-by-cell basis (inter-cell variability) identified two sup-populations of tumor cells in trastuzumab-treated animals, while an uni-modal cellular distribution was identified for NADH τ_m (Fig. 4.7e-g). High resolution analysis revealed that intra-cellular variability in redox ratios and FAD τ_m increased ($P<0.05$) in trastuzumab-treated samples (Fig. 4.7h). These results fully characterize OMI and demonstrate its potential for monitoring early drug response in cell culture and mouse xenografts on a single-cell level.

4.5 Discussion

OMI is advantageous for live cell and animal imaging due to several features, including direct and dynamic assessment of cellular metabolism *in vivo*, cellular and sub-cellular resolution imaging capabilities, rapid acquisition, low-cost, use of intrinsic signals (no contrast agents, no radioactivity), and high sensitivity to metabolic changes. Our results have significant implications for rapid assessment of drug action in pre-clinical models, which would greatly accelerate drug development studies.

These results are the first to correlate OMI with a standard assay of metabolic behavior. While the optical redox ratio is inferred from theory as the relative rates of glycolysis and oxidative phosphorylation within cells, we confirm a strong positive correlation ($r = 0.89$, $P=0.03$) with a standard measure of cellular glycolytic levels (Fig. 4.3). In contrast, NADH τ_m and FAD τ_m are not correlated with the glycolytic index (Appendix A Table A.2). The proportion of free NADH (α_1) has been interpreted as an analog to the optical redox ratio (27); however, we did not find a correlation between the optical redox ratio and NADH α_1 (Appendix A Table A.2). Given the physical nature of these fluorescence lifetime measurements, which are sensitive to protein-binding, relative fractions of free and bound components, and proximity to quenchers, it is not surprising that they are sensitive to more cellular processes than just glycolysis. For example, changes in the distribution of NADH and FAD enzyme binding sites associated with preferred metabolic pathways in breast cancer sub-types may be responsible for the changes in protein-bound lifetimes between cell lines (36). The changes in the lifetimes of the free components of NADH and FAD may reflect changes in dynamic quenching (22). Taken together, the data (Fig. 4.3, Appendix A Table A.2) indicate that the redox ratio, NADH and FAD lifetimes provide independent measures of cellular metabolism and the molecular microenvironment. The varied dynamics of these endpoints due to HER2 inhibition suggest that all three OMI endpoints provide added value when measured together.

We used these tools to differentiate breast cancer cells by sub-type, defined by ER and/or HER2 expression or absence (Fig. 4.3). OMI is sensitive to metabolic behaviors caused by ER and HER2 (Fig. 4.3), known oncogenic drivers of glycolytic metabolism in breast cancer cells (3, 8, 37, 38). ER regulates gene expression of glucose transporter proteins and proteins involved in oxidative phosphorylation and the citric acid cycle such as isocitrate dehydrogenase which actively reduces NAD^+ to NADH (37, 39-41). HER2 mediates metabolism through signaling of the PI3K/Akt/mTOR pathway which directs transcription of glycolytic enzymes (2, 3). When combined, the redox ratio and NADH lifetime fully separate the distinct sub-types of breast cancer (Fig. 4.3d), indicating that the complementary measures of the redox ratio and fluorescence lifetime allow robust characterization of cellular metabolism and molecular microenvironments associated with breast cancer sub-types.

We further show that the OMI endpoints optical redox ratio, NADH τ_m, and FAD τ_m, reflect impaired metabolic activity in trastuzumab-responsive BT474 cells (Fig. 4.4) *in vitro*, suggesting a large metabolic response of HER2-amplified cells to trastuzumab. Only one of the OMI endpoints, NADH τ_m, decreased in the trastuzumab-resistant HR6 cells (Fig. 4.4). While HR6 cells maintain HER2-overexpression and PTEN and P-Akt protein levels in the presence of trastuzumab, blockage of HER2 with trastuzumab may affect internal signaling (28). Due to its highly sensitive nature, NADH τ_m may be reporting such minute metabolism differences.

A subset of variables also resolved metabolic changes induced by trastuzumab in poorly responsive HER2-amplified cells (MDA-MB-361) *in vitro* (Fig. 4.4). Behavioral heterogeneity inherent to the MDA-MB-361 cell line suggests that 25% of the overall population would be growth inhibited by trastuzumab *in vitro* (42). Our data detected a 30% sub-population within MDA-MB-361 cells that responded to trastuzumab through decreased redox ratios (Fig. 4.4d), suggesting correlative evidence that high resolution optical imaging is capable of detecting responders and non-responders at the single cell level in the context of a heterogeneous tumor cell population with a mixed response. The complementary metabolic information gained from the OMI endpoints allowed identification of a large metabolic response to trastuzumab (BT474) but also resolved negative (HR6) and partial (MDA-MB-361) responses, demonstrating high sensitivity and resolution of OMI.

Finally, we measured the *in vivo* metabolic response to trastuzumab in HER2-overexpressing mouse xenografts. Trastuzumab-induced metabolic repression in BT474 and MDA-MB-361 tumors was detected by 48hrs post-treatment (Fig. 4.5, 4.7). The redox ratio and FAD τ_m did not change in trastuzumab-resistant HR6 tumors treated with the antibody (Fig. 4.6). However, NADH τ_m decreased in trastuzumab-treated HR6 tumors compared to controls at 48hrs (Fig. 4.6), which was consistent with the *in vitro* results (Fig. 4.4). Modeling of the inter-cellular variation of MDA-MB-361 xenograft tumors identified two sub-populations in response to trastuzumab for the optical redox ratio and FAD τ_m (Fig. 4.7), suggesting *in vivo* cell-to-cell heterogeneity. This heterogeneous *in vivo* response is consistent with the *in vitro* results (in Fig. 4.4). We attempted to include only tumor cells in our image analysis, by evaluation of the cell morphology with respect to histology, but acknowledge that non-tumor cell populations could have been included in this analysis. We speculate the greater intra-cellular variation of both the redox ratio and FAD τ_m observed in the MDA-MB-361 tumors treated with trastuzumab (Fig. 4.7h) is due to heterogeneous responses of individual mitochondria (43). Elucidation of this possibility will require additional research.

The tumor size measurements and IHC analysis of cellular proliferation and apoptosis were consistent with an antitumor effect of trastuzumab against BT474 tumors and a lack of an effect against HR6 tumors (Fig. 4.5, 4.6). Tumor size measurements first identified a difference in control versus trastuzumab-treated BT474 tumor size at 8 days after treatment was initiated (Fig. 4.5a), 6 days later than the first significant change in OMI endpoints between control and trastuzumab-treated tumors (day 2, Fig. 4.5g). While Ki67 staining of BT474 tumors identified reduced proliferation in BT474 tumors treated with trastuzumab at 2 and 5 days post-treatment, OMI is advantageous over IHC as a measure of tumor response because OMI provides a dynamic measure of cellular metabolism and can be performed *in vivo* and over time within the same animal. While *in vivo* OMI data is presented here, OMI endpoints remain robust measures of metabolism in freshly excised tissues (21) allowing implementation of this metabolic imaging technique in situations when *in vivo* measurements are not feasible.

FDG-PET has also been explored as a potential tool for assessing response to therapeutic agents. Consistent with a prior study (7), in this study, FDG-PET failed to identify a metabolic difference between control and trastuzumab-treated BT474 tumors (Fig. 4.5). FDG uptake did increase over time as the control tumors continued to grow. Unlike OMI, PET cannot resolve cellular sub-populations of differing response that are critical for investigating drug resistance mechanisms (7, 13-17, 44). Furthermore, PET requires large upfront and continued costs due to radiolabeled tracers, while OMI can be implemented in low-cost, wide-field or confocal microscopes without the need for external dyes (45-47). In addition, OMI allows for fast, accurate, dynamic *in vivo* monitoring of early therapeutic response, potentially reducing time and animals required for drug development. Our studies have focused on breast cancer and HER2 inhibition, but the methods developed are also applicable to the array of diseases that are treated with metabolism-modulating drugs (48-50).

The results of this study validate OMI as a powerful tool for quantifying cellular metabolism, which is an active area of investigation across multiple diseases. As we demonstrate using human breast cancer cells and xenografts, optical metabolic measurements are sensitive to distinct tumor cell sub-types. Additionally, we present significant findings suggesting that OMI can be used as an early indicator of metabolic response to treatment with a targeted therapy, both in cell culture and *in vivo*. These results represent the culmination of multiple imaging technologies, analysis tools, and their validation with standard assays and FDG-PET. The results in breast cancer cells and xenografts provide the first direct measurements relating cellular metabolism, HER2 expression, HER2 inhibition, and resistance to HER2 inhibitors in live cells and tissues. Additionally, these methodologies are potentially broadly applicable outside the cancer and imaging communities, including those in drug development and metabolism research across multiple diseases. While we see OMI as an immediately powerful tool in preclinical models, it also may directly impact patient care as an adjunct to current practice, either on freshly excised tissue (21) or through *in vivo* endoscopes adapted for fluorescence imaging.

4.6 Acknowledgments

We thank K. Poole, W. Sit, and M. Schultis for assistance with cell culture and animal imaging. Funding sources include NCI SPORE in Breast Cancer (P50 CA098131), NSF Graduate Research Fellowship (DGE-0909667; for AJW), VICC Young Ambassadors Discovery Grant. The VUMC Flow Cytometry Shared Resource and Translational Pathology Lab are supported by the Vanderbilt Ingram Cancer Center (P30 CA68485) and the Vanderbilt Digestive Disease Research Center (DK058404). The VU Small Animal Imaging Institute is supported by NCI P30 CA068485.

4.7 References

1. Warburg O. On the origin of cancer cells. Science. 1956;123(3191):309-14.
2. Plas DR, Thompson CB. Akt-dependent transformation: there is more to growth than just surviving. Oncogene. 2005;24(50):7435-42.
3. Harari D, Yarden Y. Molecular mechanisms underlying ErbB2/HER2 action in breast cancer. Oncogene. 2000;19(53):6102-14.
4. Ross JS, Fletcher JA. The HER-2/neu oncogene in breast cancer: prognostic factor, predictive factor, and target for therapy. Stem Cells. 1998;16(6):413-28.
5. Vogel CL, Cobleigh MA, Tripathy D, Gutheil JC, Harris LN, Fehrenbacher L, Slamon DJ, Murphy M, Novotny WF, Burchmore M, Shak S, Stewart SJ, Press M. Efficacy and safety of trastuzumab as a single agent in first-line treatment of HER2-overexpressing metastatic breast cancer. Journal of Clinical Oncology. 2002;20(3):719-26.
6. Yakes FM, Chinratanalab W, Ritter CA, King W, Seelig S, Arteaga CL. Herceptin-induced inhibition of phosphatidylinositol-3 kinase and Akt Is required for antibody-mediated effects on p27, cyclin D1, and antitumor action. Cancer Res. 2002;62(14):4132-41.
7. Shah C, Miller TW, Wyatt SK, McKinley ET, Olivares MG, Sanchez V, Nolting DD, Buck JR, Zhao P, Ansari MS, Baldwin RM, Gore JC, Schiff R, Arteaga CL, Manning HC. Imaging biomarkers predict response to anti-HER2 (ErbB2) therapy in preclinical models of breast cancer. Clin Cancer Res. 2009;15(14):4712-21.
8. Walsh A, Cook RS, Rexer B, Arteaga CL, Skala MC. Optical imaging of metabolism in HER2 overexpressing breast cancer cells. Biomedical optics express. 2012;3(1):75-85.
9. Brown RS, Wahl RL. Overexpression of Glut-1 glucose transporter in human breast cancer. An immunohistochemical study. Cancer. 1993;72(10):2979-85.

10. Wang L, Zhang Q, Zhang J, Sun S, Guo H, Jia Z, Wang B, Shao Z, Wang Z, Hu X. PI3K pathway activation results in low efficacy of both trastuzumab and lapatinib. BMC Cancer. 2011;11(1):248.

11. Zhang D, Tai LK, Wong LL, Chiu LL, Sethi SK, Koay ES. Proteomic study reveals that proteins involved in metabolic and detoxification pathways are highly expressed in HER-2/neu-positive breast cancer. Mol Cell Proteomics. 2005;4(11):1686-96.

12. Nguyen QD, Perumal M, Waldman TA, Aboagye EO. Glucose Metabolism Measured by [F]Fluorodeoxyglucose Positron Emission Tomography Is Independent of PTEN/AKT Status in Human Colon Carcinoma Cells. Transl Oncol. 2011;4(4):241-8.

13. Specht JM, Kurland BF, Montgomery SK, Dunnwald LK, Doot RK, Gralow JR, Ellis GK, Linden HM, Livingston RB, Allison KH, Schubert EK, Mankoff DA. Tumor Metabolism and Blood Flow as Assessed by Positron Emission Tomography Varies by Tumor Subtype in Locally Advanced Breast Cancer. Clinical Cancer Research. 2010;16(10):2803-10.

14. Basu S, Chen W, Tchou J, Mavi A, Cermik T, Czerniecki B, Schnall M, Alavi A. Comparison of triple-negative and estrogen receptor-positive/progesterone receptor-positive/HER2-negative breast carcinoma using quantitative fluorine-18 fluorodeoxyglucose/positron emission tomography imaging parameters: a potentially useful method for disease characterization. Cancer. 2008;112(5):995-1000.

15. Jacobs MA, Ouwerkerk R, Wolff AC, Gabrielson E, Warzecha H, Jeter S, Bluemke DA, Wahl R, Stearns V. Monitoring of neoadjuvant chemotherapy using multiparametric, (23)Na sodium MR, and multimodality (PET/CT/MRI) imaging in locally advanced breast cancer. Breast cancer research and treatment. 2011;128(1):119-26.

16. Mankoff DA, Dunnwald LD, L. K., Doot RK, Specht JM, Gralow JR, Ellis GK, Livingston RB, Linden HM, Gadi VK, Kurland BF, Schubert EK, Muzi M. PET Tumor Metabolism in Locally Advanced Breast Cancer Patients Undergoing Neoadjuvant Chemotherapy: Value of Static versus Kinetic Measures of Fluorodeoxyglucose Uptake. Clinical Cancer Research. 2011;17(8):2400-9.

17. Minami H, Kawada K, Murakami K, Sato T, Kojima Y, Ebi H, Mukai H, Tahara M, Shimokata K. Prospective study of positron emission tomography for evaluation of the activity of lapatinib, a dual inhibitor of the ErbB1 and ErbB2 tyrosine kinases, in patients with advanced tumors. Japanese Journal of Clinical Oncology. 2007;37(1):44-8.

18. Reilly RM, McLarty K, Fasih A, Scollard DA, Done SJ, Vines DC, Green DE, Costantini DL. (18)F-FDG Small-Animal PET/CT Differentiates Trastuzumab-Responsive from Unresponsive Human Breast Cancer Xenografts in Athymic Mice. Journal of Nuclear Medicine. 2009;50(11):1848-56.

19. Chance B, Schoener B, Oshino R, Itshak F, Nakase Y. Oxidation-reduction ratio studies of mitochondria in freeze-trapped samples. NADH and flavoprotein fluorescence signals. J Biol Chem. 1979;254(11):4764-71.

20. Skala MC, Riching KM, Gendron-Fitzpatrick A, Eickhoff J, Eliceiri KW, White JG, Ramanujam N. In vivo multiphoton microscopy of NADH and FAD redox states, fluorescence lifetimes, and cellular morphology in precancerous epithelia. Proc Natl Acad Sci U S A. 2007;104(49):19494-9.

21. Walsh AJ, Poole KM, Duvall CL, Skala MC. Ex vivo optical metabolic measurements from cultured tissue reflect in vivo tissue status. Journal of biomedical optics. 2012;17(11):116015.

22. Lakowicz J. Principles of fluorescence spectroscopy. New York: Plenum Publishers; 1999.

23. Lakowicz JR, Szmacinski H, Nowaczyk K, Johnson ML. Fluorescence Lifetime Imaging of Free and Protein-Bound Nadh. Proc Natl Acad Sci U S A. 1992;89(4):1271-5.

24. Nakashima N, Yoshihara K, Tanaka F, Yagi K. Picosecond fluorescence lifetime of the coenzyme of D-amino acid oxidase. J Biol Chem. 1980;255(11):5261-3.

25. Maeda-Yorita K, Aki K. Effect of nicotinamide adenine dinucleotide on the oxidation-reduction potentials of lipoamide dehydrogenase from pig heart. J Biochem. 1984;96(3):683-90.

26. Sidani M, Wyckoff J, Xue CS, Segall JE, Condeelis J. Probing the microenvironment of mammary tumors using multiphoton microscopy. J Mammary Gland Biol. 2006;11(2):151-63.

27. Bird DK, Yan L, Vrotsos KM, Eliceiri KW, Vaughan EM, Keely PJ, White JG, Ramanujam N. Metabolic mapping of MCF10A human breast cells via multiphoton fluorescence lifetime imaging of the coenzyme NADH. Cancer Res. 2005;65(19):8766-73.

28. Ritter CA, Perez-Torres M, Rinehart C, Guix M, Dugger T, Engelman JA, Arteaga CL. Human breast cancer cells selected for resistance to trastuzumab in vivo overexpress epidermal growth factor receptor and ErbB ligands and remain dependent on the ErbB receptor network. Clin Cancer Res. 2007;13(16):4909-19.

29. Miller TW, Forbes JT, Shah C, Wyatt SK, Manning HC, Olivares MG, Sanchez V, Dugger TC, de Matos Granja N, Narasanna A, Cook RS, Kennedy JP, Lindsley CW, Arteaga CL. Inhibition of mammalian target of rapamycin is required for optimal antitumor effect of HER2 inhibitors against HER2-overexpressing cancer cells. Clin Cancer Res. 2009;15(23):7266-76.

30. Gee MS, Upadhyay R, Bergquist H, Alencar H, Reynolds F, Maricevich M, Weissleder R, Josephson L, Mahmood U. Human breast cancer tumor models: molecular imaging of drug susceptibility and dosing during HER2/neu-targeted therapy. Radiology. 2008;248(3):925-35.

31. Dandekar M, Tseng JR, Gambhir SS. Reproducibility of 18F-FDG microPET studies in mouse tumor xenografts. Journal of Nuclear Medicine. 2007;48(4):602-7.

32. Fueger BJ, Czernin J, Hildebrandt I, Tran C, Halpern BS, Stout D, Phelps ME, Weber WA. Impact of animal handling on the results of 18F-FDG PET studies in mice. Journal of Nuclear Medicine. 2006;47(6):999-1006.

33. McKinley ET, Bugaj JE, Zhao P, Guleryuz S, Mantis C, Gokhale PC, Wild R, Manning HC. 18FDG-PET predicts pharmacodynamic response to OSI-906, a dual IGF-1R/IR inhibitor, in preclinical mouse models of lung cancer. Clin Cancer Res. 2011;17(10):3332-40.

34. Akaike H. A new look at the statistical model identification. Automatic Control, IEEE Transactions on. 1974;19(6):716-23.

35. Huang S, Heikal AA, Webb WW. Two-photon fluorescence spectroscopy and microscopy of NAD(P)H and flavoprotein. Biophys J. 2002;82(5):2811-25.

36. Yu Q, Heikal AA. Two-photon autofluorescence dynamics imaging reveals sensitivity of intracellular NADH concentration and conformation to cell physiology at the single-cell level. J Photochem Photobiol B. 2009;95(1):46-57.

37. Cheng CM, Cohen M, Wang J, Bondy CA. Estrogen augments glucose transporter and IGF1 expression in primate cerebral cortex. FASEB J. 2001;15(6):907-15.

38. Ostrander JH, McMahon CM, Lem S, Millon SR, Brown JQ, Seewaldt VL, Ramanujam N. Optical redox ratio differentiates breast cancer cell lines based on estrogen receptor status. Cancer Res. 2010;70(11):4759-66.

39. Chen JQ, Brown TR, Russo J. Regulation of energy metabolism pathways by estrogens and estrogenic chemicals and potential implications in obesity associated with increased exposure to endocrine disruptors. Biochimica Et Biophysica Acta. 2009;1793(7):1128-43.

40. Yadav RN. Isocitrate dehydrogenase activity and its regulation by estradiol in tissues of rats of various ages. Cell Biochem Funct. 1988;6(3):197-202.

41. Pastorelli R, Carpi D, Airoldi L, Chiabrando C, Bagnati R, Fanelli R, Moverare S, Ohlsson C. Proteome analysis for the identification of in vivo estrogen-regulated proteins in bone. Proteomics. 2005;5(18):4936-45.

42. Narayan M, Wilken JA, Harris LN, Baron AT, Kimbler KD, Maihle NJ. Trastuzumab-induced HER reprogramming in "resistant" breast carcinoma cells. Cancer Res. 2009;69(6):2191-4.

43. Kuznetsov AV, Usson Y, Leverve X, Margreiter R. Subcellular heterogeneity of mitochondrial function and dysfunction: evidence obtained by confocal imaging. Mol Cell Biochem. 2004;256-257(1-2):359-65.

44. Benard F, Aliaga A, Rousseau JA, Cadorette J, Croteau E, van Lier JE, Lecomte R. A small animal positron emission tomography study of the effect of chemotherapy and hormonal therapy on the uptake of 2-deoxy-2-[F-18]fluoro-D-glucose in murine models of breast cancer. Molecular Imaging and Biology. 2007;9(3):144-50.

45. Drezek R, Brookner C, Pavlova I, Boiko I, Malpica A, Lotan R, Follen M, Richards-Kortum R. Autofluorescence microscopy of fresh cervical-tissue sections reveals alterations in tissue biochemistry with dysplasia. Photochem Photobiol. 2001;73(6):636-41.

46. Skala MC, Fontanella A, Lan L, Izatt JA, Dewhirst MW. Longitudinal optical imaging of tumor metabolism and hemodynamics. Journal of biomedical optics. 2010;15(1):011112.

47. Suhling K, French PM, Phillips D. Time-resolved fluorescence microscopy. Photochem Photobiol Sci. 2005;4(1):13-22.

48. Kamohara S, Burcelin R, Halaas JL, Friedman JM, Charron MJ. Acute stimulation of glucose metabolism in mice by leptin treatment. Nature. 1997;389(6649):374-7.

49. Hundal RS, Petersen KF, Mayerson AB, Randhawa PS, Inzucchi S, Shoelson SE, Shulman GI. Mechanism by which high-dose aspirin improves glucose metabolism in type 2 diabetes. The Journal of clinical investigation. 2002;109(10):1321-6.

50. Kantor PF, Lucien A, Kozak R, Lopaschuk GD. The antianginal drug trimetazidine shifts cardiac energy metabolism from fatty acid oxidation to glucose oxidation by inhibiting mitochondrial long-chain 3-ketoacyl coenzyme A thiolase. Circulation Research. 2000;86(5):580-8.

CHAPTER 5

Ex Vivo Optical Metabolic Measurements from Cultured Tissue Reflect in Vivo Tissue Status

Walsh AJ, Poole KM, Duvall CL, Skala, MC. "Ex vivo optical metabolic measurements from culture tissue reflect in vivo tissue status." *J Biomed Optics*. 2012;17(11):116015.

5.1 Abstract

Optical measurements of metabolism are ideally acquired *in vivo*; however, intravital measurements are often impractical. Accurate *ex vivo* assessments would greatly broaden the applicability of optical measurements of metabolism. In this study, we investigate the use of live tissue culture experiments to serve as a surrogate for *in vivo* metabolic measurements. To validate this approach, NADH and FAD fluorescence intensity and lifetime images were acquired with a two-photon microscope from hamster cheek pouch epithelia *in vivo*, from biopsies maintained in live tissue culture up to 48 hours, and from flash frozen and thawed biopsies. We found that the optical redox ratio (fluorescence intensity of NADH / FAD) of the cultured biopsy was statistically identical to the *in vivo* measurement until 24h, while the redox ratio of the frozen-thawed samples decreased by 15% ($p<0.01$). The NADH mean fluorescence lifetime (τ_m) remained unchanged ($p>0.05$) during the first 8h of tissue culture, while the NADH τ_m of frozen-thawed samples increased by 13% ($p<0.001$). Cellular morphology did not significantly change between *in vivo*, cultured, and frozen-thawed tissues ($p>0.05$). All results were consistent across multiple depth layers in this stratified squamous epithelial tissue. Histological markers for proliferation and apoptosis also confirm the viability of tissues maintained in culture. This study suggests that short-term *ex vivo* tissue culture may be more appropriate than frozen-thawed tissue for optical metabolic and morphologic measurements that approximate *in vivo* status.

5.2 Introduction

Optical imaging is a powerful tool for monitoring the metabolic status of cells and tissues due to the auto-fluorescence properties of the metabolic co-enzymes NADH and FAD. NADH is the principal electron acceptor in glycolysis and electron donor in oxidative phosphorylation while FAD is the primary electron acceptor in oxidative phosphorylation. The optical "redox ratio" (fluorescence intensity of NADH divided by that of FAD) is widely used to monitor cellular metabolism in cells, *ex vivo* tissues, and *in vivo* tissues in order to diagnose disease (1, 2) , monitor cellular differentiation (3), and characterize other metabolic perturbations (4, 5).

Recently, the fluorescence lifetimes of NADH and FAD have also been evaluated as optical metabolic biomarkers (2, 6-10). The fluorescence lifetime is the time a fluorophore remains in the excited state before returning to the ground state and emitting a fluorescent photon. Fluorescence lifetimes are self-referenced and more robust than fluorescence intensity measurements in regard to inter-system and intra-system variability (7). Additionally, fluorescence lifetimes are sensitive to changes in pH, temperature, and proximity to quenchers (7, 11). Often, the fluorescence lifetime decay curves for NADH and FAD are each fit to a two-component exponential decay (2, 6, 12). The two lifetime components represent the two most probable configurations of NADH and FAD, which are free in solution or bound to a protein (12, 13). The short lifetimes and long lifetimes of NADH represent the free and protein-bound components, respectively. Conversely, the short and long lifetimes of FAD represent the protein-bound and free components, respectively. For these reasons, the fluorescence lifetimes of NADH and FAD are robust reporters for metabolic differences between tissues. Auto-fluorescence lifetime imaging has been used for monitoring pre-cancers and cancers in oral cancer models and breast cancer models (2, 6, 10, 14-18).

Ideally, optical metabolic measurements should be performed *in vivo*. Thus, these techniques have been predominantly used in easily accessible tissues, such as the skin and oral cancer models (2, 8, 19, 20). The growing development of endoscopes capable of confocal fluorescence microscopy is enabling measurements of previously inaccessible tissue (21, 22). Yet, fluorescence endoscopes are still somewhat specialized, cumbersome, and represent a significant technical and regulatory burden for feasibility studies, especially in tissue sites that are difficult to access (i.e. outside of the gastrointestinal tract). As a result, many feasibility studies in this field are performed on fixed tissue slides, immortalized cell lines, or excised tissue (6, 15, 23), which may not accurately represent the metabolic state of live, intact tissue. Furthermore, the use of optical metabolic techniques would be greatly expanded by the development of an effective tissue handling protocol that allowed for *ex vivo* tissue interrogation that accurately reflects the *in vivo* metabolic state. However, the effect of *ex vivo* sample preparation on optical metabolic measurements has not been explored.

The goal of this study is to investigate live tissue culture as an alternative sample preparation for optical metabolic imaging when *in vivo* measurements are not feasible. Current protocols to represent *in vivo* metabolic activity in excised tissue require flash-freezing of the tissue (4), however such a procedure requires tissue submersion in liquid nitrogen and may induce changes in sensitive fluorescence lifetime endpoints. Live tissue culture may address these limitations. Live tissue culture maintains the tissue in tissue culture media that provides oxygen, glucose, and other necessary nutrients. Furthermore, chilled tissue media has been used in previous optical studies (23, 24) because it contains more dissolved oxygen than media maintained at body temperature. However, this chilled media procedure for maintaining tissue culture has not been rigorously compared to *in vivo* metabolic measurements.

We hypothesized that, for a discrete period of time following harvest, excised tissue maintained in chilled tissue culture media will provide metabolic measurements that are representative of the *in vivo* metabolic state. To test this hypothesis, the NADH and FAD fluorescence intensity and lifetime, as well as cellular morphology, of the cheek pouch epithelium of 16 Golden Syrian hamsters were measured *in vivo*, *ex vivo* from biopsies maintained in live culture over 48 hours, and *ex vivo* from flash frozen and thawed tissue biopsies. Both high and low time resolution protocols were followed to investigate both short-term and long-term changes in the cellular metabolism of the cultured biopsies. For the high resolution protocol, optical metabolic measurements were obtained every 30 minutes for 4 hours from a single epithelial depth. For the low resolution protocol, images of two different epithelial depths were acquired at 4, 8, 12, 24, and 48 hours.

5.3 Materials and Methods

5.3.1 Hamster Protocol

For this study, sixteen male Golden Syrian hamsters were evaluated (103 ± 5 g). This study was approved by the Vanderbilt University Animal Care and Use Committee and meets the National Institutes of Health guidelines for animal welfare. Hamsters were anesthetized with a mixture of 200 mg/kg ketamine and 5 mg/kg xylazine with an intraperitoneal injection. The mucosa of the cheek pouch was exposed and secured against a coverslip for imaging. All images were acquired from the stratum spinosum or basal epithelial layers at depths of approximately 20 µm or 30 µm, respectively. *In vivo* measurements of the cheek pouch were obtained from the cheek epithelium. Then, two 6 mm biopsies of the cheek pouch were acquired immediately after the *in vivo* measurements from the same region that was imaged *in vivo*. For 10 hamsters, one biopsy per hamster was flash-frozen in liquid nitrogen (frozen-thawed sample). This sample was placed immediately in a -80°C freezer. The second 6 mm biopsy (live tissue culture sample) was immediately placed in a glass-bottom petri dish with chilled (3° C), sterile tissue culture media (DMEM without phenol red, GIBCO). The stratum spinosum layer of the epithelium was immediately measured and sequentially measured every 30 minutes for 4 hours after the time of the biopsy from the live tissue culture sample. For this high time-resolution protocol, a single tissue layer was interrogated to allow for comparisons between time-points and to minimize tissue warming at room temperature during imaging. This high time-resolution, short time-frame protocol was chosen to investigate acute changes in the metabolism of the tissue immediately after excision. For the remaining six hamsters, after *in vivo* imaging, two biopsies were obtained and both were placed in chilled tissue media for the long-term (low time-resolution) imaging studies. This low time-resolution, long time-frame protocol investigates the maximum duration over which optical metabolic measurements in live culture correspond with *in vivo* measurements. One of the biopsies was imaged after 4, 8, 12, 24, and 48 hours at two different depths corresponding to the spinous and basal regions. The second biopsy was fixed in formalin for histological analysis after 4, 8, 12, 24, or 48 hours in live culture. Each measurement in live tissue culture over this time course was conducted within 5 minutes at room temperature (22°C), and the sample was refrigerated (3°C) between measurements. Prior to measurement of the frozen biopsy, the specimen was thawed in chilled tissue culture media for 15-20 minutes (25). Each animal was sacrificed after both biopsies had been obtained.

5.3.2 Imaging Instrumentation

All data were acquired using a custom built, commercial two-photon imaging system (Prairie Technologies, Middleton, WI) within the Biophotonics Laboratory at Vanderbilt University. A titanium sapphire laser (Coherent Inc., Santa Clara, CA) provided the excitation source. The excitation and emission light were coupled through an inverted microscope (TiE; Nikon, Melville, NY) with either a 40X water-immersion objective (1.15 NA) or a 40X oil-immersion objective (1.3 NA). For NADH excitation and FAD excitation, the laser was tuned to 750 nm and 890 nm, respectively. The average power incident on the sample was ~7.5-7.8 mW for NADH excitation and ~8.4-8.6 mW for FAD excitation. A pixel dwell time of 4.8 □s was used for all 256x256 pixel images. NADH and FAD images were acquired sequentially. A 400-480 nm bandpass filter isolated NADH emission onto the PMT detector. A dichroic mirror directed wavelengths greater than 500 nm onto a 500—600 nm bandpass filter, thus removing collagen second harmonic generation (SHG) signals from the FAD image. Fluorescence lifetime images were acquired with time-correlated single photon counting electronics (SPC-150, Becker and Hickl, Germany) and a GaAsP PMT (Hamamatsu, Japan). Isolation of NADH and FAD collection for this system was confirmed by treating cells with cyanide (26) and observing an increase in NADH fluorescence intensity and a decrease in FAD fluorescence intensity (data not shown).

The instrument response function was measured by imaging the SHG signal of urea crystals with excitation at 900 nm. The instrument system response has a full width at half-maximum of 260 ps. This measured system response was used in the lifetime fit model. The fluorescence lifetime of a standard, Fluoresbrite YG microspheres (20 µm, Polysciences Inc.), was measured daily. Fit to a single decay curve, the fluorescence lifetime of the microspheres has a value of 2.14± 0.05 ns (n=14), which is consistent with previous studies (2, 6, 10, 27).

5.3.3 Fluorescence Lifetime Imaging

For the *in vivo* measurement, the hamster was placed face down with the cheek pouch mucosa in contact with a cover slip and exposed to the objective. The epithelium of the cheek pouch was identified and imaged at a depth of ~20 µm. This depth was imaged across all samples (*in vivo, ex vivo,* and frozen tissues), as determined by stage translation distance from the surface of the tissue and by visual inspection of cell size. The six hamsters imaged for the longer live culture time course were also interrogated at a depth of ~30 μm, corresponding to the basal epithelium. One NADH lifetime measurement was acquired over an integration time of 60s. Sequentially, an FAD lifetime image was acquired, also for 60s, at the same location. Imaging parameters such as laser power, PMT voltage, pixel integration time, and lifetime collection time were maintained across all animals and measurements including the *ex vivo* and frozen samples. Photon count rates (~5 x 10^5 photons/s) were maintained throughout all imaging sessions, ensuring that photobleaching did not occur. In addition, it was assured that no quantifiable change in fluorescence intensity was observed between sequential images of the same location, further confirming that photobleaching did not occur.

5.3.4 Quantification of Cellular Morphology

In order to monitor any change in cellular morphology in the live tissue culture, cell size and nuclear-cytoplasmic ratio (NCR) were computed from the high resolution NADH fluorescence images. A region of well-defined cells was identified within each image and the total number of cells in the region of interest (ROI) was counted. The average cell cross sectional area was determined by dividing the total number of pixels within the ROI (consisting of nuclear and cytoplasmic pixels) by the number of cells in the ROI and converting the area from pixels to μm^2. Next, each image was thresholded to assign pixels within the nucleus to 0 and pixels within the cytoplasm to 1 for quantification of the number of nuclear pixels and cytoplasmic pixels. The NCR was calculated by dividing the number of nuclear pixels by cytoplasmic pixels. This analysis was done in ImageJ (NIH, http://rsbweb.nih.gov/ij/).

5.3.5 Quantification of the Optical Redox Ratio

Fluorescence intensity images were constructed from the fluorescence lifetime images by integrating over time, summing all photons for each pixel. Any regions of non-cellular structures, such as wrinkles within the tissue, were excluded from analysis. Additionally, a threshold was applied to isolate fluorescence from the cytoplasm and exclude nuclear fluorescence. The redox ratio was computed for each pixel by dividing the NADH fluorescence intensity by the FAD fluorescence intensity. The mean redox ratio for the image was computed by averaging the redox ratios from all cells, excluding the nuclear region. For each hamster, the cultured biopsy and frozen biopsy redox ratio measurements were normalized to the matched *in vivo* measurement to account for inter-animal and system variation. This analysis was done in Matlab (Natick, MA).

5.3.6 Quantification of the Fluorescence Lifetime

A commercial software program, SPCImage (Becker and Hickl, Germany), was utilized to analyze the fluorescence decay data. In SPCImage, the measured system response of the second harmonic generation of urea crystals was de-convolved from the data. The resulting decay curve was then fit to the following model:

$$I(t) = \alpha_1 exp^{-t/\tau_1} + \alpha_2 exp^{-t/\tau_2} + C$$

where I(t) is the fluorescence intensity at time t after the excitation pulse, α_1 and α_2 are the fractional contributions of the first and second emitting species (i.e. $\alpha_1 + \alpha_2 = 1$), τ_1 and τ_2 are the fluorescence lifetimes of the first and second emitting species, and C accounts for background light. Within the SPCImage software, after a threshold was set to isolate cytoplasmic fluorescence, the fluorescence decay for each pixel was evaluated. Then, matrices of τ_1, τ_2, α_1, and α_2 were exported for further analysis. The mean τ_1, τ_2, α_1, and α_2 for each image were averaged across all pixels in Matlab (Natick, MA). Additionally, the mean fluorescence lifetime (τ_m) was computed as a weighted average of τ_1 and τ_2.

$$\tau_m = \alpha_1\tau_1 + \alpha_2\tau_2$$

5.3.7 Statistical Analysis

A Wilcoxon rank sum test was used to test for differences between the *in vivo* mean values of the redox ratio, NADH and FAD τ_1, τ_2, τ_m, and α_1/ α_2 ratio and each cultured biopsy time point. Likewise, a Wilcoxon rank sum test was used to test for significance between optical measurements from *in vivo* and frozen-thawed tissue. For all tests, an α level < 0.05 indicates significance.

5.3.8 Histological Analysis

Hamster cheek pouch biopsies were collected and placed in chilled tissue media and refrigerated for 4, 8, 12, 24, or 48 hours. The biopsy was placed in buffered formalin, paraffin embedded, sliced, and stained for Ki67 (a marker of proliferation) and cleaved caspase-3 (a marker of apoptotic cells). Traditional H&E staining was also performed to help visualize the epithelial layer. Ki67 and cleaved caspase-3 staining protocols were verified in positive control samples of the mouse small intestine and mouse thymus, respectively (data not shown).

5.4 Results

Optical redox ratio values and NADH and FAD fluorescence lifetime values were acquired from the cheek pouch epithelium of sixteen hamsters *in vivo*, from a cultured biopsy, and from a frozen-thawed biopsy. Fig. 5.1 shows representative images of the normalized redox ratio, mean NADH lifetime, and mean FAD lifetime from the spinosum and basal layers of the epithelium *in vivo*, cultured tissue at 4, 12, 24, and 48 hours post excision, and frozen-thawed tissue for the normal hamster epithelium. The redox ratio of the *in vivo* tissue appears to be similar to the cultured biopsy at 4 hours and less than the cultured biopsy at 24 hours. The frozen-thawed tissue appears to have a lower redox ratio than the *in vivo* tissue (Fig. 5.1). For the mean lifetimes of both NADH and FAD, the cultured tissue appears to have a similar lifetime to the *in vivo* tissue after 4 hours; however, the frozen tissue shows an increased mean NADH lifetime relative to *in vivo* values (Fig. 5.1). No significant changes in cellular morphology are observed in the cultured or frozen tissue relative to the *in vivo* tissue measurements.

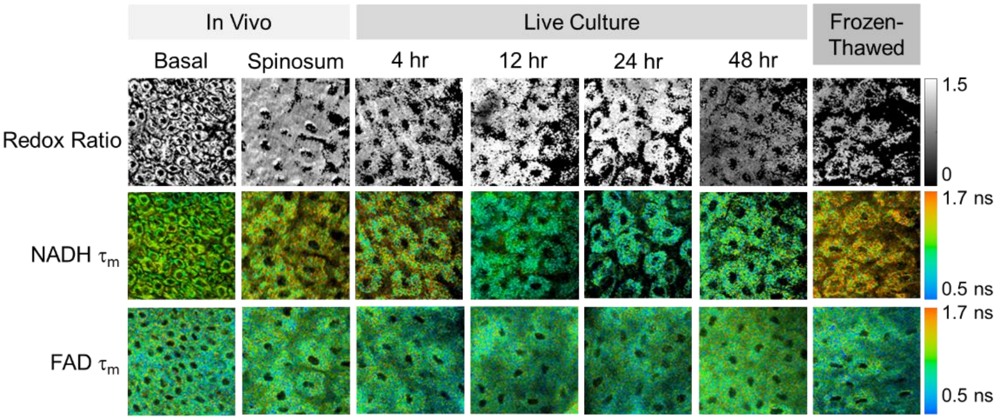

Figure 5.1. **Representative OMI images of live cultured tissues.** Representative redox ratio (first row), NADH τ_m (second row), and FAD τ_m (third row) images from *in vivo* hamster epithelium at the basal (first column) and spinosum (second column) regions, tissue maintained in live culture 4, 12, 24, and 48 hours after excision (third-sixth columns), and frozen-thawed tissue (last column). Each image is 100x100 μm. τ_m is the mean lifetime ($\tau_1*\alpha_1 + \tau_2*\alpha_2$).

To compare deviations from the *in vivo* optical redox ratio in the cultured and frozen-thawed tissue samples, the optical redox ratio was normalized to the *in vivo* measurement. The variance in the redox ratio among *in vivo* measurements from the same hamster is 0.053, corresponding to a coefficient of variation (COV) of 8%. Fig. 5.2 shows the normalized redox ratio of the *in vivo* tissue, cultured tissue over 4h, and frozen-thawed tissue. No significant changes ($p > 0.05$) in the redox ratio are observed at any time point for the 4 hours the cultured biopsy was imaged (Fig. 5.2A). The mean redox ratio of the cultured biopsy up to 4 hours after excision is within 8% of the *in vivo* value. The redox ratio of the frozen-thawed sample, however, is 85% of the *in vivo* tissue measurement and this difference is significant ($p < 0.01$).

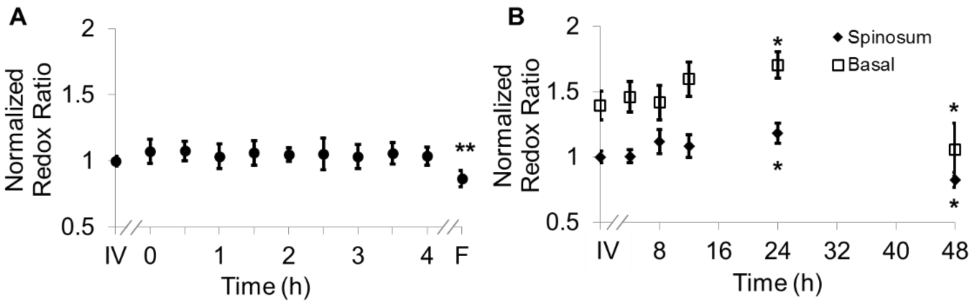

Figure 5.2. Redox ratio of live cultured tissues and frozen thawed tissues. A. The redox ratio value of frozen-thawed (F) hamster epithelium is significantly reduced from the *in vivo* (IV) value, while live tissue culture maintains redox ratio values similar to *in vivo* measures over the 4 hours of live culture measurement (mean ± SE of n=10 measurements). B. The redox ratios of the spinosum and basal epithelial layers of the live-culture biopsies over 48 hours (mean ± SE of n=6). Asterisk denotes significant difference between *in vivo* and the indicated measurement (* $p < 0.05$; ** $p < 0.01$).

The metabolic activity of the stratified squamous epithelium is known to change with depth, with the most metabolically active cells occupying the basal layer of the epithelium (28). Therefore, an analysis of the metabolic change in multiple epithelial layers was evaluated over time. The redox ratio of the basal region is greater than that of the spinosum region at all time-points ($p < 0.05$, Fig. 5.2B). No significant change in the redox ratio is observed with time in live culture until 24 hours, when the redox ratio of both the spinosum and basal cells increases ($p < 0.05$, Fig. 5.2B). By 48 hours, the redox ratio in both regions decreases ($p < 0.05$, Fig. 5.2B).

Table 5.1. Mean (SE) for *in vivo* measurements of NADH and FAD lifetime components (n=10). τ_m is the mean lifetime ($\tau_1*\alpha_1 + \tau_2*\alpha_2$).

	τ_m	τ_1	τ_2	α_1/α_2
NADH	1.149 (0.015)	0.562 (0.007)	2.953 (0.018)	2.91 (0.08)
FAD	0.829 (0.032)	0.347 (0.014)	2.477 (0.013)	3.02 (0.10)

Quantitative parameters (mean ± SE) of NADH and FAD fluorescence lifetimes (τ_m, τ_1, τ_2, and α_1/α_2) for the *in vivo* images are presented in Table 5.1. The mean lifetime (τ_m) is a weighted average of the short (τ_1) and long lifetime (τ_2) components. Changes in hamster epithelium NADH fluorescence lifetime components relative to the *in vivo* values are shown in Fig. 5.3A. Over the first four hours, all of the mean NADH τ_m values from the live cultured biopsy are within 2.5% of the *in vivo* value ($p > 0.05$), while the frozen-thawed NADH τ_m is +13% of the *in vivo* value which is a statistically significant difference ($p < 0.001$; Fig. 5.3A). Similarly, for NADH τ_1, all cultured biopsy measurements from the first four hours are within 2% of the *in vivo* value ($p > 0.05$) while the frozen-thawed τ_1 is +7% ($p < 0.01$; Fig. 5.3A). For NADH τ_2, the cultured biopsy values are within 1% of the *in vivo* NADH τ_2 value ($p > 0.05$) and the frozen-thawed mean τ_2 is +2% ($p < 0.05$; Fig. 5.3A). The four hour cultured biopsy NADH α_1/α_2 measurements are within 10% of the *in vivo* α_1/α_2 ratio ($p > 0.05$) while the frozen-thawed biopsy mean α_1/α_2 is 81% of the *in vivo* value ($p < 0.05$; Fig. 5.3A).

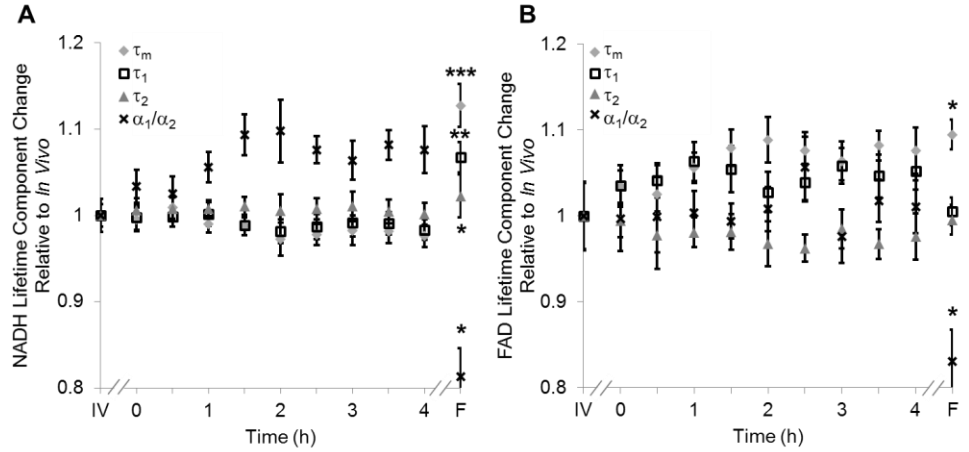

Figure 5.3. NADH and FAD lifetimes of live cultured and frozen thawed tissues. Changes (mean ± SE of n=10 measurements) relative to *in vivo* (IV) values of NADH (A) and FAD (B) τ_m (diamond), τ_1 (square), τ_2 (triangle), and α_1/α_2 (cross) observed in tissues maintained in live culture for 4 hours, and in frozen-thawed (F) tissues. τ_m is mean lifetime ($\tau_1 * \alpha_1 + \tau_2 * \alpha_2$). Asterisk denotes significant difference between *in vivo* and indicated measurement (* $p < 0.05$; ** $p < 0.01$; *** $p < 0.001$).

Similar trends are observed in the FAD lifetime values (Fig. 5.3B). Over the first 4 hours, the mean FAD τ_m of the cultured biopsy increases slightly but stays within 8% of the *in vivo* FAD τ_m ($p > 0.05$; Fig. 5.3B). The frozen-thawed FAD τ_m is 9.5% greater than the *in vivo* FAD τ_m ($p < 0.05$, Fig. 5.3B). Changes in FAD τ_1 are within 6% for the cultured biopsy measurement and frozen-thawed samples ($p > 0.05$; Fig. 5.3B). Likewise, the FAD τ_2 values for the cultured and frozen-thawed samples vary less than 4% from the *in vivo* FAD τ_2 ($p > 0.05$; Fig. 5.3B). While no significant difference is observed in the FAD α_1/α_2 ratio between the four hour cultured biopsy and the *in vivo* FAD α_1/α_2 (p-value > 0.05), the frozen-thawed measurement is 83% of the *in vivo* FAD α_1/α_2 ratio ($p < 0.05$; Fig. 5.3B).

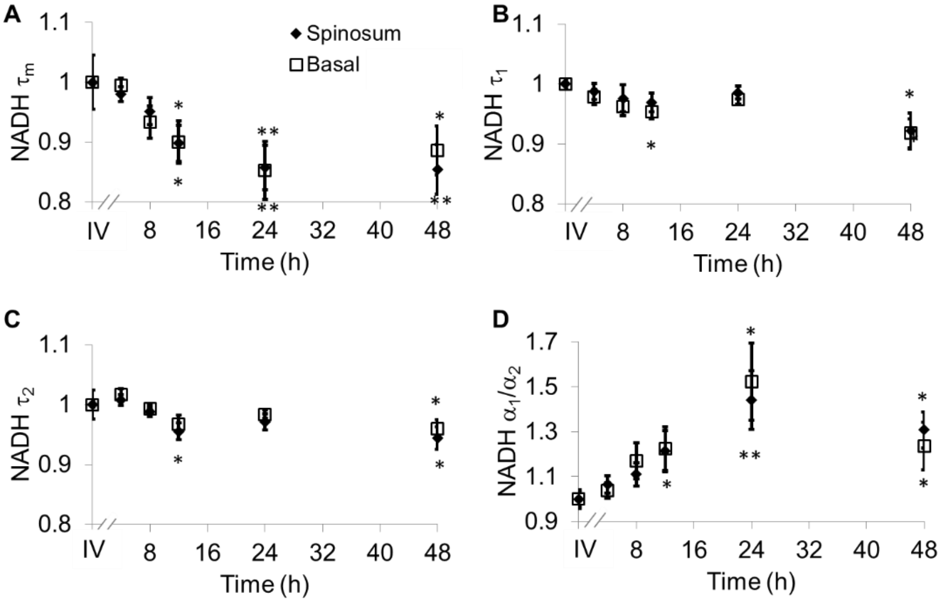

Figure 5.4. Relative NADH lifetime changes over 48hr. Changes (mean ± SE of n=6 measurements) relative to *in vivo* (IV) values of NADH τ_m (A), τ_1 (B), τ_2 (C), and α_1/α_2 (D) observed from both the spinosum (diamond) and basal (square) epithelial layers of tissues maintained in live culture for 48 hours. τ_m is mean lifetime ($\tau_1 * \alpha_1 + \tau_2 * \alpha_2$). Asterisk denotes significant difference between *in vivo* and indicated measurement (* $p < 0.05$; ** $p < 0.01$).

When the cultured biopsy is assessed past four hours, significant changes in the NADH fluorescence lifetime components are observed (Fig. 5.4). Both the spinosum and basal layers follow the same trends. By 12 hours, NADH τ_m significantly decreases by 10% and remains significantly lower than the *in vivo* value out to 48h in both the spinosum and basal layers ($p < 0.05$, Fig. 5.4A). Again, at 12 hours after excision, NADH τ_1 and τ_2 significantly decrease in both tissue layers ($p < 0.05$, Fig. 5.4B,C). NADH α_1/α_2 is increased from the *in vivo* measurement at 12, 24, and 48 hours post excision ($p < 0.05$, Fig. 5.4D).

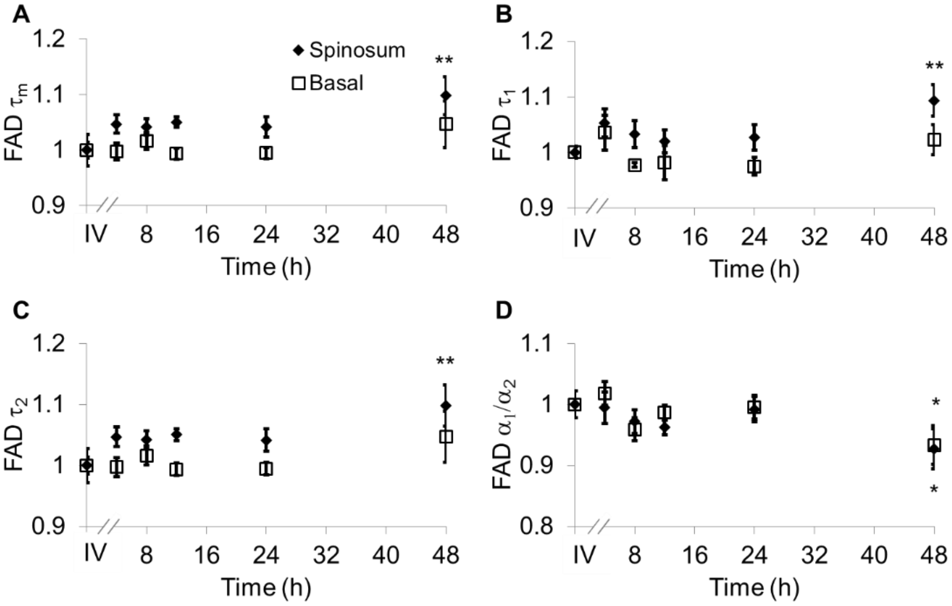

Figure 5.5. Relative FAD lifetime changes over 48hr. Changes (mean ± SE of n=6 measurements) relative to *in vivo* (IV) values of FAD τ_m (A), τ_1 (B), τ_2 (C), and α_1/α_2 (D) observed from both the spinosum (diamond) and basal (square) epithelial layers of tissues maintained in live culture for 48 hours. τ_m is mean lifetime ($\tau_1{*}\alpha_1 + \tau_2{*}\alpha_2$). Asterisk denotes significant difference between *in vivo* and indicated measurement (* $p < 0.05$, ** $p < 0.01$).

Changes in the FAD lifetime of the spinosum layer are observed in the cultured biopsy at 48 hours, when the FAD τ_m is significantly increased over the *in vivo* value ($p < 0.01$, Fig. 5.5A). Both FAD τ_1 ($p < 0.01$) and τ_2 ($p < 0.01$) of the spinosum also increase at 48 hours (Fig. 5.5B,C). FAD α_1/α_2 decreased at 48 hours in both the spinosum ($p < 0.05$) and basal cells ($p < 0.05$, Fig. 5.5D).

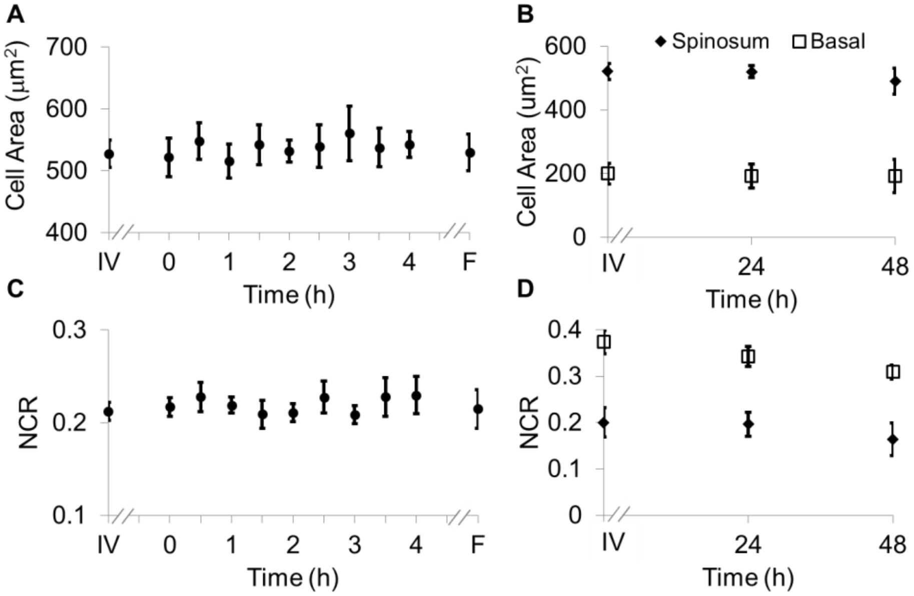

Figure 5.6. Cell morphology of fresh cultured and frozen-thawed tissues. Cellular morphology, as measured by cell cross-sectional area (A, B) and nuclear-to-cytoplasmic ratio (C, D) remains unchanged ($p>0.05$) from *in vivo* (IV) values within both the spinosum and basal epithelial layers of tissues maintained in live culture over 48 hours and in frozen-thawed (F) tissues (mean ± SE of n=10 [n=6 for B,D] measurements of a minimum of 20 cells per image).

Cellular morphology is maintained across the tissues regardless of preservation method (Fig. 5.6). No significant change ($p > 0.05$) is measured in the average cellular cross sectional area between the *in vivo* tissue, cultured biopsy, and frozen biopsy (Fig. 5.6A, B). Likewise, the NCR remains unchanged ($p > 0.05$) among the *in vivo* tissue, cultured biopsy, and frozen biopsy (Fig. 5.6C,D).

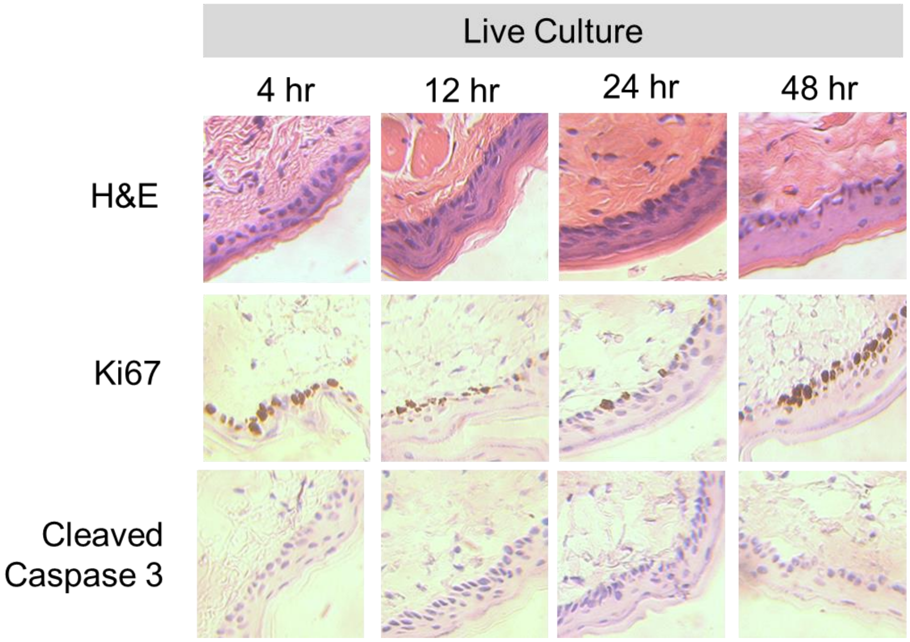

Figure 5.7. Representative histology of the hamster epithelium. H&E staining demonstrates an intact epithelium (first row). Nuclear Ki67 staining (brown) of the basal cells suggests cellular proliferation at each time point (middle row). An absence of staining by anti-cleaved caspase-3 suggests no apoptosis (third row). Images were acquired using a 40X air objective.

Histological analysis further confirms that the live tissue culture method maintains tissue viability. Hematoxylin and eosin stains reveal similar structure in the epithelial layer of the tissue at 4, 12, 24, and 48 hours post excision (Fig. 5.7). Positive staining with antibodies against Ki67 reveals proliferating cells in the basal layer at all time points (Fig. 5.7). Furthermore, no apoptotic cells are observed in cleaved-caspase 3 stains of the epithelium at any time point (Fig. 5.7). Together, the histological analysis suggests that the cells of the hamster epithelium remain alive in tissue culture for 48 hours post-excision.

5.5 Discussion

The goal of this study is to determine whether optical metabolic imaging of *ex vivo* tissues maintained in live culture reflects *in vivo* measurements. Optical endpoints include the optical redox ratio, NADH fluorescence lifetimes, and FAD fluorescence lifetimes, which are measured from *in vivo* tissue, a biopsy maintained in chilled tissue media, and a flash-frozen and thawed biopsy. Minimal changes, within 10% for the redox ratio and within 8% for the lifetime values, were observed between the *in vivo* hamster epithelium and the cultured tissue through 8 hours post-excision. However, statistically significant changes were observed in the frozen-thawed tissue. These results suggest that optical metabolism measurements from cultured tissue within 8 hours post excision represent the *in vivo* metabolic state of the tissue, especially when compared to frozen-thawed tissue.

Live tissue culture is used in many applications, including optical metabolic imaging and biochemical metabolic studies, to maintain viability of excised tissue (23, 29-31). However, the temporal impact of *ex vivo* culture on the metabolic state of tissues has not been quantitatively assessed previously. Often, studies use the tissue for several days (30) rather than the few hours investigated here. Cell viability studies have shown that for epithelial tissue, less than 2% cell death occurs over the first 5 days (30). However, no previous studies have confirmed that this live tissue culture approach provides optical metabolic measurements that are consistent with *in vivo* values, as we have shown in the current study. This live tissue culture approach is particularly attractive for optical imaging because these methods interrogate superficial layers of tissue (~200 μm for two-photon microscopy, depending on tissue type), so that oxygen and nutrients can diffuse into the tissue and maintain viability (32, 33). These superficial interrogation volumes also avoid the necrotic and hypoxic cores that are found in some live tissue culture preparations (34).

The optical redox ratio has been previously used to quantify metabolic differences among normal tissue, pre-cancerous tissue, and cancerous tumors (1, 2, 26, 35, 36). In the current study, two epithelial depth layers were interrogated because stratified squamous epithelial tissues are known to have a gradient of cellular metabolic activity, with the basal cells being most active and the superficial cells being least active (2, 28). As shown in Fig. 5.2B, the redox ratio of the basal region is greater ($p<0.05$) than the spinous region *in vivo* and at every time point during the live culture experiment, as expected. Additionally, Fig. 5.2A suggests that the optical redox ratio of frozen-thawed tissue does not completely describe the *in vivo* metabolic state. While the optical redox ratio is significantly reduced in frozen-thawed samples ($p < 0.01$), no significant difference is observed in the cultured tissue until 24 hours after biopsy (Fig. 5.2B). The change in redox ratio in the frozen-thawed tissue is due to both a decrease in the NADH fluorescence intensity and an increase in FAD fluorescence intensity (data not shown), which is consistent with decreased NADH fluorescence intensity observed between fresh and frozen-thawed hamster and cervical tissues (25, 31). The NADH and FAD fluorescence intensities did not change significantly in the live tissue culture over 4 hours ($p > 0.05$).

The mean NADH lifetime of the hamster cheek epithelium is 1.149 ns (Table 5.1), which is consistent with previously reported NADH lifetime values (2, 6, 10, 37, 38). The mean NADH fluorescence lifetime is the averaged effect of the free and protein-bound lifetime components (2, 11). While only minimal changes are observed in the NADH lifetime components of the cultured tissue until 12 hours post-biopsy, the frozen-thawed tissue has an increased τ_m, τ_1, and τ_2 and a decreased α_1/α_2 ratio (Fig. 5.3, 5.4). These results indicate that the fluorescence lifetimes of both the bound and free NADH are increased in the frozen-thawed tissue and that a greater portion of NADH exists in the bound conformation. Cells undergoing stress, such as apoptosis, have also shown increased mean NADH fluorescence lifetimes and increased proportions of bound NADH, suggesting that the freeze-thaw process exerts more stress than the live culture technique (37).

Likewise, the observed FAD mean lifetime of 0.829 ns (Table 5.1) is similar to reported FAD lifetime measurements (2, 39). For the FAD lifetime components, the frozen-thawed tissue has an increased τ_m and a decreased α_1/α_2 (Fig. 5.3). The decreased α_1/α_2 ratio indicates an increase in the relative amount of free (long-lifetime) FAD. This shift in relative amounts of the free and bound lifetime contributions explains the increased FAD τ_m. No significant change is observed in the FAD τ_1 and τ_2, so the FAD fluorescence lifetime may be less sensitive to the cellular stress involved in the freeze-thaw process than the NADH fluorescence lifetime.

Consistent cellular morphology across the *in vivo*, cultured, and frozen-thawed tissue indicates maintenance of tissue structure. The average cell cross sectional areas observed in the hamster epithelial spinosum and basal layers are 530 μm^2 and 200 μm^2, respectively (Fig. 5.6A, B), which is consistent with published cell cross sectional areas of hamster epithelium (40). Likewise, the observed NCR of the spinosum and basal layers of 0.2 and 0.4, respectively, (Fig. 5.6C,D) is consistent with previous reports (40, 41). The current study is also consistent with previous studies reporting that cell size and NCR do not change in frozen-thawed cells/tissues or in live tissue culture relative to *in vivo* values (41, 42).

While the optical metabolic measurements varied from the *in vivo* values after 8 hours in live culture, cellular morphology and histological analysis revealed no changes in cellular morphology, proliferation, or cell death over the 48h time-course (Fig. 5.6, 5.7). Therefore, optical metabolic imaging endpoints may be more sensitive to sub-cellular molecular changes than the histological or morphological analyses. Previous studies of the live tissue culture method have used histology to verify cell viability (30, 33); however, our results suggest that molecular metabolic changes occur before changes in cellular proliferation or cell death. Thus, optical metabolic imaging may be a more sensitive endpoint than histology for detecting changes in cell status.

To validate live tissue culture as an effective protocol for maintaining *in vivo* metabolic characteristics in excised tissue, the optical redox ratio, NADH fluorescence lifetime, and FAD fluorescence lifetime were quantified from hamster cheek epithelia *in vivo*, in live cultured biopsies followed for 48 hours, and in frozen-thawed samples. The live tissue culture approach resulted in no significant change in any optical endpoint relative to *in vivo* measures until 12 hours, when a decreased NADH τ_m was observed. Several significant differences, including a reduced redox ratio, increased NADH τ_m, and increased FAD τ_m were observed in the frozen-thawed samples. These results indicate that the live tissue culture method represents the *in vivo* state more accurately than the frozen-thawed procedure. Therefore, when *in vivo* optical measurements are not feasible, excised tissue may be maintained in chilled tissue media up to 12 hours for close representation of *in vivo* metabolic states.

5.6 Acknowledgments

Funding sources include the NCI SPORE in Breast Cancer (P50 CA098131) and Vanderbilt University Provost Graduate Fellowship.

5.7 References

1. Ostrander JH, McMahon CM, Lem S, Millon SR, Brown JQ, Seewaldt VL, Ramanujam N. Optical redox ratio differentiates breast cancer cell lines based on estrogen receptor status. Cancer Res. 2010;70(11):4759-66.

2. Skala MC, Riching KM, Gendron-Fitzpatrick A, Eickhoff J, Eliceiri KW, White JG, Ramanujam N. In vivo multiphoton microscopy of NADH and FAD redox states, fluorescence lifetimes, and cellular morphology in precancerous epithelia. Proc Natl Acad Sci U S A. 2007;104(49):19494-9.

3. Rice WL, Kaplan DL, Georgakoudi I. Two-photon microscopy for non-invasive, quantitative monitoring of stem cell differentiation. PLoS One. 2010;5(4):e10075.

4. Chance B, Schoener B, Oshino R, Itshak F, Nakase Y. Oxidation-reduction ratio studies of mitochondria in freeze-trapped samples. NADH and flavoprotein fluorescence signals. J Biol Chem. 1979;254(11):4764-71.

5. Georgakoudi I, Quinn KP. Optical imaging using endogenous contrast to assess metabolic state. Annu Rev Biomed Eng. 2012;14:351-67.

6. Bird DK, Yan L, Vrotsos KM, Eliceiri KW, Vaughan EM, Keely PJ, White JG, Ramanujam N. Metabolic mapping of MCF10A human breast cells via multiphoton fluorescence lifetime imaging of the coenzyme NADH. Cancer Res. 2005;65(19):8766-73.

7. Suhling K, French PM, Phillips D. Time-resolved fluorescence microscopy. Photochem Photobiol Sci. 2005;4(1):13-22.

8. Galletly NP, McGinty J, Dunsby C, Teixeira F, Requejo-Isidro J, Munro I, Elson DS, Neil MA, Chu AC, French PM, Stamp GW. Fluorescence lifetime imaging distinguishes basal cell carcinoma from surrounding uninvolved skin. The British journal of dermatology. 2008;159(1):152-61.

9. Patalay R, Talbot C, Alexandrov Y, Munro I, Neil MA, Konig K, French PM, Chu A, Stamp GW, Dunsby C. Quantification of cellular autofluorescence of human skin using multiphoton tomography and fluorescence lifetime imaging in two spectral detection channels. Biomedical optics express. 2011;2(12):3295-308.

10. Skala MC, Riching KM, Bird DK, Gendron-Fitzpatrick A, Eickhoff J, Eliceiri KW, Keely PJ, Ramanujam N. In vivo multiphoton fluorescence lifetime imaging of protein-bound and free nicotinamide adenine dinucleotide in normal and precancerous epithelia. Journal of biomedical optics. 2007;12(2):024014.

11. Lakowicz J. Principles of fluorescence spectroscopy. New York: Plenum Publishers; 1999.

12. Lakowicz JR, Szmacinski H, Nowaczyk K, Johnson ML. Fluorescence Lifetime Imaging of Free and Protein-Bound Nadh. Proc Natl Acad Sci U S A. 1992;89(4):1271-5.

13. Tanaka F, Tamai N, Yamazaki I. Picosecond-resolved fluorescence spectra of D-amino-acid oxidase. A new fluorescent species of the coenzyme. Biochemistry. 1989;28(10):4259-62.

14. Provenzano PP, Eliceiri KW, Keely PJ. Multiphoton microscopy and fluorescence lifetime imaging microscopy (FLIM) to monitor metastasis and the tumor microenvironment. Clin Exp Metastasis. 2009;26(4):357-70.

15. Conklin MW, Provenzano PP, Eliceiri KW, Sullivan R, Keely PJ. Fluorescence lifetime imaging of endogenous fluorophores in histopathology sections reveals differences between normal and tumor epithelium in carcinoma in situ of the breast. Cell Biochem Biophys. 2009;53(3):145-57.

16. Tadrous PJ, Siegel J, French PM, Shousha S, Lalani el N, Stamp GW. Fluorescence lifetime imaging of unstained tissues: early results in human breast cancer. The Journal of pathology. 2003;199(3):309-17.

17. Jo JA, Applegate BE, Park J, Shrestha S, Pande P, Gimenez-Conti IB, Brandon JL. In Vivo Simultaneous Morphological and Biochemical Optical Imaging of Oral Epithelial Cancer. Ieee Transactions on Biomedical Engineering. 2010;57(10):2596-9.

18. Chen HM, Chiang CP, You C, Hsiao TC, Wang CY. Time-resolved autofluorescence spectroscopy for classifying normal and premalignant oral tissues. Lasers in Surgery and Medicine. 2005;37(1):37-45.

19. De Beule PA, Dunsby C, Galletly NP, Stamp GW, Chu AC, Anand U, Anand P, Benham CD, Naylor A, French PM. A hyperspectral fluorescence lifetime probe for skin cancer diagnosis. The Review of scientific instruments. 2007;78(12):123101.

20. Hanson KM, Behne MJ, Barry NP, Mauro TM, Gratton E, Clegg RM. Two-photon fluorescence lifetime imaging of the skin stratum corneum pH gradient. Biophys J. 2002;83(3):1682-90.

21. Mizeret J, Wagnieres G, Stepinac T, Van Den Bergh H. Endoscopic tissue characterization by frequency-domain fluorescence lifetime imaging (FD-FLIM). Lasers Med Sci. 1997;12(3):209-17.

22. Requejo-Isidro J, McGinty J, Munro I, Elson DS, Galletly NP, Lever MJ, Neil MA, Stamp GW, French PM, Kellett PA, Hares JD, Dymoke-Bradshaw AK. High-speed wide-field time-gated endoscopic fluorescence-lifetime imaging. Optics letters. 2004;29(19):2249-51.

23. Drezek R, Brookner C, Pavlova I, Boiko I, Malpica A, Lotan R, Follen M, Richards-Kortum R. Autofluorescence microscopy of fresh cervical-tissue sections reveals alterations in tissue biochemistry with dysplasia. Photochem Photobiol. 2001;73(6):636-41.

24. Pavlova I, Sokolov K, Drezek R, Malpica A, Follen M, Richards-Kortum R. Microanatomical and biochemical origins of normal and precancerous cervical autofluorescence using laser-scanning fluorescence confocal microscopy. Photochem Photobiol. 2003;77(5):550-5.

25. Palmer GM, Marshek CL, Vrotsos KM, Ramanujam N. Optimal methods for fluorescence and diffuse reflectance measurements of tissue biopsy samples. Lasers Surg Med. 2002;30(3):191-200.

26. Huang S, Heikal AA, Webb WW. Two-photon fluorescence spectroscopy and microscopy of NAD(P)H and flavoprotein. Biophys J. 2002;82(5):2811-25.

27. Schonle A, Glatz M, Hell SW. Four-dimensional multiphoton microscopy with time-correlated single-photon counting. Appl Opt. 2000;39(34):6306-11.

28. Alberts B, Johnson A, Lewis J, Raff M, Roberts K, Walter P. Molecular biology of the cell. New York: Garland Science; 2002 2002.

29. Krebs HA. Body size and tissue respiration. Biochimica Et Biophysica Acta. 1950;4(1-3):249-69.

30. Trowell OA. The culture of mature organs in a synthetic medium. Experimental Cell Research. 1959;16(1):118-47.

31. Brookner CK, Follen M, Boiko I, Galvan J, Thomsen S, Malpica A, Suzuki S, Lotan R, Richards-Kortum R. Autofluorescence patterns in short-term cultures of normal cervical tissue. Photochem Photobiol. 2000;71(6):730-6.

32. So PT, Dong CY, Masters BR, Berland KM. Two-photon excitation fluorescence microscopy. Annu Rev Biomed Eng. 2000;2:399-429.

33. Verwer RW, Hermens WT, Dijkhuizen P, ter Brake O, Baker RE, Salehi A, Sluiter AA, Kok MJ, Muller LJ, Verhaagen J, Swaab DF. Cells in human postmortem brain tissue slices remain alive for several weeks in culture. FASEB J. 2002;16(1):54-60.

34. Evans SM, Hahn S, Pook DR, Jenkins WT, Chalian AA, Zhang P, Stevens C, Weber R, Weinstein G, Benjamin I, Mirza N, Morgan M, Rubin S, McKenna WG, Lord EM, Koch CJ. Detection of hypoxia in human squamous cell carcinoma by EF5 binding. Cancer Res. 2000;60(7):2018-24.

35. Xu HN, Nioka S, Glickson JD, Chance B, Li LZ. Quantitative mitochondrial redox imaging of breast cancer metastatic potential. Journal of biomedical optics. 2010;15(3):036010.

36. Zhang Z, Li H, Liu Q, Zhou L, Zhang M, Luo Q, Glickson J, Chance B, Zheng G. Metabolic imaging of tumors using intrinsic and extrinsic fluorescent markers. Biosens Bioelectron. 2004;20(3):643-50.

37. Wang HW, Gukassyan V, Chen CT, Wei YH, Guo HW, Yu JS, Kao FJ. Differentiation of apoptosis from necrosis by dynamic changes of reduced nicotinamide adenine dinucleotide fluorescence lifetime in live cells. Journal of biomedical optics. 2008;13(5):054011.

38. Wakita M, Nishimura G, Tamura M. Some characteristics of the fluorescence lifetime of reduced pyridine nucleotides in isolated mitochondria, isolated hepatocytes, and perfused rat liver in situ. J Biochem. 1995;118(6):1151-60.

39. Nakashima N, Yoshihara K, Tanaka F, Yagi K. Picosecond fluorescence lifetime of the coenzyme of D-amino acid oxidase. J Biol Chem. 1980;255(11):5261-3.

40. Eveson JW, MacDonald DG. Quantitative histological changes during early experimental carcinogenesis in the hamster cheek pouch. The British journal of dermatology. 1978;98(6):639-44.

41. White FH, Gohari K. Cellular and nuclear volumetric alterations during differentiation of normal hamster cheek pouch epithelium. Arch Dermatol Res. 1982;273(3-4):307-18.

42. Hauschka TS, Mitchell JT, Niederpruem DJ. A reliable frozen tissue bank: viability and stability of 82 neoplastic and normal cell types after prolonged storage at -78 degrees C. Cancer Res. 1959;19(6, Part 1):643-53.

CHAPTER 6

Quantitative Optical Imaging of Primary Tumor Organoid Metabolism Predicts Drug Response in Breast Cancer

Walsh AJ, Cook RS, Sanders ME, Arteaga CL, Skala MC, "Quantitative optical imaging of primary tumor organoid metabolism predicts drug response in breast cancer" *Cancer Research*, 2014; 74(18): 5184-94.

6.1 Abstract

There is a need for technologies that predict the efficacy of cancer treatment in individual patients. We demonstrate that optical metabolic imaging of organoids derived from primary tumors can predict therapeutic response of xenografts and measure anti-tumor drug responses in human-tumor derived organoids. Optical metabolic imaging quantifies the fluorescence intensity and lifetime of NADH and FAD, co-enzymes of metabolism. As early as 24 hours after treatment with clinically relevant anti-cancer drugs, the optical metabolic imaging index of responsive organoids decreased ($p<0.001$) and was further reduced when effective therapies were combined ($p<5x10^{-6}$), with no change in drug-resistant organoids. Drug response in xenograft-derived organoids was validated with tumor growth measurements *in vivo* and stains for proliferation and apoptosis. Heterogeneous cellular responses to drug treatment were also resolved in organoids. Optical metabolic imaging shows potential as a high-throughput screen to test the efficacy of a panel of drugs to select optimal drug combinations.

6.2 Introduction

With the ever-increasing number of drugs approved to treat cancers, selection of the optimal treatment regimen for an individual patient is challenging. Physicians weigh the potential benefits of the drugs against the side-effects to the patient. Currently, drug regimens for breast cancer are chosen based on tumor expression of several proteins, including estrogen receptor (ER), progesterone receptor (PR), and high levels of human epidermal growth factor receptor 2 (HER2), assessed in the diagnostic biopsy, and drug effectiveness is determined after weeks of treatment from tumor size measurements. A personalized medicine approach would identify the optimal treatment regimen for an individual patient and reduce morbidity from overtreatment.

Current methods to assess therapy response include tumor size, measured by mammography, MRI, or ultrasound. These methods evaluate the regimen that the patient received. Molecular changes induced by anti-tumor drugs precede changes in tumor size and may provide proximal endpoints of drug response. Cellular metabolism may provide biomarkers of early treatment response, because oncogenic drivers typically affect metabolic signaling (1, 2). Indeed FDG-PET has been explored as a predictor of response but lacks the resolution and sensitivity to accurately predict therapy response on a cellular level (3, 4).

Optical metabolic imaging (OMI) provides unique sensitivity to detect metabolic changes that occur with cellular transformation (5-10) and upon treatment with anti-cancer drugs (11). OMI utilizes the intrinsic fluorescence properties of NADH and FAD, co-enzymes of metabolic reactions. OMI endpoints include the optical redox ratio (the fluorescence intensity of NADH divided by the fluorescence intensity of FAD), the NADH and FAD fluorescence lifetimes, and the "OMI index" (a linear combination of these three endpoints). The optical redox ratio provides a dynamic readout of cellular metabolism (12), with increased redox ratio (NADH/FAD) (8) observed in malignant cells exhibiting the Warburg effect (increased glycolysis despite the presence of oxygen (13)). Fluorescence lifetime values report differences in fluorophore conformation, binding, and microenvironment, such as pH, temperature, and proximity to quenchers such as free oxygen (14). OMI endpoints report early, molecular changes due to anti-cancer drug treatment (11) and are powerful biomarkers of drug response.

Primary tumors can be cultured *ex vivo* as organoids, which contain the malignant tumor cells and the supporting cells from the tumor environment, such as fibroblasts, leukocytes, endothelial cells, and hematopoietic cells (15). Interactions between cancer cells and stromal cells have been shown to mediate therapeutic resistance in tumors (16). Therefore, organoid cultures provide an attractive platform to test cancer cell response to drugs in a relevant, "body-like" environment. Furthermore, multiple organoids can be generated from one biopsy, enabling high-throughput tests of multiple drug combinations with a small amount of tissue.

OMI of primary tumor organoids enables high-throughput screening of potential drugs and drug combinations to identify the most effective treatment for an individual patient. Here, we validate OMI in primary tumor organoid cultures as an accurate, early predictor of *in vivo* tumor drug response in mouse xenografts, and present the feasibility of this approach on primary human tissues. The cellular-resolution of this technique also allows for subpopulations of cells to be tracked over time with treatment, to identify therapies that affect all cells in a heterogeneous population.

6.3 Materials and Methods

6.3.1 Mouse xenografts

This study was approved by the Vanderbilt University Animal Care and Use Committee and meets the National Institutes of Health guidelines for animal welfare. BT474 cells or HR6 cells (10^8) in 100µl Matrigel were injected in the inguinal mammary fat pads of female athymic nude mice (J:NU; Jackson Laboratories). Tumors grew to $\geq$200mm^3. Tumor-bearing mice were treated twice weekly with the following drugs: control human IgG (10 mg/kg, IP; R&D Systems), trastuzumab (10 mg/kg, IP; Vanderbilt Pharmacy), paclitaxel (2.5 mg/kg, IP; Vanderbilt Pharmacy), XL147 (10 mg/kg, oral gavage; Selleckchem), trastuzumab + XL147, trastuzumab +

paclitaxel, trastuzumab + paclitaxel + XL147. Tumor volume was calculated from caliper measurements of tumor length (L) and width (W), $(L*W^2)/2$ twice a week.

6.3.2 Primary human tissue collection

This study was approved by the Vanderbilt University Institutional Review Board and informed consent was obtained from all subjects. A primary tumor biopsy, removed from the tumor mass after surgical resection, was provided by an expert breast pathologist (M.E.S.). The tumor was placed immediately in sterile DMEM, transported on ice to the laboratory (~5 minute walk), and generated into organoids within 3 hours of tissue resection. Pathology and receptor status of the tissue were obtained from the patient's medical chart.

6.3.3 Organoid generation and culture

Breast tumors (xenografts and primary) were washed three times with PBS. Tumors were mechanically dissociated into 100-300 μm macro-suspensions in 0.5 ml PMEC media (DMEM:F12 + EGF (10 ng/ml) + hydrocortisone (5 μg/ml) + insulin (5 μg/ml) + 1% penicillin: streptomycin) by cutting the tissues with a scalpel or by spinning in a C-tube (Miltenyi Biotec). Macro-suspension solutions were combined with Matrigel in a 1:2 ratio, and 100 μl of the solution was placed on cover slips. The gels solidified at room temperature for 30 minutes and then for 1 hour in the incubator. The gels were over-lain with PMEC media supplemented with drugs. The following *in vitro* drug dosages were used to replicate *in vivo* doses (17-19): control (control human IgG + DMSO), trastuzumab (25 μg/ml), paclitaxel (0.5 μM), XL147 (25 nM), tamoxifen (2 μM), fulvestrant (1 μM), and A4 (10 μg/ml, Takis, Inc.).

6.3.4 Fluorescence lifetime instrumentation

Fluorescence lifetime imaging was performed on a custom built multi-photon microscope (Prairie Technologies), as described previously (11, 20). Excitation and emission light were coupled through a 40X oil immersion objective (1.3 NA) within an inverted microscope (Nikon, TiE). A titanium:sapphire laser (Coherent Inc.) was tuned to 750 nm for NADH excitation (average power 7.5-7.9 mW) and 890 nm for FAD excitation (average power 8.4-6 mW). Bandpass filters, 440/80 nm for NADH and 550/100 nm for FAD, isolated emission light. A pixel dwell time of 4.8 μs was used to acquire 256x256 pixel images. Each fluorescence lifetime image was collected using time correlated single photon counting electronics (SPC-150, Becker and Hickl) and a GaAsP PMT (H7422P-40, Hamamatsu). Photon count rates were maintained above $5x10^5$ for the entire 60s image acquisition time, ensuring no photobleaching occurred. The instrument response full width at half maximum was 260 ps as measured from the second harmonic generation of a urea crystal. Daily fluorescence lifetime validation was confirmed by imaging of a fluorescent bead (Polysciences Inc). The measured lifetime of the bead (2.1 ± 0.06 ns) concurs with published values (10, 20, 21).

6.3.5 Organoid imaging

Fluorescence lifetime images of organoids were acquired at 24, 48, and 72 hours post-drug treatment. Organoids were grown in 35-mm glass-bottom petri dishes (MatTek Corp) and imaged directly through the coverslip on the bottom of the petri dish. Six representative organoids from each treatment group were imaged. The 6 organoids imaged contained collectively approximately 60-300 cells per treatment group for statistical and subpopulation analyses. First, an NADH image was acquired and a subsequent FAD image was acquired of the exact same field of view.

6.3.6 Immunofluorescence

A previously reported protocol (22) was adapted for immunofluorescent staining of organoids. Briefly, gels were washed with PBS and fixed with 2 ml 4% paraformaldehyde in PBS. Gels were washed with PBS, and then 0.15M glycine in PBS was added for 10 minutes. Gels were washed in PBS, and then added to 0.02% Triton X-100 in PBS. Gels were washed with PBS then overlain with 1% fatty acid-free BSA, 1% donkey serum in PBS. The next day, the solution was removed and 100 μl of antibody solution (diluted antibody in PBS with 1% donkey serum) was added to each gel. The gels were incubated for 30 minutes at room temperature, washed in PBS 3 times, and then incubated in 100 μl of secondary antibody solution for 30 minutes at room temperature. The gels were washed in PBS 3 times, washed in water 2 times, and then mounted to slides using 30 μl of ProLong Antifade Solution (Molecular Probes).

The primary antibodies used were anti-cleaved caspase 3 (Life Technologies) and anti-Ki67 (Life Technologies). Both were diluted at 1:100. A goat anti-rabbit IgG FITC secondary antibody was used (Life Technologies). FITC fluorescence was obtained by excitation at 980 nm on the multiphoton microscope described above, and a minimum of 6 organoids were imaged. Positive staining of cleaved caspase 3 and Ki67 was confirmed by staining mouse thymus and mouse small intestine, respectively. Immunofluorescence images were quantified by manual counting of the total number of cells and the number of positively stained cells in each field of view. Immunofluorescence results were presented as percentage of positively stained cells, quantified from six organoids, approximately 200 cells.

6.3.7 Generation of OMI endpoint images

Photon counts for 9 surrounding pixels were binned (SPCImage). Fluorescence lifetime components were extracted from the photon decay curves by deconvolving the measured system response and fitting the decay to a two component model, $I(t) = \alpha_1 \exp^{-t/\tau_1} + \alpha_2 \exp^{-t/\tau_2} + C$, where $I(t)$ is the fluorescence intensity at time t after the laser pulse, α_1 and α_2 are the fractional contributions of the short and long lifetime components, (i.e. $\alpha_1 + \alpha_2 = 1$), τ_1 and τ_2 are the fluorescence lifetimes of the short and long lifetime components, and C accounts for background light. A two-component decay was used to represent the lifetimes of the free and bound configurations of NADH and FAD (10, 23, 24) and yielded the lowest Chi^2 values (0.99-1.1), indicative of optimal fit. Matrices of the lifetime components were exported as ascii files for further processing in Matlab.

6.3.8 Automated image analysis software

To streamline cellular-level processing of organoid images, an automated image analysis routine, as previously described (25), was used in Cell Profiler in Matlab. Briefly, a customized threshold code identified pixels belonging to nuclear regions that were brighter than background but not as bright as cell cytoplasms. These nuclear pixels were smoothed and the resulting round objects between 6 and 25 pixels in diameter were segmented and saved as the nuclei within the image. , Cells were identified by propagating out from the nuclei. An Otsu Global threshold was used to improve propagation and prevent propagation into background pixels. Cell cytoplasms were defined as the cells minus the nuclei. Cytoplasm values were measured from each OMI image (redox ratio, NADH τ_m, NADH τ_1, NADH τ_2, NADH α_1, FAD τ_m, FAD τ_1, FAD τ_2 , FAD α_1).

6.3.9 Computation of OMI index

The redox ratio, NADH τ_m, and FAD τ_m were norm-centered across cell values from all treatment groups within a sample, resulting in unit-less parameters with a mean of 1. The OMI index is the linear combination of the norm-centered redox ratio, NADH τ_m, and FAD τ_m with the coefficients (1, 1, -1), respectively, computed for each cell. . The three endpoints, redox ratio, NADH τ_m, and FAD τ_m are independent variables (11) and are thus weighted equally. The signs of the coefficients were chosen to maximize difference between control and drug-responding cells.

6.3.10 Subpopulation analysis

Subpopulation analysis was performed by generating histograms of all cell values within a group as previously reported (11). Each histogram was fit to a 1, 2, and 3 component Gaussian curves. The lowest Akaike information criterion (AIC) signified the best fitting probability density function for the histogram (26). Probability density functions were normalized to have an area under the curve equal to 1.

6.3.11 Statistical tests

Differences in OMI endpoints between treatment groups were tested using a student's t-test with a Bonferroni correction. An α significance level less than 0.05 was used for all statistical tests.

6.4 Results

6.4.1 Response of BT474 organoids to a panel of anti-cancer drugs

Validation of an organoid-OMI screen for drug response was first tested in two isogenic HER2-amplified breast cancer xenografts. BT474 xenografts are sensitive to the HER2 antibody trastuzumab, while HR6 xenografts, derived as a sub-line of BT474, are trastuzumab-resistant. The following single drugs and drug combinations were tested: paclitaxel (P, chemotherapy), trastuzumab (H, anti-HER2 antibody), XL147 [X, phosphatidylinositol-3 kinase (PI3K) small molecule inhibitor] (27), H+P, H+X, and H+P+X. Paclitaxel and trastuzumab are standard-of-care drugs, and XL147 is in clinical trials and preclinical studies support combination therapy of XL147 with trastuzumab for patients who have developed a resistance to trastuzumab (27, 28).

Representative redox ratio, NADH τ_m, and FAD τ_m images of BT474 xenograft-derived organoids demonstrate mixed multicellular morphology and highlight the sub-cellular resolution of this technique (Fig. 6.1A-F). A longitudinal study of tumor growth demonstrated that the

BT474 xenografts responded to each treatment arm (Fig. 6.1G), with significant reduction in tumor volume, as determined from caliper measurements, on day 7 for all treatment groups except trastuzumab, which had significant reduction on day 11 (Fig. 6.1H).

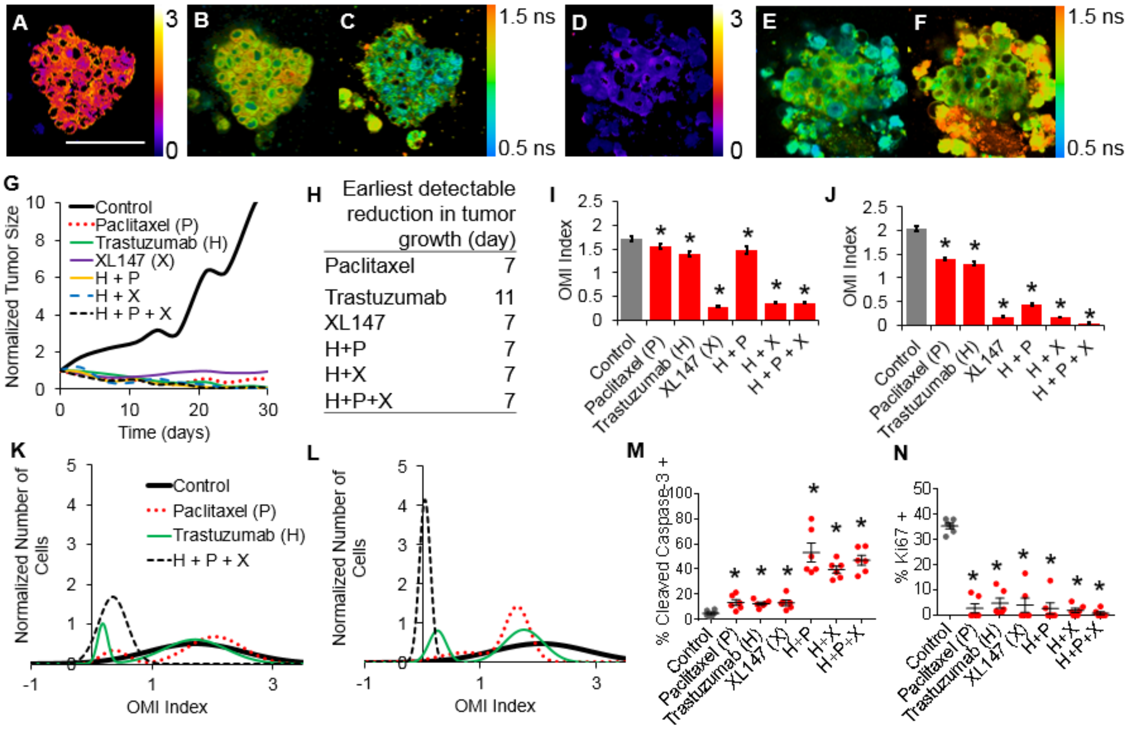

	Earliest detectable reduction in tumor growth (day)
Paclitaxel	7
Trastuzumab	11
XL147	7
H+P	7
H+X	7
H+P+X	7

Figure 6.1. OMI of organoids derived from trastuzumab-responsive xenografts. A. Redox ratio image of a control BT474 (ER+/HER2+) organoid at 72hr. Scale bar is 100 μm. B. NADH τ_m image of a control BT474 organoid at 72hr. C. FAD τ_m image of a control BT474 organoid at 72hr. D. Redox ratio image of a trastuzumab (anti-HER2) plus paclitaxel (chemotherapy) plus XL147 (anti-PI3K) (H+P+X) treated BT474 organoid at 72hr. E. NADH τ_m image of a trastuzumab plus paclitaxel plus XL147 (H+P+X) treated BT474 organoid at 72hr. F. FAD τ_m image of a trastuzumab plus paclitaxel plus XL147 (H+P+X) treated BT474 organoid at 72hr. G. Tumor growth response of BT474 tumors grown in athymic nude mice and treated with single and combination treatments. H. Table of earliest detectable ($p<0.05$) reduction in tumor size for control vs. treated mice. I. OMI index decreases in BT474 organoids treated with single and combination therapies at 24 hr. J. OMI index of BT474 organoids treated for 72hr. Red bars denote $p<0.05$ for treated organoids vs. control. K. Population density modeling of the mean OMI index per cell in control, paclitaxel, trastuzumab, and H+P+X treated organoids at 24 hr. L. Population density modeling of the OMI index for control, paclitaxel, trastuzumab, and H+P+X BT474 organoids treated for 72hr. M. Immunofluorescence staining of cleaved caspase 3 in control and treated BT474 organoids at 72hr. N. Immunofluorescence staining of Ki67 in control and treated BT474 organoids at 72hr. $^*p<0.05$.

A composite endpoint, the OMI index, was computed as a linear combination of the mean-normalized optical redox ratio, NADH τ_m, and FAD τ_m for each cell. After 24 hr of treatment, the OMI index was significantly reduced in all treated BT474 organoids, compared to the control ($p<0.05$, Fig. 6.1I). By 72 hr, the OMI index decreased further in all treatment groups ($p<5x10^{-7}$, Fig. 6.41J). The redox ratio, NADH τ_m, and FAD τ_m values showed similar trends (Appendix B, Fig. B.1). Changes in short and long lifetime values and in the portion of free NADH or FAD contributed to the changes in τ_m (Appendix B Table B.1).

The high resolution capabilities of OMI allowed single cell analysis and population modeling for quantification of cellular subpopulations with varying OMI indices. Visual inspection of cell morphology suggested that the majority of cells are tumor epithelial cells; stromal cells with obvious morphological differences were eliminated from the analysis. Population density modeling of cellular distributions of the OMI index revealed two populations with high and low OMI index values in all of the BT474 treated organoids at 24 hr (Fig. 6.1K, Appendix B Fig. B.2). By 72 hr, the XL147, H+P, H+X, and H+P+X treated organoids have a single population with narrower peaks (Fig. 6.1L, Appendix B Fig. B.2). The trastuzumab treated organoids have two populations at 72 hr, both lower than the mean OMI index of the control organoids (Fig. 1L). Immunofluorescent staining of cleaved caspase-3 and Ki67 of BT474 organoids treated for 72 hr confirmed increased apoptosis and decreased proliferation in drug treated organoids, with the greatest increases in cell death with combined treatments (Fig. 6.1M-N).

6.4.2 Response of HR6 organoids to a panel of anti-cancer drugs

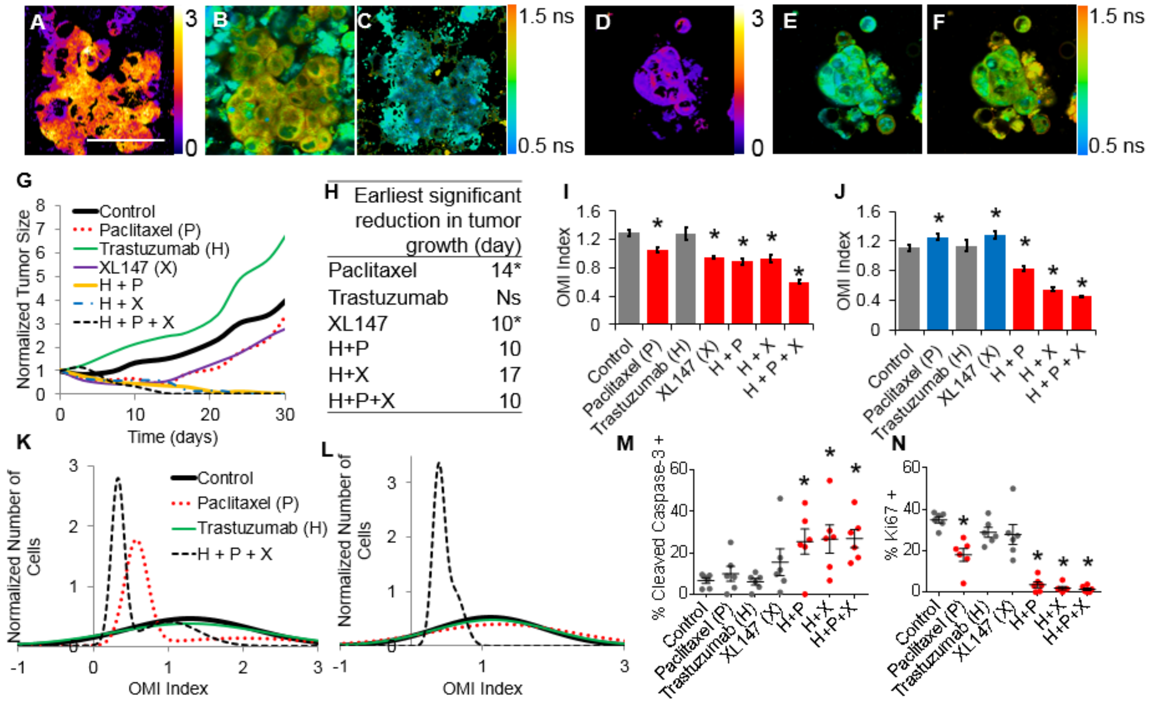

Earliest significant reduction in tumor growth (day)	
Paclitaxel	14*
Trastuzumab	Ns
XL147	10*
H+P	10
H+X	17
H+P+X	10

Figure 6.2. OMI of organoids derived from trastuzumab-resistant xenografts. A. Redox ratio image of a control HR6 (ER+/HER2+) organoid at 72hr. Scale bar is 100 μm. B. NADH τ_m image of a control HR6 organoid at 72hr. C. FAD τ_m image of a control HR6 organoid at 72hr. D. Redox ratio image of a trastuzumab (anti-HER2) plus paclitaxel (chemotherapy) plus XL147 (anti-PI3K) (H+P+X) treated HR6 organoid at 72hr. E. NADH τ_m image of an H+P+X treated HR6 organoid at 72hr. F. FAD τ_m image of an H+P+X treated HR6 organoid at 72hr. G. Tumor growth response of HR6 tumors grown in athymic nude mice and treated with single and combination treatments. H. Table of earliest detectable ($p<0.05$) reduction in tumor size for control vs. treated mice. * Denotes tumors that initially shrank and then grew. NS, not significant. I. OMI index initially decreases in HR6 organoids treated with paclitaxel, XL147, and combination therapies at 24 hr. J. OMI index of HR6 organoids treated for 72hr. Red bars indicate significant reductions in OMI index, $p<0.05$, for treated organoids vs. control. Blue bars indicate significant increases in OMI index, $p<0.05$, for treated organoids vs. control. K. Population density modeling of the mean OMI index per cell in control, paclitaxel, trastuzumab, and H+P+X organoids at 24 hr. L. Population density modeling of the OMI index for HR6 control, paclitaxel, trastuzumab, and H+P+X organoids treated for 72 hr. M. Immunofluorescence staining of cleaved caspase 3 in control and treated HR6 organoids at 72hr. N. Immunofluorescence staining of Ki67 in control and treated HR6 organoids at 72hr. * $p<0.05$

Next, the OMI-organoid screen was tested on trastuzumab-resistant HR6 xenografts (29). Representative images show HR6 organoid morphology and spatial distributions of OMI endpoints (Fig. 6.2A-F). These HER2 overexpressing tumors had continued growth with trastuzumab treatment (Fig. 6.2G). Treatment with paclitaxel and XL147 initially caused HR6 tumor regression ($p<0.05$ on day 10 for XL147 and on day 14 for paclitaxel) but then resumed growth (Fig. 6.2G-H). Mice treated with the H+P, H+X, and H+P+X combination therapies exhibited sustained HR6 tumor reduction (Fig. 6.2G-H).

After 24 hr of treatment, significant reductions in the OMI index were detected in HR6 organoids treated with paclitaxel, XL147, H+P, H+X, and H+P+X ($p<0.05$, Fig. 6.2I). At 72 hr, the OMI index of the paclitaxel and XL147 treated organoids was significantly greater than that of the control organoids ($p<0.05$, Fig. 6.2J), consistent with the recovery of HR6 tumor growth after prolonged therapy (Fig. 6.2G). The organoids treated with drug combinations (H+P, H+X, H+P+X) continued to have significantly lower OMI index values ($p<10^{-6}$) at 72 hr, compared to untreated controls. Individual OMI endpoints showed similar trends (Appendix B Fig. B.3, Appendix B Table B.2). Subpopulation analysis revealed two subpopulations in the OMI index for all treated groups except for trastuzumab at 24 hr (Fig. 6.2K, Appendix B Fig. B.4). By 72 hr, the paclitaxel and XL147 treated organoids had a single population (Fig. 6.2L, Appendix B Fig. B.4). Immunofluorescent staining of cleaved caspase 3 of organoids treated for 72 hr revealed increased cell death in HR6 organoids treated with H+P, H+X and H+P+X ($p<0.05$, Fig. 6.2M). The percentage of Ki67 positive cells at 72 hr decreased with paclitaxel, H+P, H+X, and H+P+X treatment ($p<0.005$, Fig. 6.2N).

6.4.3. OMI endpoints identify breast cancer subtypes

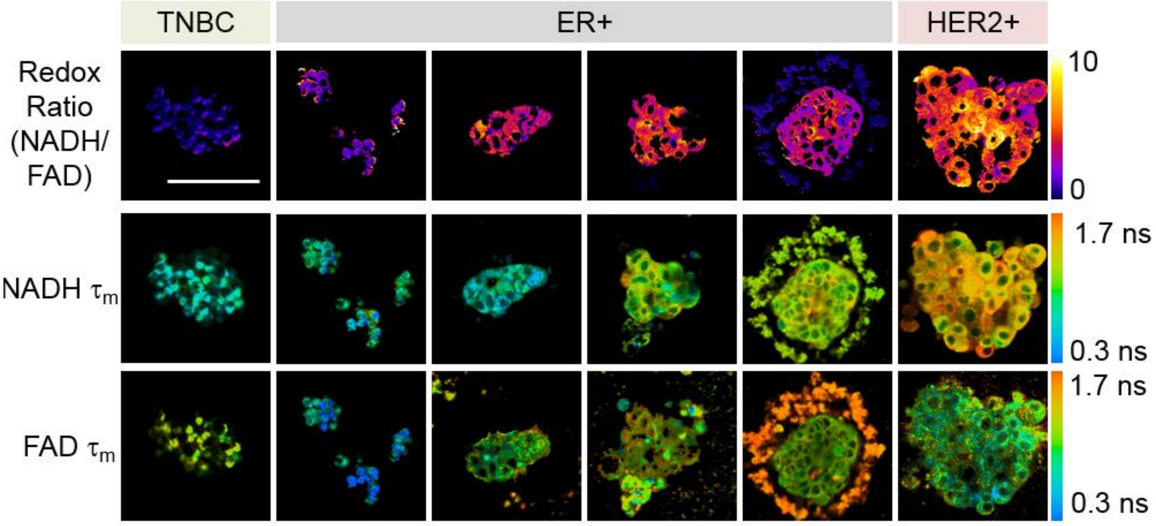

Figure 6.3. Representative redox ratio, NADH τ_m, and FAD τ_m images of organoids derived from primary, human breast tumors. Redox ratio (NADH/FAD; first row), NADH τ_m (second row), and FAD τ_m (third row) images of organoids generated from primary human breast tissue obtained from resection surgeries. TBNC = Triple negative breast cancer. Scale bar is 100 μm.

We tested these methods on primary breast cancer biopsies obtained from surgical resection. Tumors were obtained fresh from de-identified mastectomy specimens not required for further diagnostic purposes, and dissociated into organoids within 1-3 hr post-resection. Cancer drugs were added and organoids were imaged with OMI. Representative redox ratio, NADH τ_m, and FAD τ_m images (Fig. 6.3) demonstrate the varying morphology of organoids derived from ER+, HER2+ and triple negative breast cancers.

When quantified, the OMI endpoints differed between cancer subtypes. In immortalized cell lines, the redox ratio was elevated in ER+/HER2- cells and was greatest in HER2+/ER- cells ($p<5x10^{-5}$, Fig. 6.4A). Similarly, NADH τ_m was increased in immortalized ER+/HER2- and

HER2+/ER- breast cancer cells as compared to triple negative breast cancer (TNBC) cells ($p<5x10^{-8}$, Fig. 6.4B). FAD τ_m was greatest in ER+/HER2- cells ($p<0.05$, Fig. 6.4C). Overall, the OMI index was lowest in TNBC and greatest in HER2+/ER- cells ($p<5x10^{-8}$, Fig. 6.4D), suggesting that HER2 and ER expression influence cellular metabolism.

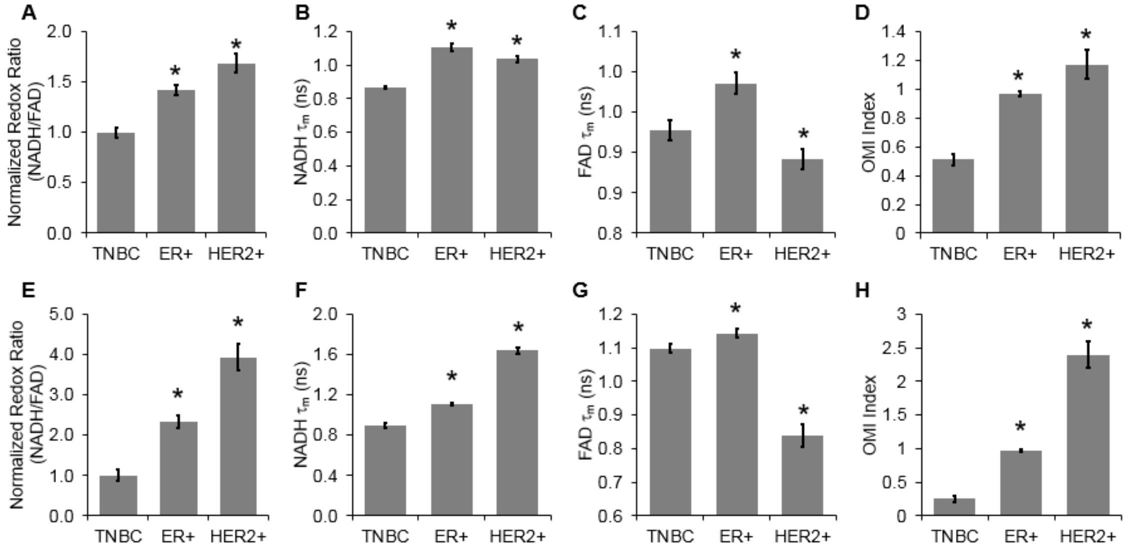

Figure 6.4. OMI endpoints differ among breast cancer subtypes. A. Redox ratio (NADH/FAD) of TNBC cells (MDA-MB-231), ER+ (HER2-negative) cells (MCF7), and HER2+ (ER-negative) cells (SKBr3, BT474, MDA-MB-361). B. NADH τ_m of TNBC, ER+, and HER2+ immortalized cell lines. C. FAD τ_m of TNBC, ER+, and HER2+ immortalized cell lines. D. OMI index increases in ER+ and HER2+ immortalized cell lines. E. Redox ratio (NADH/FAD) of organoids derived from triple negative, ER+ (HER2-negative), and HER2+ (ER-negative) primary human tumors. F. NADH τ_m of organoids derived from triple negative, ER+, and HER2+ primary human tumors. G. FAD τ_m of organoids derived from triple negative, ER+, and HER2+ primary human tumors. H. OMI index of organoids derived from triple negative, ER+, and HER2+ primary human tumors. * $p<0.05$

Similar trends were observed for the OMI endpoints in organoids derived from primary breast tumor specimens cultured under basal conditions. The redox ratio was increased in organoids from ER+/HER2- tumors and was greatest in HER2+/ER- organoids ($p<5x10^{-12}$, Fig. 6.4E, Appendix B Table B.3). Likewise, NADH τ_m increased with ER and HER2 expression ($p<5x10^{-8}$, Fig. 6.4F). FAD τ_m was increased in ER+ organoids and reduced in HER2+ organoids

($p<0.05$, Fig. 6.4G). The OMI index was lowest for TNBC, and greatest for HER2+ organoids ($p<5x10^{-3}$, Fig. 6.4H).

6.4.4 Organoid response of ER+ primary human tumors

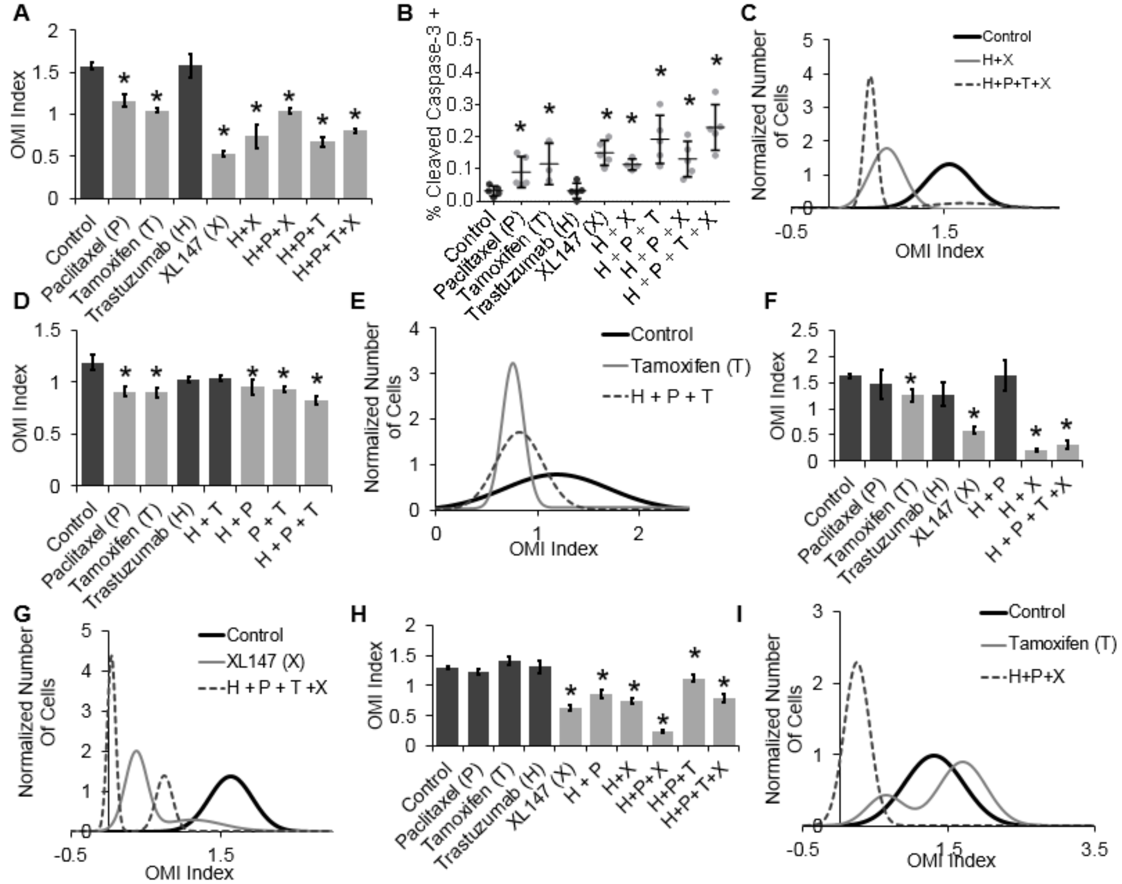

Figure 6.5. OMI index measures drug response and heterogeneous populations in ER+ primary tumor derived organoids. A. OMI index of organoids derived from an ER+ (HER2-negative) primary human tumor decreases with paclitaxel (chemotherapy), tamoxifen (ER antagonist), XL147 (anti-PI3K) and combined therapies at 72hr. Light gray bars indicate significant ($p<0.05$) reductions in OMI index with treatment, versus control organoids. B. Quantification of immunofluorescence staining of cleaved caspase 3 for organoids derived from the same tumor sample as in (A) and treated for 72hr. C. Population density modeling of the control, H+X, and H+P+T+X treated organoids presented in (A). D. OMI index is reduced with paclitaxel, tamoxifen, and combined treatments in organoids derived from a different ER+ patient at 72hr. E. Population density modeling of the control, tamoxifen, and H+P+T treated organoids presented in (D). F. OMI index is reduced in organoids from a third ER+ patient treated with tamoxifen, XL147, H+X, and H+P+T+X at 24hr. G. Population density modeling of the control, XL147, and H+P+T+X treated organoids presented in F. H. Organoids derived from a fourth ER+ patient have significant reductions in OMI index when treated with XL147 and combination therapies at 72hr. I. Population density modeling of the control, tamoxifen, and H+P+X treated organoids in (H) reveals multiple populations with tamoxifen treatment. * $p<0.05$.

Organoids were generated from four ER positive (HER2-negative) primary human tumors and treated with the chemotherapeutic drug paclitaxel, the selective ER modulator tamoxifen, the HER2 antibody trastuzumab and the pan-PI3K inhibitor XL147. Organoids derived from the first ER+ tumor had significantly reduced OMI index values upon treatment with paclitaxel, tamoxifen, XL147, H+X, H+P+T, H+P+X and H+P+T+X for 72 hr ($p<5x10^{-5}$, Fig. 6.5A). Immunofluorescence of cleaved caspase-3 showed increased cell death in parallel organoids treated for 72 hr with paclitaxel, tamoxifen, XL147, H+X, H+P+T, H+P+X, and H+P+T+X (Fig. 6.5B). Subpopulation analysis revealed less variability (narrower histogram peaks) within responsive treatment groups compared to the cells of control and trastuzumab-treated organoids (Fig. 6.5C, Appendix B Fig. B.5). Corresponding OMI endpoints showed similar trends (Appendix B Fig. B.6, Appendix B Table B.4).

Organoids derived from a second ER+ tumor responded similarly. The OMI index decreased upon treatment with paclitaxel, tamoxifen, H+P, P+T and H+P+T at 72 hr ($p<5x10^{-5}$, Fig. 6.5D). Subpopulation analysis revealed a single population of control cells that shifted to lower OMI indexes with paclitaxel, tamoxifen, H+P, P+T, and H+P+T treatments (Fig. 6.5E, Appendix B Fig. B.7). Corresponding OMI endpoints showed similar trends (Appendix B Fig. B.8, Appendix B Table B.5).

The third and fourth ER+ clinical samples yielded organoids with variable responses to treatment. Organoids derived from the third patient had significant reductions in OMI index after 24 hr treatment with tamoxifen, XL147, H+X, and H+P+T+X treatments ($p<0.005$, Fig. 6.5F). Subpopulation analysis revealed two populations with high and low OMI index values for the H+P and paclitaxel-treated organoids (Fig. 6.5G; Appendix B Fig. B.9). Two populations, both with mean OMI index values less than that of the control organoids, were apparent in the organoids treated with XL147 and with H+P+T+X (Fig. 6.5G, Appendix B Fig. B.9). Organoids from the fourth ER+ patient had reduced OMI indices following treatment with XL147, H+P, H+X, H+P+X, H+P+T and H+P+T+X for 72 hr (p<0.01, Fig. 6.5H). Subpopulation analysis of cells from these organoids revealed single populations with shifted mean OMI indices for all treatments except tamoxifen, H+P, and H+X, which had two populations (Fig. 6.5I, Appendix B Fig. B.10). Corresponding OMI endpoints showed similar trends (Appendix B Fig. B.11-12, Appendix B Tables B.6-7).

6.4.5 Organoid Response of HER+ and TNBC primary human tumors

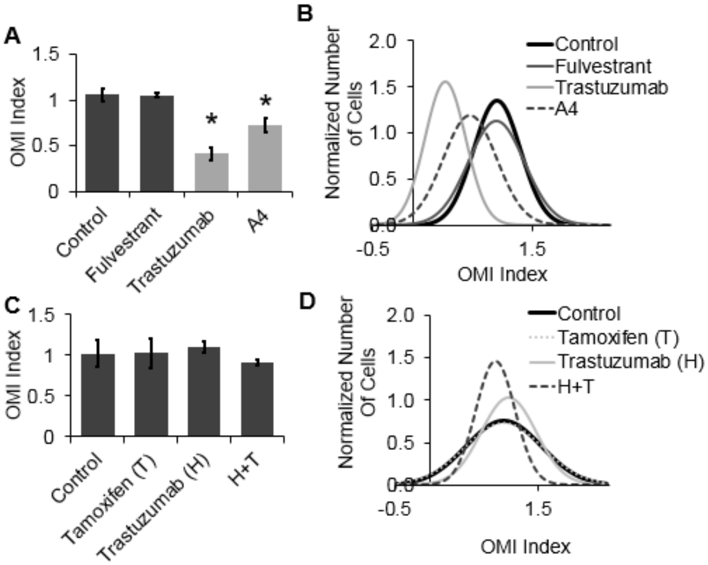

Figure 6.6. OMI index detects response of HER2+ organoids to trastuzumab and resolves no response in TNBC. A. Organoids derived from a HER2+(ER-negative) clinical tumor have reduced OMI indices with trastuzumab (anti-HER2) and A4 (anti-ErbB3) treatment, and no change with fulvestrant treatment (ER antagonist) at 24hr. Light gray bars signify significant reductions in OMI index due to drug treatment compared to control organoids (*p<0.05). (B). Population density modeling of the organoids derived from a HER2+ tumor reveals single populations. C. Organoids derived from a TNBC tumor have no significant changes (p>0.3) in OMI index with treatment of targeted therapies, tamoxifen (ER antagonist) and trastuzumab at 48hr. D. Population density modeling reveals single populations within the TNBC organoids.

OMI was also performed on organoids derived from HER2+ (ER negative) and TNBC specimens. Organoids derived from the HER2+ primary tumor were treated with the ER down-regulator fulvestrant, the HER2 antibody trastuzumab, and the anti-ErbB3 antibody A4 (30). The OMI index was significantly decreased in the organoids treated for 24 hr with trastuzumab and A4 ($p<0.005$, Fig. 6.6A). Subpopulation analysis revealed shifts in the mean OMI index values with these treatments within a single population of cells (Fig. 6.6B). Organoids derived from the TNBC specimen were treated with tamoxifen, the HER2 antibody trastuzumab, and the combination of trastuzumab plus tamoxifen (H+T). No significant changes were observed with these treatments in TNBC organoids after 24 hr ($p>0.3$, Fig. 6.6C). Subpopulation analysis revealed a single population of cells from TNBC organoids (Fig. 6.6D). Corresponding OMI endpoints showed similar trends (Appendix B Fig. B.7-8, Appendix B Tables B.8-9).

6.5 Discussion

Primary tumor organoids are an attractive platform for drug screening because they are grown from intact biopsies, thus maintaining the tumor cells within the same tumor microenvironment (15). OMI is sensitive to early metabolic changes, achieves high resolution to allow analysis of tumor cell heterogeneity, and uses endogenous contrast in living cells for repeated measurements and longitudinal studies (11). The OMI index is a holistic reporter of cellular metabolism because the redox ratio and NADH and FAD lifetimes are independent measurements (11). The mean lifetime captures not only changes in free-to-bound protein ratios but also preferred protein binding and relative concentrations of NADH to NADPH (31). Cancer drugs have been shown to down-regulate certain metabolism enzymes; for example, trastuzumab down-regulates lactate dehydrogenase in breast cancer and paclitaxel resistant cells have been shown to have more lactate dehydrogenase expression and activity (32). The OMI index captures these drug-induced changes in metabolism enzyme activity. Organoids remain viable with stable OMI endpoints in controlled culture conditions (33), thus making them an attractive system to evaluate tumor response to drugs. We used OMI to assess the response of primary breast tumor organoids to a panel of clinically relevant anti-cancer agents used singly or in combination. Early OMI-measured response in organoids (24-72 hr post-treatment) corroborated with standard tumor growth curves in xenografts, and the feasibility of this approach was confirmed in organoids derived from primary human breast tumors.

The OMI index was first evaluated as a reporter of tumor response in organoids derived from BT474 (ER+/HER2+) xenografts. Significant reductions in OMI index upon treatment with paclitaxel, trastuzumab, XL147 and combinations thereof, at both 24 and 72 hr, correlated with reduction of tumor growth (Fig. 6.1). Biochemically, cellular rates of glycolysis, and NADH and FAD protein-binding decrease with drug treatment in responsive cells (32), resulting in decreased redox ratios and NADH τ_m, and increased FAD τ_m in agreement with the decreased OMI index observed in drug-treated BT474 organoids. Significant reductions in tumor growth occurred 7-11 days post-treatment initiation whereas the OMI index detected response at 24-72 hr post-treatment. Cellular analysis revealed an initial heterogeneous response among cells within organoids treated with paclitaxel and H+P at 24 hr, which, by 72 hr, became a uniform response. The heterogeneity of trastuzumab treated BT474 organoids persisted over 72 hr, suggesting an intrinsic subpopulation more susceptible to acquire drug resistance. This heterogeneity was not seen in the combination treatments, suggesting the combination treatments trump this drug resistance-prone subpopulation. OMI measured response corroborated with increased cell death and decreased proliferation due to single and combination drug treated organoids, measured with destructive post-mortem techniques. The XL147-treated BT474 organoids have a much lower OMI index at 72 hr, but only a modest increase in cleaved caspase 3 activity. The same decrease was not observed in the HR6 cells that have alternative metabolism pathways activated due to their acquired resistance to trastuzumab. The OMI index detects changes in cellular metabolism that predict drug efficacy, but do not necessarily correlate with IHC.

In the current standard of care, patients with innate drug resistance are not identified *a priori*. We tested the capabilities of OMI to predict drug resistance using trastuzumab-resistant HR6 (ER+/HER2+) tumors (29). XL147 is a novel PI3K inhibitor under investigation for combined therapy with trastuzumab to improve response of resistant tumors (27). Significant reductions in the OMI index of HR6 organoids treated for 72 hr identified drug combinations (H+X, H+P, and H+P+X) that induced a sustained reduction in tumor growth *in vivo* (Fig. 6.2). The reduction in tumor growth upon treatment with H+X was consistent with previous reports of greater anti-tumor effects of the combination over trastuzumab and XL147 alone (27). Subpopulation analysis revealed multiple responses within the HR6 organoids after treatment with single drugs and combinations, suggesting increased heterogeneity compared to the parental BT474 organoids.

The OMI index of paclitaxel and XL147 treated HR6-organoids initially decreased at 24 hr, and then increased at 72 hr, mirroring the tumor growth in mice after prolonged therapy, and indicating that the adaptations that allow HR6 cells to survive trastuzumab treatment also affect response to additional drugs. This relapse of HR6 tumors treated with paclitaxel and XL147 was not apparent until 2-3 weeks of drug treatment; yet, the OMI index identified a resistant population within both paclitaxel and XL147 treated organoids at 24 hours and showed a selection of this population by 72hr. Subpopulation analysis of the paclitaxel and XL147 treated HR6 organoids revealed heterogeneous responses at 24 hr, suggesting that OMI is capable of early detection of resistant cells within a heterogeneous tumor. These results indicate that OMI of primary tumor organoids is able to identify heterogeneous responses within tumors on a cellular level, and potentially guide therapy selection early for maximal response. The ability to detect innate resistance at a cellular level prior to treatment may provide leads for identification of drugs that target such refractory subpopulations before they are selected by the primary therapy.

We next examined the feasibility of this approach utilizing fresh tumor biopsies obtained from primary tumor surgical resections. OMI measurements *in vivo* and corresponding measurements from freshly excised tissues within 8 hr of surgery are statistically identical (20), providing ample time for specimen acquisition and transport to the laboratory. The morphology of organoids differed among patients and within breast cancer subtypes (Fig. 6.3), demonstrating a greater heterogeneity within primary tumors compared to xenografts.

Previously published studies report differences in OMI endpoints due to the presence or absence of ER and HER2 (8, 11, 34). Both ER and HER2 signaling pathways can influence metabolism: ER by inducing increased glucose transport (1), and HER2 through activation of PI3K (2), among other signal transducers. We compared OMI endpoints from immortalized cells and human tissue-derived organoids of three subtypes of breast cancer: ER+, HER2-overexpressing, and triple negative breast cancer (TNBC). The OMI index of immortalized cell lines increased with ER expression and was highest in HER2 overexpressing cells (consistent with prior studies (11)), and these trends were replicated in organoids derived from primary human tumors. Notably, NADH τ_m was significantly increased ($p<0.05$) in the HER2+ organoids compared to ER+ organoids, but this trend was not observed in the immortalized cell lines. This difference could be due to molecular changes induced by the immortalization process, media components, primary tumor heterogeneity, and/or the heterogeneity within a primary breast tumor. Regardless, the results shown (Fig. 6.4) suggest breast cancer subtypes, ER+, HER2+ and TNBC, have different OMI profiles.

Organoids derived from human breast tumors were treated with a panel of breast cancer drugs (Fig. 6.5-6). Differences in the drug response of these organoids suggest heterogeneity across ER+/HER- tumors. Organoids from one of the four ER+ tumors did not exhibit reduced OMI indices after treatment with tamoxifen. Organoids derived from two of the four ER+ samples did not have reduced OMI indices after paclitaxel treatment. These variable responses are consistent with variable responses seen with these drugs in the clinic (35-38). None of the organoids had reduced OMI indices with trastuzumab, which is expected because the organoids were derived from HER2 negative tumors. Generally, the OMI index was reduced further upon treatment with drug combinations, supporting the use of drug combinations clinically.

Subpopulation analysis revealed cells within organoid treatment groups that exhibit different OMI indices after treatment, suggesting that subpopulations of cells with different drug sensitivities preexist and develop within primary tumors. Some of these cells may represent the cancer stem-like population with increased renewal capacity, metastatic potential, and drug resistance (39). The populations of organoids derived from human tumors have more variability (broader population curves) than those derived from xenografts, reflecting an inherent greater heterogeneity within primary tumors. This corroborates previous reports (40) of greater intra-tumoral heterogeneity in primary tumors than in xenografts derived from clonal cell lines. Thus, OMI imaging allows identification of heterogeneous cellular response to drug treatment in a dynamic population, which potentially enables drug selection to maximize therapeutic efficacy.

Organoids derived from HER2+/ER- and TNBC primary tumors have OMI responses consistent with their clinical characteristics: reduced OMI index with trastuzumab treatment and no change with fulvestrant (ER antagonist) treatment in the HER2+/ER- organoids (41), and no OMI index reductions after treatment with trastuzumab or tamoxifen in the TNBC organoids (42, 43) (Fig. 6.6a,c). HER3 is an emerging target for breast cancer (30, 44) and the anti-HER3 antibody A4 reduced the OMI index of HER2+/ER- organoids.

The results of this study support the validity of OMI for monitoring organoid response to anti-cancer drugs. We demonstrate high selectivity of the OMI index to directly measure drug response of organoids derived from breast cancer xenografts to single anti-cancer drugs and their combinations, and validated OMI measured response with gold standard tumor growth in two xenograft models. We have shown that the OMI index measured in primary tumor organoids resolves response and non-response within 72 hours, compared to the 3 weeks required to resolve this response with tumor size measurements. Further, we extend this approach and generate drug response information from organoids derived from three subtypes of primary human tumors, TNBC, ER+, and HER2+. The high resolution of OMI allows subpopulation analysis for identification of heterogeneous tumor response to drugs in dynamic tumor cell populations. Altogether, these results suggest that OMI of primary tumor organoids may be a powerful test to predict the action of anti-cancer drugs and tailor treatment decisions accordingly.

6.6 Acknowledgements

We thank C. Nixon, W. Sit, M. Madonna, and B. Stanley for assistance. Funding includes DOD-BC121998, NIH R00-CA142888, NCI Breast Cancer SPORE P50-CA098131, NSF DGE-0909667, VICC Young Ambassadors Discovery Grant, AIRC-IG10334**.**

6.7 References

1. Cheng CM, Cohen M, Wang J, Bondy CA. Estrogen augments glucose transporter and IGF1 expression in primate cerebral cortex. FASEB J. 2001;15(6):907-15.

2. Zhang D, Tai LK, Wong LL, Chiu LL, Sethi SK, Koay ES. Proteomic study reveals that proteins involved in metabolic and detoxification pathways are highly expressed in HER-2/neu-positive breast cancer. Mol Cell Proteomics. 2005;4(11):1686-96.

3. Minami H, Kawada K, Murakami K, Sato T, Kojima Y, Ebi H, Mukai H, Tahara M, Shimokata K. Prospective study of positron emission tomography for evaluation of the activity of lapatinib, a dual inhibitor of the ErbB1 and ErbB2 tyrosine kinases, in patients with advanced tumors. Japanese Journal of Clinical Oncology. 2007;37(1):44-8.

4. Mankoff DA, Dunnwald LD, L. K., Doot RK, Specht JM, Gralow JR, Ellis GK, Livingston RB, Linden HM, Gadi VK, Kurland BF, Schubert EK, Muzi M. PET Tumor Metabolism in Locally Advanced Breast Cancer Patients Undergoing Neoadjuvant Chemotherapy: Value of Static versus Kinetic Measures of Fluorodeoxyglucose Uptake. Clinical Cancer Research. 2011;17(8):2400-9.

5. Conklin MW, Provenzano PP, Eliceiri KW, Sullivan R, Keely PJ. Fluorescence lifetime imaging of endogenous fluorophores in histopathology sections reveals differences between normal and tumor epithelium in carcinoma in situ of the breast. Cell Biochem Biophys. 2009;53(3):145-57.

6. Mujat C, Greiner C, Baldwin A, Levitt JM, Tian F, Stucenski LA, Hunter M, Kim YL, Backman V, Feld M, Munger K, Georgakoudi I. Endogenous optical biomarkers of normal and human papillomavirus immortalized epithelial cells. Int J Cancer. 2008;122(2):363-71.

7. Provenzano PP, Eliceiri KW, Keely PJ. Multiphoton microscopy and fluorescence lifetime imaging microscopy (FLIM) to monitor metastasis and the tumor microenvironment. Clin Exp Metastasis. 2009;26(4):357-70.

8. Walsh A, Cook RS, Rexer B, Arteaga CL, Skala MC. Optical imaging of metabolism in HER2 overexpressing breast cancer cells. Biomedical optics express. 2012;3(1):75-85.

9. Skala MC, Riching KM, Bird DK, Gendron-Fitzpatrick A, Eickhoff J, Eliceiri KW, Keely PJ, Ramanujam N. In vivo multiphoton fluorescence lifetime imaging of protein-bound and free nicotinamide adenine dinucleotide in normal and precancerous epithelia. Journal of biomedical optics. 2007;12(2):024014.

10. Skala MC, Riching KM, Gendron-Fitzpatrick A, Eickhoff J, Eliceiri KW, White JG, Ramanujam N. In vivo multiphoton microscopy of NADH and FAD redox states, fluorescence lifetimes, and cellular morphology in precancerous epithelia. Proc Natl Acad Sci U S A. 2007;104(49):19494-9.

11. Walsh AJ, Cook RS, Manning HC, Hicks DJ, Lafontant A, Arteaga CL, Skala MC. Optical metabolic imaging identifies glycolytic levels, subtypes, and early-treatment response in breast cancer. Cancer Res. 2013;73(20):6164-74.

12. Chance B, Schoener B, Oshino R, Itshak F, Nakase Y. Oxidation-reduction ratio studies of mitochondria in freeze-trapped samples. NADH and flavoprotein fluorescence signals. J Biol Chem. 1979;254(11):4764-71.

13. Warburg O. On the origin of cancer cells. Science. 1956;123(3191):309-14.

14. Lakowicz J. Principles of fluorescence spectroscopy. New York: Plenum Publishers; 1999.

15. Campbell JJ, Davidenko N, Caffarel MM, Cameron RE, Watson CJ. A multifunctional 3D co-culture system for studies of mammary tissue morphogenesis and stem cell biology. PLoS One. 2011;6(9):e25661.

16. Straussman R, Morikawa T, Shee K, Barzily-Rokni M, Qian ZR, Du J, Davis A, Mongare MM, Gould J, Frederick DT, Cooper ZA, Chapman PB, Solit DB, Ribas A, Lo RS, Flaherty KT, Ogino S, Wargo JA, Golub TR. Tumour micro-environment elicits innate resistance to RAF inhibitors through HGF secretion. Nature. 2012;487(7408):500-4.

17. Chakrabarty A, Sanchez V, Kuba MG, Rinehart C, Arteaga CL. Feedback upregulation of HER3 (ErbB3) expression and activity attenuates antitumor effect of PI3K inhibitors. Proc Natl Acad Sci U S A. 2012;109(8):2718-23.

18. Miller TW, Forbes JT, Shah C, Wyatt SK, Manning HC, Olivares MG, Sanchez V, Dugger TC, de Matos Granja N, Narasanna A, Cook RS, Kennedy JP, Lindsley CW, Arteaga CL. Inhibition of mammalian target of rapamycin is required for optimal antitumor effect of HER2 inhibitors against HER2-overexpressing cancer cells. Clin Cancer Res. 2009;15(23):7266-76.

19. Xia W, Bacus S, Hegde P, Husain I, Strum J, Liu L, Paulazzo G, Lyass L, Trusk P, Hill J, Harris J, Spector NL. A model of acquired autoresistance to a potent ErbB2 tyrosine kinase inhibitor and a therapeutic strategy to prevent its onset in breast cancer. Proc Natl Acad Sci U S A. 2006;103(20):7795-800.

20. Walsh AJ, Poole KM, Duvall CL, Skala MC. Ex vivo optical metabolic measurements from cultured tissue reflect in vivo tissue status. Journal of biomedical optics. 2012;17(11):116015.

21. Bird DK, Yan L, Vrotsos KM, Eliceiri KW, Vaughan EM, Keely PJ, White JG, Ramanujam N. Metabolic mapping of MCF10A human breast cells via multiphoton fluorescence lifetime imaging of the coenzyme NADH. Cancer Res. 2005;65(19):8766-73.

22. Wozniak MA, Keely PJ. Use of three-dimensional collagen gels to study mechanotransduction in T47D breast epithelial cells. Biol Proced Online. 2005;7:144-61.

23. Nakashima N, Yoshihara K, Tanaka F, Yagi K. Picosecond fluorescence lifetime of the coenzyme of D-amino acid oxidase. J Biol Chem. 1980;255(11):5261-3.

24. Lakowicz JR, Szmacinski H, Nowaczyk K, Johnson ML. Fluorescence Lifetime Imaging of Free and Protein-Bound Nadh. Proc Natl Acad Sci U S A. 1992;89(4):1271-5.

25. Walsh AJ, Skala MC. An automated image processing routine for segmentation of cell cytoplasms in high-resolution autofluorescence images. SPIE Proceedings. 2014;8948(56).

26. Akaike H. A new look at the statistical model identification. Automatic Control, IEEE Transactions on. 1974;19(6):716-23.

27. Chakrabarty A, Bhola NE, Sutton C, Ghosh R, Kuba MG, Dave B, Chang JC, Arteaga CL. Trastuzumab-resistant cells rely on a HER2-PI3K-FoxO-survivin axis and are sensitive to PI3K inhibitors. Cancer Res. 2013;73(3):1190-200.

28. Shapiro GI, Rodon J, Bedell C, Kwak EL, Baselga J, Brana I, Pandya SS, Scheffold C, Laird AD, Nguyen LT, Xu Y, Egile C, Edelman G. Phase I Safety, Pharmacokinetic, and Pharmacodynamic Study of SAR245408 (XL147), an Oral Pan-Class I PI3K Inhibitor, in Patients with Advanced Solid Tumors. Clin Cancer Res. 2014;20(1):233-45.

29. Ritter CA, Perez-Torres M, Rinehart C, Guix M, Dugger T, Engelman JA, Arteaga CL. Human breast cancer cells selected for resistance to trastuzumab in vivo overexpress epidermal growth factor receptor and ErbB ligands and remain dependent on the ErbB receptor network. Clin Cancer Res. 2007;13(16):4909-19.

30. Aurisicchio L, Marra E, Luberto L, Carlomosti F, De Vitis C, Noto A, Gunes Z, Roscilli G, Mesiti G, Mancini R, Alimandi M, Ciliberto G. Novel anti-ErbB3 monoclonal antibodies show therapeutic efficacy in xenografted and spontaneous mouse tumors. Journal of cellular physiology. 2012;227(10):3381-8.

31. Blacker TS, Mann ZF, Gale JE, Ziegler M, Bain AJ, Szabadkai G, Duchen MR. Separating NADH and NADPH fluorescence in live cells and tissues using FLIM. Nature communications. 2014;5:3936.

32. Zhao Y, Butler EB, Tan M. Targeting cellular metabolism to improve cancer therapeutics. Cell death & disease. 2013;4:e532.

33. Walsh AJ, Cook RS, Arteaga CL, Skala MC. Optical metabolic imaging of live tissue cultures. SPIE Proceedings. 2013;8588.

34. Ostrander JH, McMahon CM, Lem S, Millon SR, Brown JQ, Seewaldt VL, Ramanujam N. Optical redox ratio differentiates breast cancer cell lines based on estrogen receptor status. Cancer Res. 2010;70(11):4759-66.

35. Chang J, Powles TJ, Allred DC, Ashley SE, Makris A, Gregory RK, Osborne CK, Dowsett M. Prediction of clinical outcome from primary tamoxifen by expression of biologic markers in breast cancer patients. Clin Cancer Res. 2000;6(2):616-21.

36. Arpino G, Green SJ, Allred DC, Lew D, Martino S, Osborne CK, Elledge RM. HER-2 amplification, HER-1 expression, and tamoxifen response in estrogen receptor-positive metastatic breast cancer: a southwest oncology group study. Clin Cancer Res. 2004;10(17):5670-6.

37. Holmes FA, Walters RS, Theriault RL, Forman AD, Newton LK, Raber MN, Buzdar AU, Frye DK, Hortobagyi GN. Phase II trial of taxol, an active drug in the treatment of metastatic breast cancer. Journal of the National Cancer Institute. 1991;83(24):1797-805.

38. Seidman AD, Tiersten A, Hudis C, Gollub M, Barrett S, Yao TJ, Lepore J, Gilewski T, Currie V, Crown J, et al. Phase II trial of paclitaxel by 3-hour infusion as initial and salvage

chemotherapy for metastatic breast cancer. Journal of clinical oncology : official journal of the American Society of Clinical Oncology. 1995;13(10):2575-81.

39. Velasco-Velazquez MA, Homsi N, De La Fuente M, Pestell RG. Breast cancer stem cells. Int J Biochem Cell Biol. 2012;44(4):573-7.

40. Al-Hajj M, Wicha MS, Benito-Hernandez A, Morrison SJ, Clarke MF. Prospective identification of tumorigenic breast cancer cells. Proc Natl Acad Sci U S A. 2003;100(7):3983-8.

41. Mohsin SK, Weiss HL, Gutierrez MC, Chamness GC, Schiff R, Digiovanna MP, Wang CX, Hilsenbeck SG, Osborne CK, Allred DC, Elledge R, Chang JC. Neoadjuvant trastuzumab induces apoptosis in primary breast cancers. J Clin Oncol. 2005;23(11):2460-8.

42. Dent R, Trudeau M, Pritchard KI, Hanna WM, Kahn HK, Sawka CA, Lickley LA, Rawlinson E, Sun P, Narod SA. Triple-negative breast cancer: clinical features and patterns of recurrence. Clin Cancer Res. 2007;13(15 Pt 1):4429-34.

43. Bauer KR, Brown M, Cress RD, Parise CA, Caggiano V. Descriptive analysis of estrogen receptor (ER)-negative, progesterone receptor (PR)-negative, and HER2-negative invasive breast cancer, the so-called triple-negative phenotype: a population-based study from the California cancer Registry. Cancer. 2007;109(9):1721-8.

44. Aurisicchio L, Marra E, Roscilli G, Mancini R, Ciliberto G. The promise of anti-ErbB3 monoclonals as new cancer therapeutics. Oncotarget. 2012;3(8):744-58.

CHAPTER 7

Conclusions and Future Directions

7.1 Summary and Conclusions

The primary goal of this dissertation is to characterize and develop optical metabolic imaging endpoints as biomarkers for drug response in breast cancer. Clinically, therapy selection remains difficult due to the large number of patients that present *de novo* and acquired drug resistance. Currently, there are no technologies to predict which patients will not respond to traditional therapies. While optical techniques, such as diffuse optical tomography, have been used to monitor therapy response (1-4), optical metabolic imaging is more sensitive to early drug-induced changes and achieves higher spatial resolution, which allows analysis of tumor heterogeneity. Furthermore, while similar optical metabolic imaging techniques have been used for optical diagnosis (5, 6), this is the first application of these technologies for dynamic imaging of drug response.

The objective of Chapter 2 is to provide relevant background information and a framework for the work reported in the rest of the Dissertation. Chapter 2 contains a discussion on the current standard of care and therapy treatment regimens for breast cancer patients. Furthermore, cellular metabolism is defined and motivated as a source of contrast for drug efficacy. Chapter 2 concludes with an introduction to fluorescence lifetime imaging which is utilized in optical metabolic imaging and a brief introduction to organoid culture which enables clinical translation of optical metabolic imaging.

The primary objective of Chapter 3 is to develop an analysis method to evaluate and quantify cellular heterogeneity within optical metabolic imaging data sets. Solid tumors are highly heterogeneous and heterogeneity contributes to tumor aggression, invasion, metastases, and therapy resistance (7-11). Therefore, single-cell resolution and tumor heterogeneity analysis is important for a drug-response monitoring technology. Chapter 3 develops and characterizes optical metabolic imaging subpopulation analysis (OMI-SPA). OMI-SPA uses mixed Gaussian distributions to model cellular populations to identify the number and parameters of cellular subpopulations. This chapter presents the theoretical limitations of SPA and demonstrates utility in co-cultures of two breast cancer cell lines. The main conclusions of this work are that OMI-SPA can identify cancer cell subpopulations based on OMI endpoints. Furthermore, this work quantified the relationships between sample size, standard deviation, and mean separation distance for SPA to robustly characterize two populations with minimal error. These results are presented graphically, and may act as a look up table for future experiments when the means and standard deviations of populations are unknown or estimated. Chapter 3 addresses the first Aim, "characterize subpopulation analysis of OMI data to quantify heterogeneous cell populations."

Chapter 4 addresses Aim 2 outlined in Chapter 1, "determine the sensitivity of OMI to breast cancer subtypes and therapeutic response *in vitro* and validate OMI measures of response in human breast cancer xenografts *in vivo*." In this chapter, an *in vitro* experiment was performed to determine the basal and post-therapy metabolism, as measured by OMI, in a panel of breast cancers with varying receptor expressions. In addition, an *in vivo* xenograft experiment was performed on three different xenografts to determine the sensitivity of OMI endpoints to drug-induced changes in metabolism. These studies demonstrated that OMI is highly sensitive to drug-induced metabolism changes, with significant reductions in all endpoints as early as 24 hr post-treatment in cells and 48hr in xenografts. To our knowledge, this is the earliest detected response to trastuzumab *in vivo*. Furthermore, OMI endpoints of trastuzumab-resistant cells and tumors were not significantly affected by trastuzumab treatment, proving specificity of OMI. Additionally, OMI-measured response was directly compared with a clinically used technology FDG-PET. FDG uptake did not significantly change with trastuzumab treatment in either responsive or resistant tumors over the entire time course, highlighting the advantages of OMI. Finally, Chapter 4 also demonstrates the application of advanced imaging analysis protocols which are able to identify heterogeneous cell populations in cell cultures and tumors imaged *in vivo*. The main conclusion of Chapter 4 is that OMI is highly sensitive to drug-induced changes in cellular metabolism in responding cells and *in vivo* tumors.

Chapter 5 addresses Aim 3, "characterize OMI endpoints in excised tissues." Due to challenges and limitations with clinical *in vivo* OMI imaging of deep tissue sites such as the breast, OMI was performed on *in vivo* hamster cheek pouch tissue and compared with OMI of freshly excised, live cultured tissues, and frozen biopsy samples. The results of this study demonstrate that OMI endpoints remain unchanged up to 8 hours post excision in live culture conditions. Frozen tissue samples however, expressed differences up to 15% compared to *in vivo*. These results demonstrate that meaningful OMI data can be obtained from freshly excised, live cultured samples. This study defined the time-window for OMI measurements on excised tissues and characterizes the metabolic changes that occur in frozen-thawed tissues.

The main goal of Chapter 6 was to validate that OMI-measured drug response in organoids correlated with *in vivo* drug response in xenograft models and prove feasibility of an organoid-OMI screen for clinical use. This chapter addressed Aim 4, "validate organoid-OMI measured tumor response with *in vivo* OMI in human breast cancer xenografts and compare organoid-OMI measured tumor response with measures of response in human breast cancers." To expedite clinical utility of OMI measured drug response, an OMI-organoid drug screen was developed and validated. Organoids are 3D cultures of primary tumor sections and contain all the cells and microenvironment of the original tumor, including malignant cells, fibroblasts, leukocytes, and endothelial cells (12). Organoids are an attractive platform for an OMI-based drug screen because they recapitulate *in vivo* tumor environments and cell signaling networks which have been shown to mediate drug resistance (13). Furthermore, organoids are inexpensive and easy to image.

The work in Chapter 6 is the first to demonstrate that OMI-measured organoid drug response agrees with *in vivo* drug response, as measured by changes in tumor size. Furthermore, the drug response of organoids over 72 hours predicted for drug response of *in vivo* tumors treated for three weeks. Heterogeneity analysis revealed subpopulations with different OMI profiles following drug response and these subpopulations could be tracked over the 72-hr time course. Additionally, Chapter 6 defines the OMI index, a combination of the redox ratio, NADH mean lifetime, and FAD mean lifetime, as a composite variable which enables direct correlation between cellular metabolism and drug response. Finally, Chapter 6 proved feasibility of an organoid-OMI approach to measuring drug response in 6 clinical samples. Altogether, this Chapter validates the organoid-OMI drug screen approach in two xenograft models and demonstrates feasibility in human breast tumors.

This dissertation characterizes OMI for monitoring and predicting drug response. OMI is an attractive platform because it is high-resolution, non-invasive, uses non-ionizing radiation, and is highly sensitive to changes in cellular metabolism. When combined with image processing techniques and cellular-level analysis, OMI is capable of resolving cellular heterogeneity, which is increasing important for identifying cancer stem cells and non-responding subpopulations. Furthermore, this dissertation has defined time windows for robust OMI measurements of excised tissues and developed an organoid-drug screen for universality and clinical application of OMI.

7.2 Future Directions

Test Organoid-OMI Screen in Immune-Competent Mice

Chapter 6 validated OMI-measured drug response of organoids with *in vivo* tumor growth curves of two xenograft mouse models, one responsive to trastuzumab and one resistant to trastuzumab. These experiments demonstrated corroboration between organoid-OMI detected response and *in vivo* response. However, xenograft tumors must be grown in immune-compromised mice and these models of breast cancer and tumor response may not fully recapitulate clinical disease and response (14). Many drugs, including trastuzumab, modulate immune function and the full effects may not be well represented in xenograft studies. Genetically engineered mouse models of breast cancer are grown in immune-competent mice and may reveal interactions between tumor, drugs, and the immune system. Future experiments in immune-competent mice are warranted to ensure an organoid-OMI screen retains its prognostic capability.

Validate Organoid-OMI Screen in Clinical Neoadjuvant Study

Validation of the organoid-OMI screen in patients is challenging due to the long follow-up time, variety of treatments, and lack of robust clinical measures of response. However, the neoadjuvant therapy setting in breast cancer provides an opportunity to test organoid-OMI predicted response with actual patient outcomes. Neoadjuvant therapy is systemic chemotherapy or targeted therapy given to a cancer patient before surgical removal of the primary tumor. Neoadjuvant therapy is used to improve surgical outcomes, obtain information on tumor response, and obtain long-term disease-free survival (15). Studies have shown that patients that achieve pathological response to neoadjuvant chemotherapy have better survival (16). Response to neoadjuvant therapy is determined pathologically at the time of surgical resection of the primary tumor. Therefore, the neoadjuvant setting provides a window for validating organoid-OMI drug response. In this study, pre-treatment tissue would be obtained by core needle biopsy prior to chemotherapy. Organoids would be generated from the tissue and treated with the same drug cocktail received by the patient. Organoid-OMI drug response would be compared with pathological response determined at the time of surgery.

Investigate Biochemical Source of OMI Contrast

OMI probes the fluorescence intensities and lifetimes of NADH and FAD. Assuming constant imaging parameters and sample optical properties, changes in the fluorescence intensity of NADH and FAD are most likely due to changes in the concentration of the fluorophore (17). However, the physiological source of changes in the fluorescence lifetime of NADH and FAD are less defined. NADH and FAD can exist in free and bound states and changes in the mean lifetime may be due to changes in the proportion of free and bound fluorophore which would manifest as changes in α_1 and α_2. Changes in the bound lifetime may be due to different conformations of the fluorophore and binding to different enzyme complexes. Future experiments in solutions and cell culture will elucidate the physiological basis for significant changes in fluorescence lifetimes of NADH and FAD.

Investigate Organoid-OMI Screen for Additional Diseases

Abnormal cellular metabolism is a hallmark of many additional cancers and diseases. An organoid-OMI screen has the potential to guide therapy selection for additional diseases, and not be limited to breast cancer. Future studies will explore the validity and usefulness of OMI technology for additional diseases and cancers.

Automate Imaging Acquisition and Increase Speed for High Throughput Measurements

For widespread clinical adoption of an organoid-OMI screen, OMI needs to be faster, less expensive, and automated. Recent advances in time correlated single photon counting electronics and computing power have allowed faster FLIM. For clinical use, OMI should be incorporated into an automated plate reader which could automatically identify and image organoids. A sophisticated system would include an environmental chamber. Furthermore, with faster FLIM capabilities, image stacks throughout the organoid could be imaged to improve sampling.

Optimize Organoid Growth Conditions

The organoid generation and growth protocol could be optimized. The organoid generation protocol presented in Chapter 6 uses mechanical dissociation to generate organoids and the organoids grow in matrigel. Additional protocols could be tested, such as addition of extracellular matrix degredation enzymes, collagenases, to optimize organoid generation (18). Furthermore, organoids could be grown in a variety of gels. While matrigel facilitates organoid growth, gel mechanical properties could be controlled by growing organoids on collagen gels. Organoid growth on gels of varying stiffness could be investigated as well as organoid invasion (18, 19).

7.3 Contribution to the Field and Societal Impact

Innovation in Biophotonics

The studies in this dissertation have led to several innovations within the field of biophotonics. First, these studies are the first to characterize OMI endpoints in regards to other measures of cellular metabolism. In Chapter 4, OMI endpoints, the redox ratio, NADH mean lifetime, and FAD mean lifetime, are robustly compared with measurements of glucose-uptake and lactate secretion by cells, and FDG-PET in xenograft tumors. This characterization of OMI endpoints provides insights on the physiological source of contract.

Additionally, this work is the first to develop OMI for monitoring anti-cancer therapy. Outside of these studies, no OMI endpoint has been exploited for predicting the outcome of any therapy in animal models or clinical settings. Traditionally, the field of biophotonics has largely focused its efforts on diagnostics, such as optical biopsy, and breast cancer margin assessment (20-23). This work presents a novel application of optical technologies, using OMI endpoints as measures of drug response. While diffuse optical tomography has also been used to detect response (2-4), diffuse optical tomography is low resolution and limited to the treatment received by the patient. The novelty of the research presented in this dissertation is the combined organoid-OMI screen which shifts from a focus of measuring response and reacting to non-response to being able to directly test all drugs and drug combinations to guide initial therapy decisions. *In vivo* functional imaging methods are inherently low-throughput, because they are limited to assessing only the drugs that the patient has already received. The combination of functional measures (OMI) of live tumors (organoids) in a high-throughput screening format is completely unprecedented in the research literature. The organoid-OMI approach also provides a potentially powerful system to test an individual's response to multiple treatment schemes, rather than infer a possible response from biomarkers. This combination of optical imaging of metabolism, organoid drug screens, and single cell analysis is highly innovative and opens up additional research avenues.

The fluorescence lifetimes of NADH and FAD are significantly under-studied, with only a handful of labs around the world that investigate any of these endpoints alone in any context. The work in this dissertation has characterized the fluorescence lifetimes of NADH and FAD *in vivo*, in live cultured, freshly excised tissues, frozen tissues, and organoids. Traditionally, metabolism endpoints are thought to significantly change upon removal from the body and thus metabolic imaging studies have been limited to *in vivo* studies. However, the results of Chapter 5 suggest that optical metabolic endpoints, particularly the fluorescence lifetime of NADH and FAD remain stable up to 8 hr post removal. These findings enable optical metabolic imaging in an array of experiments and situations when *in vivo* imaging is not practical.

Additionally, this dissertation presents novel image analysis techniques that are applicable and translatable to microscopy research, and not limited to optical metabolic imaging data. An automated image segmentation algorithm was developed in CellProfiler to segment autofluorescence images of clumped cells and organoids into cells, nuclei, and cytoplasms (Appendix D). To our knowledge, this is the first published code for segmentation of clumped cells in auto-fluorescence images. Additionally, image analysis techniques were developed to analyze images and data sets on a single cell level to quantify cellular heterogeneity and identify cell subpopulations (Chapter 3). Both of these techniques can be used in future optical metabolic imaging studies and applied to additional microscopy techniques and applications.

Contributions to Cancer Biology

Cancer cells are known to exhibit abnormal cellular metabolism (24). Furthermore, oncogenic signaling often regulates cellular metabolism processes. For example, in breast cancer, the estrogen receptor regulates gene expression of glucose transporter proteins and proteins involved in oxidative phosphorylation and the citric acid cycle (25-27). Additionally, HER2 mediates metabolism through signaling of the PI3K pathway (28, 29). Therefore, oncogenic inhibition by anti-cancer drugs may affect cellular metabolism and as demonstrated in this dissertation, cellular metabolism provides a robust indicator of drug response. This dissertation contributes research and evidence on the relationships between metabolism, cancer, and drug response.

Furthermore, cellular metabolism is difficult to quantify. Cellular metabolism can be investigated by measuring quantities of fuel sources, metabolic products, flux of metabolic enzymes, or by imaging methods such as histology, diffuse optical tomography or FDG-PET; however, each of these methods is sensitive to only a small subset of the cellular metabolism process. Fluorescence imaging of NADH and FAD provides a global measure of cellular metabolism because the source of contrast, NADH and FAD, are coenzymes used throughout metabolism. The studies and experiments reported in this dissertation fully characterize NADH and FAD fluorescence and fluorescence lifetimes as biomarkers of cellular metabolism for use in future studies of cancer biology.

There is a growing body of evidence that interactions between cancer cells and surrounding cells in the tumor microenvironment may mediate resistance to cancer drugs (30). Therefore, organoid cultures provide an attractive platform for drug response studies because organoids retain the malignant tumor cells and the native tumor microenvironment. To date, primary tumor organoid cultures are understudied and underutilized. Chapter 6 and Appendix E present novel methods for the generation and culture of primary xenograft and human tumor-derived organoids. This work is innovative and applicable for future organoid studies. Furthermore, the work in Appendix E demonstrates feasibility of growth of organoids from frozen-thawed tissues. This will enable broad adoption of organoid techniques, even where fresh tissues are not available.

Bridging the Gap Between Preclinical and Clinical Research

Currently, the costs to develop a new drug are astronomical and many new drugs that show potential in preclinical experiments fail to show efficacy in expensive clinical trials (31). More relevant disease models are needed to bridge the gap between preclinical and clinical research. In oncology, preclinical models include immortalized cell lines, human xenografts grown in mice from immortalized cell lines, and genetically engineered mouse cancers. Recently, patient-derived xenograft models have also been proposed as a relevant cancer model (32, 33), however, patient derived xenografts are expensive, difficult to grow, and require lengthy growth periods and multiple passages. Primary tumor-derived organoids present an attractive platform for preclinical studies and may help bridge the gap between preclinical and clinical studies. Organoid generation and culture is inexpensive, fast, and highly reproducible with nearly 100% of tumors able to grow organoids. Organoids contain all the innate cells of the tumor and maintain tumor-stroma interactions. Therefore, organoids may better represent cancer physiology than immortalized cells or 2D culture. For these reasons, organoids may provide a missing link for preclinical trials.

Potential Impact on Preclinical Drug Trials

Development of OMI to measure therapeutic response would have a revolutionary effect on pre-clinical studies of drug development and efficacy. Currently, the gold standard of drug efficacy is tumor regression or growth. Early identification of responding tumors requires IHC staining of drug targets, apoptotic cells, and proliferating cells. IHC can only be performed on excised tissue and thus, requires the sacrifice of cohorts of mice at each time point in a longitudinal study. Long-term drug efficacy trials can require hundreds of mice to obtain the statistical power for conclusive results. OMI can be performed *in vivo*, through a coverslip, or window chamber (34). In such manner, OMI data from the same animal and tumor can be acquired over time, reducing the need for parallel cohorts. This reduction in animal burden would reduce the cost and greatly accelerate preclinical studies.

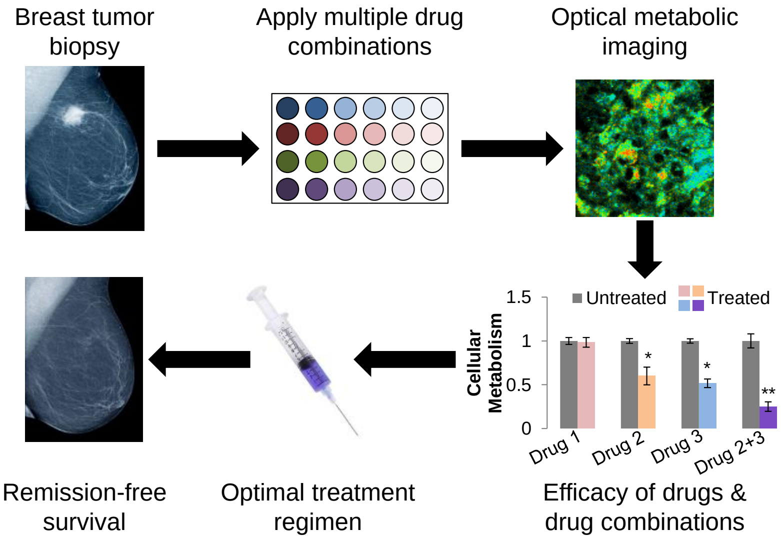

Figure 7.1 Clinical impact of OMI-organoid drug screen. The potential impact of the live tumor (organoid) and optical metabolic imaging (OMI) system on breast cancer care. A small breast tumor biopsy is broken up and grown in multiple organoid macro-suspensions. Each organoid is treated with a different drug or drug combination, and subsequently imaged with OMI. Changes in cellular metabolism are used to assess the efficacy of each drug and drug combination. The individually-tailored optimal treatment regimen is then applied to the patient, increasing the chances of remission-free survival.

Implications of an Organoid-OMI Drug Screen for Breast Cancer Care

Development of a live-culture tissue technique combined with OMI will enable a high-throughput screen of potential drugs and drug combinations to identify the most effective treatment for each breast cancer patient. In such a system, a tumor sample is removed via a routine biopsy, organoids are generated from the tissue biopsy and treated with potential drugs and drug combinations, OMI is performed to measure metabolic response of the organoids, and the ideal drug or drug combination is identified and administered to the patient (Fig. 7.1). This technology will revolutionize patient care by predicting response to multiple treatment regimens, rather than reacting to a prescribed treatment. Optimal matching of a patient to a drug regimen will result in earlier effective treatment for the ~300,000 breast cancer patients diagnosed each year, resulting in increased survival. Also, this screen will save patients from the emotional, temporal, and financial cost of ineffective therapies and spare patients the increased toxicities of exposure to ineffective drugs.

7.4 References

1. Cerussi A, Hsiang D, Shah N, Mehta R, Durkin A, Butler J, Tromberg BJ. Predicting response to breast cancer neoadjuvant chemotherapy using diffuse optical spectroscopy. Proc Natl Acad Sci U S A. 2007;104(10):4014-9.

2. Cerussi AE, Tanamai VW, Hsiang D, Butler J, Mehta RS, Tromberg BJ. Diffuse optical spectroscopic imaging correlates with final pathological response in breast cancer neoadjuvant chemotherapy. Philosophical transactions Series A, Mathematical, physical, and engineering sciences. 2011;369(1955):4512-30.

3. Jakubowski DB, Cerussi AE, Bevilacqua F, Shah N, Hsiang D, Butler J, Tromberg BJ. Monitoring neoadjuvant chemotherapy in breast cancer using quantitative diffuse optical spectroscopy: a case study. Journal of biomedical optics. 2004;9(1):230-8.

4. Shah N, Gibbs J, Wolverton D, Cerussi A, Hylton N, Tromberg BJ. Combined diffuse optical spectroscopy and contrast-enhanced magnetic resonance imaging for monitoring breast cancer neoadjuvant chemotherapy: a case study. Journal of biomedical optics. 2005;10(5):051503.

5. Sun Y, Phipps JE, Meier J, Hatami N, Poirier B, Elson DS, Farwell DG, Marcu L. Endoscopic fluorescence lifetime imaging for in vivo intraoperative diagnosis of oral carcinoma. Microscopy and microanalysis : the official journal of Microscopy Society of America, Microbeam Analysis Society, Microscopical Society of Canada. 2013;19(4):791-8.

6. Skala MC, Riching KM, Gendron-Fitzpatrick A, Eickhoff J, Eliceiri KW, White JG, Ramanujam N. In vivo multiphoton microscopy of NADH and FAD redox states, fluorescence lifetimes, and cellular morphology in precancerous epithelia. Proc Natl Acad Sci U S A. 2007;104(49):19494-9.

7. Almendro V, Cheng YK, Randles A, Itzkovitz S, Marusyk A, Ametller E, Gonzalez-Farre X, Munoz M, Russnes HG, Helland A, Rye IH, Borresen-Dale AL, Maruyama R, van Oudenaarden A, Dowsett M, Jones RL, Reis-Filho J, Gascon P, Gonen M, Michor F, Polyak K. Inference of tumor evolution during chemotherapy by computational modeling and in situ analysis of genetic and phenotypic cellular diversity. Cell reports. 2014;6(3):514-27.

8. Fisher R, Pusztai L, Swanton C. Cancer heterogeneity: implications for targeted therapeutics. British journal of cancer. 2013;108(3):479-85.

9. Kiviet DJ, Nghe P, Walker N, Boulineau S, Sunderlikova V, Tans SJ. Stochasticity of metabolism and growth at the single-cell level. Nature. 2014;514(7522):376-9.

10. Polyak K. Tumor Heterogeneity Confounds and Illuminates: A case for Darwinian tumor evolution. Nature medicine. 2014;20(4):344-6.

11. Visvader JE, Lindeman GJ. Cancer stem cells in solid tumours: accumulating evidence and unresolved questions. Nature Reviews Cancer. 2008;8(10):755-68.

12. Campbell JJ, Davidenko N, Caffarel MM, Cameron RE, Watson CJ. A multifunctional 3D co-culture system for studies of mammary tissue morphogenesis and stem cell biology. PLoS One. 2011;6(9):e25661.

13. Straussman R, Morikawa T, Shee K, Barzily-Rokni M, Qian ZR, Du J, Davis A, Mongare MM, Gould J, Frederick DT, Cooper ZA, Chapman PB, Solit DB, Ribas A, Lo RS, Flaherty KT, Ogino S, Wargo JA, Golub TR. Tumour micro-environment elicits innate resistance to RAF inhibitors through HGF secretion. Nature. 2012;487(7408):500-4.

14. Vargo-Gogola T, Rosen JM. Modelling breast cancer: one size does not fit all. Nature reviews Cancer. 2007;7(9):659-72.

15. Kaufmann M, Hortobagyi GN, Goldhirsch A, Scholl S, Makris A, Valagussa P, Blohmer JU, Eiermann W, Jackesz R, Jonat W, Lebeau A, Loibl S, Miller W, Seeber S, Semiglazov V, Smith R, Souchon R, Stearns V, Untch M, von Minckwitz G. Recommendations from an international expert panel on the use of neoadjuvant (primary) systemic treatment of operable breast cancer: an update. Journal of clinical oncology : official journal of the American Society of Clinical Oncology. 2006;24(12):1940-9.

16. Liedtke C, Mazouni C, Hess KR, Andre F, Tordai A, Mejia JA, Symmans WF, Gonzalez-Angulo AM, Hennessy B, Green M, Cristofanilli M, Hortobagyi GN, Pusztai L. Response to neoadjuvant therapy and long-term survival in patients with triple-negative breast cancer. Journal of clinical oncology : official journal of the American Society of Clinical Oncology. 2008;26(8):1275-81.

17. Lakowicz J. Principles of fluorescence spectroscopy. New York: Plenum Publishers; 1999.

18. Nguyen-Ngoc KV, Cheung KJ, Brenot A, Shamir ER, Gray RS, Hines WC, Yaswen P, Werb Z, Ewald AJ. ECM microenvironment regulates collective migration and local dissemination in normal and malignant mammary epithelium. Proc Natl Acad Sci U S A. 2012;109(39):E2595-604.

19. Ewald AJ, Huebner RJ, Palsdottir H, Lee JK, Perez MJ, Jorgens DM, Tauscher AN, Cheung KJ, Werb Z, Auer M. Mammary collective cell migration involves transient loss of epithelial features and individual cell migration within the epithelium. Journal of cell science. 2012;125(Pt 11):2638-54.

20. Masters BR, So PT, Gratton E. Multiphoton excitation microscopy of in vivo human skin. Functional and morphological optical biopsy based on three-dimensional imaging, lifetime measurements and fluorescence spectroscopy. Ann N Y Acad Sci. 1998;838:58-67.

21. McGinty J, Galletly NP, Dunsby C, Munro I, Elson DS, Requejo-Isidro J, Cohen P, Ahmad R, Forsyth A, Thillainayagam AV, Neil MA, French PM, Stamp GW. Wide-field fluorescence lifetime imaging of cancer. Biomedical optics express. 2010;1(2):627-40.

22. Brown JQ, Bydlon TM, Richards LM, Yu B, Kennedy SA, Geradts J, Wilke LG, Junker M, Gallagher J, Barry W, Ramanujam N. Optical assessment of tumor resection margins in the breast. IEEE J Sel Top Quantum Electron. 2010;16(3):530-44.

23. Wilke LG, Brown JQ, Bydlon TM, Kennedy SA, Richards LM, Junker MK, Gallagher J, Barry WT, Geradts J, Ramanujam N. Rapid noninvasive optical imaging of tissue composition in breast tumor margins. American journal of surgery. 2009;198(4):566-74.

24. Warburg O. On the origin of cancer cells. Science. 1956;123(3191):309-14.

25. Chen JQ, Brown TR, Russo J. Regulation of energy metabolism pathways by estrogens and estrogenic chemicals and potential implications in obesity associated with increased exposure to endocrine disruptors. Biochimica Et Biophysica Acta. 2009;1793(7):1128-43.

26. Cheng CM, Cohen M, Wang J, Bondy CA. Estrogen augments glucose transporter and IGF1 expression in primate cerebral cortex. FASEB J. 2001;15(6):907-15.

27. Yadav RN. Isocitrate dehydrogenase activity and its regulation by estradiol in tissues of rats of various ages. Cell Biochem Funct. 1988;6(3):197-202.

28. Harari D, Yarden Y. Molecular mechanisms underlying ErbB2/HER2 action in breast cancer. Oncogene. 2000;19(53):6102-14.

29. Plas DR, Thompson CB. Akt-dependent transformation: there is more to growth than just surviving. Oncogene. 2005;24(50):7435-42.

30. Straussman R, Morikawa T, Shee K, Barzily-Rokni M, Qian ZR, Du J, Davis A, Mongare MM, Gould J, Frederick DT. Tumour micro-environment elicits innate resistance to RAF inhibitors through HGF secretion. Nature. 2012;487(7408):500-4.

31. Paul SM, Mytelka DS, Dunwiddie CT, Persinger CC, Munos BH, Lindborg SR, Schacht AL. How to improve R&D productivity: the pharmaceutical industry's grand challenge. Nature reviews Drug discovery. 2010;9(3):203-14.

32. DeRose YS, Wang G, Lin YC, Bernard PS, Buys SS, Ebbert MT, Factor R, Matsen C, Milash BA, Nelson E, Neumayer L, Randall RL, Stijleman IJ, Welm BE, Welm AL. Tumor grafts derived from women with breast cancer authentically reflect tumor pathology, growth, metastasis and disease outcomes. Nature medicine. 2011;17(11):1514-20.

33. Marangoni E, Vincent-Salomon A, Auger N, Degeorges A, Assayag F, de Cremoux P, de Plater L, Guyader C, De Pinieux G, Judde JG, Rebucci M, Tran-Perennou C, Sastre-Garau X, Sigal-Zafrani B, Delattre O, Dieras V, Poupon MF. A new model of patient tumor-derived breast cancer xenografts for preclinical assays. Clin Cancer Res. 2007;13(13):3989-98.

34. Shan SQ, Sorg B, Dewhirst MW. A novel rodent mammary window of orthotopic breast cancer for intravital microscopy. Microvasc Res. 2003;65(2):109-17.

APPENDIX A

Supplementary Figures and Tables for Chapter 4

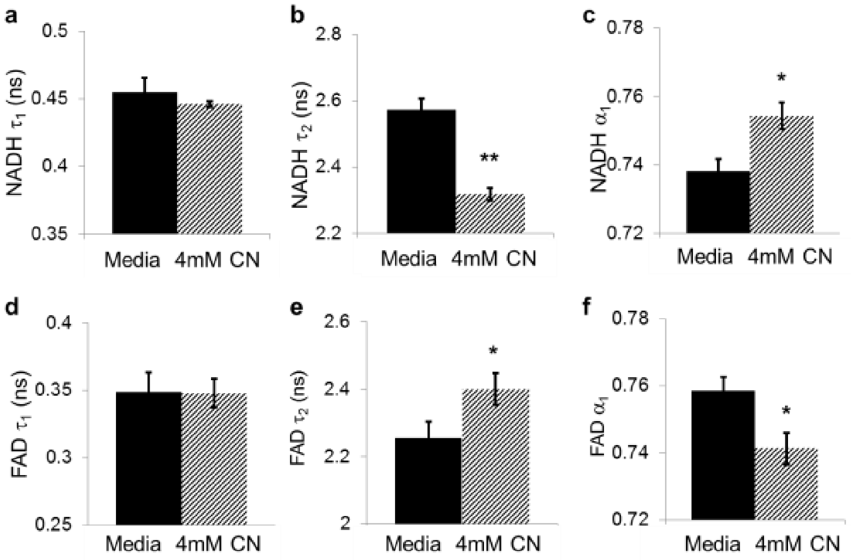

Figure A.1: NADH (a-c) and FAD (d-f) fluorescence lifetime components in MCF10A cells before and after exposure to 4 mM NaCN. NADH τ_1 and τ_2 correspond to the free and protein-bound components of the lifetime, respectively. FAD τ_1 and τ_2 correspond to the protein-bound and free components of the lifetime, respectively. α_1 corresponds to the relative contribution of τ_1 to the overall decay, such that $\alpha_1+\alpha_2=1$.** $P < 0.001$, * $P < 0.05$

Table A.1: Breast cancer cell lines and receptor expression. Eight cell lines were investigated in this study, with ER and HER2 status provided. The last three columns provide the number of images (*in vitro*) or tumors (*in vivo*) collected to compile the results in Fig. 2-6.

Cell	ER	HER2	n (*in vitro*)	n (OMI *in vivo*)	*n* (FDG-PET)
MCF10A	Low	Low	58	NA	NA
MDA-MB-231	-	-	18	NA	NA
MCF7	+	-	18	NA	NA
MDA-MB-361	+	+	18	5	NA
BT474	+	+	18	6	10
SKBr3	+	-	18	NA	NA
HR6	+	+	18	6	10

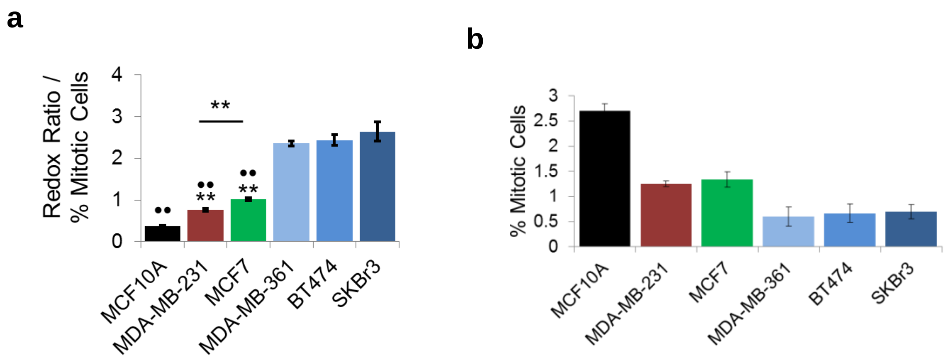

Figure A.2: Relationship between redox ratio and cell proliferation. (a) Redox ratio results normalized to % mitotic cells. The optical redox ratio increases with ER (MCF7, green) and HER2 (MDA-MB-361, BT474, and SKBr3, blue) expression relative to non-malignant (MCF10A, black) cells. The redox ratio is also increased in HER2+ cells relative to triple negative (MDA-MB-231, red) and ER+ cells, and in ER+ cells relative to triple negative cells. Unless indicated with a line, stars (*) indicate statistically significant differences with the MCF10A (non-malignant) cells and bullets (•) indicate statistically significant differences with the HER2+ cells grouped together. ** $P<0.001$, •• $P<0.001$, • $P<0.05$. (b) Percentage of mitotic cells measured for each cell line.

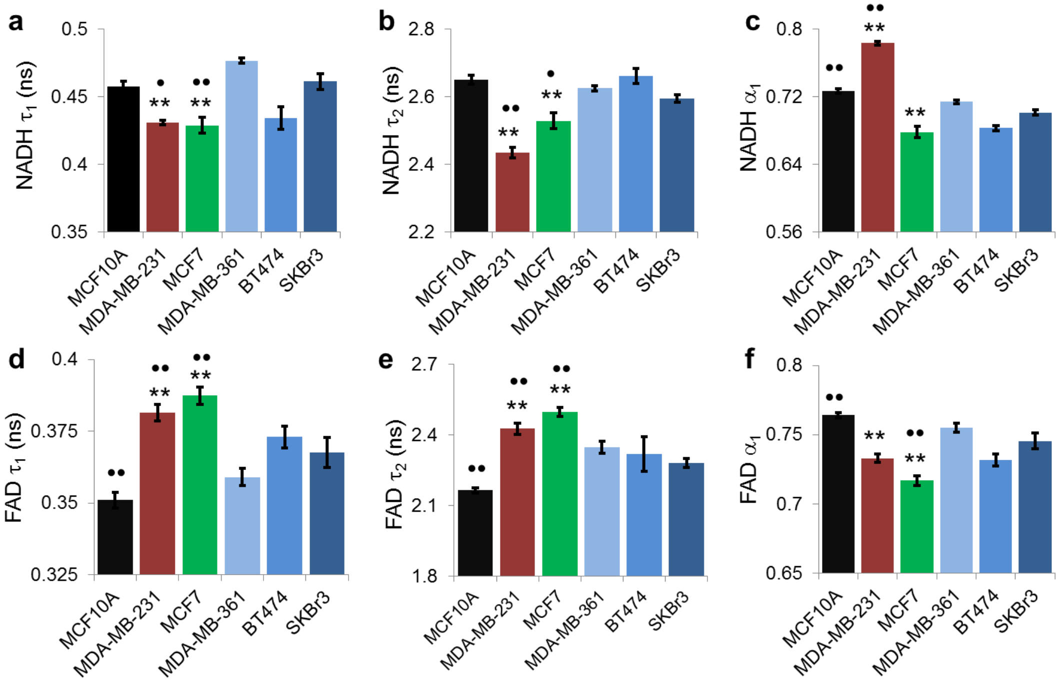

Figure A.3: Fluoresccence lifetime components for a panel of breast cancer cells. NADH (a-c) and FAD (d-f) lifetime components (τ_1, short lifetime; τ_2, long lifetime; and $\alpha_{1,}$ relative contribution of the short lifetime) for a non-malignant (MCF10A, black), a triple-negative breast cancer (MDA-MB-361; red), an ER+ (MCF7, green), and three HER2+ (MDA-MB-361, BT474, and SKBr3; blue) cell lines. Stars (*) indicate statistically significant differences with the MCF10A (non-malignant) cells and bullets (•) indicate statistically significant differences with the HER2+ cells grouped together. ** $P<0.001$, •• $P < 0.001$, • $P<0.05$

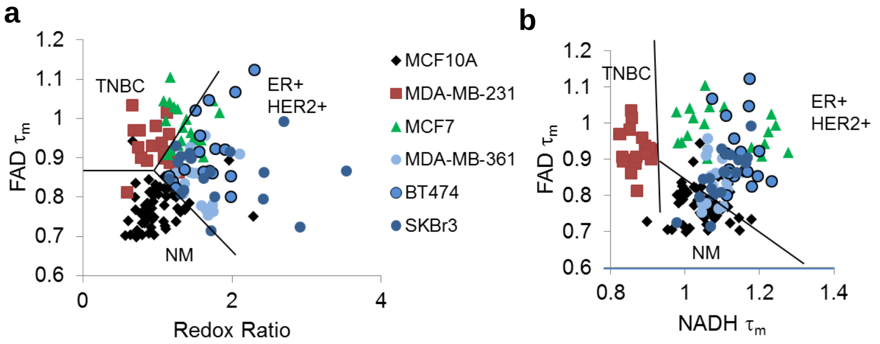

Figure A.4: Scatterplots of OMI endpoints. (a) A scatterplot of FAD τ_m versus redox ratio/proliferation provides visual separation of the different molecular sub-types of breast cancer [non-malignant (NM), ER+, HER2+, and triple negative (TNBC)]. (b) A scatterplot of FAD τ_m versus NADH τ_m provides visual separation of the different molecular sub-types of breast cancer [non-malignant (NM), ER+, HER2+, and triple negative (TNBC)].

Table A.2: Spearman's rank correlation coefficients (*P*-value) for comparisons of metabolic measures. NADH and FAD τ_m are computed from τ_1, τ_2, and α_1 ($\tau_m = \tau_1 * \alpha_1 + \tau_2 * \alpha_2$). Shaded boxes highlight significant ($P<0.05$) correlations.

		Glycolytic Index	Redox Ratio/ Proliferation	NADH				FAD			
				τ_m	τ_1	τ_2	α_1	τ_m	τ_1	τ_2	α_1
Glycolytic Index		1	0.89 (0.03)	0.26 (0.66)	0.54 (0.30)	0.09 (0.92)	-0.14 (0.80)	-0.09 (0.92)	-0.03 (1)	-0.03 (1)	-0.09 (0.92)
Redox Ratio / Proliferation			1	0.66 (0.18)	0.37 (0.50)	0.20 (0.72)	-0.54 (0.30)	0.09 (0.92)	0.09 (0.92)	-0.09 (0.92)	-0.26 (0.66)
NADH	τ_m			1	-0.14 (0.80)	0.43 (0.42)	-0.94 (0.02)	0.31 (0.56)	0.31 (0.56)	0.09 (0.92)	-0.60 (0.24)
	τ_1				1	0.43 (0.42)	0.26 (0.66)	-0.43 (0.42)	-0.83 0.06	-0.60 (0.24)	0.77 (0.10)
	τ_2					1	-0.20 (0.71)	-0.60 (0.24)	-0.60 (0.24)	-0.66 (0.18)	0.31 (0.56)
	α_1						1	-0.43 (0.42)	-0.43 (0.42)	-0.26 (0.66)	0.66 (0.18)
FAD	τ_m							1	1 0.003	0.83 0.06	-0.94 (0.02)
	τ_1								1	0.83 0.06	-0.94 (0.02)
	τ_2									1	-0.71 (0.14)
	α_1										1

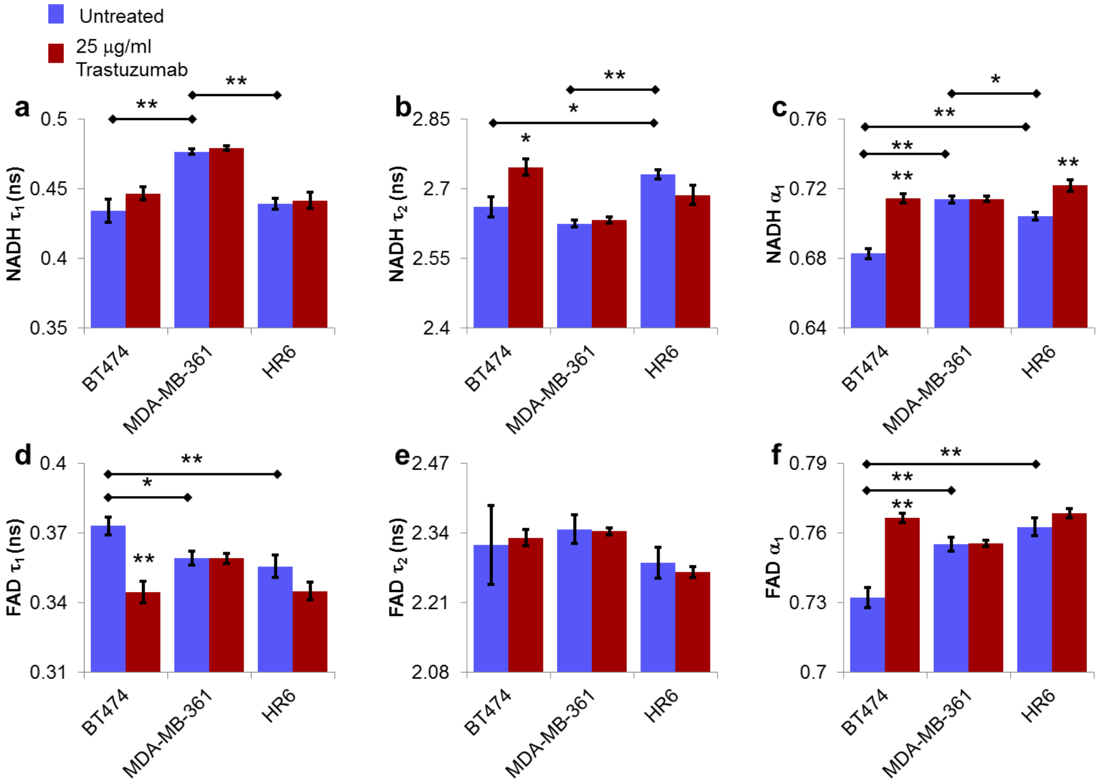

Figure A.5: Fluorescence lifetime components for *in vitro* trastuzumab experiment. NADH (a-c) and FAD (d-f) lifetime components (τ_1, short lifetime; τ_2, long lifetime; and $\alpha_{1,}$ relative contribution of the short lifetime) for trastuzumab perturbation of BT474, MDA-MB-361, and HR6 cells. ** $P < 0.001$; * $P < 0.05$

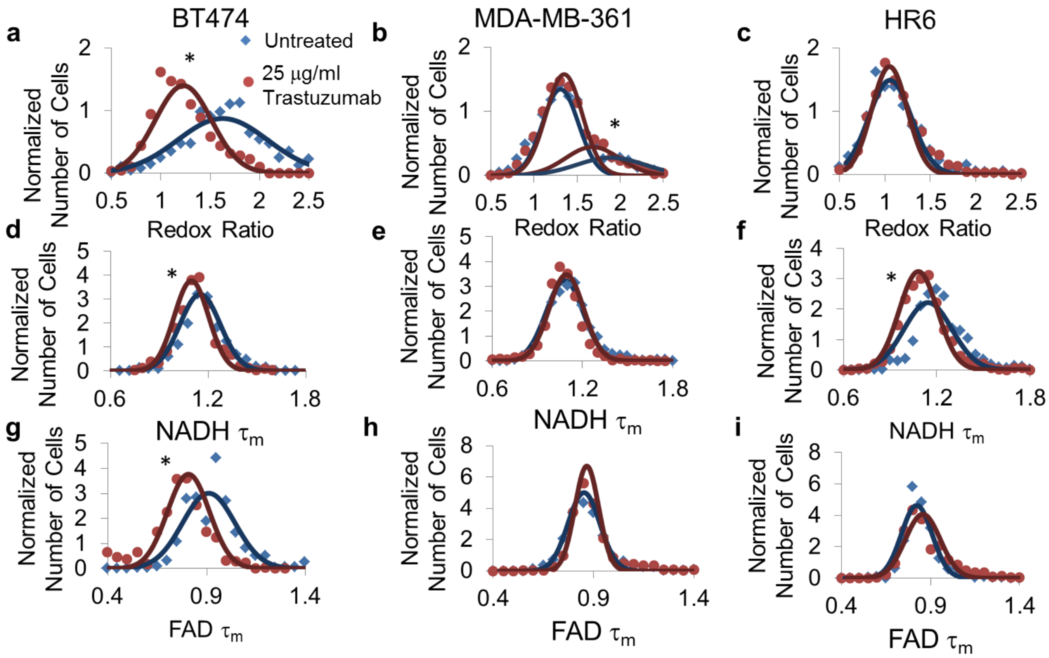

Figure A.6: Distribution density modeling of OMI endpoints for *in vitro* trastuzumab experiment. (a, c) Distribution density modeling reveals one population of cells in BT474 (a) and HR6 (c) in control (blue) and trastuzumab (red) treated cultures. (b) Distribution density modeling reveals two distinct populations of MDA-MB-361 cells for the redox ratio with a significant decrease in the mean of the minority peak (30% of cells) with trastuzumab treatment, suggesting trastuzumab response in a sub-population of cells. (d-i) Distribution density modeling of cellular NADH τ_m (d-f) and FAD τ_m (g-i) reveals one population of cells for control (blue) and trastuzumab (red) treated BT474 (d,g), MDA-MB-361 (e,h) and HR6 (f, i) cells. τ_m is the mean lifetime $(\tau_1*\alpha_1 + \tau_2*\alpha_2)$. * $P<0.05$

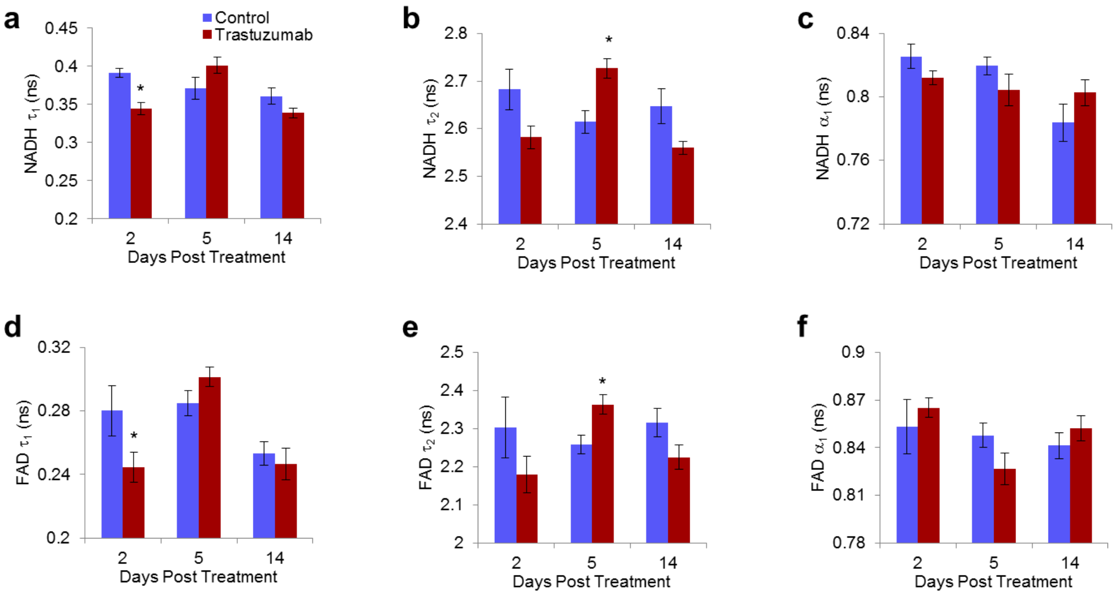

Figure A.7 Fluorescence lifetime components for BT474 xenografts. NADH (a-c) and FAD (d-f) lifetime components (τ_1, short lifetime; τ_2, long lifetime; and α_1, relative contribution of the short lifetime) for control IgG-treated and trastuzumab-treated (10 μg/kg, 2x weekly) BT474 xenografts, measured at 2, 5, and 14 days after treatment was initiated. $^*P<0.05$

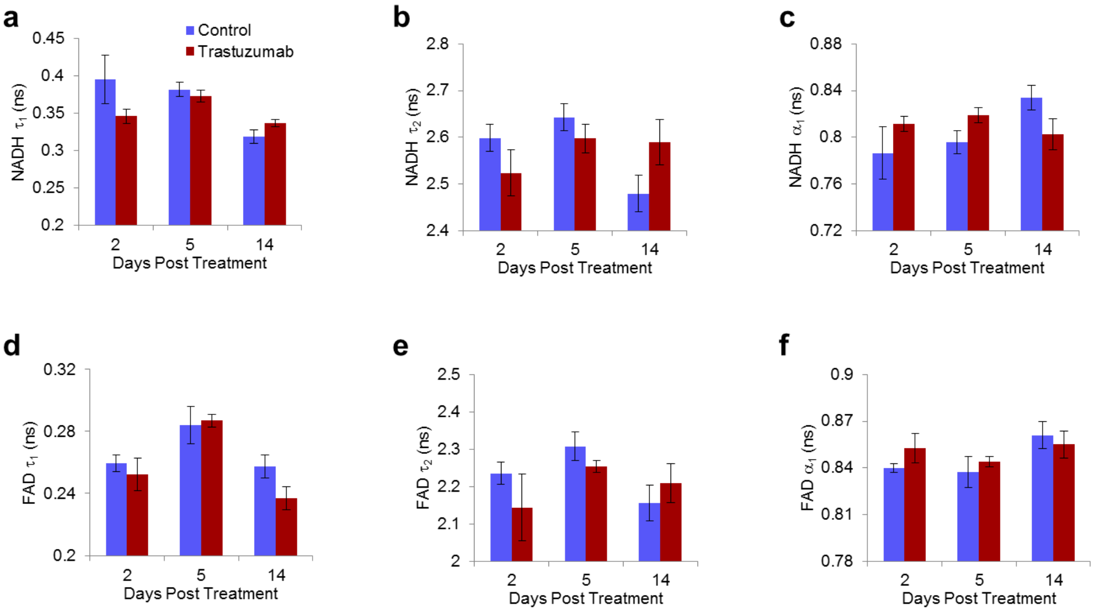

Figure A.8 Fluorescence lifetime components for HR6 xenografts. NADH (a-c) and FAD (d-f) lifetime components (τ_1, short lifetime; τ_2, long lifetime; and α_1, relative contribution of the short lifetime) for control IgG-treated and trastuzumab-treated (10 μg/kg, 2x weekly) HR6 xenografts, measured at 2, 5, and 14 days after treatment was initiated.

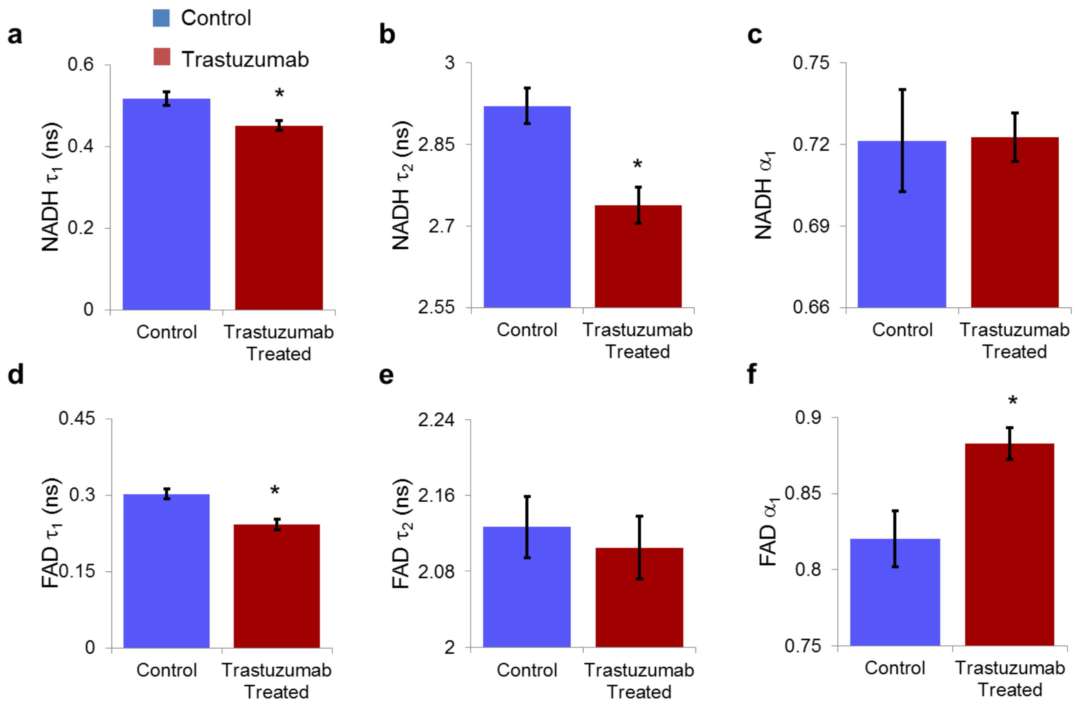

Figure A.9 Fluorescence lifetime components for MDA-MB-231 xenografts. NADH (a-c) and FAD (d-f) lifetime components (τ_1, short lifetime; τ_2, long lifetime; and $\alpha_{1,}$ relative contribution of the short lifetime) for control IgG-treated and trastuzumab-treated (10 µg/kg, 48 hours) MDA-MB-361 xenografts, measured 48h after treatment. * *P* <0.05

APPENDIX B

Supplementary Figures and Tables for Chapter 6

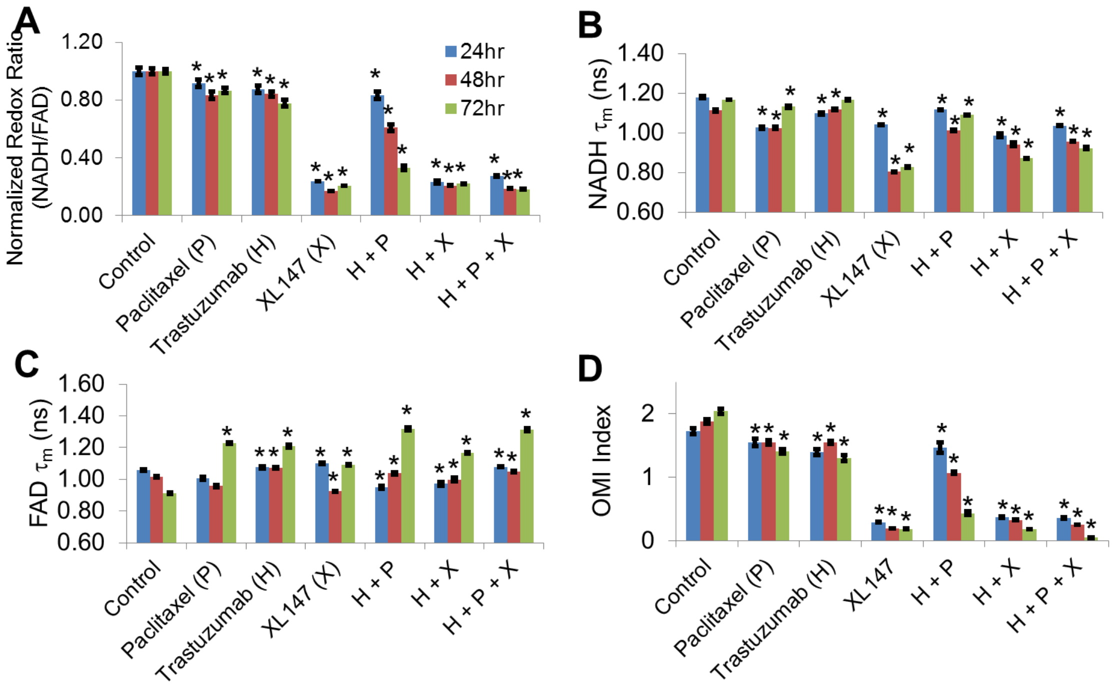

Figure B.1: OMI endpoints of organoids derived from a trastuzumab-responsive xenograft tumor. A. Redox ratio of BT474 xenograft-derived organoids treated with paclitaxel (P), trastuzumab (H), XL147 (X), and the combined drug treatments H+P, H+X, H+P+X at 24 (blue), 48 (red), and 72hr (green). B. NADH τ_m of BT474 xenograft-derived drug treated organoids at 24 (blue), 48 (red), and 72hr (green). C. FAD τ_m of BT474 xenograft-derived drug treated organoids at 24 (blue), 48 (red), and 72hr (green). D. OMI index (composite endpoint of weighted redox ratio, NADH τ_m, and FAD τ_m) of BT474 xenograft-derived drug treated organoids at 24 (blue), 48 (red), and 72hr (green). *$p<0.05$, for treated vs. control within a time point.

Table B.1: NADH and FAD lifetime component values of BT474-xenograft derived organoids (mean, standard deviation) from a two-component exponential fit of the fluorescence decay, ($I(t)=\alpha_1 \exp^{-t/\tau_1}+\alpha_2 \exp^{-t/\tau_2}+C$). Boxes shaded pink represent a significant decrease in mean value vs. control. Boxes shaded blue represent a significant increase in mean value vs. control. NADH τ_1/α_1 is attributed to free NADH, NADH τ_2/α_2 is attributed to bound NADH. FAD τ_1/α_1 is attributed to bound FAD, FAD τ_2/α_2 is attributed to free FAD.

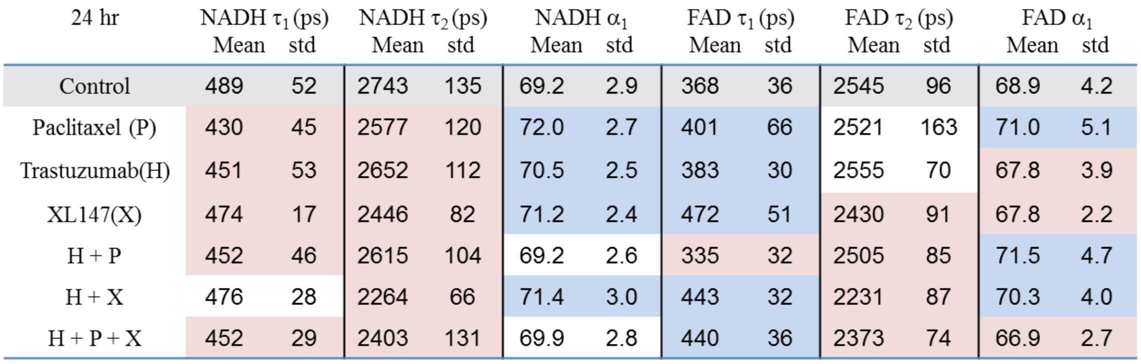

24 hr	NADH τ_1 (ps)		NADH τ_2 (ps)		NADH α_1		FAD τ_1 (ps)		FAD τ_2 (ps)		FAD α_1	
	Mean	std	Mean	std	Mean	std	Mean	std	Mean	std	Mean	std
Control	489	52	2743	135	69.2	2.9	368	36	2545	96	68.9	4.2
Paclitaxel (P)	430	45	2577	120	72.0	2.7	401	66	2521	163	71.0	5.1
Trastuzumab(H)	451	53	2652	112	70.5	2.5	383	30	2555	70	67.8	3.9
XL147(X)	474	17	2446	82	71.2	2.4	472	51	2430	91	67.8	2.2
H + P	452	46	2615	104	69.2	2.6	335	32	2505	85	71.5	4.7
H + X	476	28	2264	66	71.4	3.0	443	32	2231	87	70.3	4.0
H + P + X	452	29	2403	131	69.9	2.8	440	36	2373	74	66.9	2.7

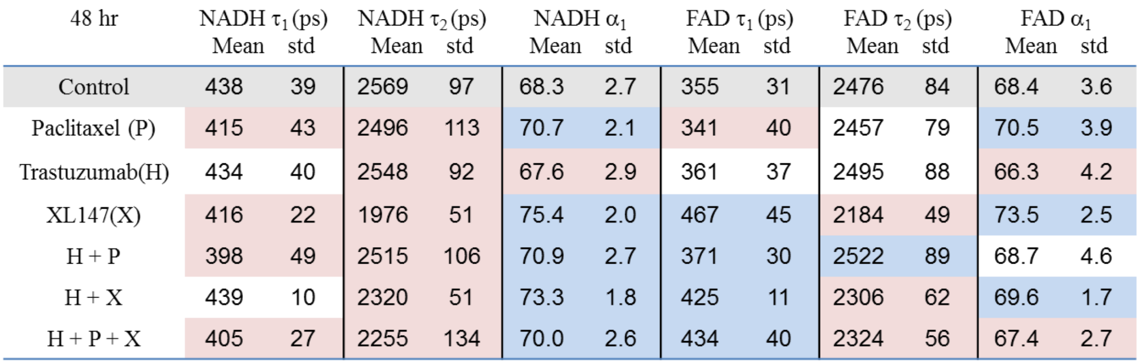

48 hr	NADH τ_1 (ps)		NADH τ_2 (ps)		NADH α_1		FAD τ_1 (ps)		FAD τ_2 (ps)		FAD α_1	
	Mean	std	Mean	std	Mean	std	Mean	std	Mean	std	Mean	std
Control	438	39	2569	97	68.3	2.7	355	31	2476	84	68.4	3.6
Paclitaxel (P)	415	43	2496	113	70.7	2.1	341	40	2457	79	70.5	3.9
Trastuzumab(H)	434	40	2548	92	67.6	2.9	361	37	2495	88	66.3	4.2
XL147(X)	416	22	1976	51	75.4	2.0	467	45	2184	49	73.5	2.5
H + P	398	49	2515	106	70.9	2.7	371	30	2522	89	68.7	4.6
H + X	439	10	2320	51	73.3	1.8	425	11	2306	62	69.6	1.7
H + P + X	405	27	2255	134	70.0	2.6	434	40	2324	56	67.4	2.7

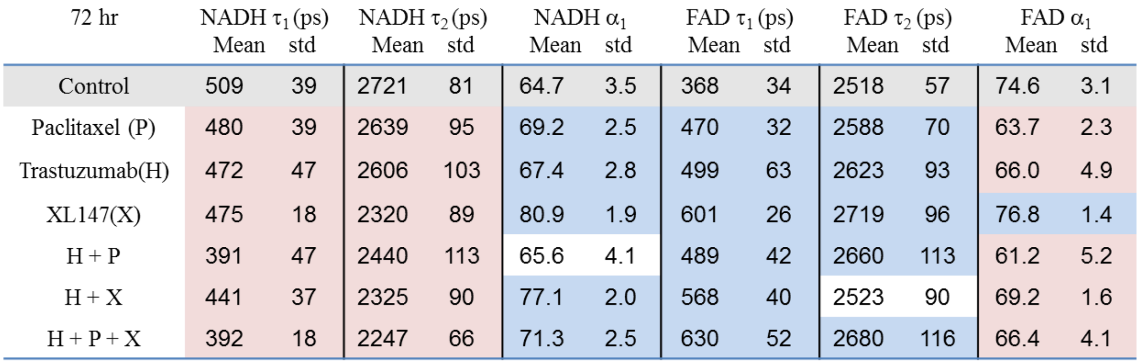

72 hr	NADH τ_1 (ps)		NADH τ_2 (ps)		NADH α_1		FAD τ_1 (ps)		FAD τ_2 (ps)		FAD α_1	
	Mean	std	Mean	std	Mean	std	Mean	std	Mean	std	Mean	std
Control	509	39	2721	81	64.7	3.5	368	34	2518	57	74.6	3.1
Paclitaxel (P)	480	39	2639	95	69.2	2.5	470	32	2588	70	63.7	2.3
Trastuzumab(H)	472	47	2606	103	67.4	2.8	499	63	2623	93	66.0	4.9
XL147(X)	475	18	2320	89	80.9	1.9	601	26	2719	96	76.8	1.4
H + P	391	47	2440	113	65.6	4.1	489	42	2660	113	61.2	5.2
H + X	441	37	2325	90	77.1	2.0	568	40	2523	90	69.2	1.6
H + P + X	392	18	2247	66	71.3	2.5	630	52	2680	116	66.4	4.1

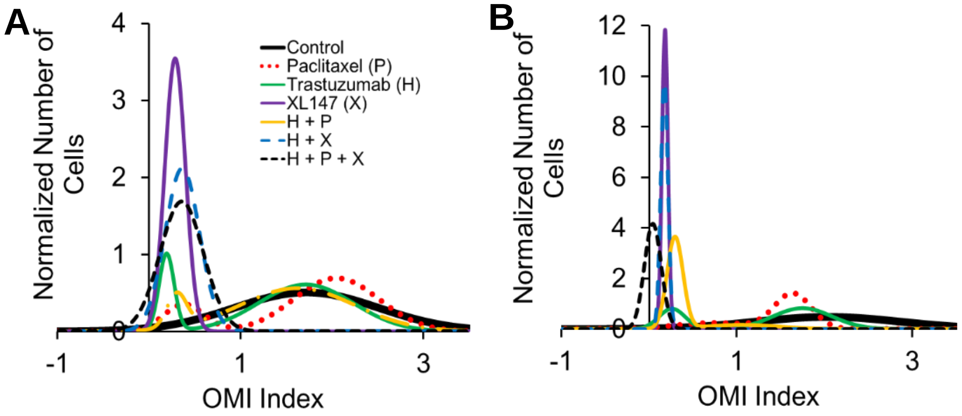

Figure B.2: Population modeling identifies heterogeneous drug responses of BT474 cells. A. Population density modeling of the mean OMI index per cell in control and treated BT474 organoids at 24 hr. B. Population density modeling of the OMI index for BT474 organoids treated for 72hr.

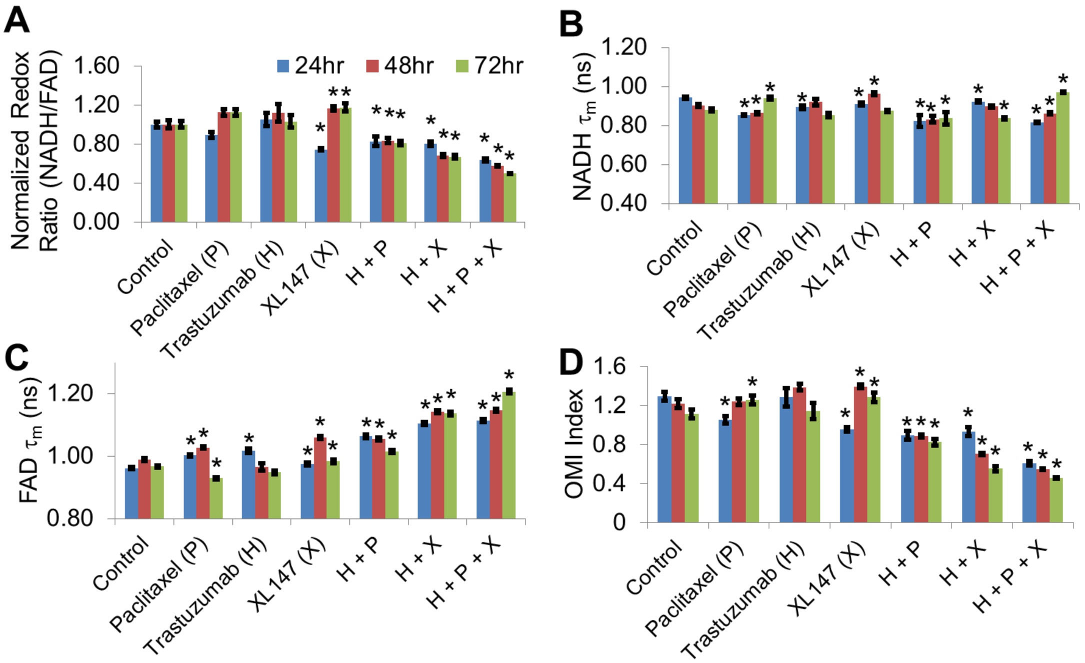

Figure B.3: OMI endpoints of organoids derived from a trastuzumab-resistant xenograft tumor. A. Redox ratio of HR6 xenograft-derived organoids treated with paclitaxel (P), trastuzumab (H), XL147 (X), and the combined drug treatments H+P, H+X, H+P+X at 24 (blue), 48 (red), and 72hr (green). B. NADH τ_m of HR6 xenograft-derived drug treated organoids at 24 (blue), 48 (red), and 72hr (green). C. FAD τ_m of HR6 xenograft-derived drug treated organoids at 24 (blue), 48 (red), and 72hr (green). D. OMI index (composite endpoint of weighted redox ratio, NADH τ_m, and FAD τ_m) of HR6 xenograft-derived drug treated organoids at 24 (blue), 48 (red), and 72hr (green). *$p<0.05$, for treated vs. control within a time point.

Table B.2: **NADH and FAD lifetime component values of HR6-xenograft derived organoids** (mean, standard deviation) from a two-component exponential fit of the fluorescence decay, ($I(t) = \alpha_1 \exp^{-t/\tau_1} + \alpha_2 \exp^{-t/\tau_2} + C$). Boxes shaded pink represent a significant decrease in mean value vs. control. Boxes shaded blue represent a significant increase in mean value vs. control. NADH τ_1/α_1 is attributed to free NADH, NADH τ_2/α_2 is attributed to bound NADH. FAD τ_1/α_1 is attributed to bound FAD, FAD τ_2/α_2 is attributed to free FAD.

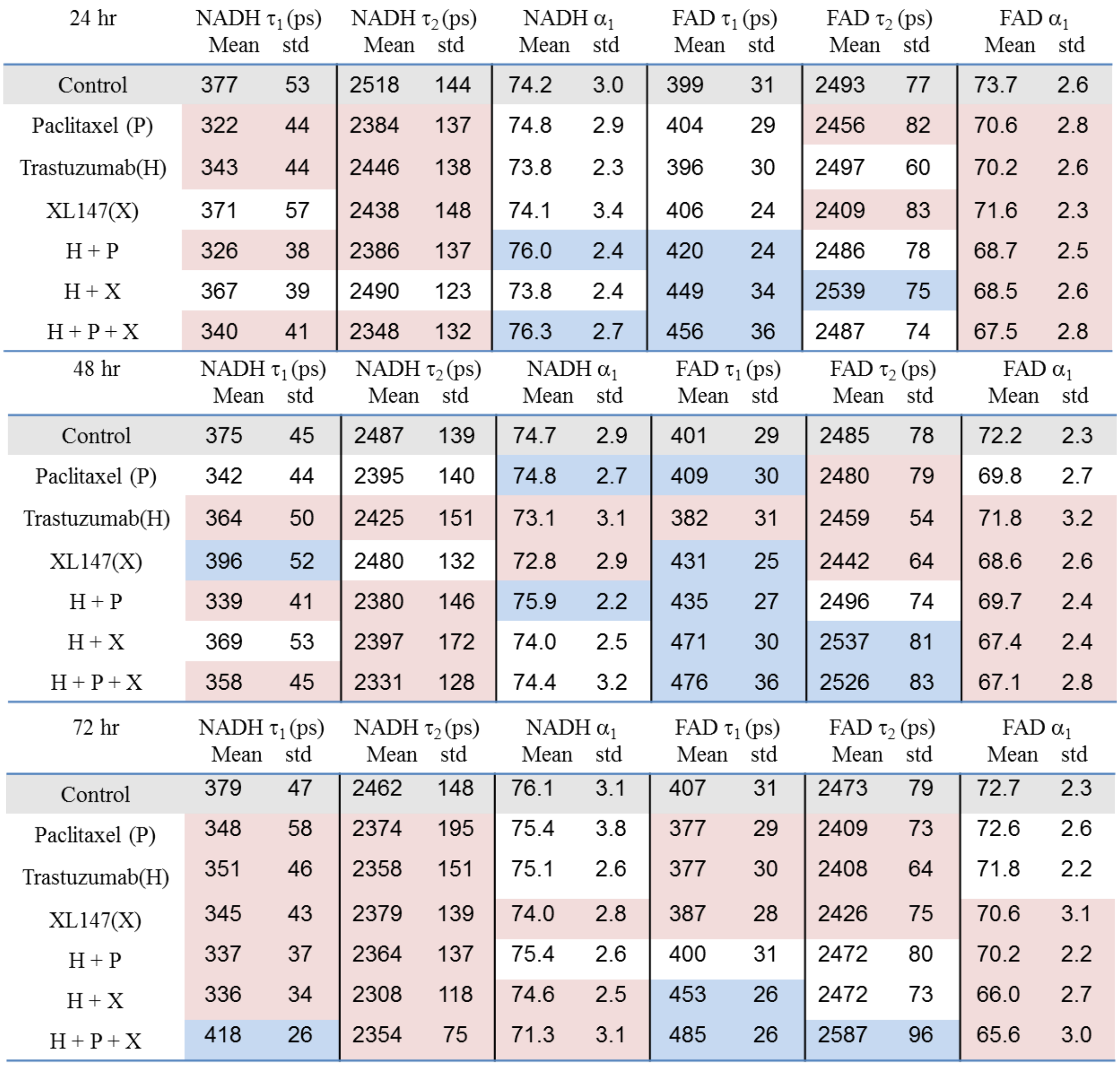

24 hr	NADH τ_1 (ps)		NADH τ_2 (ps)		NADH α_1		FAD τ_1 (ps)		FAD τ_2 (ps)		FAD α_1	
	Mean	std	Mean	std	Mean	std	Mean	std	Mean	std	Mean	std
Control	377	53	2518	144	74.2	3.0	399	31	2493	77	73.7	2.6
Paclitaxel (P)	322	44	2384	137	74.8	2.9	404	29	2456	82	70.6	2.8
Trastuzumab(H)	343	44	2446	138	73.8	2.3	396	30	2497	60	70.2	2.6
XL147(X)	371	57	2438	148	74.1	3.4	406	24	2409	83	71.6	2.3
H + P	326	38	2386	137	76.0	2.4	420	24	2486	78	68.7	2.5
H + X	367	39	2490	123	73.8	2.4	449	34	2539	75	68.5	2.6
H + P + X	340	41	2348	132	76.3	2.7	456	36	2487	74	67.5	2.8

48 hr	NADH τ_1 (ps)		NADH τ_2 (ps)		NADH α_1		FAD τ_1 (ps)		FAD τ_2 (ps)		FAD α_1	
	Mean	std	Mean	std	Mean	std	Mean	std	Mean	std	Mean	std
Control	375	45	2487	139	74.7	2.9	401	29	2485	78	72.2	2.3
Paclitaxel (P)	342	44	2395	140	74.8	2.7	409	30	2480	79	69.8	2.7
Trastuzumab(H)	364	50	2425	151	73.1	3.1	382	31	2459	54	71.8	3.2
XL147(X)	396	52	2480	132	72.8	2.9	431	25	2442	64	68.6	2.6
H + P	339	41	2380	146	75.9	2.2	435	27	2496	74	69.7	2.4
H + X	369	53	2397	172	74.0	2.5	471	30	2537	81	67.4	2.4
H + P + X	358	45	2331	128	74.4	3.2	476	36	2526	83	67.1	2.8

72 hr	NADH τ_1 (ps)		NADH τ_2 (ps)		NADH α_1		FAD τ_1 (ps)		FAD τ_2 (ps)		FAD α_1	
	Mean	std	Mean	std	Mean	std	Mean	std	Mean	std	Mean	std
Control	379	47	2462	148	76.1	3.1	407	31	2473	79	72.7	2.3
Paclitaxel (P)	348	58	2374	195	75.4	3.8	377	29	2409	73	72.6	2.6
Trastuzumab(H)	351	46	2358	151	75.1	2.6	377	30	2408	64	71.8	2.2
XL147(X)	345	43	2379	139	74.0	2.8	387	28	2426	75	70.6	3.1
H + P	337	37	2364	137	75.4	2.6	400	31	2472	80	70.2	2.2
H + X	336	34	2308	118	74.6	2.5	453	26	2472	73	66.0	2.7
H + P + X	418	26	2354	75	71.3	3.1	485	26	2587	96	65.6	3.0

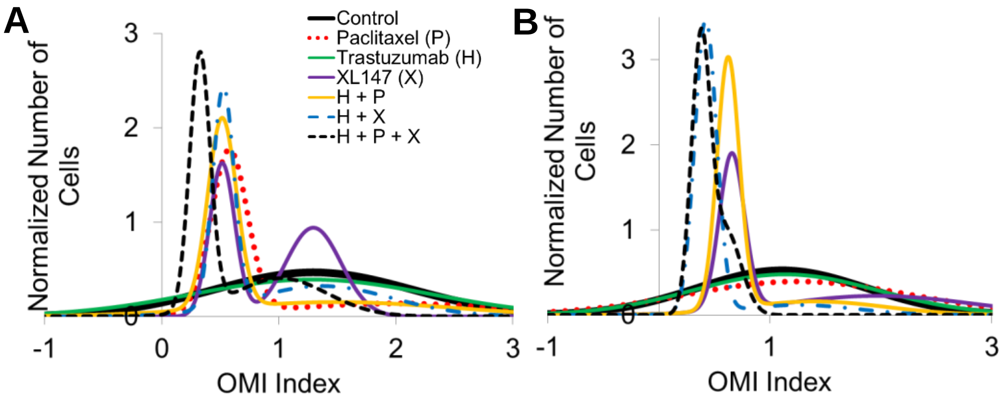

Figure B.4: **Population modeling identifies heterogeneous drug responses of HR6 cells.** A. Population density modeling of the mean OMI index per cell in control and treated HR6 organoids at 24 hr. B. Population density modeling of the OMI index for HR6 organoids treated for 72hr.

Table B.3: Grade, proliferation rate, estrogen receptor expression, progesterone receptor expression, and HER2 receptor expression of the patient samples.

Sample	Grade	Proliferative rate	ER intensity (% cells)	PR intensity (% cells)	Her2 FISH	Her2:Cep17 ratio	Figures
1	high	high	3+ (95)	3+ (95)	Not Amp	1.7	Fig. 5A-C, Sup. Fig. 3
2	Inter-mediate	Intermediate	3+ (90)	3+ (90)	Not Amp	1.4	Fig. 5D,E Sup. Fig. 4
3	high	high	3+ (95)	3+ (99)	Not Amp	1	Fig. 5F,G Sup. Fig. 5
4	high	Intermediate	3+ (95)	3+ (70)	Not Amp	1.1	Fig. 5H,I Sup. Fig. 6
5	high	high	0 (0)	0 (0)	Amp	7.95	Fig. 6A,B Sup. Fig. 7
6	high	high	2+ (3)	2+(3)	Not Amp	0.9	Fig. 6C,D Sup. Fig. 8

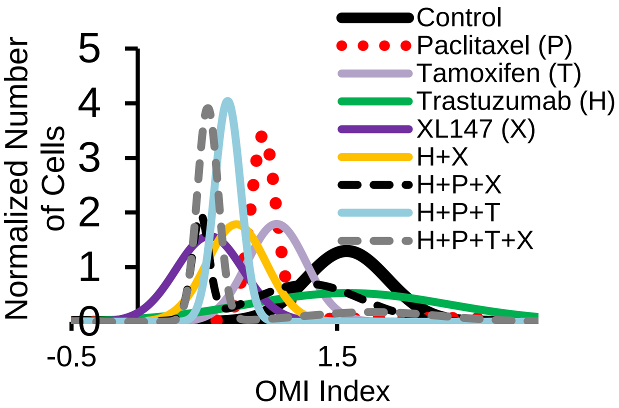

Figure B.5: **Population modeling identifies heterogeneous drug responses of organoids from patient sample #1 (ER+/HER2-).** Population density modeling of the mean OMI index per cell in control and treated organoids derived from patient sample #1 (ER+/HER2+) at 72 hr.

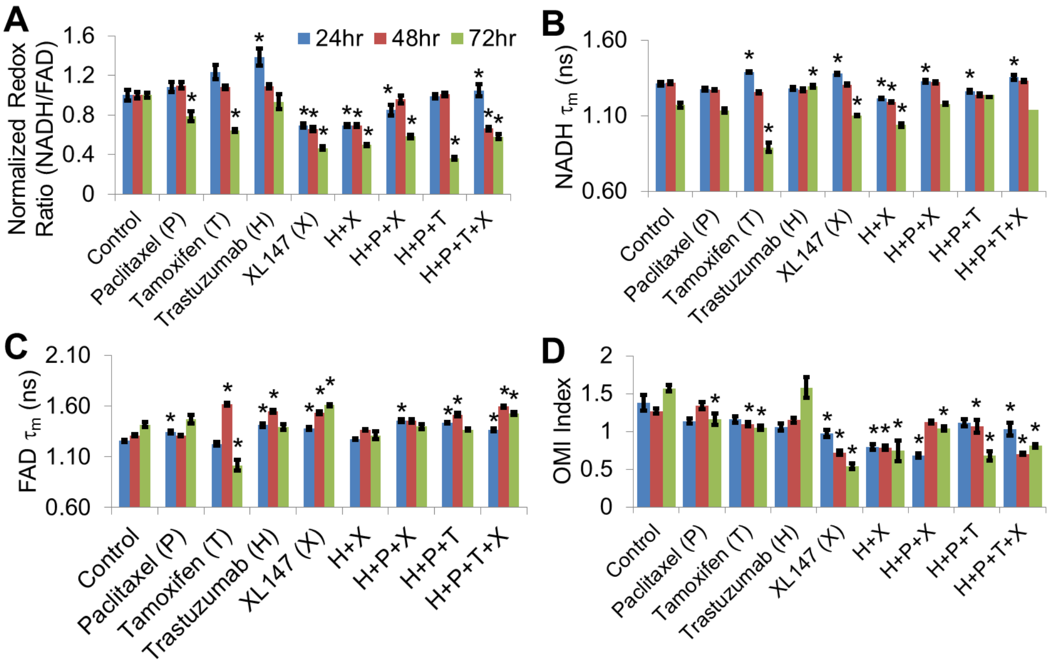

Figure B.6: OMI endpoints of organoids derived from a ER+ primary tumor. A. Redox ratio of organoids derived from an ER+ primary tumor treated with paclitaxel (P), tamoxifen (T), trastuzumab (H), XL147 (X), and the combined drug treatments H+X, H+P+X, H+P+T, and H+P+T+X at 24 (blue), 48 (red), and 72hr (green). B. NADH τ_m of organoids derived from an ER+ primary tumor at 24 (blue), 48 (red), and 72hr (green). C. FAD τ_m of organoids derived from an ER+ primary tumor at 24 (blue), 48 (red), and 72hr (green). D. OMI index (composite endpoint of weighted redox ratio, NADH τ_m, and FAD τ_m) of organoids derived from an ER+ primary tumor at 24 (blue), 48 (red), and 72hr (green). $^*p<0.05$, for treated vs. control within a time point.

Table B.4: **NADH and FAD lifetime component values of organoids derived from an ER+ primary tumor** (mean, standard deviation). Boxes shaded pink represent a significant decrease in mean value vs. control. Boxes shaded blue represent a significant increase in mean value vs. control. NADH τ_1/α_1 is attributed to free NADH, NADH τ_2/α_2 is attributed to bound NADH. FAD τ_1/α_1 is attributed to bound FAD, FAD τ_2/α_2 is attributed to free FAD.

24 hr	NADH τ_1 (ps)		NADH τ_2 (ps)		NADH α_1		FAD τ_1 (ps)		FAD τ_2 (ps)		FAD α_1	
	Mean	std	Mean	std	Mean	std	Mean	std	Mean	std	Mean	std
Control	566	81	2715	142	64.5	2.3	428	53	2676	124	62.7	4.1
Paclitaxel (P)	518	50	2623	110	63.2	2.6	466	78	2693	148	60.0	3.9
Tamoxifen (T)	571	128	2745	247	61.7	3.1	428	81	2613	157	63.0	5.5
Trastuzumab(H)	521	42	2579	112	62.5	3.6	505	60	2759	125	59.2	5.5
XL147 (X)	643	42	2499	176	60.1	1.8	610	71	2645	102	62.1	4.3
H + X	537	34	2418	135	63.5	3.2	493	33	2560	85	62.0	4.6
H + P +X	584	50	2516	143	59.7	3.7	604	76	2711	117	59.9	3.9
H + P + T	470	25	2551	121	61.5	2.2	493	39	2714	90	57.2	2.2
H + P + T + X	573	54	2585	160	60.7	2.8	547	76	2688	141	63.3	5.8

48 hr	NADH τ_1 (ps)		NADH τ_2 (ps)		NADH α_1		FAD τ_1 (ps)		FAD τ_2 (ps)		FAD α_1	
	Mean	std	Mean	std	Mean	std	Mean	std	Mean	std	Mean	std
Control	545	42	2596	110	61.7	1.8	454	40	2693	98	61.4	2.9
Paclitaxel (P)	565	32	2643	116	65.0	2.6	496	45	2746	116	63.0	4.2
Tamoxifen (T)	476	33	2479	65	60.6	2.4	652	84	2937	171	57.0	2.2
Trastuzumab(H)	493	54	2466	136	61.5	4.7	615	96	2865	187	58.3	4.5
XL147 (X)	595	26	2465	112	61.7	2.9	733	77	2852	131	61.9	2.7
H + X	523	31	2395	91	64.0	3.3	553	46	2639	91	60.8	4.5
H + P +X	573	36	2524	147	61.1	4.0	660	101	2772	149	62.2	4.7
H + P + T	480	24	2437	57	60.9	2.7	557	51	2771	95	56.3	2.2
H + P + T + X	564	33	2465	73	59.4	1.9	723	59	2871	102	59.0	2.5

72 hr	NADH τ_1 (ps)		NADH τ_2 (ps)		NADH α_1		FAD τ_1 (ps)		FAD τ_2 (ps)		FAD α_1	
	Mean	std	Mean	std	Mean	std	Mean	std	Mean	std	Mean	std
Control	446	54	2463	104	63.9	3.6	535	94	2788	166	61.4	4.5
Paclitaxel (P)	429	48	2403	94	63.7	3.4	567	144	2820	287	60.0	9.4
Tamoxifen (T)	347	230	2471	384	74.5	5.3	358	246	2627	306	70.8	8.8
Trastuzumab(H)	577	56	2826	187	67.2	2.3	546	68	2846	168	62.3	4.9
XL147 (X)	428	17	2282	63	63.6	2.6	778	57	2875	95	60.2	1.7
H + X	392	34	2267	70	65.5	3.8	535	135	2639	145	62.9	7.3
H + P +X	475	21	2461	127	64.3	3.5	676	119	2755	200	65.6	4.4
H + P + T	622	51	2866	164	71.6	1.7	554	34	2807	111	63.0	1.9
H + P + T + X	416	22	2348	123	62.1	2.9	704	91	2870	150	61.6	4.8

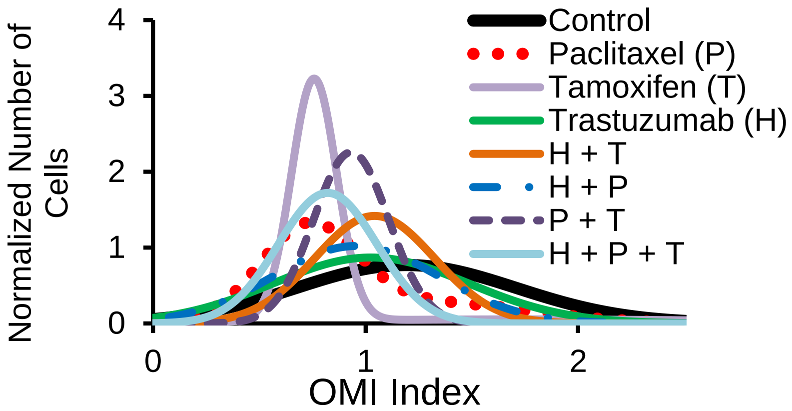

Figure B.7: **Population modeling identifies heterogeneous drug responses of organoids from patient sample #2 (ER+/HER2-).** Population density modeling of the mean OMI index per cell in control and treated organoids derived from patient sample #2 (ER+/HER2+) at 72 hr.

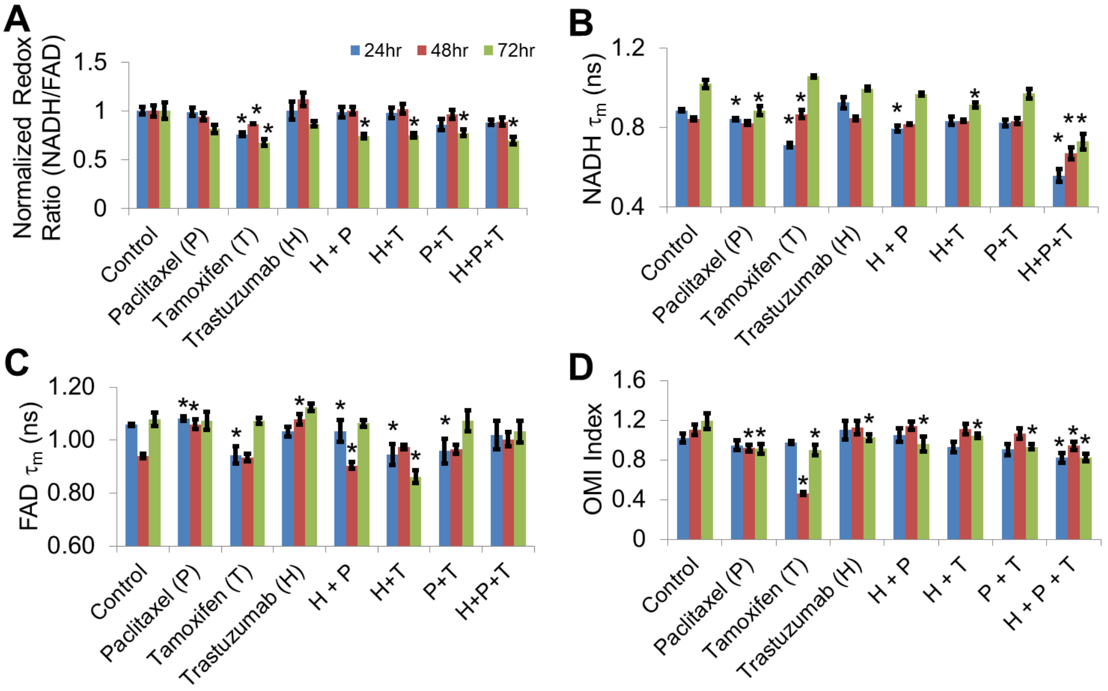

Figure B.8: OMI endpoints of organoids derived from a second ER+ primary tumor. A. Redox ratio of organoids derived from a second ER+ primary tumor treated with paclitaxel (P), tamoxifen (T), trastuzumab (H), and the combined drug treatments H+P, H+T, P+T, and H+P+T at 24 (blue), 48 (red), and 72hr (green). B. NADH τ_m at 24 (blue), 48 (red), and 72hr (green). C. FAD τ_m at 24 (blue), 48 (red), and 72hr (green). D. OMI index (composite endpoint of weighted redox ratio, NADH τ_m, and FAD τ_m) at 24 (blue), 48 (red), and 72hr (green). *$p<0.05$, for treated vs. control within a time point.

Table B.5: **NADH and FAD lifetime component values of organoids derived from a second ER+ primary tumor** (mean, standard deviation). Boxes shaded pink represent a significant decrease in mean value vs. control. Boxes shaded blue represent a significant increase in mean value vs. control. NADH τ_1/α_1 is attributed to free NADH, NADH τ_2/α_2 is attributed to bound NADH. FAD τ_1/α_1 is attributed to bound FAD, FAD τ_2/α_2 is attributed to free FAD.

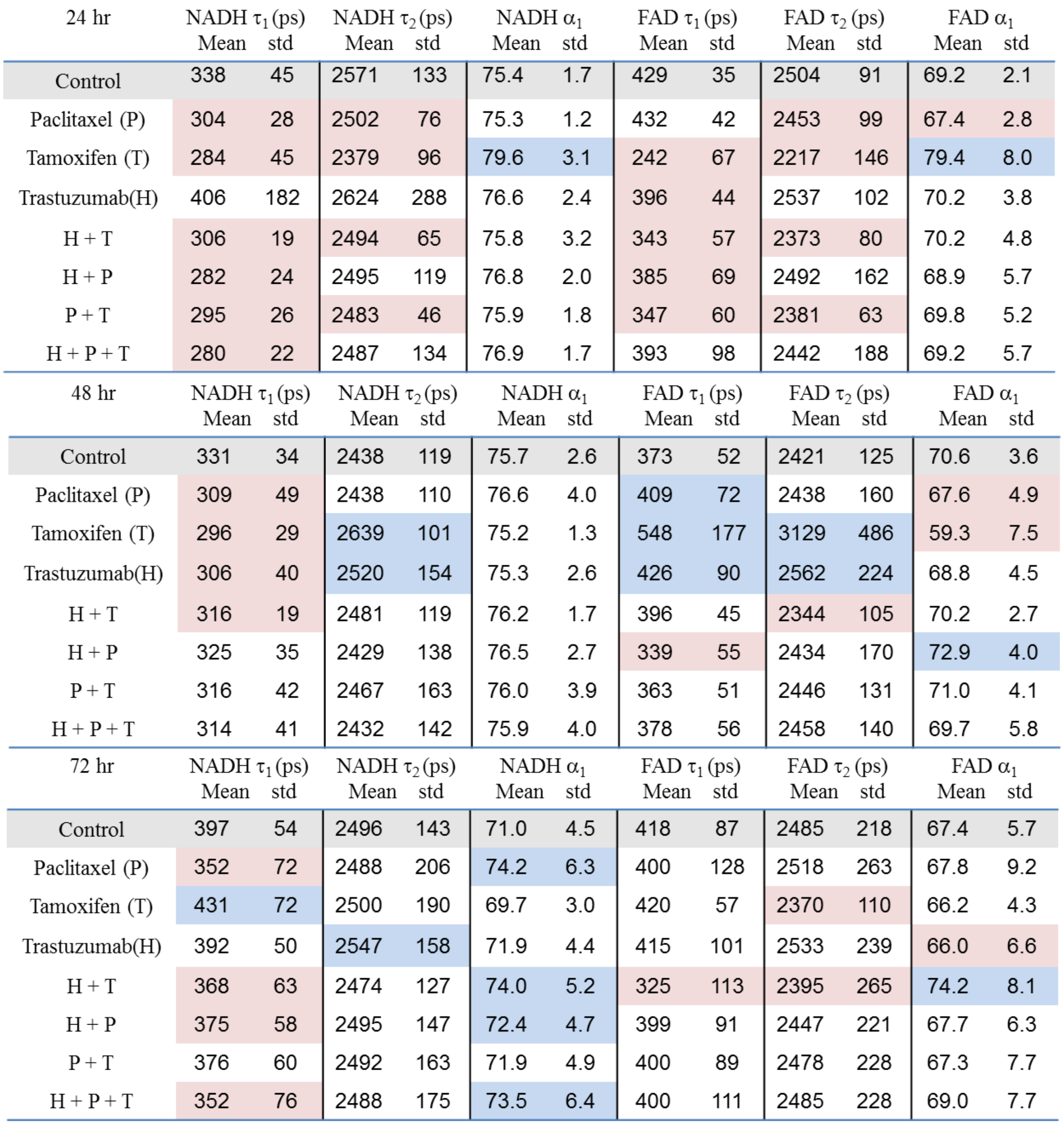

24 hr	NADH τ_1 (ps)		NADH τ_2 (ps)		NADH α_1		FAD τ_1 (ps)		FAD τ_2 (ps)		FAD α_1	
	Mean	std	Mean	std	Mean	std	Mean	std	Mean	std	Mean	std
Control	338	45	2571	133	75.4	1.7	429	35	2504	91	69.2	2.1
Paclitaxel (P)	304	28	2502	76	75.3	1.2	432	42	2453	99	67.4	2.8
Tamoxifen (T)	284	45	2379	96	79.6	3.1	242	67	2217	146	79.4	8.0
Trastuzumab(H)	406	182	2624	288	76.6	2.4	396	44	2537	102	70.2	3.8
H + T	306	19	2494	65	75.8	3.2	343	57	2373	80	70.2	4.8
H + P	282	24	2495	119	76.8	2.0	385	69	2492	162	68.9	5.7
P + T	295	26	2483	46	75.9	1.8	347	60	2381	63	69.8	5.2
H + P + T	280	22	2487	134	76.9	1.7	393	98	2442	188	69.2	5.7

48 hr	NADH τ_1 (ps)		NADH τ_2 (ps)		NADH α_1		FAD τ_1 (ps)		FAD τ_2 (ps)		FAD α_1	
	Mean	std	Mean	std	Mean	std	Mean	std	Mean	std	Mean	std
Control	331	34	2438	119	75.7	2.6	373	52	2421	125	70.6	3.6
Paclitaxel (P)	309	49	2438	110	76.6	4.0	409	72	2438	160	67.6	4.9
Tamoxifen (T)	296	29	2639	101	75.2	1.3	548	177	3129	486	59.3	7.5
Trastuzumab(H)	306	40	2520	154	75.3	2.6	426	90	2562	224	68.8	4.5
H + T	316	19	2481	119	76.2	1.7	396	45	2344	105	70.2	2.7
H + P	325	35	2429	138	76.5	2.7	339	55	2434	170	72.9	4.0
P + T	316	42	2467	163	76.0	3.9	363	51	2446	131	71.0	4.1
H + P + T	314	41	2432	142	75.9	4.0	378	56	2458	140	69.7	5.8

72 hr	NADH τ_1 (ps)		NADH τ_2 (ps)		NADH α_1		FAD τ_1 (ps)		FAD τ_2 (ps)		FAD α_1	
	Mean	std	Mean	std	Mean	std	Mean	std	Mean	std	Mean	std
Control	397	54	2496	143	71.0	4.5	418	87	2485	218	67.4	5.7
Paclitaxel (P)	352	72	2488	206	74.2	6.3	400	128	2518	263	67.8	9.2
Tamoxifen (T)	431	72	2500	190	69.7	3.0	420	57	2370	110	66.2	4.3
Trastuzumab(H)	392	50	2547	158	71.9	4.4	415	101	2533	239	66.0	6.6
H + T	368	63	2474	127	74.0	5.2	325	113	2395	265	74.2	8.1
H + P	375	58	2495	147	72.4	4.7	399	91	2447	221	67.7	6.3
P + T	376	60	2492	163	71.9	4.9	400	89	2478	228	67.3	7.7
H + P + T	352	76	2488	175	73.5	6.4	400	111	2485	228	69.0	7.7

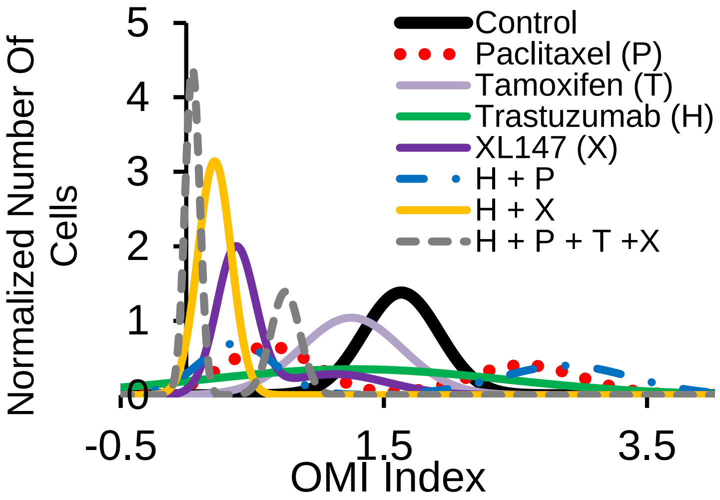

Figure B.9: **Population modeling identifies heterogeneous drug responses of organoids from patient sample #3 (ER+/HER2-).** Population density modeling of the mean OMI index per cell in control and treated organoids derived from patient sample #3 (ER+/HER2+) at 24 hr.

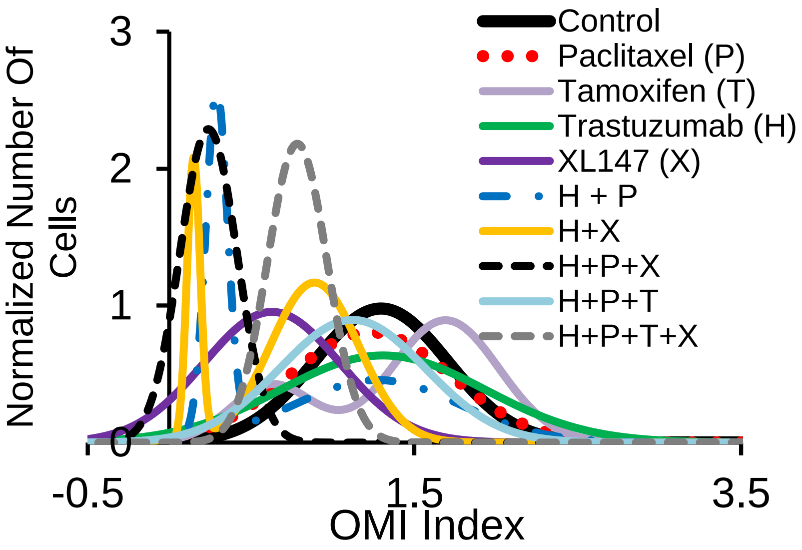

Figure B.10: **Population modeling identifies heterogeneous drug responses of organoids from patient sample #4 (ER+/HER2-).** Population density modeling of the mean OMI index per cell in control and treated organoids derived from patient sample #4 (ER+/HER2+) at 72 hr.

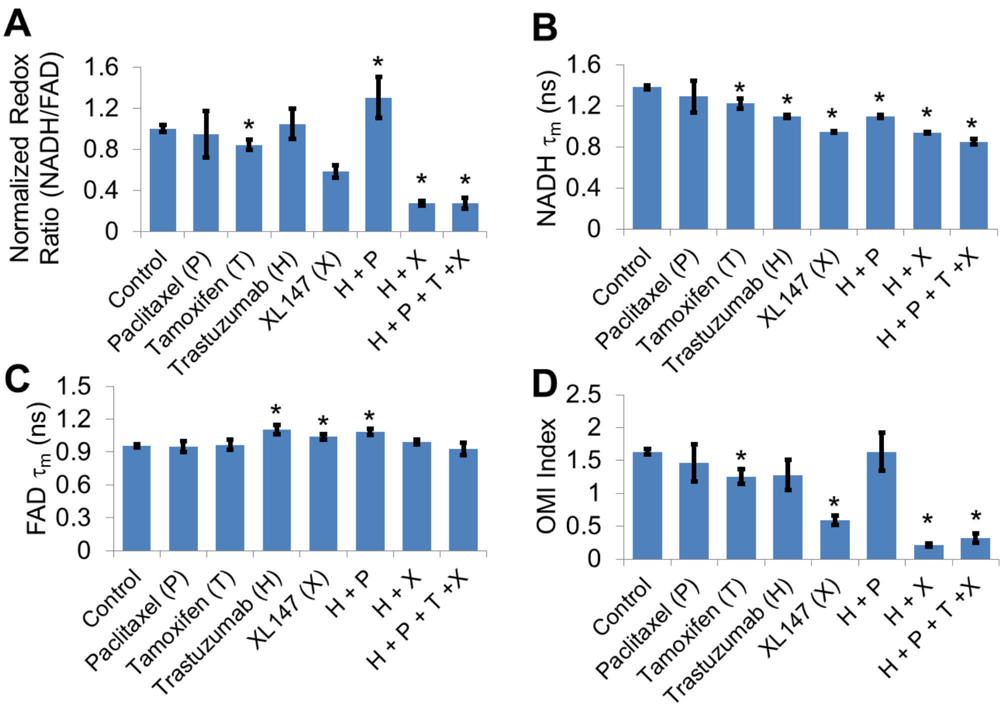

Figure B.11: OMI endpoints of organoids derived from a third ER+ primary tumor. A. Redox ratio of organoids derived from a third ER+ primary tumor treated with paclitaxel (P), tamoxifen (T), trastuzumab (H), XL147 (X) and the combined drug treatments H+P, H+X, and H+P+T+X at 24hr. B. NADH τ_m of these organoids at 24hr. C. FAD τ_m of these organoids at 24hr. D. OMI index (composite endpoint of weighted redox ratio, NADH τ_m, and FAD τ_m) at 24hr. *p<0.05, for treated vs. control.

Table B.6: **NADH and FAD lifetime component values of organoids derived from a third ER+ primary tumor** (mean, standard deviation). Boxes shaded pink represent a significant decrease in mean value vs. control. Boxes shaded blue represent a significant increase in mean value vs. control. NADH τ_1/α_1 is attributed to free NADH, NADH τ_2/α_2 is attributed to bound NADH. FAD τ_1/α_1 is attributed to bound FAD, FAD τ_2/α_2 is attributed to free FAD.

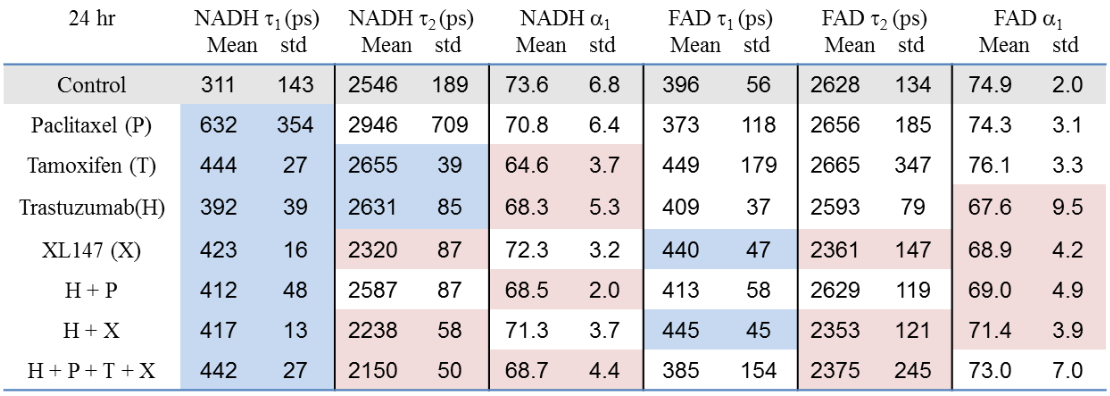

24 hr	NADH τ_1 (ps)		NADH τ_2 (ps)		NADH α_1		FAD τ_1 (ps)		FAD τ_2 (ps)		FAD α_1	
	Mean	std	Mean	std	Mean	std	Mean	std	Mean	std	Mean	std
Control	311	143	2546	189	73.6	6.8	396	56	2628	134	74.9	2.0
Paclitaxel (P)	632	354	2946	709	70.8	6.4	373	118	2656	185	74.3	3.1
Tamoxifen (T)	444	27	2655	39	64.6	3.7	449	179	2665	347	76.1	3.3
Trastuzumab(H)	392	39	2631	85	68.3	5.3	409	37	2593	79	67.6	9.5
XL147 (X)	423	16	2320	87	72.3	3.2	440	47	2361	147	68.9	4.2
H + P	412	48	2587	87	68.5	2.0	413	58	2629	119	69.0	4.9
H + X	417	13	2238	58	71.3	3.7	445	45	2353	121	71.4	3.9
H + P + T + X	442	27	2150	50	68.7	4.4	385	154	2375	245	73.0	7.0

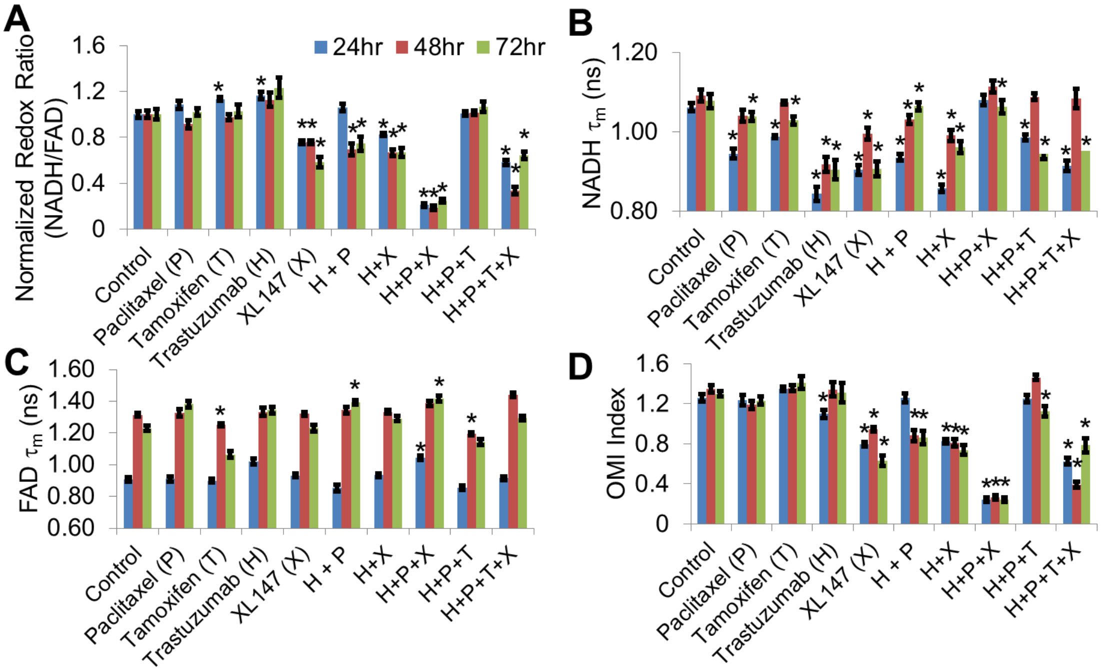

Figure B.12: OMI endpoints of organoids derived from a fourth ER+ primary tumor. A. Redox ratio of organoids derived from a fourth ER+ primary tumor treated with paclitaxel (P), tamoxifen (T), trastuzumab (H), XL147 (X) and the combined drug treatments H+P, H+X, H+P+X, H+P+T, and H+P+T+X at 24 (blue), 48 (red), and 72hr (green). B. NADH τ_m of these organoids at 24 (blue), 48 (red), and 72hr (green). C. FAD τ_m at 24 (blue), 48 (red), and 72hr (green). D. OMI index (composite endpoint of weighted redox ratio, NADH τ_m, and FAD τ_m) at 24 (blue), 48 (red), and 72hr (green). *$p<0.05$, for treated vs. control within a time point.

Table B.7: **NADH and FAD lifetime component values of organoids derived from a fourth ER+ primary tumor** (mean, standard deviation). Boxes shaded pink represent a significant decrease in mean value vs. control. Boxes shaded blue represent a significant increase in mean value vs. control. NADH τ_1/α_1 is attributed to free NADH, NADH τ_2/α_2 is attributed to bound NADH. FAD τ_1/α_1 is attributed to bound FAD, FAD τ_2/α_2 is attributed to free FAD.

24 hr	NADH τ_1 (ps)		NADH τ_2 (ps)		NADH α_1		FAD τ_1 (ps)		FAD τ_2 (ps)		FAD α_1	
	Mean	std	Mean	std	Mean	std	Mean	std	Mean	std	Mean	std
Control	475	13	2918	59	76.0	2.1	293	30	2627	101	73.2	3.0
Paclitaxel (P)	431	15	2722	58	77.6	2.8	291	43	2561	142	72.4	3.4
Tamoxifen (T)	441	17	2758	53	76.4	3.6	289	36	2560	131	72.8	2.9
Trastuzumab(H)	421	13	2664	74	81.3	3.7	326	46	2594	107	68.8	3.1
XL147 (X)	426	13	2683	75	78.9	3.9	323	31	2509	103	71.7	2.9
H + P	425	17	2778	83	78.3	3.7	293	70	2516	204	74.6	5.1
H + X	417	15	2678	75	80.6	3.2	313	39	2495	115	71.2	3.2
H + P +X	450	18	2578	171	69.7	6.6	359	25	2467	74	67.4	3.6
H + P + T	440	13	2764	57	76.6	2.3	271	36	2535	116	73.8	4.4
H + P + T + X	431	12	2749	77	79.2	2.4	327	25	2434	87	71.7	2.7

48 hr	NADH τ_1 (ps)		NADH τ_2 (ps)		NADH α_1		FAD τ_1 (ps)		FAD τ_2 (ps)		FAD α_1	
	Mean	std	Mean	std	Mean	std	Mean	std	Mean	std	Mean	std
Control	517	23	2934	70	76.2	3.8	536	57	2966	156	66.1	3.5
Paclitaxel (P)	475	36	2769	89	75.3	5.3	565	92	2966	265	67.0	5.8
Tamoxifen (T)	485	25	2821	54	74.8	4.0	515	40	2884	125	67.8	3.8
Trastuzumab(H)	448	21	2710	73	79.3	3.9	561	82	2918	210	65.7	3.2
XL147 (X)	475	28	2764	73	77.3	3.5	584	46	2883	144	66.7	2.8
H + P	444	42	2742	131	74.1	8.1	551	98	2875	236	64.6	4.8
H + X	458	20	2717	100	76.1	7.1	605	62	2878	188	66.7	5.7
H + P +X	472	13	2581	164	68.9	6.7	610	49	2732	104	63.0	3.2
H + P + T	480	14	2834	48	74.1	2.5	493	54	2897	155	69.7	3.2
H + P + T + X	464	19	2645	128	71.0	9.1	616	56	2817	119	61.7	3.6

72 hr	NADH τ_1 (ps)		NADH τ_2 (ps)		NADH α_1		FAD τ_1 (ps)		FAD τ_2 (ps)		FAD α_1	
	Mean	std	Mean	std	Mean	std	Mean	std	Mean	std	Mean	std
Control	475	54	2815	137	74.2	4.5	506	71	2908	207	69.1	4
Paclitaxel (P)	516	136	2782	204	73.8	4.2	648	200	3134	406	68.9	4.2
Tamoxifen (T)	414	59	2658	130	72.7	5.6	433	89	2702	214	71.6	4.7
Trastuzumab(H)	400	17	2585	73	77	6.8	550	85	2922	265	65.1	5.3
XL147 (X)	398	39	2551	100	76.3	6.5	543	91	2730	173	67.8	5.9
H + P	420	35	2659	109	70.9	7.8	590	92	2940	276	64.5	6.2
H + X	407	21	2602	91	74.6	6.4	554	45	2779	119	65.8	5.7
H + P +X	454	24	2572	147	70.6	7.4	644	68	2783	140	63.2	3.6
H + P + T	405	23	2597	93	75.3	5.2	464	85	2746	225	69.4	5.4
H + P + T + X	444	23	2735	105	77.7	5	590	52	2791	130	66.9	3.5

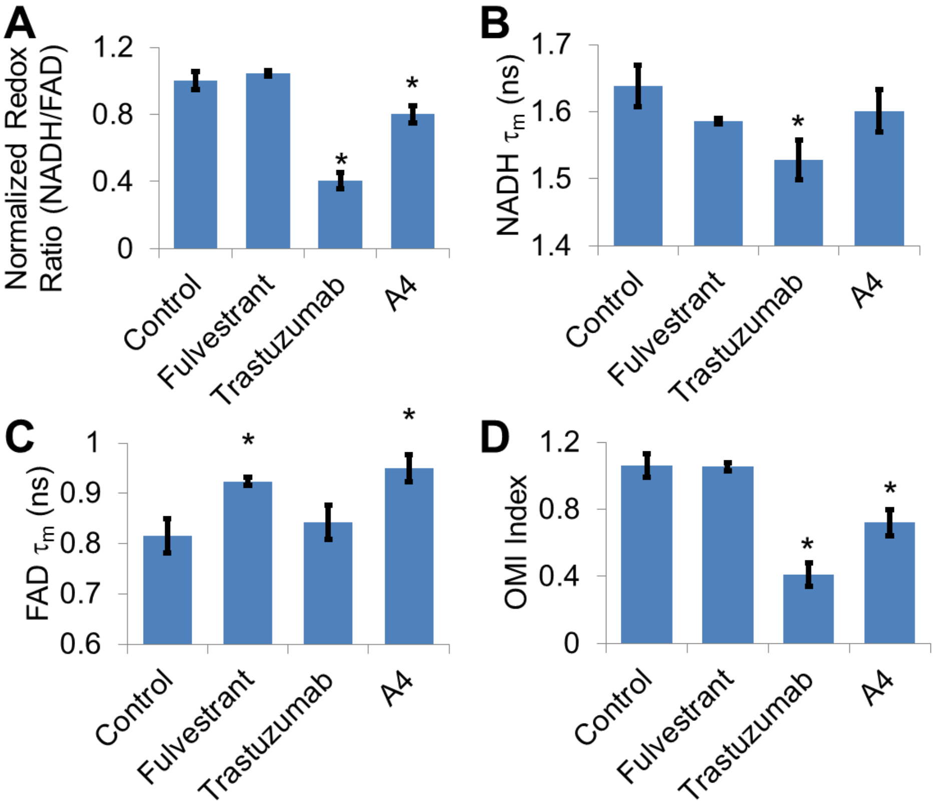

Figure B.13: OMI endpoints of organoids derived from a HER2+ primary tumor. A. Redox ratio of organoids derived from a HER2+ primary tumor treated with fulvestrant, trastuzumab, and A4 at 24hr. B. NADH τ_m of these organoids at 24hr. C. FAD τ_m at 24hr. D. OMI index (composite endpoint of weighted redox ratio, NADH τ_m, and FAD τ_m) at 24hr. *$p<0.05$, for treated vs. control.

Table B.8: **NADH and FAD lifetime component values of organoids derived from a HER2+ primary tumor** (mean, standard deviation). Boxes shaded pink represent a significant decrease in mean value vs. control. Boxes shaded blue represent a significant increase in mean value vs. control. NADH τ_1/α_1 is attributed to free NADH, NADH τ_2/α_2 is attributed to bound NADH. FAD τ_1/α_1 is attributed to bound FAD, FAD τ_2/α_2 is attributed to free FAD.

	NADH τ_1 (ps)		NADH τ_2 (ps)		NADH α_1		FAD τ_1 (ps)		FAD τ_2 (ps)		FAD α_1	
	Mean	std	Mean	std	Mean	std	Mean	std	Mean	std	Mean	std
Control	642	129	2923	171	57.5	6.0	389	62	2479	249	78.5	3.8
Fulvestrant (F)	631	78	2889	119	57.4	3.0	412	65	2565	194	75.7	3.2
Trastuzumab(H)	651	76	2922	119	56.4	2.4	383	65	2529	199	78.2	3.4
A4	619	90	2864	145	56.0	2.5	400	57	2634	158	74.8	3.3

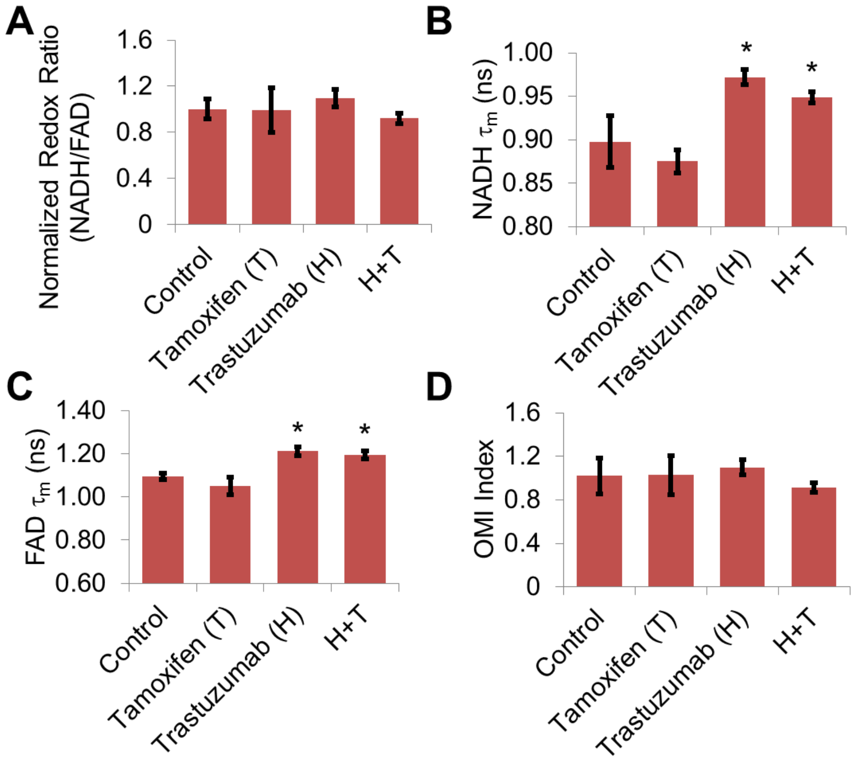

Figure B.14: OMI endpoints of organoids derived from a TNBC primary tumor. A. Redox ratio of organoids derived from a TNBC primary tumor treated with tamoxifen (T), trastuzumab (H), and the combined treatment, H+T at 48hr. B. NADH τ_m of these organoids at 48hr. C. FAD τ_m at 48hr. D. OMI index (composite endpoint of weighted redox ratio, NADH τ_m, and FAD τ_m) at 48hr. *p<0.05, for treated vs. control.

Table B.9: **NADH and FAD lifetime component values of organoids derived from a TNBC primary tumor** (mean, standard deviation). Boxes shaded pink represent a significant decrease in mean value vs. control. Boxes shaded blue represent a significant increase in mean value vs. control. NADH τ_1/α_1 is attributed to free NADH, NADH τ_2/α_2 is attributed to bound NADH. FAD τ_1/α_1 is attributed to bound FAD, FAD τ_2/α_2 is attributed to free FAD.

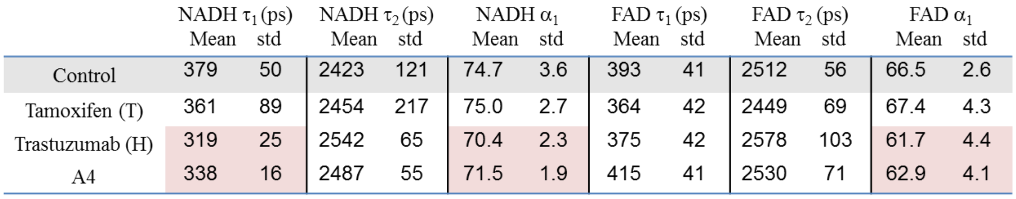

	NADH τ_1 (ps)		NADH τ_2 (ps)		NADH α_1		FAD τ_1 (ps)		FAD τ_2 (ps)		FAD α_1	
	Mean	std	Mean	std	Mean	std	Mean	std	Mean	std	Mean	std
Control	379	50	2423	121	74.7	3.6	393	41	2512	56	66.5	2.6
Tamoxifen (T)	361	89	2454	217	75.0	2.7	364	42	2449	69	67.4	4.3
Trastuzumab (H)	319	25	2542	65	70.4	2.3	375	42	2578	103	61.7	4.4
A4	338	16	2487	55	71.5	1.9	415	41	2530	71	62.9	4.1

APPENDIX C

Optical Imaging of Metabolism in HER2 Overexpressing Breast Cancer Cells

Walsh AJ, Cook RS, Rexer B, Arteaga CL, Skala MC. "Optical imaging of metabolism in HER2 overexpressing breast cancer cells." *Biomed Opt Express*. 2012;3(1):75-85.

C.1 Abstract

The optical redox ratio (fluorescence intensity of NADH divided by that of FAD), was acquired for a panel of breast cancer cell lines to investigate how overexpression of human epidermal growth factor receptor 2 (HER2) affects tumor cell metabolism, and how tumor metabolism may be altered in response to clinically used HER2-targeted therapies. Confocal fluorescence microscopy was used to acquire NADH and FAD auto-fluorescent images. The optical redox ratio was highest in cells overexpressing HER2 and lowest in triple negative breast cancer (TNBC) cells, which lack HER2, progesterone receptor, and estrogen receptor (ER). The redox ratio in ER-positive/HER2-negative cells was higher than what was seen in TNBC cells, but lower than that in HER2 overexpressing cells. Importantly, inhibition of HER2 using trastuzumab significantly reduced the redox ratio in HER2 overexpressing cells. Furthermore, the combinatorial inhibition of HER2 and ER decreased the redox ratio in ER+/HER2+ breast cancer cells to a greater extent than inhibition of either receptor alone. Interestingly, trastuzumab had little impact upon the redox ratio in a cell line selected for acquired resistance to trastuzumab. Taken together, these data indicate that the optical redox ratio measures changes in tumor metabolism that reflect the oncogenic effects of HER2 activity within the cell, as well as the response of the cell to therapeutic inhibition of HER2. Therefore, optical redox imaging holds the promise of measuring response and resistance to receptor-targeted breast cancer therapies in real time, which could potentially impact clinical decisions and improve patient outcome.

C.2 Introduction

The course of breast cancer treatment increasingly relies on the molecular phenotype of the tumor. For example, breast cancers that overexpress the estrogen receptor (ER) are often treated with ER-antagonists (e.g., tamoxifen, fulvestrant), while those that overexpress human epidermal growth factor receptor 2 (HER2) are often treated with HER2-inhibitors (e.g., trastuzumab, lapatinib). HER2 overexpressing tumors display aggressive cancer progression (1) and account for approximately 25% of all breast cancer patients. Treatment with trastuzumab (a monoclonal antibody which binds HER2) and lapatinib (a dual tyrosine kinase inhibitor that binds both HER2 and the epidermal growth factor receptor) has been shown to prolong survival in patients with HER2 overexpressing breast cancers (2-4). Due to the importance of choosing the correct treatment for breast cancer patients, breast tumors are routinely screened for expression of ER and HER2. Currently, ER and HER2 expression are determined by immunohistochemistry (IHC) and fluorescence in situ hybridization (FISH).

Unfortunately, approximately one-third of breast tumors that overexpress HER2 do not respond to trastuzumab and lapatinib therapy (4). Similarly, only 57% of patients with ER-positive breast cancers respond to tamoxifen therapy (5). However, there are reasons to remain optimistic, as novel therapeutics are in development to overcome clinical resistance to these therapeutic inhibitors (6). Early identification of those cancers that respond to targeted therapies versus those that are resistant will expedite clinical decisions regarding the course of treatment and will improve the clinical outcomes of breast cancer patients.

Methods currently under development to determine tumor response to therapy include positron emission tomography (PET), x-ray computed tomography (CT) and magnetic resonance imaging (MRI) (7-9). Evidence that tumor response to targeted inhibitors can be visualized was demonstrated with the use of fluoro-deoxyglocose (FDG)-PET, which is capable of detecting focused areas of high glucose uptake that are often seen in solid tumors. A preliminary clinical study of lapatinib-treated breast cancers showed changes in tumor metabolism after 1 month of lapatinib treatment (10). Yet, these currently available technologies provide only low resolution images, are non-portable, and usually require the use of contrast agents. Given the high cost of these procedures, it is unlikely that these will be adopted as standard of care, underscoring the need for more efficient, accurate, and cost-effective methods of identifying receptor expression and therapeutic response.

Cellular metabolism is a potentially powerful biomarker for tumor analysis. Unlike normal cells that rely on oxidative phosphorylation to generate ATP, or that use glycolysis under anaerobic conditions, cancer cells often generate ATP through aerobic glycolysis (11). Interestingly, signaling through the HER2 and ER pathways in breast cancer cells is thought to promote aerobic glycolysis. ER increases glucose transport and glycolysis (12, 13). Similarly, HER2 activated pathways may increase glucose transport into the cell and glycolysis (14, 15). HER2 signaling activates phosphatidyl inositol 3-kinase (PI3K) a major driver of aerobic glycolysis (16-19). In mouse models of HER2 overexpressing breast cancer, trastuzumab and lapatinib inhibited PI3K activity and decreased glucose uptake as measured by FDG-PET imaging (20). Conversely, breast tumor cells exhibiting resistance to HER2 inhibitors display aberrantly increased PI3K activity and active hypoxia signaling despite the presence of adequate oxygen(18). These studies suggest that differences in aerobic glycolysis may reflect not only oncogene-driven metabolic characteristics of the tumor cell, but also the effect of therapeutic inhibitors on tumor metabolism, and could therefore be used to distinguish tumors that are responsive to therapeutic inhibitors from those that are resistant.

During oxidative phosphorylation, NADH is oxidized to NAD+ and FAD is reduced to $FADH_2$. However, the process of glycolysis causes NAD+ to be reduced to NADH. Therefore, the ratio of NADH to FAD is a measurement of the balance between glycolysis (seen in tumor cells) and oxidative phosphorylation (seen in untransformed cells). NADH and FAD can be measured *in situ* using autofluorescence optical imaging techniques. The optical redox ratio (NADH fluorescence intensity divided by FAD fluorescence intensity) is a proven method of probing cellular metabolism and has been used to differentiate cancerous from non-cancerous tissues in a variety of models including oral and breast cancer (21-27). Ostrander et al. showed the optical redox ratio is also sensitive to ER expression in breast cancer cell cultures, and that treatment with tamoxifen decreased the optical redox ratio of tamoxifen-sensitive cells, but not tamoxifen-resistant cells (27).

The purpose of this study was to determine the effect of HER2 overexpression on the metabolism of breast cancer cells as measured by the optical redox ratio. The hypothesis that HER2 overexpression influences cellular redox ratios independently of ER expression was tested. Additionally, the impact of HER2 inhibition on the redox ratio in HER2 overexpressing breast cancer cells was measured. Finally, we determined if therapeutic resistance to HER2 inhibitors reflected on redox ratio measurements as a failure to reduce redox ratios in response to HER2 inhibition. HER2 overexpression was found to increase the redox ratio, independently of ER expression. While HER2 inhibition decreased the optical redox ratios in HER2 overexpressing cells, the HER2 inhibitor, trastuzumab, had no impact on redox ratios in trastuzumab resistant cells, despite continued overexpression of HER2.

C.3 Materials and methods

C.3.1 Cell culture

MCF10A cells were cultured in Mammary Epithelial Cell Growth Medium (MEGM, Lonza, Walkersville, MD) excluding the gentamycin-amphotericin B mix and supplemented with 100 ng/ml cholera toxin and 1% penicillin:streptomycin. The BT474, MDA-MB-231, MCF7, and SKBr3 cells were grown in DMEM (Invitrogen, Carlsbad, CA), supplemented with 10% fetal bovine serum and 1% penicillin:streptomycin, hereafter referred to as DMEM+. The resistant cell lines were grown in the DMEM+ at levels of the corresponding drug to maintain resistance. The lapatinib resistant cells were grown at 1 µM lapatinib (LC Laboratories, Woburn, MA) concentration and the trastuzumab resistant cells were grown at 25 µg/ml.

For imaging, all cell lines were plated at a density of $1\text{x}10^5$ cells per 35 mm plate, 48 hours prior to imaging. Glass bottom dishes (MatTek Corporation, Ashland, MA) were used to allow live cell imaging on an inverted, confocal microscope. The trastuzumab and lapatinib resistant cell redox ratio was determined from cells grown in trastuzumab and lapatinib supplemented media. For the drug perturbation experiments, the responsive BT474 cells were fed the drug supplemented media 24 hours prior to imaging. For the trastuzumab perturbation of the trastuzumab resistant cells, the cells were fed the DMEM+ media for the first 24 hours after plating and the DMEM+ with trastuzumab for the second 24 hours. Drug concentrations of the media were selected to mimic therapeutic drug dosage in patients, 25 µg/ml for trastuzumab (VUMC Pharmacy, Nashville, TN) and 2 µM for tamoxifen (Sigma-Aldrich, St. Louis, MO) (20, 28).

For the cyanide experiment to verify measurement of the redox ratio, MCF10A cells were plated at $1 \text{ x } 10^5$ cells per plate, 48 hours prior to imaging. Cells were imaged before the addition of cyanide. After 3 images from a plate were acquired, the cell media was exchanged for growth media supplemented with 4 mM NaCN (Sigma-Aldrich, St. Louis, MO). The cells were given one minute to react with the cyanide; then, three different places of each plate were imaged.

Proliferation rates of MCF10A, MCF7, and BT474 cells were determined by antibody labeling of cells grown on parallel imaging plates. Mitotic cells were first marked using a Phospho-Histone H3 (Ser10) antibody (Cell Signaling Technology, Danvers, MA). Then, labeling of the primary antibody with Alexa Fluor 488 goat anti-rabbit IgG antibody (Invitrogen, Carlsbad, CA) allowed counting by flow cytometry of the highly fluorescent mitotic cells and the less-fluorescent unlabeled cells. The percentage of proliferating cells was determined by dividing the number of highly fluorescent cells into the total number of cells counted.

C.3.2 Verification of ER and HER2 expression

Cells were homogenized in ice-cold lysis buffer [50 mM Tris pH 7.4, 100 mM NaF, 120 mM NaCl, 0.5% NP-40, 100 µM Na3VO4, 1X protease inhibitor cocktail (Roche)], sonicated for 10 s at 4ºC, 13,000 x g for 5 min. Protein concentration was determined using the BCA assay (Pierce). Proteins were separated by SDS-PAGE and transferred to nitrocellulose membranes. Membranes were blocked in 3% gelatin in TBS-T [Tris-buffered saline, 0.1% Tween-20) for 1 h, incubated in primary antibody in 3% gelatin for 2 h at room temperature, washed with TBS-T, incubated in HRP-conjugated anti-rabbit or anti-mouse IgG, washed with TBS-T, and then developed using ECL substrate (Pierce). The following primary antibodies were used: ErbB2 (HER2) (Neomarkers, InVitrogen; 1:2000); ER-alpha (Santa Criz Biotechnologies; 1:1000); beta actin (Sigma-Aldrich; 1:5000).

C.3.3 Confocal imaging

Images were acquired using an Olympus FV-1000 Inverted Confocal Microscope with a 40X/1.3 NA oil-immersion objective. Confocal microscopy was chosen over widefield fluorescence to reduce background noise for ease of NADH and FAD auto-fluorescence measurement. Additionally, the redox ratio is sensitive to measurement volumes and confocal microscopy ensures that the NADH and FAD signals can be co-registered to the same volume. For NADH fluorescence, the cells were excited at 405 nm and 410-510 nm emission was collected. FAD was excited at 488 nm and 500-600 nm emission was collected. The two images were acquired simultaneously, with NADH and FAD acquired sequentially for each pixel. A pixel dwell time of 2 μs was used. Each line was averaged 4 times to reduce noise. A single 1024x1024 pixel image required 39.0 s to acquire. To ensure the cells were not photobleaching, two images of the same field of view were acquired consecutively with no significant change in average pixel intensity. Settings for the gain, offset, and pinhole were maintained across all imaging sessions. To account for daily variations in laser power or instrumentation instability, the images were normalized to MCF10A cell measurements acquired during each imaging session. Each plate was imaged at 3 different, non-overlapping locations.

C.3.4 Image analysis

The optical redox ratio, NADH fluorescence intensity divided by FAD fluorescence intensity, was computed for each cell in the image using ImageJ software (NIH). The fluorescence signal of non-cellular regions, or background signal, was removed to ensure the fluorescence comparisons were made only for the cells. NADH and FAD used for cellular metabolism are contained within the cytoplasm and mitochondria, and the fluorescence signal from the nucleus is not involved in cellular metabolism. Therefore, the fluorescence signal from the nucleus was also removed to ensure isolation of metabolic NADH and FAD and eliminate the possibility of nuclear size as a confounding factor. Next, a NADH/FAD per pixel image was computed and the redox ratio for each cell in the image was determined. The average redox ratio value from all cells in each image was computed and normalized to the corresponding session's MCF10A measurement. Standard error was computed from the mean redox ratio value across all images from each cell line. A rank sum test was used for all statistical comparisons.

C.4 Results

The optical redox ratio of a panel of human breast-derived cell lines with varying expression of ER and HER2 were studied (Table C.1, Fig. C.1). MCF10A, a non-cancerous breast cell line with negligible or low expression of ER and HER2 was used as a control for each analysis.

Table C.1: Breast cancer cell lines with corresponding ER and HER2 expression.

Cell line	Cancerous	ER status	HER2 overexpression	n
MCF-10A	Non-cancerous	- / low	- / low	30
MDA-MB-231	Cancer	Negative	Negative	15
MCF-7	Cancer	Positive	Negative	15
BT-474	Cancer	Positive	Positive	15
SKBr3	Cancer	Negative	Positive	15
HR6 (Trastuzumab Resistant BT-474)	Cancer	Positive	Positive	15
BT-LR (Lapatinib Resistant BT-474)	Cancer	Positive	Positive	15

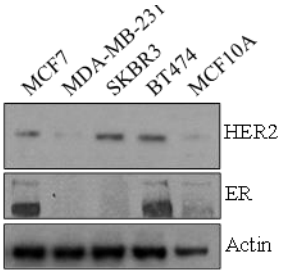

Figure C.1: Receptor expression of breast cancer cell lines. Western blot analysis demonstrates overexpression of HER2 in the SKBR3 and BT474 cells and expression of ER in the MCF7 and BT474 cells.

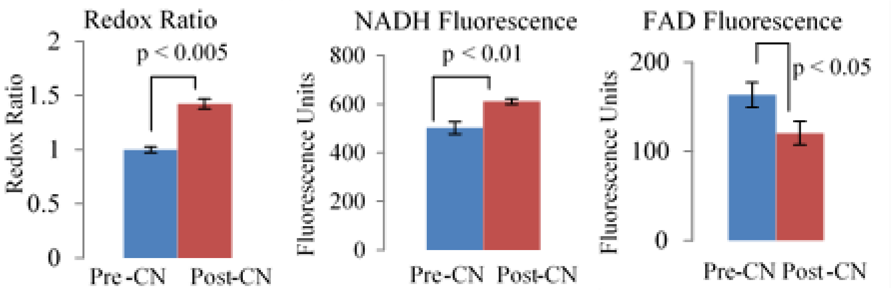

Figure C.2. Cyanide validation experiment. Addition of CN to MCF10A cells (n = 6) results in an increase in redox ratio and NADH fluorescence and a decrease in FAD fluorescence. Bar height represents mean and error bars represent SE.

To verify the use of optical imaging to measure the redox ratio, cyanide was used to disrupt the electron transport chain, thus preventing the conversion of NADH to NAD+ (29). As predicted, MCF10A cells treated with cyanide exhibited increased NADH fluorescence ($p < 0.01$, Fig. C.2) and decreased FAD fluorescence ($p < 0.05$; Fig. C.2). Therefore, the redox ratio was increased in cyanide-treated MCF10A cells as compared to untreated cells ($p < 0.005$, Fig. C.2). These results confirm that our optical imaging methods accurately reflect the balance between glycolysis and oxidative phosphorylation, and can be used to assess the metabolic state of tumor cells.

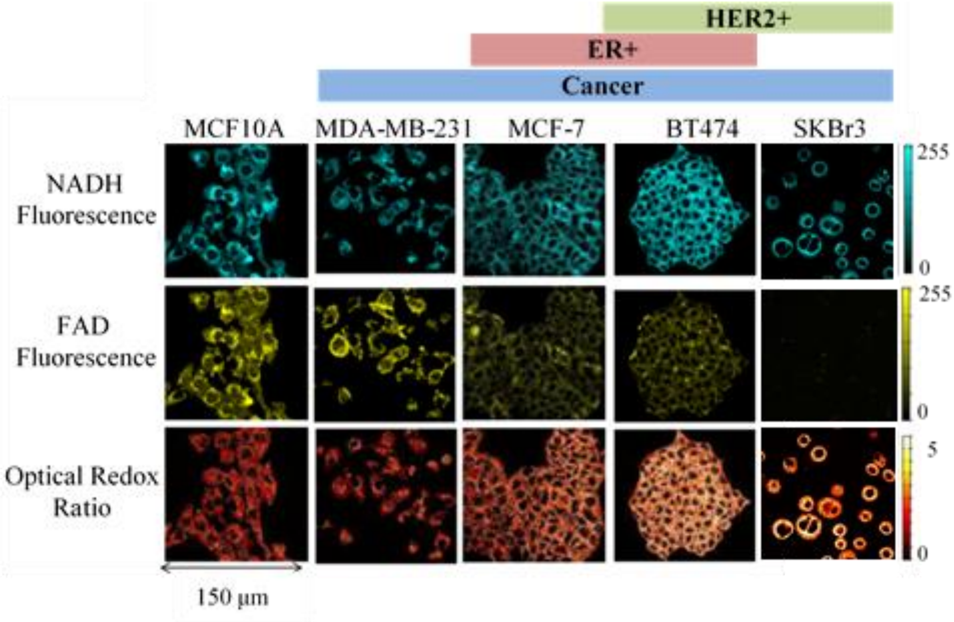

Figure C.3. Representative confocal images. Representative NADH, FAD, and redox ratio images for MCF10A, MDA-231, MCF7, BT474 and SKBr3 cells. Optical redox ratio increases with ER and HER2 expression.

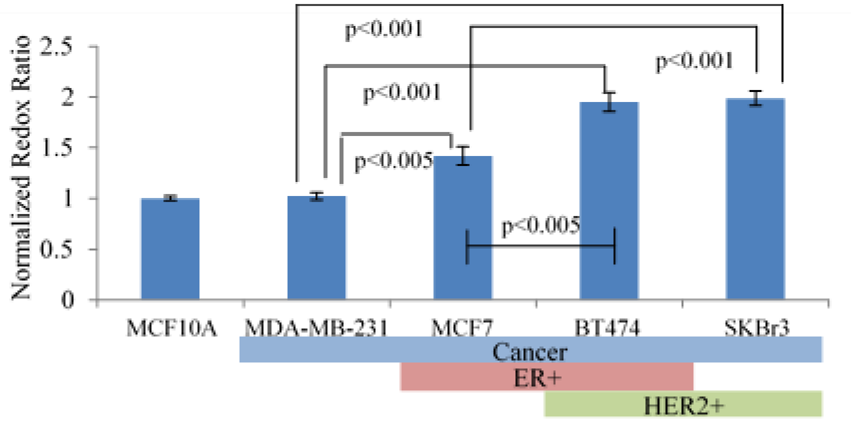

Figure C.4. Redox ratio of breast cancer cells. Quantitative representation (mean +/- SE) of the redox ratio values for the MCF10A (n=30), MDA-MB-231 (n=15), MCF7 (n=15), BT474 (n=15), and SKBr3 cells (n=15). Redox ratio is elevated in cells overexpressing HER2.

We used optical imaging to capture NADH and FAD fluorescence in five breast derived cell lines (Fig. C.3): MCF10A (untransformed breast epithelial cells), MDA-MB-231 (ER-/HER2), MCF-7 (ER+/HER2-), SKBR3 (ER-/HER2+), and BT474 (ER+/HER2+). The fluorescence intensities were used to calculate the redox ratio per cell for each cell line (Fig. C.4). While ER-/HER2- MDA-MB-231 cells displayed a redox ratio that was similar to what was seen in untransformed MCF10A cells, redox ratios were elevated in all other breast cancer cell lines ($p < 0.005$). ER+/HER2- breast cancer cell lines displayed elevated redox ratios ($p<0.005$), but not to the extent seen in HER2+ breast cancer cell lines ($p<0.001$).

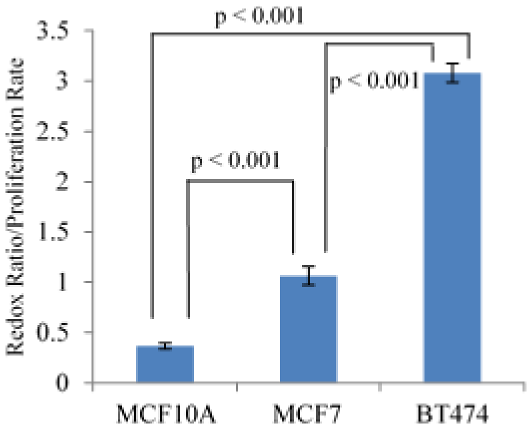

Figure C.5. Redox ratio divided by proliferation rate mean +/- SE for MCF10A (n=30), MCF7 (n = 15) and BT474 (n = 15) cells.

Controlling for differences in rates of proliferation among the MCF10A, MCF7, and BT474 cells did not reduce the significance of the redox ratio results shown in Fig. 4. In fact, controlling for proliferation (redox ratio divided by proliferation rate for each cell line) increases the differences between these three cell lines (Fig. C.5).

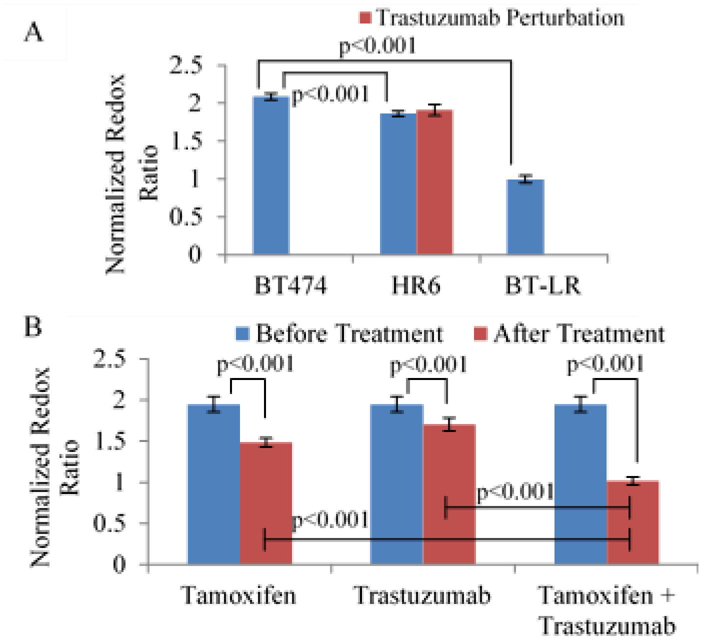

Figure C.6. Redox ratio following tamoxifen and trastuzumab treatment. (A) The redox ratio (mean +/-SE) of responsive BT474 cells is different from the trastuzumab (HR6) and lapatinib (BT-LR) resistant cells (n=15), and there was no change in the redox ratio of trastuzumab-resistant HR6 cells with trastuzumab-treatment. (B) The redox ratio of responsive BT474 cells decreased with tamoxifen (2 µM), trastuzumab (25 µg/ml), and tamoxifen + trastuzumab treatment (n=15).

The redox ratio of both the trastuzumab resistant cell line, HR6, and the lapatinib resistant cell line, BT-LR, was lower than the redox ratio for the responsive parental BT474 cells (Fig. C.6A). The HR6 cells are BT474-derived cells that continue to grow in the presence of trastuzumab (30). Likewise, the BT-LR cells are BT474-derived cells that were selected in culture with increasing concentrations of lapatinib (31). To investigate the contributions of the ER and HER2 signaling pathways to the redox ratio, BT474 cells (ER+/HER2+) were exposed to the ER antagonist tamoxifen and the anti-HER2 monoclonal antibody trastuzumab, (Fig. C.6B). Trastuzumab significantly decreased the redox ratio in ER+/HER2+ breast cancer cells ($p<0.001$; Fig. C.6B). Similarly, tamoxifen resulted in a decrease in redox ratio in the same cells ($p<0.001$, Fig. C.6B). The combination of tamoxifen with trastuzumab decreased the redox ratio in BT474 cells (ER+/HER2+) to a greater extent than single agent tamoxifen ($p<0.001$) or trastuzumab (p<0.001; Fig. C.6B). Interestingly, treatment of HR6 cells with trastuzumab did not cause any alterations in the redox ratio (Fig. C.6A). It is difficult to fully eliminate the influence of lapatinib on the BT-LR cells; and therefore, outside the scope of this paper to robustly perform a comparison of pre- and post- lapatinib treatment in these cells.

C.5 Discussion

The selective use of aerobic glycolysis over oxidative phosphorylation by cancer cells has been known for over a century. We and others have shown that this characteristic of cancer cells can be monitored *in situ* using optical imaging to measure the redox ratio, or the ratio of glycolysis to oxidative metabolism. Furthermore, we show that “driver” oncogenes in breast cancer cells also drive aerobic glycolysis in these cells. Specifically, HER2 activity was required for maximal aerobic glycolysis in breast cells overexpressing HER2, while ER signaling was required for aerobic glycolysis in ER+ breast cancer cells. These results demonstrate the effect of the HER2 and ER signaling pathways on cancer cell metabolism, as measured by the optical redox ratio. These data support the conclusion that optical imaging of redox ratios can be used to measure the tumor cell response to therapeutic inhibitors *in situ*. Finally, using HER2 overexpressing breast cancer cells with acquired resistance to HER2 inhibitors, we demonstrated that loss of oncogene dependence was reflected in the optical redox ratio measurement, such that HER2 inhibitors failed to decrease the redox ratio in a resistant cell line. Therefore, these findings could be applied to future studies using optical imaging of breast cells and tumors to predict their response to HER2 inhibitors, a development that would significantly inform clinical decisions regarding therapeutic strategies used to treat patients with HER2-positive breast cancers.

While this is the first study to correlate HER2 overexpression and activity to the redox ratio, a previous study similarly determined that ER+ breast cells exhibited a higher optical redox ratio than ER-negative cells (27). The previous study differs from the results presented herein because the previous study suggested that MCF7 cells (ER+/HER2-) exhibited a similar redox ratio to BT474 cells (ER+/HER2+). However, our results suggest that BT474 cells have significantly higher redox ratios than MCF7 cells. Several experimental factors could explain the differing results, including different excitation wavelengths for NADH, differing emission filters, and different growth media. Ostrander et al. used media supplemented with 5% FBS versus 10% used in our studies, which may have increased cellular proliferation in our experiments versus those described earlier, thus affecting tumor cell metabolism (32). However, when controlling for cell proliferation, the difference in the redox ratio between MCF7 and BT474 cells increased in the current study (Fig. C.5). Different emission filters capture different areas of the NADH and FAD emission curves, affecting absolute fluorescence intensity which may change the redox ratio. The results of the cyanide experiment ensure measurement of NADH and FAD fluorescence for this study (Fig C.2).

The results show that redox ratios in triple-negative MDA-MB-231 cells were similar to what was seen in MCF10A cells, which was less than the redox ratio seen in HER2+ or ER+ breast cancer cells. Triple-negative breast cancers (TNBC) lack HER2, ER, and PR, so they are difficult to target and no molecular targeted therapies exist for these breast cancers. Several FDG-PET studies in TNBC, ER+, and HER2+ tumors report high variability in the glucose uptake of triple negative cells (33, 34). Note that FDG-PET imaging illuminates different aspects of cellular metabolism (glucose uptake) than the optical redox ratio (relative concentrations of NADH and FAD, end products of metabolism). However, these previous reports indicate that the metabolism of TNBC is complex and heterogeneous, so a full characterization of this tumor subtype will likely require a more concentrated study.

The highest redox ratios were measured in breast cancer cell lines with HER2 overexpression. The higher redox ratio of HER2 overexpressing cells suggests that the HER2 pathway may affect cellular metabolism. Indeed, studies have found increased concentrations of glucose transporters and glycolytic enzymes present in HER2 overexpressing cells versus cells with low expression of HER2 (14, 15).

We found that HER2 inhibition with trastuzumab decreased the redox ratio of HER2 overexpressing breast cancer cells ($p< 0.001$, Fig. C.6B). This is consistent with several studies reporting reduced glucose uptake, decreased lactate secretion, and decreased glycolysis, in responsive HER2 overexpressing breast cancer cells treated with trastuzumab (35, 36). Treatment with both trastuzumab and tamoxifen decreased the redox ratio of responsive BT474 cells to levels seen in the non-cancerous MCF10A cell line (Fig. C.6B). These results suggest that both ER and HER2 signaling affects tumor cell metabolism in breast cancer cells. Mechanistic studies of receptor expression support this result. Cells expressing ER overexpress glucose transporters and have higher reported rates of glycolysis (12, 13). Similarly, HER2 overexpression is linked with increased glucose transport into cells and increased glycolysis (14, 15).

Innate and acquired resistance to HER2 inhibitors limits their current clinical success. Nearly all HER2-amplified breast cancers treated with trastuzumab or lapatinib will ultimately develop resistance to these targeted inhibitors. We examined trastuzumab-resistant cells, demonstrating that trastuzumab failed to reduce the redox ratio in the resistant cells (Fig. C.6A). These results are the first of its kind, but are consistent with an FDG-PET study of trastuzumab responsive and non-responsive breast cancer xenographs, demonstrating that HER2 inhibitors failed to reduce FDG uptake in those tumors whose growth was unaffected by trastuzumab (37). Interestingly, the redox ratio of the trastuzumab and lapatinib resistant cells are different from the pre-treatment redox ratio value of responsive BT474 cells, $p<0.001$ (Fig. C.6A). These results open up the possibility of screening HER2-inhibitor resistance with the optical redox ratio.

Future *in vivo* studies are needed to verify the influence of ER and HER2 expression on cellular metabolism. Increasing research is elucidating the importance of metabolism in cancer cells and its relationship with drug resistance. Here, upon treatment with receptor targeted therapies, the change in metabolism of resistant cells is shown to be negligible, while the metabolism of responsive cells is significant. Additionally, basal redox ratios are different in resistant versus responsive cells. Therefore, cellular redox ratios may prove an invaluable tool for research and clinical identification of receptor expression, tumor resistance to targeted therapies, and for monitoring treatment efficacy.

C.6 Acknowledgments

Experiments were performed in part through the use of the VUMC Cell Imaging Shared Resource (supported by NIH grants CA68485, DK20593, DK58404, HD15052, DK59637 and EY08126). Flow Cytometry experiments were performed in the VUMC Flow Cytometry Shared Resource. The VUMC Flow Cytometry Shared Resource is supported by the Vanderbilt Ingram Cancer Center (P30 CA68485) and the Vanderbilt Digestive Disease Research Center (DK058404). Many thanks to Madison Olive and Matthew Sundermann for help with cell culture. Funding sources: Vanderbilt University Breast Cancer SPORE Developmental Project Award; Provost Graduate Fellowship.

C.7 References

1. Ross JS, Fletcher JA. The HER-2/neu oncogene in breast cancer: prognostic factor, predictive factor, and target for therapy. Stem Cells. 1998;16(6):413-28.

2. Burris HA, 3rd, Hurwitz HI, Dees EC, Dowlati A, Blackwell KL, O'Neil B, Marcom PK, Ellis MJ, Overmoyer B, Jones SF, Harris JL, Smith DA, Koch KM, Stead A, Mangum S, Spector NL. Phase I safety, pharmacokinetics, and clinical activity study of lapatinib (GW572016), a reversible dual inhibitor of epidermal growth factor receptor tyrosine

kinases, in heavily pretreated patients with metastatic carcinomas. J Clin Oncol. 2005;23(23):5305-13.

3. Piccart-Gebhart MJ, Procter M, Leyland-Jones B, Goldhirsch A, Untch M, Smith I, Gianni L, Baselga J, Bell R, Jackisch C, Cameron D, Dowsett M, Barrios CH, Steger G, Huang CS, Andersson M, Inbar M, Lichinitser M, Lang I, Nitz U, Iwata H, Thomssen C, Lohrisch C, Suter TM, Ruschoff J, Suto T, Greatorex V, Ward C, Straehle C, McFadden E, Dolci MS, Gelber RD. Trastuzumab after adjuvant chemotherapy in HER2-positive breast cancer. The New England journal of medicine. 2005;353(16):1659-72.

4. Vogel CL, Cobleigh MA, Tripathy D, Gutheil JC, Harris LN, Fehrenbacher L, Slamon DJ, Murphy M, Novotny WF, Burchmore M, Shak S, Stewart SJ, Press M. Efficacy and safety of trastuzumab as a single agent in first-line treatment of HER2-overexpressing metastatic breast cancer. Journal of Clinical Oncology. 2002;20(3):719-26.

5. Chang J, Powles TJ, Allred DC, Ashley SE, Makris A, Gregory RK, Osborne CK, Dowsett M. Prediction of clinical outcome from primary tamoxifen by expression of biologic markers in breast cancer patients. Clin Cancer Res. 2000;6(2):616-21.

6. Esteva FJ, Yu DH, Hung MC, Hortobagyi GN. Molecular predictors of response to trastuzumab and lapatinib in breast cancer. Nat Rev Clin Oncol. 2010;7(2):98-107.

7. Jacobs MA, Ouwerkerk R, Wolff AC, Gabrielson E, Warzecha H, Jeter S, Bluemke DA, Wahl R, Stearns V. Monitoring of neoadjuvant chemotherapy using multiparametric, (23)Na sodium MR, and multimodality (PET/CT/MRI) imaging in locally advanced breast cancer. Breast cancer research and treatment. 2011;128(1):119-26.

8. Mankoff DA, Dunnwald LD, L. K., Doot RK, Specht JM, Gralow JR, Ellis GK, Livingston RB, Linden HM, Gadi VK, Kurland BF, Schubert EK, Muzi M. PET Tumor Metabolism in Locally Advanced Breast Cancer Patients Undergoing Neoadjuvant Chemotherapy: Value of Static versus Kinetic Measures of Fluorodeoxyglucose Uptake. Clinical Cancer Research. 2011;17(8):2400-9.

9. Li SP, Makris A, Beresford MJ, Taylor NJ, Ah-See MLW, Stirling JJ, d'Arcy JA, Collins DJ, Kozarski R, Padhani AR. Use of Dynamic Contrast-enhanced MR Imaging to Predict Survival in Patients with Primary Breast Cancer Undergoing Neoadjuvant Chemotherapy. Radiology. 2011;260(1):68-78.

10. Minami H, Kawada K, Murakami K, Sato T, Kojima Y, Ebi H, Mukai H, Tahara M, Shimokata K. Prospective study of positron emission tomography for evaluation of the activity of lapatinib, a dual inhibitor of the ErbB1 and ErbB2 tyrosine kinases, in patients with advanced tumors. Japanese Journal of Clinical Oncology. 2007;37(1):44-8.

11. Warburg O. On the origin of cancer cells. Science. 1956;123(3191):309-14.

12. Furman E, Rushkin E, Margalit R, Bendel P, Degani H. Tamoxifen induced changes in MCF7 human breast cancer: in vitro and in vivo studies using nuclear magnetic resonance spectroscopy and imaging. J Steroid Biochem Mol Biol. 1992;43(1-3):189-95.

13. Cheng CM, Cohen M, Wang J, Bondy CA. Estrogen augments glucose transporter and IGF1 expression in primate cerebral cortex. FASEB J. 2001;15(6):907-15.

14. Suarez E, Bach D, Cadefau J, Palacin M, Zorzano A, Guma A. A novel role of neuregulin in skeletal muscle. Neuregulin stimulates glucose uptake, glucose transporter translocation, and transporter expression in muscle cells. J Biol Chem. 2001;276(21):18257-64.

15. Zhang D, Tai LK, Wong LL, Chiu LL, Sethi SK, Koay ES. Proteomic study reveals that proteins involved in metabolic and detoxification pathways are highly expressed in HER-2/neu-positive breast cancer. Mol Cell Proteomics. 2005;4(11):1686-96.

16. Engelman JA, Luo J, Cantley LC. The evolution of phosphatidylinositol 3-kinases as regulators of growth and metabolism. Nat Rev Genet. 2006;7(8):606-19.

17. Wang L, Zhang Q, Zhang J, Sun S, Guo H, Jia Z, Wang B, Shao Z, Wang Z, Hu X. PI3K pathway activation results in low efficacy of both trastuzumab and lapatinib. BMC Cancer. 2011;11(1):248.

18. Berns K, Horlings HM, Hennessy BT, Madiredjo M, Hijmans EM, Beelen K, Linn SC, Gonzalez-Angulo AM, Stemke-Hale K, Hauptmann M, Beijersbergen RL, Mills GB, van de Vijver MJ, Bernards R. A functional genetic approach identifies the PI3K pathway as a major determinant of trastuzumab resistance in breast cancer. Cancer Cell. 2007;12(4):395-402.

19. Cooper C, Liu GY, Niu YL, Santos S, Murphy LC, Watson PH. Intermittent hypoxia induces proteasome-dependent down-regulation of estrogen receptor alpha in human breast carcinoma. Clin Cancer Res. 2004;10(24):8720-7.

20. Miller TW, Forbes JT, Shah C, Wyatt SK, Manning HC, Olivares MG, Sanchez V, Dugger TC, de Matos Granja N, Narasanna A, Cook RS, Kennedy JP, Lindsley CW, Arteaga CL. Inhibition of mammalian target of rapamycin is required for optimal antitumor effect of HER2 inhibitors against HER2-overexpressing cancer cells. Clin Cancer Res. 2009;15(23):7266-76.

21. Drezek R, Brookner C, Pavlova I, Boiko I, Malpica A, Lotan R, Follen M, Richards-Kortum R. Autofluorescence microscopy of fresh cervical-tissue sections reveals alterations in tissue biochemistry with dysplasia. Photochem Photobiol. 2001;73(6):636-41.

22. Chance B, Schoener B, Oshino R, Itshak F, Nakase Y. Oxidation-reduction ratio studies of mitochondria in freeze-trapped samples. NADH and flavoprotein fluorescence signals. J Biol Chem. 1979;254(11):4764-71.

23. Gulledge CJ, Dewhirst MW. Tumor oxygenation: a matter of supply and demand. Anticancer Res. 1996;16(2):741-9.

24. Kirkpatrick ND, Zou C, Brewer MA, Brands WR, Drezek RA, Utzinger U. Endogenous fluorescence spectroscopy of cell suspensions for chemopreventive drug monitoring. Photochem Photobiol. 2005;81(1):125-34.

25. Mujat C, Greiner C, Baldwin A, Levitt JM, Tian F, Stucenski LA, Hunter M, Kim YL, Backman V, Feld M, Munger K, Georgakoudi I. Endogenous optical biomarkers of normal and human papillomavirus immortalized epithelial cells. Int J Cancer. 2008;122(2):363-71.

26. Skala MC, Riching KM, Gendron-Fitzpatrick A, Eickhoff J, Eliceiri KW, White JG, Ramanujam N. In vivo multiphoton microscopy of NADH and FAD redox states, fluorescence lifetimes, and cellular morphology in precancerous epithelia. Proc Natl Acad Sci U S A. 2007;104(49):19494-9.

27. Ostrander JH, McMahon CM, Lem S, Millon SR, Brown JQ, Seewaldt VL, Ramanujam N. Optical redox ratio differentiates breast cancer cell lines based on estrogen receptor status. Cancer Res. 2010;70(11):4759-66.

28. Xia W, Bacus S, Hegde P, Husain I, Strum J, Liu L, Paulazzo G, Lyass L, Trusk P, Hill J, Harris J, Spector NL. A model of acquired autoresistance to a potent ErbB2 tyrosine kinase inhibitor and a therapeutic strategy to prevent its onset in breast cancer. Proc Natl Acad Sci U S A. 2006;103(20):7795-800.

29. Eng J, Lynch RM, Balaban RS. Nicotinamide adenine dinucleotide fluorescence spectroscopy and imaging of isolated cardiac myocytes. Biophys J. 1989;55(4):621-30.

30. Ritter CA, Perez-Torres M, Rinehart C, Guix M, Dugger T, Engelman JA, Arteaga CL. Human breast cancer cells selected for resistance to trastuzumab in vivo overexpress epidermal growth factor receptor and ErbB ligands and remain dependent on the ErbB receptor network. Clin Cancer Res. 2007;13(16):4909-19.

31. Rexer BN, Ham AJ, Rinehart C, Hill S, de Matos Granja-Ingram N, Gonzalez-Angulo AM, Mills GB, Dave B, Chang JC, Liebler DC, Arteaga CL. Phosphoproteomic mass spectrometry profiling links Src family kinases to escape from HER2 tyrosine kinase inhibition. Oncogene. 2011;30(40):4163-74.

32. Griffith.Jb. Role of Serum, Insulin and Amino-Acid Concentration in Contact Inhibition of Growth of Human Cells in Culture. Experimental Cell Research. 1972;75(1):47-&.

33. Specht JM, Kurland BF, Montgomery SK, Dunnwald LK, Doot RK, Gralow JR, Ellis GK, Linden HM, Livingston RB, Allison KH, Schubert EK, Mankoff DA. Tumor Metabolism and Blood Flow as Assessed by Positron Emission Tomography Varies by Tumor Subtype in Locally Advanced Breast Cancer. Clinical Cancer Research. 2010;16(10):2803-10.

34. Basu S, Chen W, Tchou J, Mavi A, Cermik T, Czerniecki B, Schnall M, Alavi A. Comparison of triple-negative and estrogen receptor-positive/progesterone receptor-positive/HER2-negative breast carcinoma using quantitative fluorine-18 fluorodeoxyglucose/positron emission tomography imaging parameters: a potentially useful method for disease characterization. Cancer. 2008;112(5):995-1000.

35. Tan M, Zhao YH, Liu H, Liu ZX, Ding Y, LeDoux SP, Wilson GL, Voellmy R, Lin YF, Lin WS, Nahta R, Liu BL, Fodstad O, Chen JQ, Wu Y, Price JE. Overcoming Trastuzumab Resistance in Breast Cancer by Targeting Dysregulated Glucose Metabolism. Cancer Res. 2011;71(13):4585-97.

36. Smith TAD, Cheyne RW, Trembleau L, McLaughlin A. Changes in 2-fluoro-2-deoxy-D-glucose incorporation, hexokinase activity and lactate production by breast cancer cells responding to treatment with the anti-HER-2 antibody trastuzumab. Nuclear Medicine and Biology. 2011;38(3):339-46.

37. Reilly RM, McLarty K, Fasih A, Scollard DA, Done SJ, Vines DC, Green DE, Costantini DL. (18)F-FDG Small-Animal PET/CT Differentiates Trastuzumab-Responsive from Unresponsive Human Breast Cancer Xenografts in Athymic Mice. Journal of Nuclear Medicine. 2009;50(11):1848-56.

APPENDIX D

An Automated Image Processing Routine for Segmentation of Cell Cytoplasms in High-Resolution Autofluorescence Images

Walsh AJ, Skala MC. “An automated image processing routine for segmentation of cell cytoplasms in high-resolution autofluorescence images.” *SPIE Proceedings*. 2014; 8948.

D.1 Abstract

The heterogeneity of genotypes and phenotypes within cancers is correlated with disease progression and drug-resistant cellular sub-populations. Therefore, robust techniques capable of probing majority and minority cell populations are important both for cancer diagnostics and therapy monitoring. Herein, we present a modified CellProfiler routine to isolate cytoplasmic fluorescence signal on a single cell level from high resolution auto-fluorescence microscopic images.

D.2 Introduction

Solid tumors contain many cell types including the malignant cancer cells, immune cells, endothelial cells, and fibroblasts. Depending on the tumor, the majority of the tumor mass may be immune and stromal cells. Furthermore, within the malignant cell population, cells contain different genes and express different phenotypes, most likely arising due to the mutagenic nature of cancer (1, 2). A stem-cell-like population of cells, capable of establishing phenotypically diverse xenografts, may exist in solid cancers and tumor heterogeneity is thought to contribute to tumor resistance (3). Drugs selectively kill only portions of a tumor and the remaining resistant cells are able to proliferate and grow in the presence of the drug. Therefore, studies of tumor physiology and drug treatment should be performed at high resolution to ensure data is from the correct malignant cells. Further, cellular-level analysis may elucidate patterns and differences within cell types otherwise masked by the phenotype of the majority of cells.

Optical microscopy techniques, particularly fluorescence imaging of NADH and FAD, are high resolution, are non-invasive, and yield quantitative endpoints. The optical redox ratio, the fluorescence intensity of NADH divided by the fluorescence intensity of FAD, provides a dynamic read-out of cellular metabolism and is often elevated in malignant cells (4, 5), breast cancer cells overexpressing the estrogen receptor, and breast cancer cells expressing human epidermal growth factor receptor 2 (HER2) (6, 7). Further, the optical redox ratio detects drug-induced changes in cellular metabolism and may be an early reporter of drug efficacy (6). Within a breast cancer xenograft containing both cells responsive and resistant to the HER2 inhibitor trastuzumab, *in vivo* fluorescence imaging and subsequent single cell analysis revealed a heterogeneous population of cells characterized by two populations, one with a lower redox ratio (responding to the drug) and one with a higher redox ratio (no effect by the drug) (6).

These papers highlight the relevance of fluorescence imaging for mapping tumor metabolism and the potential information that can be obtained from single-cell analysis. However, manual segmentation of cells and nuclei is time-consuming and not practical for large data sets, high-throughput experiments, or clinical translation. Therefore, we have developed a computational routine for automated image segmentation. The program presented here identifies and segments the cells, nuclei, and cytoplasms of a high-resolution auto-fluorescence image.

D.3 Methods

The automated image analysis code was created using standard and customized modules within Cell Profiler (Fig. D.1) and Matlab (http://www.cellprofiler.org/). The steps of the code are outlined in Table D.1. First, the images are loaded. Next, the original images are rescaled to have pixel values between 0 and 1. Then, a customized threshold code identifies pixels belonging to nuclear regions that are brighter than background but not as bright as cell cytoplasms (see Table

D.1 for custom code). Next, several image processing steps remove the background and define cell edges to improve the automated nucleus and cell identification routines. Finally, the resulting round objects between 6 and 25 pixels (6.12-25.5 μm) in diameter in the nucleus image are segmented and saved as the primary objects within the image. Secondary objects, or cells, are identified by propagating out from the nuclei. An Otsu Global threshold is used to improve propagation. Cell cytoplasms are defined as the secondary objects (cells) minus the primary objects (nuclei). The final modules measure the pixel intensity values from the original images.

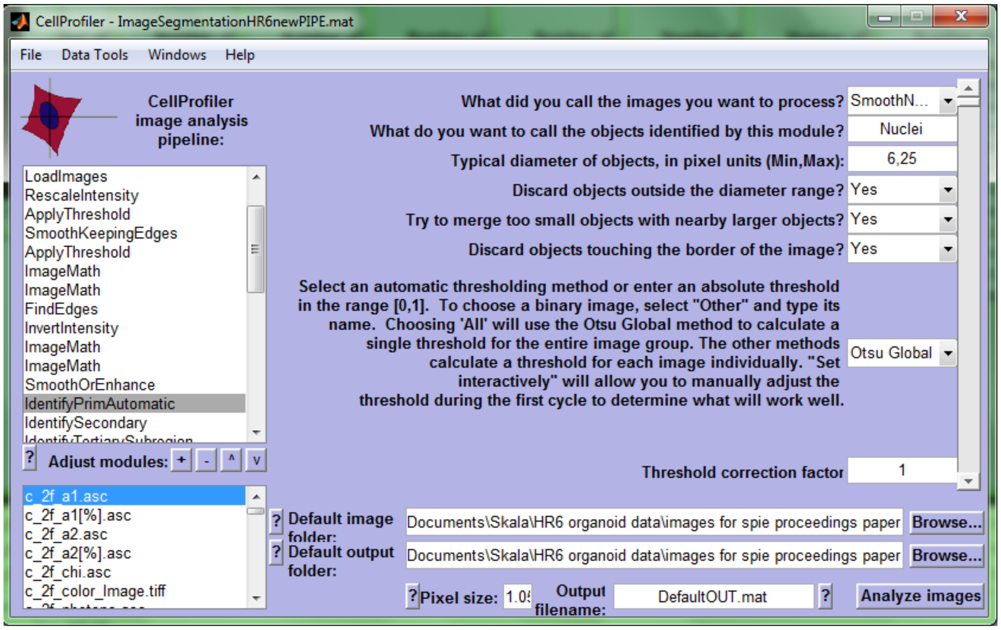

LoadImages
RescaleIntensity
ApplyThreshold
SmoothKeepingEdges
ApplyThreshold
ImageMath
ImageMath
FindEdges
InvertIntensity
ImageMath
ImageMath
SmoothOrEnhance
IdentifyPrimAutomatic
IdentifySecondary
IdentifyTertiarySubregion

c_2f_a1.asc
c_2f_a1[%].asc
c_2f_a2.asc
c_2f_a2[%].asc
c_2f_chi.asc
c_2f_color_Image.tiff

What did you call the images you want to process? SmoothN...
What do you want to call the objects identified by this module? Nuclei
Typical diameter of objects, in pixel units (Min,Max): 6,25
Discard objects outside the diameter range? Yes
Try to merge too small objects with nearby larger objects? Yes
Discard objects touching the border of the image? Yes

Select an automatic thresholding method or enter an absolute threshold in the range [0,1]. To choose a binary image, select "Other" and type its name. Choosing 'All' will use the Otsu Global method to calculate a single threshold for the entire image group. The other methods calculate a threshold for each image individually. "Set interactively" will allow you to manually adjust the threshold during the first cycle to determine what will work well. Otsu Global

Threshold correction factor 1

Default image folder: Documents\Skala\HR6 organoid data\images for spie proceedings paper
Default output folder: Documents\Skala\HR6 organoid data\images for spie proceedings paper
Pixel size: 1.0
Output filename: DefaultOUT.mat

Figure D.1. CellProfiler graphical user interface.

Table D.1. Steps of CellProfiler pipeline.

Pipeline	Purpose	Notes
Load Images	Load images	Changes to code must be made to load .txt or .asc image files
Rescale Intensity	Rescale fluorescence image to have pixel values between 0 and 1	Necessary for several image processing commands
Apply Threshold	Create an image with just the nuclei pixels using a multithreshold technique to determine pixel values of background, nuclei, and cytoplasm	Code added to ApplyThreshold.m:

```
if HighThreshold == 0 & LowThreshold ==0;
        pix = OrigImage( : );
        Options = statset('MaxIter',400);
        obj = gmdistribution.fit(pix,4,'Options',Options);
        [mu,ind] = sort(obj.mu);
    LowThreshold = mu(3)-sqrt(obj.Sigma(ind(3)));
    HighThreshold = mu(3);
end
```

** A four-component fit modeled this data best, with two peaks for background pixels, 1 for nuclei, and 1 for cytoplasm. The number of modes in the pixel distribution fit (gmdistribution.fit(pix,**4**,'Options',Options) and the Low and High threshold values should be optimized for a given data set.

Pipeline	Purpose	Notes
Smooth Keeping Edges Apply Threshold Image Math	Create a mask to isolate the cells and remove the background	
Find Edges Invert Intensity Image Math Image Math	Finds edges of the cells/cell clump and creates a mask	These steps set a hard edge boundary to prevent propagation of the secondary objects into the background and remove artifacts from nuclei image at cell boundaries.
Smooth or Enhance	Smooths the result of the nuclei thresholding	Eliminates noise pixels
Identify Primary Automatic	Identify nuclei	
Identify Secondary	Identify cell boundaries	Cells are found by propagating out from the primary objects (nuclei). This works best if the image has some pre-processing, removal of background and edge definition.
Identify Tertiary Subregion	Identify cytoplasms	Subtracts nuclei from cells
Measure Object Intensity	Measure and report statistical information for the identified regions	

D.4 Results

The results of the image segmentation code are presented here for a representative image of an organoid grown from a breast cancer xenograft. The original image is an NADH fluorescence image, characterized by bright cytoplasms and dark nuclei and background. Figure D.2 shows the rescaled image (Fig. D.2A) and the result of the customized thresholding code to isolate the nuclei (Fig. D.2B).

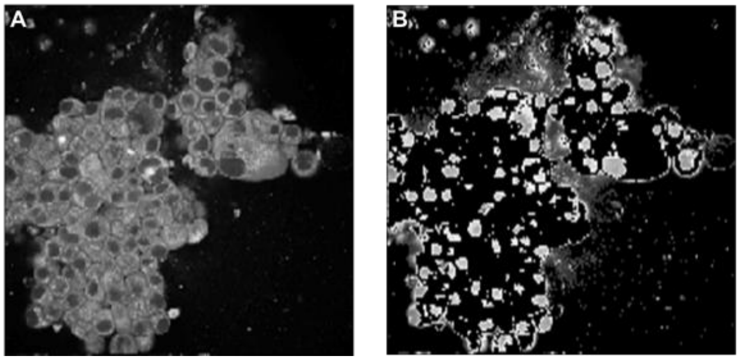

Figure D.2. Result of threshold. A. Original image rescaled to have all pixel values between 0 and 1. B. Result of thresholding code, nuclei remain, background and cytoplasms removed.

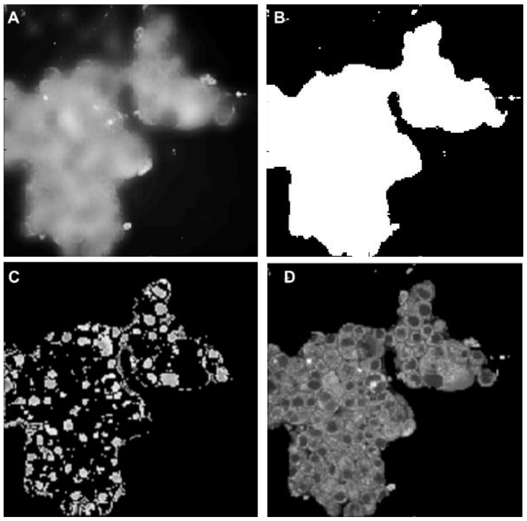

Figure D.3. Image processing steps. A. Smoothed image allows masking of cell clumps. B. Zeros (black) and ones (white) cell clump mask. C. Resulting image of the product of the nuclei image and cell clump mask (Fig. shown in B). D. Resulting image of the product of the original image and cell clump mask (Fig. shown in B).

The next steps include image processing to improve the automated routines that identify the nuclei and cells. The background pixels are set to 0 by smoothing the cell clumps (Fig.D.3A), generating a cell clump mask (Fig. D.3B), and multiplying the original and nuclei images by the mask (Fig. D.3C-D). Likewise, the edges of the cell clump are found using an edge detect routine (Fig. D.4A), a mask is created (Fig. D.4B), and these edges are subtracted from the nuclei image and the cell image (Fig. D.4C-D). The removal of the edges from the nuclei image removes artifacts in the nuclei image at the edges of the cell clump.

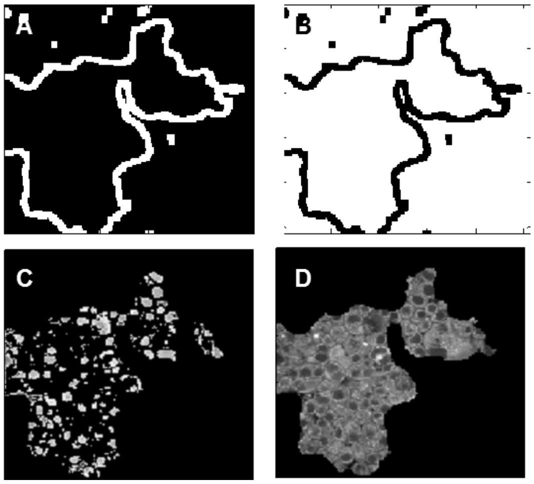

Figure D.4. Edge detect. A. Edge detect to identify the edges of the cell clumps or regions of interest. B. Zeros (black) and ones (white) edges mask. C. Resulting image of the product of the nuclei image and edge mask (Fig. shown in B). D. Resulting image of the product of the original image and edge mask (Fig. shown in B).

After the image processing steps, the CellProfiler modules are used to find the primary objects (nuclei), secondary objects (cells), and tertiary objects (cytoplasms) are used to segment out the cell components. First, the nuclei are identified from the post-processed nuclei image (Fig. D.5A). Objects within the set diameter size are outlined in green and nuclei that exceed the size (25 pixels) or are too small (less than 6 pixels, in diameter) are excluded from analysis and identified in red. From the primary objects identified in Fig. D.5A, the secondary objects, or cells, are identified by propagating outward until a boundary is reached (as identified from a Otsu Global threshold) or another propagating boundary is met (Fig. D.5B). The tertiary objects are the secondary minus the primary (Fig. D.5C). An overlap of the cytoplasm outlines and the original image is shown in Fig. D.6.

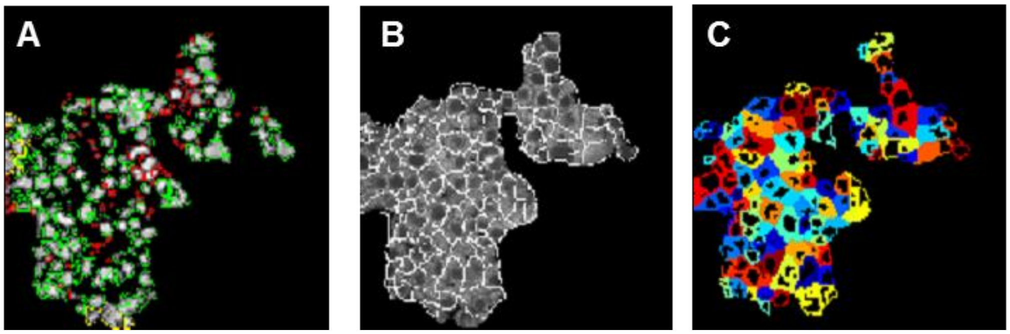

Figure D.5. Segmented nuclei and cells. A. Primary objects (nuclei) outlined in green, objects with diameters outside the target range (6-25 pixels) are outlined in red. B. Outlines of secondary objects. C. Tertiary objects.

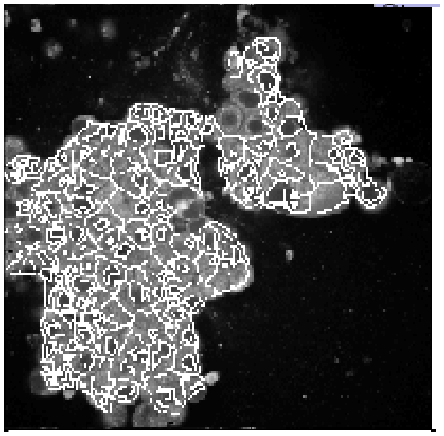

Figure D.6. Cytoplasm outlines. Image of tertiary object (cytoplasms) outlines overlain on the original image.

D.5 Discussion

Segmentation of autofluorescence images of tissues and highly confluent cell cultures is challenging due to the clumping nature of cells. This paper presents a novel method which utilizes a multi-level threshold to identify cell nuclei, which are typically brighter than the background and darker than the cytoplasms, and propagates out from the nuclei to identify the cells. Cell cytoplasms are then the cells minus the nuclei.

This method has been used on NADH autofluorescence images of confluent cell cultures, organoid cultures, and tissues imaged *in vivo*. Thresholding parameters are optimized for a data set to ensure optimal segmentation of nuclei. Typical processing times for a single image are approximately 20 seconds, which is a 10-20 fold improvement over manual segmentation. The segmentation code performs admirably and error with respect to manual segmentation is less than 10%. However, the program does have a few limitations including an inability to identify cells without a nuclei, increased error around the edges of the cell clumps, and thresholding problems in images with non-uniform illumination.

Due to the heterogeneity of cancers and the contributions of minority populations to tumor drug resistance, it is important to study not only the characteristics of the majority of cells but also analyze single cells and sub-populations of cells. The automated image segmentation code presented above demonstrates one method of isolating cells, nuclei, and cytoplasms from high-resolution NADH auto-fluorescence images.

D.5 References

1. Eroles P, Bosch A, Bermejo B, Lluch A. Mechanisms of resistance to hormonal treatment in breast cancer. Clin Transl Oncol. 2010;12(4):246-52.
2. Locasale JW. Metabolic rewiring drives resistance to targeted cancer therapy. Mol Syst Biol. 2012;8:597.
3. Al-Hajj M, Wicha MS, Benito-Hernandez A, Morrison SJ, Clarke MF. Prospective identification of tumorigenic breast cancer cells. Proc Natl Acad Sci U S A. 2003;100(7):3983-8.
4. Skala MC, Riching KM, Bird DK, Gendron-Fitzpatrick A, Eickhoff J, Eliceiri KW, Keely PJ, Ramanujam N. In vivo multiphoton fluorescence lifetime imaging of protein-bound and free nicotinamide adenine dinucleotide in normal and precancerous epithelia. Journal of biomedical optics. 2007;12(2):024014.

5. Skala MC, Riching KM, Gendron-Fitzpatrick A, Eickhoff J, Eliceiri KW, White JG, Ramanujam N. In vivo multiphoton microscopy of NADH and FAD redox states, fluorescence lifetimes, and cellular morphology in precancerous epithelia. Proc Natl Acad Sci U S A. 2007;104(49):19494-9.

6. Walsh AJ, Cook RS, Manning HC, Hicks DJ, Lafontant A, Arteaga CL, Skala MC. Optical metabolic imaging identifies glycolytic levels, subtypes, and early-treatment response in breast cancer. Cancer Res. 2013;73(20):6164-74.

7. Walsh A, Cook RS, Rexer B, Arteaga CL, Skala MC. Optical imaging of metabolism in HER2 overexpressing breast cancer cells. Biomedical optics express. 2012;3(1):75-85.

APPENDIX E

Autofluorescence Imaging of Drug Response in Organoids Generated from Frozen Primary Tumor Tissues

E.1 Abstract

Primary tumor organoids grown in three-dimensional culture provide a robust platform for studying tumor progression, invasion, and drug response. However, organoid generation protocols require fresh tissue, which limits the application of organoid-based experiments and drug-response studies to medical centers with co-localized operating rooms and research facilities. The purpose of this study is to investigate tissue-freezing methods that will preserve tissues for organoid generation. We tested two freezing protocols, flash-freezing in liquid nitrogen and slow-freezing of bulk tissue samples in DMSO-supplemented media, on primary breast cancer xenografts. Additionally, organoids were derived from flash frozen human breast cancer biopsies, to evaluate the use of banked tissue. Our results demonstrate that organoids can be grown from flash-frozen or slow, DMSO frozen tissues and these organoids have similar morphologies and rates of proliferation and apoptosis as organoids derived from fresh tissues. Furthermore, while the freezing process affects the basal metabolic rate of the cells, optical metabolic imaging can be used to detect drug response of organoids derived from frozen-thawed tissues. These results validate the two freezing methods, which can be performed at the site of tissue extraction and do not require specialized tissue culture equipment, for tissue preservation and subsequent organoid generation.

E.2 Introduction

Primary three-dimensional organoid culture of tumors is an attractive platform for studies of malignant tissues. Organoids contain all components of the original tissue. When derived from tumor samples, organoids contain malignant epithelial cells, endothelial cells, leukocytes, and fibroblasts. Three-dimensional organoid cultures recapitulate *in vitro* tissue structural organization, functional differentiation, chemical and mechanical signals, and therefore, may be more physiologically relevant than 2D cultures of primary or immortalized cells (1-3). Traditionally, cancer models are limited to immortalized cell lines, xenograft models, or murine models of cancer. While these models are readily accessible and allow studies of cancer progression and drug testing, the models often fail to fully represent human cancers and therefore many drugs fail in initial stages of clinical trials (2, 4, 5). Organoid culture of primary human tumors may help overcome these limitations of traditional cancer models.

Organoid culture of primary tumor tissues enables dynamic studies of cancer development (3), invasion (6-8), and drug response (9). Optical imaging, particularly multi-photon fluorescence imaging, is well suited to study organoids due to the spatial scale, depth of imaging, and functional fluorescence endpoints. Recently, we have shown that optical metabolic imaging (OMI) of organoids generated from primary breast tumors provides a dynamic and powerful assessment of drug response for both individualized patient treatment planning and exploratory studies of novel anti-cancer drugs (9). OMI utilizes both the fluorescence intensity and lifetime of the metabolic co-enzymes, NAD(P)H and FAD, to detect early metabolic shifts in response to anti-cancer therapy. These metabolic shifts, detected non-invasively, correlate well with drug-induced inhibition of proliferation and induction of apoptosis within the organoids, as well as with *in vivo* drug response (9). Due to its non-destructive nature and endogenous source of contrast, OMI is attractive for longitudinal studies of dynamic changes in cellular metabolism.

To date, all studies of primary organoids have been performed on organoids generated from fresh tissues (6, 9, 10). However, fresh primary human tissues are not always available, and limit organoid-based therapeutics and research to sites with co-localized operating rooms and cell culture facilities. Optimizing organoid generation protocols to use preserved tissues will allow research on banked tissues and enable transport of tissue from the hospital to research or testing facilities. Tissue is often preserved for biomedical research either as formalin-fixed paraffin embedded samples or flash frozen in liquid nitrogen. Preservation of cells in cell culture utilizes DMSO supplemented media and a slow-freezing procedure. This study investigates these two tissue freezing techniques for subsequent organoid generation. The use of frozen tissues will greatly enhance the applications and clinical use of organoid-based drug screens and research.

This study tests the hypothesis that organoids can be grown from frozen/thawed tissues and that organoids derived from frozen-thawed tissues will have the same drug response as organoids grown from fresh tissues. To test this hypothesis, organoids were generated from primary fresh tumor tissue, flash frozen and thawed tumor tissue, and tissue placed in tissue culture media + 5% DMSO and slowly frozen (an alternative tissue banking method). Organoid viability was assessed by immunofluorescence (IF) assessment of proliferation and apoptosis proteins, Ki67 and cleaved caspase 3, respectively. Organoid drug response was assessed with OMI and IF. Both freezing protocols were performed on two xenograft models of HER2-overexpressing breast cancers, BT474 and HR6 tumors, to compare the two freezing techniques for optimal organoid viability and drug response. The flash-frozen experiments were additionally performed on two primary human breast cancer biopsies to evaluate the use of frozen tissues in tissue banks.

E.3 Methods

E.3.1 Mouse Xenografts

This study was approved by the Vanderbilt University Animal Care and Use Committee and meets the NIH guidelines for animal welfare. BT474 or HR6 cells (10^8) in 100 μl Matrigel were injected in the inguinal mammary fad pads of two female athymic nude mice (J:NU; The Jackson Laboratory). BT474 and HR6 tumors are both estrogen receptor positive and HER2 overexpressing. The HR6 tumors were extracted from a BT474 tumor that developed acquired resistance to the drug trastuzumab in a murine model (11). The HR6 cells and tumors used herein retain HER2 overexpression but lack response to trastuzuamb (9, 11), thus the BT474 and HR6 tumors represent trastuzumab responsive and trastuzumab-resistant tumors, respectively. When tumors were ~500 mm^3, mice were humanly sacrificed and the tumors removed. Each tumor was cut into three approximately equal sections, ~150mm^3. One section was processed immediately into organoids, one section was flash frozen, and one section was slowly frozen in DMSO supplemented media.

E.3.2 Clinical Breast Cancer Samples

This study was approved by the Vanderbilt University Institutional Review Board and informed consent was obtained from all subjects. Two primary tumor biopsies from separate patients were provided by an expert breast pathologist (ME Sanders). Tumor biopsies were obtained from the tumor mass following surgical excision. The tumor biopsies were placed in sterile DMEM and transported on ice to the laboratory (~5 minute walk). The tumor biopsies were cut into two approximately equal sections, ~200mm^2. One section was processed into organoids immediately, and the second section was flash frozen.

E.3.3 Freezing Protocols

For flash freezing in liquid nitrogen, samples were placed in a histology cassette and submerged in liquid nitrogen for 30 seconds. Then, the cassette was removed, wrapped in foil, and stored in a -80°C freezer. For the slow freezing method, samples were placed in a cryotube with 950 μl tissue culture media and 50 μl DMSO. Samples were slowly frozen by placement in a Styrofoam container in a -80°C freezer. Samples were stored at -80°C until use. All samples were stored at -80°C for 6-12 months.

E.3.4 Organoid Generation

Frozen samples were thawed in PBS at room temperature for ten minutes. All samples were washed three times with sterile PBS. Tissue samples were placed in 0.5 ml primary mammary epithelial cell (PMEC) media [DMEM:F12 + EGF (10 ng/ml) + hydrocortisone (5 μg/ml) + insulin (5 μg/ml) + 1% penicillin:streptomycin] and mechanically dissociated into macrosuspensions of tissue approximately 50-300 μm in diameter by mechanical cutting of the tissue with a scalpel and surgical scissors. Matrigel was added to the macrosuspension solutions in a 2:1 ratio and 100 μl of the matrigel/macrosuspension solution was placed on coverslips. The gels solidified at room temperature for 30 minutes and then in the incubator for 1 hour. Then, gels were overlain with PMEC media.

Organoids generated from fresh tissues were treated immediately. BT474 and HR6 organoids were treated with the following drugs and combination: control (human control IgG + DMSO), trastuzumab (25 μg/ml), paclitaxel (25 nmol/L), XL147 (25 nmol/ml), and trastuzumab + paclitaxel + XL147. The organoids derived from the clinical biopsies were treated with control (human control IgG + DMSO), trastuzumab (25 μg/ml), paclitaxel (25 nmol/L), tamoxifen (2 μmol/ml), and trastuzumab + paclitaxel + tamoxifen. Organoids derived from frozen tissues were grown for a recovery period of 3 or 7 days (media replaced every 2-3 days) and then treated with the same drugs and combination as the fresh-tissue derived organoids.

E.3.5 Optical Metabolic Imaging

Fluorescence lifetime imaging was performed on a multiphoton microscope (Bruker) modified for fluorescence lifetime imaging, as previously described (9, 12, 13). Briefly, a titanium-sapphire laser, tuned to 750 nm for NAD(P)H excitation and tuned to 890 nm for FAD excitation, provides the excitation light. A 40X objective (1.3 NA) couples excitation and emission light. Customized filter sets isolate NAD(P)H emission between 400-480nm and FAD emission between 500-600nm. A GaAS PMT (H7422P-40; Hamamatsu) detects emitted photons and time correlated single photon counting electronics (SPC-150; Becker and Hickl) enable fluorescence lifetime imaging. Images, 256x256 pixels, were collected for 60s with a pixel dwell time of 4.8 μs. Photon count rates were maintained above 5 x 10^5 to ensure adequate photon counts for lifetime fits and no photobleaching occurred. The instrument response full width at half maximum was 260 picoseconds as measured from the second harmonic generation of a urea crystal. Daily fluorescence lifetime validation was confirmed by imaging a fluorescent bead (Polysciences Inc.). The measured lifetime of the bead (2.1 ± 0.04 nanoseconds) agrees with published values (9, 12, 14, 15).

NAD(P)H and FAD fluorescence lifetime images of the organoids were acquired at 24, 48, and 72 hours after drug treatment. For each organoid, the NAD(P)H image was acquired first and followed immediately by the FAD image. Organoids were imaged through glass coverslips on the inverted microscope. One image from each of six representative organoids were collected per group (6 organoids/group; n=30-300 cells/group), at an imaging depth through the center of the organoid.

Fluorescence lifetime images were analyzed as described previously (9, 12, 16). Briefly, fluorescence lifetime decay curves were deconvolved from the measured instrument response function and fit to a two component model, $I(t) = \alpha_1 \exp\left(-\frac{t}{\tau_1}\right) + \alpha_2 \exp\left(-\frac{t}{\tau_2}\right) + C$, where I(t) is the fluorescence intensity at time *t* after the laser pulse, α_1 and α_2 are the fractional contributions of the short and long lifetime components, (i.e. $\alpha_1 + \alpha_2 = 1$), τ_1 and τ_2 are the fluorescence lifetimes of the short and long lifetime components, and C accounts for background light (SPCImage). A two component model was used to fit the lifetime decays of NAD(P)H and FAD because

NAD(P)H and FAD exist physiologically in both free and protein-bound forms (17, 18). The free and protein-bound forms have different lifetimes depending on fluorescence quenching (19). NAD(P)H self-quenches in the free state and thus has a short lifetime associated with free NAD(P)H and a long lifetime with bound NAD(P)H (17, 19). FAD is quenched when bound and has a short bound lifetime and long free lifetime (18). The mean lifetime, $\tau_{\square}$, is calculated as a weighted average of τ_1 and τ_2, $\tau_m = \alpha_1 * \tau_1 + \alpha_2 * \tau_2$.

Using an automated cell segmentation routine in CellProfiler, the images were segmented into cells, nuclei, and cytoplasms (16). The following endpoints were extracted from the fluorescence lifetime data sets for both the NAD(P)H and FAD image for each cell: fluorescence intensity, mean fluorescence lifetime, α_1, τ_1, and τ_2. A redox ratio image was computed by dividing the NAD(P)H intensity by the FAD intensity at every pixel in the image. The average redox ratio for each cell was also extracted. As determined previously, the optical redox ratio, NAD(P)H mean lifetime, and FAD mean lifetime are independent measures of cellular metabolism (12) and a combination index, the optical metabolic imaging index, provides a robust endpoint for evaluating drug response (9). The OMI index was calculated for each cell as follows, $OMI\ Index = \frac{RR_i}{\langle RR \rangle} + \frac{NADH\tau m_i}{\langle NADH\tau m \rangle} - \frac{FAD\tau m_i}{\langle FAD\tau m \rangle}$ (9).

E.3.6 Immunofluorescence

Immunofluorescence labeling of cleaved caspase 3 and Ki67 was performed as previously described (9, 20). Briefly, gels were fixed with 2 mL of a 4% paraformaldehyde solution and neutralized with a 0.15 mol/L glycine solution. A 0.02% Triton X-100 solution was used to permeabolize cellular membranes. Gels soaked in a blocking solution (1% fatty acid-free BSA, 1% donkey serum) over night at room temperature. The next day, gels were incubated for 30 minutes at room temperature with 100 μl of the primary antibody solution: either anti-cleaved caspase 3 (Life Technologies) or anti-Ki67 (Life Technologies) diluted 1:100 in a 1% donkey serum PBS solution. Gels were washed 3X with PBS and 100 μl of the secondary antibody solution (goat anti-rabbit IgG FITC probe diluted 1:100 in a 1% donkey serum PBS solution) was added to each gel. Gels were washed 3X with PBS and 2X in water then mounted on slides with 30 μl of ProLong Antifade Solution (Molecular Probes). Positive staining was confirmed in mouse small intestine for Ki67 and mouse thymus for cleaved caspase 3. Immunofluorescence results are presented as the percentage of positively stained cells from 6 organoids imaged at 40X (1.3 NA).

E.3.7 Quantification of Cell Morphology

Cellular morphology was assessed from the NAD(P)H fluorescence lifetime image, integrated over time to yield an intensity image. Average cell size and nuclear-to-cytoplasm ratio (NCR) were extracted from the CellProfiler segmentation routine outputs. Average nucleus diameter was determined by manually measuring the longest axis through the center of each cell in ImageJ.

E.3.8 Statistical Analysis

A student's t-test with a Bonferoni correction for multiple comparisons was used to assess differences in immunofluorescence results, morphology, and fluorescence lifetime endpoints between fresh and frozen control organoids. Time course drug response OMI data was analyzed with multiple t-tests with a Bonferoni correction for multiple comparisons between control and drug treated organoids at each time point. For all statistical comparisons, an alpha level of 0.05 was used for significance. The number of cells per group varied between 30 and 300.

E.4 Results

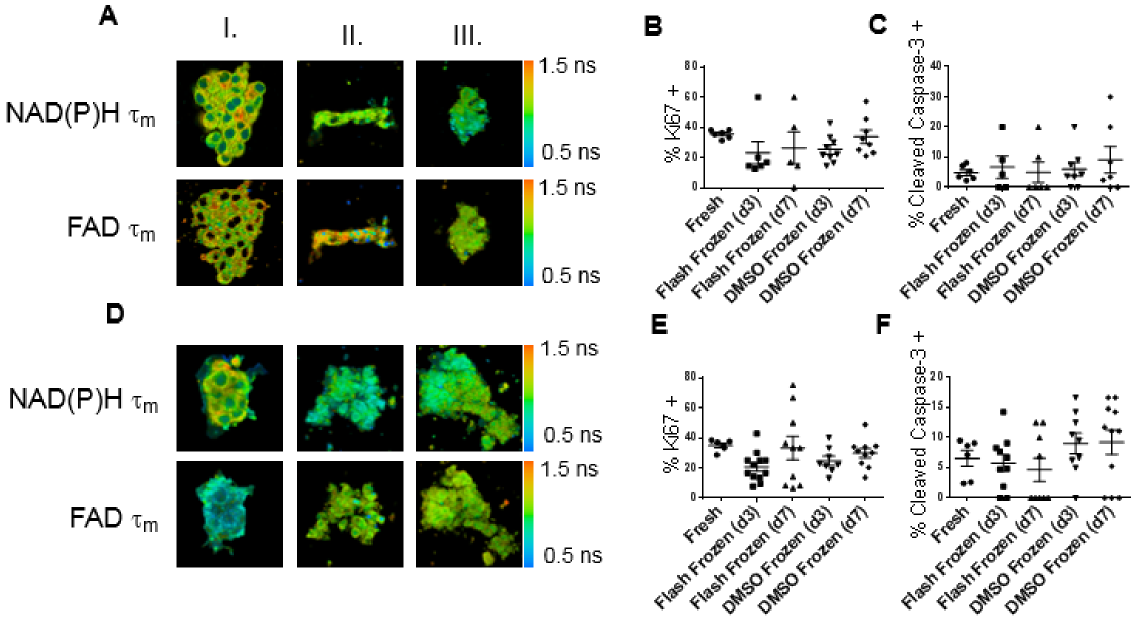

Figure E.1 Viability of organoids derived from frozen-thawed xenograft tumors. (A) Representative NAD(P)H τ_m and FAD τ_m images of BT474 organoids derived from fresh (I), flash-frozen (II), and DMSO frozen tissues (III). (B) Ki67 and (C) cleaved caspase 3 staining of control organoids derived from fresh, flash-frozen and DMSO frozen BT474 tumors. (D) Representative NAD(P)H τ_m and FAD τ_m images of HR6 organoids derived from fresh (I), flash-frozen (II), and DMSO frozen tissues (III). (E) Ki67 and (F) cleaved caspase 3 staining of control organoids derived from fresh, flash-frozen and DMSO frozen HR6 tumors. d3/d7 represents organoids grown for 3 or 7 days after generation.

E.4.1 Viability of Organoids Derived from Frozen-thawed Xenograft Samples

Organoids were successfully grown from fresh, flash-frozen, and DMSO frozen samples of BT474 xenograft tumors (Fig. E.1 A-C). The organoids generated from flash-frozen and DMSO frozen BT474 tissue samples had similar expression of Ki67 and cleaved caspase 3, markers of proliferation and apoptosis, respectively, as compared to organoids derived from a fresh BT474 tumor sample (Fig. E.1B, C). Likewise, the organoids generated from flash-frozen and DMSO frozen HR6 tumor samples grew (Fig. E.1D) and had similar percentages of Ki67 and cleaved caspase 3 positively stained cells as compared to organoids generated from fresh HR6 tissue (Fig. E.1E, F).

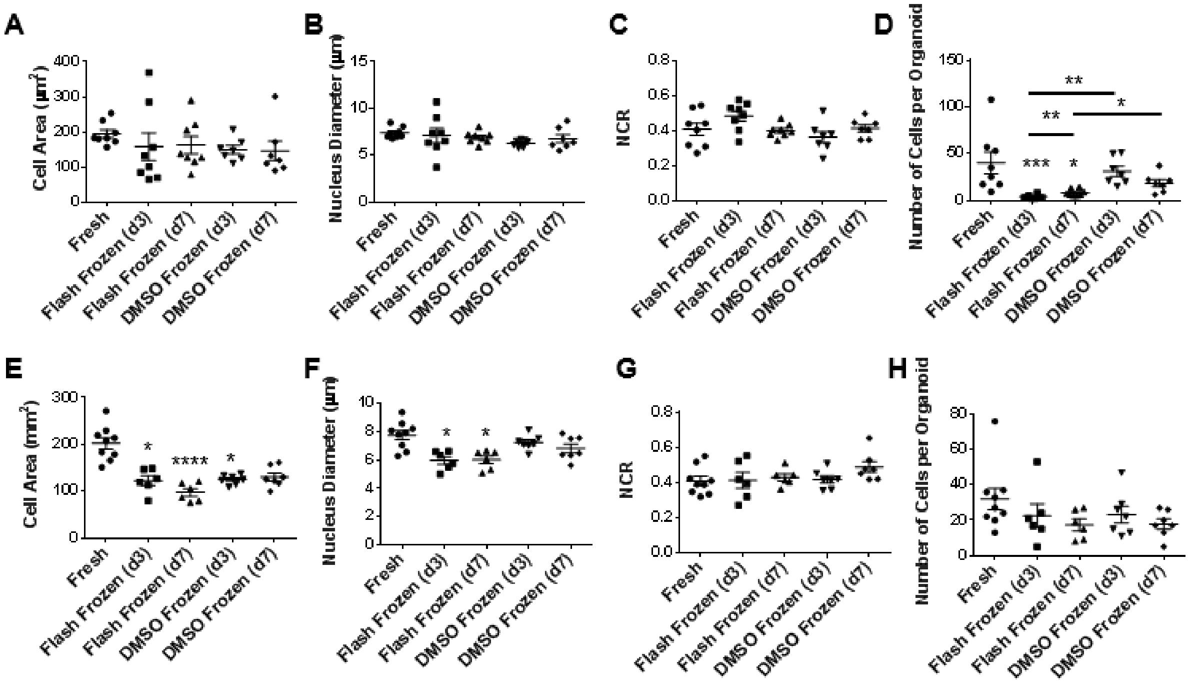

Figure E.2 Morphology of organoids derived from frozen/thawed xenograft tumors. (A) Cell area, (B) nucleus diameter, and (C) nucleus to cytoplasm ratio for BT474 organoids derived from fresh and frozen/thawed tissues. (D) Number of cells per organoid for BT474 organoids derived from fresh and frozen/thawed tissues. (E) Cell area, (F) nucleus diameter, and (G) nucleus to cytoplasm ratio for HR6 organoids derived from fresh and frozen/thawed tissues. (H) Number of cells per organoid for HR6 organoids derived from fresh and frozen/thawed tissues. d3/d7 represents organoids grown for 3 or 7 days after generation. * $p<0.05$; ** $p<0.01$, *** $p<0.001$, **** $p<0.0001$, versus Fresh except where indicated.

E.4.2 Morphology of Organoids Derived from Frozen-thawed Xenograft Samples

Next, cellular morphology was quantified and compared between organoids generated from fresh and frozen tissues. No change in cell area, nucleus diameter, or nucleus to cytoplasm ratio (NCR) was detected for the cells within organoids generated from frozen-thawed BT474 tumor samples compared to organoids generated from fresh BT474 tumor samples (Fig. E.2A-C). However, there was a significant reduction in the number of cells within each organoid for the organoids generated from flash-frozen BT474 tumors compared to organoids generated from fresh tissues (Fig. E.2 D). This reduction was significant for organoids grown for both 3 and 7 days

(Fig. E.2D). A significant reduction in number of cells within each organoid was not observed for organoids generated from BT474 DMSO frozen tissues (Fig. E.2D).

In contrast to the BT474 results, the cells grown from frozen HR6 tumor samples showed morphological differences compared to cells grown from fresh tumor samples. The cell area of HR6 cells was significantly reduced for cells within organoids generated from flash-frozen sections grown for 3 or 7 days, and in organoids generated from DMSO frozen tissue grown for 3 days (Fig. E.2E). Likewise, the nucleus diameter was significantly reduced for cells within organoids generated from flash-frozen tissue (Fig. E.2F). The NCR of HR6 cells did not significantly change due to either freezing method or growing time (Fig. E.2G). Also, no significant change in the number of HR6 cells within each organoid was detected for either freezing protocol or length of growing time (Fig. E.2H).

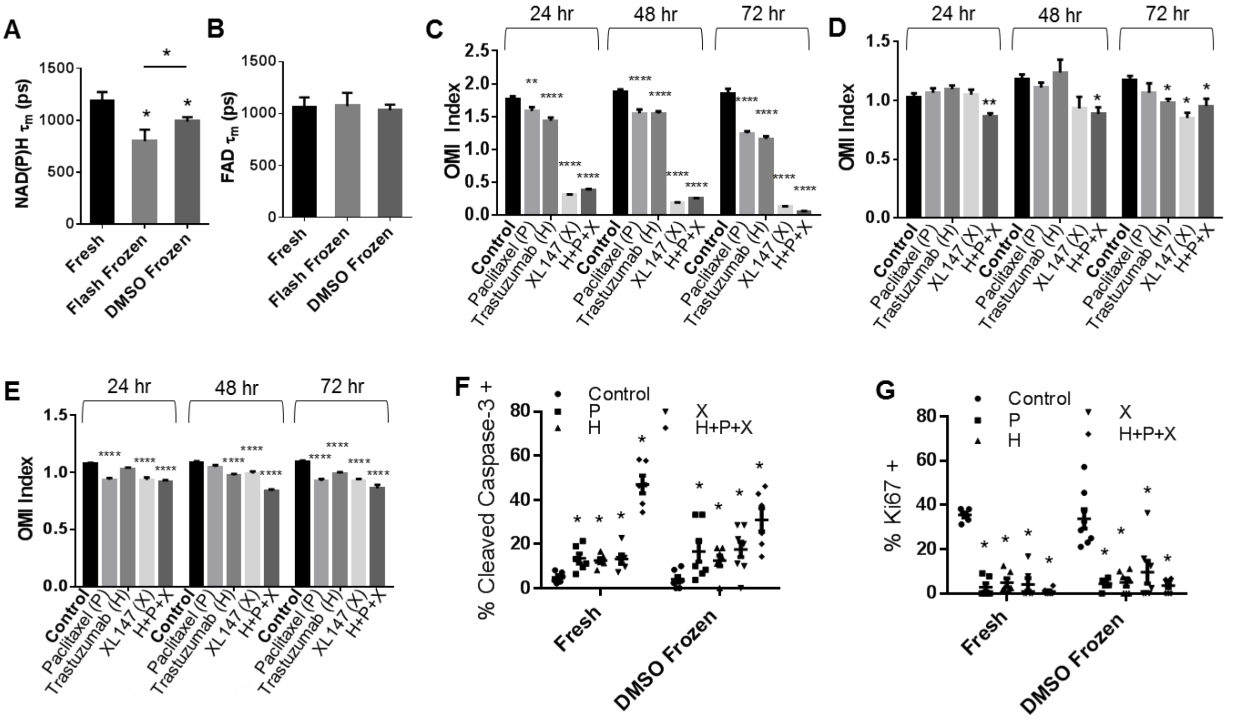

Figure E.3 Drug Response of BT474 Organoids Generated from Frozen Tissues (A) NAD(P)H τ_m and (B) FAD τ_m measured from BT474 organoids derived from fresh or frozen tissues grown for 7 days. * $p<0.05$ vs. Fresh, except where indicated. (C) Drug response of BT474 organoids derived from fresh tissue at 24, 48, and 72hr. (D) Drug response of BT474 organoids derived from flash-frozen tissues grown for 7 days and treated for 24, 48, and 72hr. (E) Drug response of BT474 organoids derived from DMSO frozen tissues grown for 7 days and treated for 24, 48, and 72hr. (F) Cleaved caspase 3 staining of 72 hr drug-treated organoids derived from fresh and DMSO frozen (grown for 7 days) tissues. (G) Ki67 staining of 72 hr drug-treated organoids derived from fresh and DMSO frozen (grown for 7 days) tissues. * $p<0.05$; ** $p<0.01$, *** $p<0.001$, **** $p<0.0001$ versus control.

E.4.3 Drug Response of BT474 Organoids Generated from Frozen Tissues

OMI endpoints were evaluated for metabolism differences between organoids grown from fresh tissues and organoids grown from frozen/thawed tissues. For the BT474 tumors, NAD(P)H τ_m was significantly decreased in cells from organoids generated with both freezing methods on day 7 (Fig. E.3A). However, FAD τ_m showed no significant differences between organoid generated from fresh and frozen BT474 tumors (Fig. E.3B). The 72-hour time course for drug response of BT474 organoids generated from fresh tissues showed a significant reduction in the

OMI index with paclitaxel (P), trastuzumab (H), XL147 (X), and the combination, H+P+X at 24hr, 48hr, and 72hr of drug treatment (Fig. E.3C). For the BT474 organoids derived from flash-frozen tissues grown for 7 days prior to drug treatment, the OMI index was significantly reduced with only the combination treatment, H+P+X, at 24 and 48 hr of drug exposure (Fig. E.3D). By 72 hr, trastuzumab, XL147, and H+P+X induced significant reductions in the OMI index (Fig. E.3D). Organoids derived from the BT474 tumor sample slowly frozen in DMSO supplemented media, showed response to anti-cancer drugs (Fig. E.3E). By 72hr, paclitaxel, trastuzumab, XL147, and H+P+X treated organoids all had significant reductions in OMI index (Fig. E.3E). Immunofluorescence staining of Ki67 and cleaved caspase 3 of organoids derived from fresh and DMSO frozen BT474 tumors treated for 72hr with anti-cancer drugs, revealed increased cleaved caspase 3 expression in organoids treated with paclitaxel, trastuzumab, XL147, and H+P+X (Fig. E.3F). Likewise, reduced expression of Ki67 was observed in organoids treated with all anti-cancer therapies (Fig. E.3G).

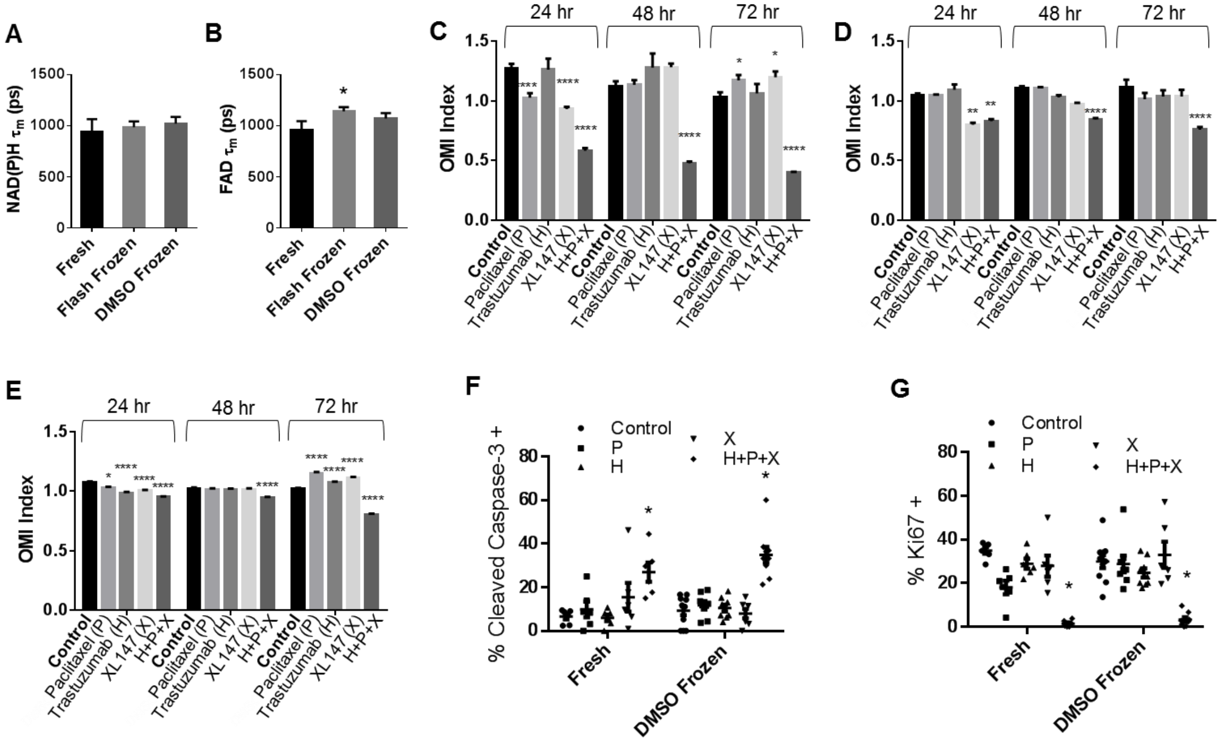

Figure E.4 Drug Response of HR6 Organoids Generated from Frozen Tissues (A) NAD(P)H τ_m and (B) FAD τ_m measured from HR6 organoids derived from fresh or frozen tissues grown for 7 days. * $p<0.05$ vs. Fresh. (C) Drug response of HR6 organoids derived from fresh tissue at 24, 48, and 72hr. (D) Drug response of HR6 organoids derived from flash-frozen tissues grown for 7 days and treated for 24, 48, and 72hr. (E) Drug response of HR6 organoids derived from DMSO frozen tissues grown for 7 days and treated for 24, 48, and 72hr. (F) Cleaved caspase 3 staining of 72 hr drug-treated organoids derived from fresh and DMSO frozen (grown for 7 days) tissues. (G) Ki67 staining of 72hr drug-treated organoids derived from fresh and DMSO frozen (grown for 7 days) tissues. * $p<0.05$; ** $p<0.01$, *** $p<0.001$, **** $p<0.0001$, versus control.

E.4.4 Drug Response of HR6 Organoids Generated from Frozen Tissues

The effect of freezing HR6 tumors before generating organoids was also evaluated with OMI of organoid drug response. No change in NAD(P)H τ_m was observed between organoids generated from fresh HR6 tumors and flash frozen or DMSO frozen tumors on day 7 after organoid generation (Fig. E.4A). A slight increase in FAD τ_m was observed in organoids generated from flash-frozen HR6 tumors compared to organoids generated from fresh HR6 tumors ($p<0.05$, Fig.

E.4B); however, no significant change in FAD τ_m was observed in the organoids generated from DMSO frozen HR6 tissue ($p>0.05$, Fig. E.4B).

Organoids generated from fresh HR6 tumors have a significantly reduced OMI index at 24 hr due to paclitaxel, trastuzumab, and H+P+X treatment (Fig. E.4C). By 48 and 72hr, only H+P+X induces a significant reduction in the OMI index (Fig. E.4C). For the HR6 organoids derived from flash-frozen HR6 tumors, at 24hr, both XL147 and H+P+X induce significant reductions in the OMI index (Fig. E.4D). By 48 and 72hr, only the H+P+X treated organoids have a significant reduction in OMI index (Fig. E.4D). Likewise, HR6 organoids derived from the DMSO frozen tumor showed significant reductions in OMI index with paclitaxel, trastuzumab, XL147, and H+P+X treatment at 24hr (Fig. E.4E). By 48hr and 72hr, only the H+P+X treatment induced a significant reduction in the OMI index (Fig. E.4E). At 72hr, the paclitaxel and XL147 treated HR6 organoids induced a significant increase ($p<0.05$) in the OMI index in both organoids generated from fresh (Fig. E.4C) and DMSO frozen tumors (Fig. E.4E), but this increase was not detected in the organoids derived from flash-frozen tumors (Fig. E.4D). Immunofluorescence staining of cleaved caspase 3 and Ki67 of organoids derived from fresh and DMSO frozen tumors treated for 72hr revealed an increased proportion of cells stained cleaved caspase 3 positive and a reduced proportion of cells stained Ki67 positive in H+P+X treated HR6 organoids (Fig. E.4F, G).

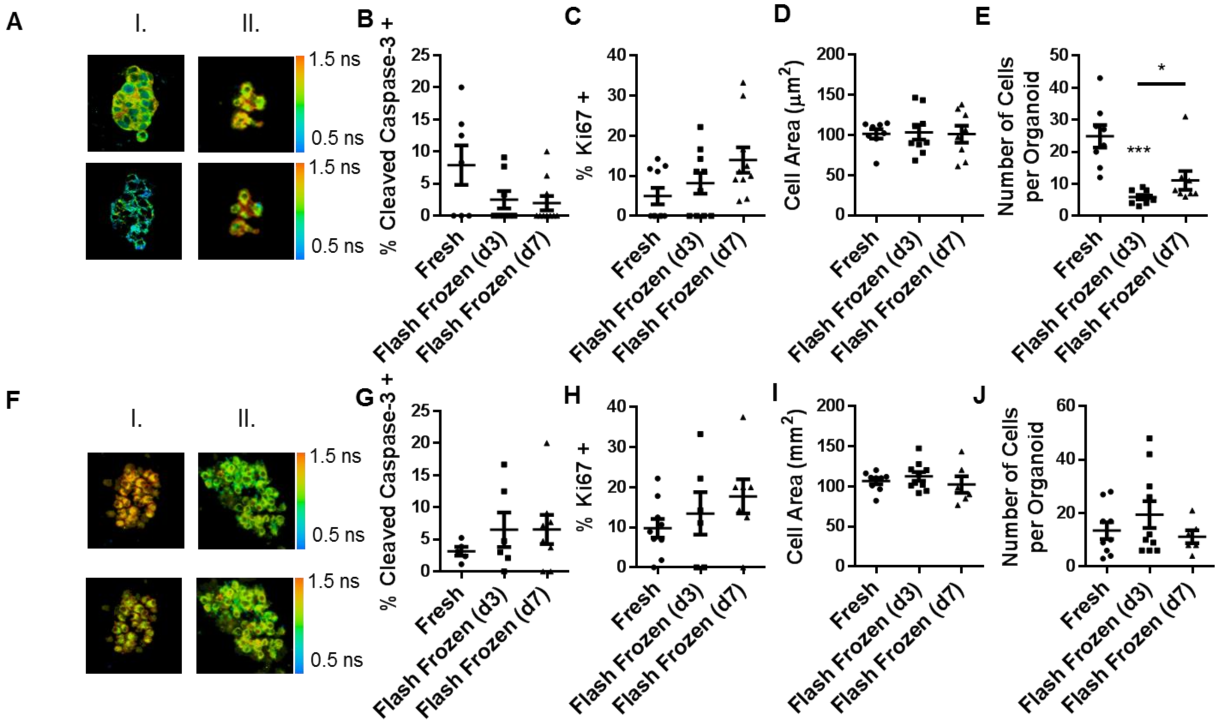

Figure E.5 Viability of Organoids Derived from Frozen-thawed Human Breast Cancer Biopsies (A) Representative NAD(P)H τ_m and FAD τ_m images of organoids derived from fresh (I) and flash frozen/thawed (II) Patient Sample 1. (B) Cleaved caspase 3 staining, (C) Ki67 staining, (D) cell area, and (E) number of cells per organoid for organoids derived from fresh and flash-frozen/thawed Patient Sample 1. (F) Representative NAD(P)H τ_m and FAD τ_m images of organoids derived from fresh (I) and flash frozen/thawed (II) Patient Sample 2. (G) Cleaved caspase 3 staining, (H) Ki67 staining, (I) cell area, and (J) number of cells per organoid for organoids derived from fresh and flash-frozen/thawed Patient Sample 2. * $p<0.05$; *** $p<0.001$, versus Fresh, except as indicated. d3/d7 represents organoids grown for 3 or 7 days after generation.

E.4.5 Viability of Organoids Derived from Frozen-thawed Human Breast Cancer Biopsies

To test whether organoids could be grown from flash frozen primary human breast tumors, two primary human breast cancer biopsies were acquired and cut into two pieces, one for fresh organoid generation and one which was flash-frozen, stored at -80°C for months (mimicking current tissue banking procedures), and then thawed and generated into organoids. For Patient 1,organoids grew from both the fresh primary human tumor sample (Fig. E.5AI) and from the flash-frozen/thawed sample (Fig. E.5AII). Immunofluorescence staining revealed similar percentages of cleaved caspase 3 positive and Ki67 positive cells between organoids generated from fresh tumor and organoids generated from flash-frozen tumor (Fig. E.5B, C). No differences were observed in Ki67 and cleaved caspase 3 staining between organoids generated from flash-frozen tumor grown for 3 or 7 days (Fig. E.5B, C). Likewise, there were no differences in the morphology of the cells, cell size, nucleus diameter or NCR ratio, between organoids generated from fresh tumor and organoids derived from the flash-frozen tumor (Fig. E.5D, and Fig. E.6). However, there was a significant reduction in the number of cells per organoid that were grown 3 days after generating organoids from the flash-frozen and thawed tumor from Patient 1 compared to organoids generated from fresh tumor from the same patient (Fig. E.5E). No significant difference in number of cells within each organoid was detected for the organoids derived from flash-frozen tumor grown for 7 days versus organoids derived from fresh tumor from the same patient (Fig. 5E).

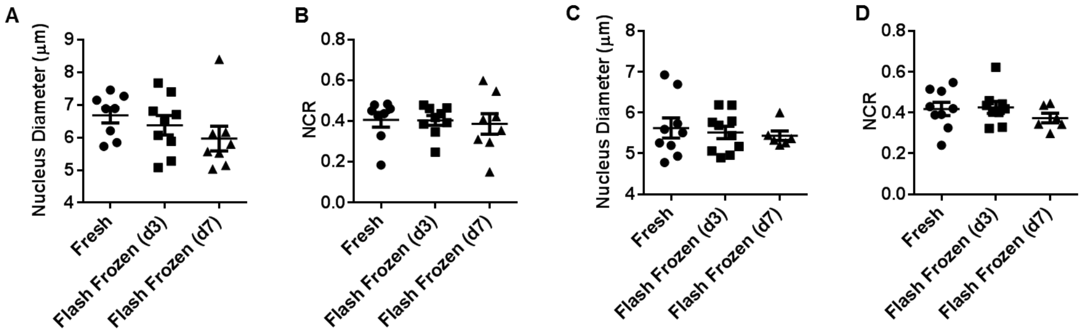

Figure E.6 Morphology of Organoids Derived from Frozen-thawed Human Breast Cancer Biopsies (A) Nucleus diameter and (B) nuclear to cytoplasm ratio (NCR) for organoids derived from fresh and flash-frozen sections of Patient Sample 1. (C) Nucleus diameter and (D) nuclear to cytoplasm ratio (NCR) for organoids derived from fresh and flash-frozen sections of Patient Sample 2. d3/d7 represents organoids grown for 3 or 7 days after generation.

Likewise, organoids from Patient Sample 2 grew robustly from fresh and flash-frozen tissues (Fig. E.5F, G-H). No significant changes were observed in the percentage of cells that stained cleaved caspase positive or Ki67 positive between organoids derived from fresh tumor and organoids derived from flash-frozen tumor grown for 3 or 7 days (Fig. E.5G, H). Likewise, no significant differences in cell morphology (cell area, nucleus diameter, or NCR) were detected between organoids derived from fresh tumor versus organoids derived from flash-frozen tumor for Patient 2 (Fig. E.5I, and Fig. E.6). Additionally, the number of cells within each organoid remained unchanged in organoids derived from flash-frozen tumor verses organoids derived from fresh tumor for Patient 2 (Fig. E.5J).

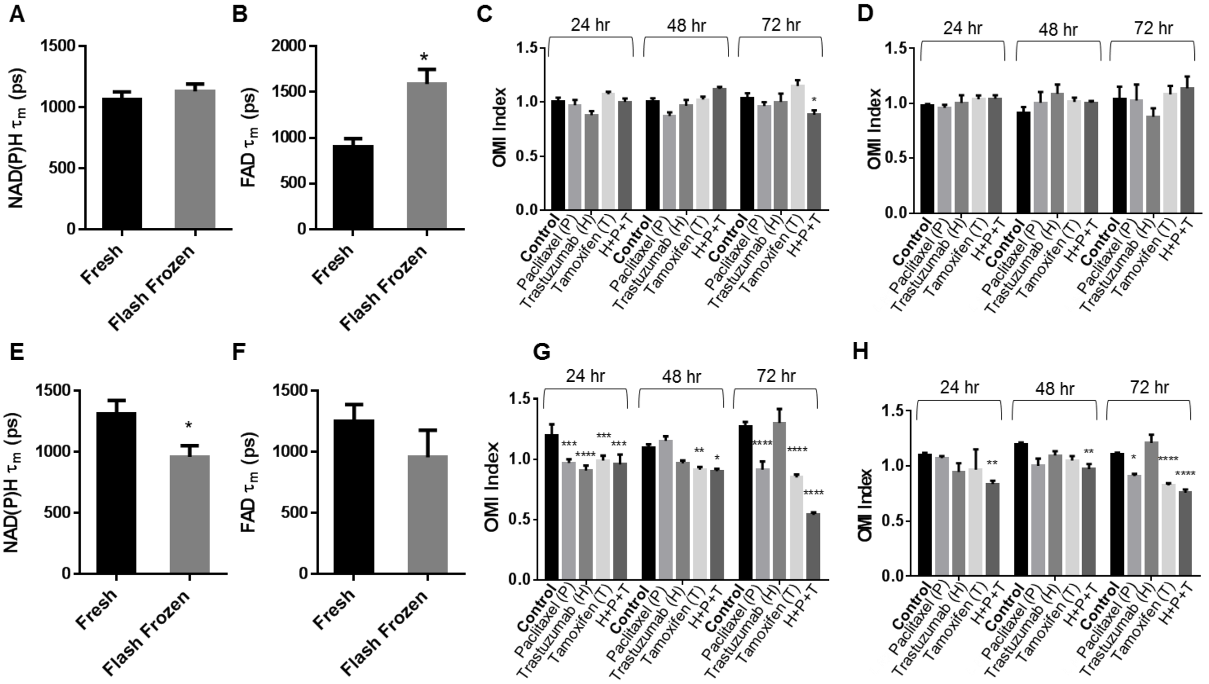

Figure E.7 Drug Response of Organoids Generated from Flash-Frozen Human Breast Cancer Biopsies (A) NAD(P)H τ_m and (B) FAD τ_m measured from Patient Sample 1 organoids derived from fresh or frozen tissues (grown for 7 days). * p<0.05, versus Fresh. (C) Drug response of Patient Sample 1 organoids derived from fresh tissue at 24, 48, and 72hr. (D) Drug response of Patient Sample 1 organoids derived from flash-frozen tissues grown for 7 days and treated for 24, 48, and 72hr. (E) NAD(P)H τ_m and (F) FAD τ_m measured from Patient Sample 2 organoids derived from fresh or frozen tissues. * p<0.05, versus Fresh. (G) Drug response of Patient Sample 2 organoids derived from fresh tissue at 24, 48, and 72hr. (H) Drug response of Patient Sample 2 organoids derived from flash-frozen tissues grown for 7 days and treated for 24, 48, and 72hr. * p<0.05; ** p<0.01, *** p<0.001, **** p<0.0001, versus control.

E.4.6 Drug Response of Organoids Generated from Flash-Frozen Human Breast Cancer Biopsies

As with the xenograft tumors, OMI measurements of drug response were compared between organoids derived from fresh and flash-frozen patient tumor (frozen preparation was allowed to grow for 3 or 7 days before imaging and treatment). Both samples were derived from estrogen receptor positive, HER2 negative tumors and the subsequent organoids were treated with the clinically relevant drugs, paclitaxel (P), trastuzumab (H), tamoxifen (T), and the combination, H+P+T. For Patient Sample 1, no difference in NAD(P)H τ_m was detected between the organoids generated from fresh tumor and flash-frozen tumor grown for 7 days (Fig. E.7A). However, a significant increase in FAD τ_m was detected between organoids generated from fresh versus flash-frozen tumor from Patient 1 ($p<0.05$, Fig. E.7B). The OMI index was significantly decreased with H+P+T after 72 hr of treatment in organoids derived from fresh tumor from Patient 1 (Fig. E.7C). None of the treatments induced a significant reduction in the OMI index for the organoids generated from flash-frozen tumor, grown for 3 (Table E.1) or 7 days (Fig. E.7D).

Finally, organoids derived from Patient Sample 2 showed significant response to the anti-cancer drugs. First, NAD(P)H τ_m was significantly reduced in the organoids derived from the flash-frozen tumor compared to the organoids derived from fresh tumor (Fig. E.7E), but the FAD τ_m showed no significant difference (Fig. E.7F). The OMI index was significantly reduced in organoids derived from fresh tumor due to all drug treatments at 24hr, tamoxifen and H+P+T at 48hr, and paclitaxel, tamoxifen, and H+P+T at 72 hr (Fig. E.7G). Likewise, the paclitaxel, tamoxifen, and H+P+T treated organoids derived from the flash-frozen tumor showed significant reductions in OMI index at 72 hr (Fig. E.7H), while only the combination treatment, H+P+T, induced reductions in the OMI index at 24 and 48hr. Altogether, these results suggest that viable organoids can be grown from frozen tumors and the cells remain sensitive to anti-cancer drugs.

Table E.1 Drug induced changes in OMI index at 72hr drug treatment for different organoid generation protocols.

Sample	Drug	Fresh	Flash Frozen d3	Flash Frozen d7	DMSO Frozen d3	DMSO Frozen d7
BT474	Paclitaxel	Decrease	No change	No change	Decrease	Decrease
	Trastuzumab	Decrease	No change	Decrease	No change	Decrease
	XL147	Decrease	Decrease	Decrease	Decrease	Decrease
	H+P+X	Decrease	Decrease	Decrease	Decrease	Decrease
HR6	Paclitaxel	Increase	No change	No change	Increase	Increase
	Trastuzumab	No change	No change	No change	Increase	Increase
	XL147	Increase	No change	No change	Increase	Increase
	H+P+X	Decrease	Decrease	Decrease	Decrease	Decrease
Patient Sample 1	Paclitaxel	No change	No change	No change		
	Trastuzumab	No change	No change	No change		
	Tamoxifen	No change	No change	No change		
	H+P+T	Decrease	No change	No change		
Patient Sample 2	Paclitaxel	Decrease	Decrease	Decrease		
	Trastuzumab	No change	No change	No change		
	Tamoxifen	Decrease	Decrease	Decrease		
	H+P+T	Decrease	Decrease	Decrease		

E.4.7 Comparison of Freezing Methods

OMI measured drug response was compared between fresh-tissue generated organoids and organoids generated from frozen-thawed tissues. Both freezing methods, flash frozen and slow, DMSO frozen were compared for optimal drug response outcomes, as were the recovery times, 3 or 7 days, between organoid generation and drug treatment. The response of organoids grown for 7 days and treated for 72 hr better reflected the response of fresh-tissue generated organoids with only 4/24 (16%) inconsistences versus 7/24 (30%) inconsistencies for organoids grown for 3 days before treatment (Table E.1). The response of the organoids derived from DMSO frozen tissues resembled that of the organoids derived from fresh tissues after 72hr of drug treatment with fewer inconsistencies than flash-frozen preparations, 3/16 (19%) vs. 9/32 (28%) (Table E.1).

E.5 Discussion

Primary cells grown in 3D culture as organoids provide a robust and relevant model for investigations of cancer progression, drug development, and individualized treatment planning in the clinic. Typically, organoids are generated by mechanical dissociation of fresh, primary tissue into small pieces that are embedded and grown in collagen or extracellular matrix gels. Organoid culture of primary cells more accurately preserves cell-cell interactions and recapitulates the *in vivo* environment than 2D culture of single cell lines (1, 2, 10, 21). However, current organoid generation protocols require fresh tissue (9, 22), which limits the use of primary human tumor organoids to labs in close proximity to hospitals, and also limits the applicability of organoid-based individualized drug screens to hospitals with expertise in organoid generation. In order to ensure widespread use of primary tumor organoids for research and clinical treatment planning, tissue preservation methods must be assessed and alternative organoid generation protocols developed. This study tested two methods of tissue preservation by freezing, which would maintain cancer tissue for subsequent organoid generation and drug response studies. Both flash-freezing tissue in liquid nitrogen and slow freezing in media supplemented with 5% DMSO were tested, because flash freezing is the current method for tissue banking yet slow freezing in DMSO is known to preserve tissue viability (23). Four samples were used, two HER2 overexpressing xenografts and two estrogen receptor positive human breast cancer samples. For all samples, organoids were generated from a piece of the fresh tissue and compared with organoids generated from a portion of the same tumor that was frozen and thawed.

Organoids grew from all fresh and frozen tissue samples, for both the xenograft tissues (Fig 1) and the human biopsies (Fig. E.5). However, for two of the samples frozen by flash freezing in liquid nitrogen, the BT474 xenograft and one of the patient samples, there was a significant decrease in the number of cells per organoid, suggesting that some cells do not survive the freeze/thawing process as well as others. However, for the cells that did survive the freeze/thaw process, no significant differences in cellular expression of proliferation or apoptosis proteins were (Fig. E.1B, C, E, F; Fig. E.5B, C, G, H), suggesting the organoids generated from frozen/thawed tissues are viable and proliferate similarly to the organoids generated from fresh tissues. Furthermore, no significant differences in cellular morphology were quantified for the cells generated from frozen/thawed BT474 tissues or from the frozen/thawed patient samples (Fig. E.2A-C, E-G; Fig. E.5A, E, B, I). The HR6 cells did show significant reductions in cell area and nucleus diameter (Fig. E.2E, F), which may reflect that either smaller HR6 cells were more suited to survive the freeze/thaw protocols or that the freeze/thaw process induces changes within the HR6 cells which reduced the cell size. Prior studies of frozen/thawed cells have demonstrated that cells exposed to flash freezing methods have reduced volumes upon thawing compared to non-frozen control cells and these morphological differences are reduced in slow-frozen cells (23).

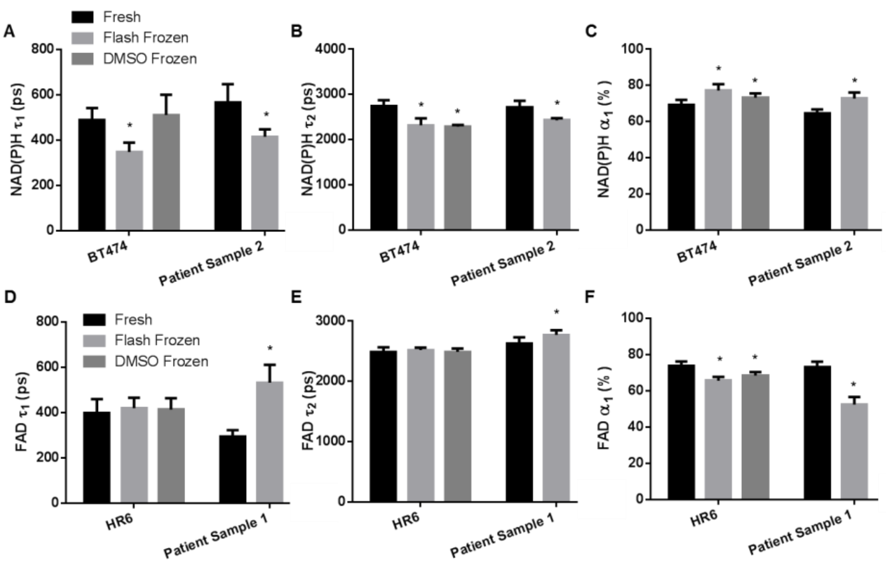

Figure E.8 Fluorescence lifetime components of organoids derived from frozen/thawed tissue. (A) NAD(P)H τ_1, (B) NAD(P)H τ_2, and (C) NAD(P)H α_1 for organoids derived from fresh tissues and organoids derived from frozen tissues and grown for 7 days. (D) FAD τ_1, (E) FAD τ_2, and (F) FAD α_1 for organoids derived from fresh tissues and organoids derived from frozen tissues and grown for 7 days. * $p<0.05$ vs. Fresh

The fluorescence lifetime results indicate that the freeze/thaw protocols induce significant biochemical changes within the cells. In 2/4 samples (BT474 Fig. E.3A; Patient 2 Fig. E.7E), the mean NAD(P)H lifetime decreased in organoids derived from frozen/thawed tissue compared to organoids derived from fresh tissues. Likewise, in 2/4 samples (HR6 Fig. E.4B, Patient 1 Fig. E.7B) the mean FAD lifetime increased in organoids derived from frozen/thawed tissue compared to organoids derived from fresh tissue. The changes in the free lifetime components (τ_1 for NAD(P)H and τ_2 for FAD, Fig. E.8) suggest morphological changes to NAD(P)H and FAD, and changes in the microenvironment surrounding NAD(P)H and FAD (17-19). The changes in bound protein fluorescence lifetimes (τ_2 for NAD(P)H and τ_1 for FAD, Fig. E.8) may be indicative of morphological changes in the enzyme-substrate conformations, changes in preferred protein binding, or differences in the microenvironment of surrounding NAD(P)H and FAD enzyme structures (17, 19). A previous study of *in vivo*, freshly excised tissue, and frozen hamster cheek pouch tissues also identified an increased FAD τ_m in frozen tissues (13). A cryopreservation study has previously identified freezing-induced inactivation of metabolic enzymes, such as lactate dehydrogenase, and suggest some intracellular molecules may have protective properties (24), further indicating changes in metabolism coenzyme environment after tissue freezing.

The OMI index is a robust, dynamic endpoint of cellular metabolism and has been shown to accurately measure early drug response in anti-cancer drug-treated cells, tumors imaged *in vivo*, and organoids (9, 12). We used the OMI index to test the drug-response of organoids generated from frozen/thawed tissues, and compared this response with that of fresh organoids. OMI detects drug-induced changes in cellular metabolism and the frozen/thawed organoids had significant differences in basal metabolism endpoints compared with fresh organoids, so all comparisons were between DMSO/IgG control and drug-treated organoids within each sample, preparation protocol, and time point. The OMI index is computed per group per time point and normalizes data to the means of the data set. As demonstrated previously (9), significant reductions in the OMI index between control and drug treated organoids indicate response. Drug induced increases in apoptosis and decreases in proliferation verify that a decrease in the OMI index of organoids tumors correlates with drug response (Fig. E.3, 4).

The OMI index indicated similar drug response for organoids derived from frozen/thawed tissues compared to the drug response from organoids derived from fresh tissues. However, the frozen/thawed tissues were less sensitive to anti-cancer drugs. Drugs induced a smaller change in OMI index of organoids derived from frozen/thawed tissues (Fig. E.3C-E, Fig. E.4C-E, Fig. E.7 G-H) suggesting the dynamic range of the OMI index was dampened in the organoids generated from frozen/thawed tissue. The dynamic range of the drug-induced metabolism changes may be reduced due to damage induced by the freezing protocols on the metabolic coenzymes, enzymes, and substrates (24). Furthermore, the cells that survive the freezing protocols may be more resistant to anti-cancer drugs. As indicated by 5 drug treatments that failed to induce the expected response by 72hr of treatment in OMI index (Table E.1) in organoids generated from flash frozen tissues, this freezing protocol may select for more resistant cells. The mutations and phenotypic differences that enable cells to evade drug treatment may enable the cells to survive the flash-frozen protocol.

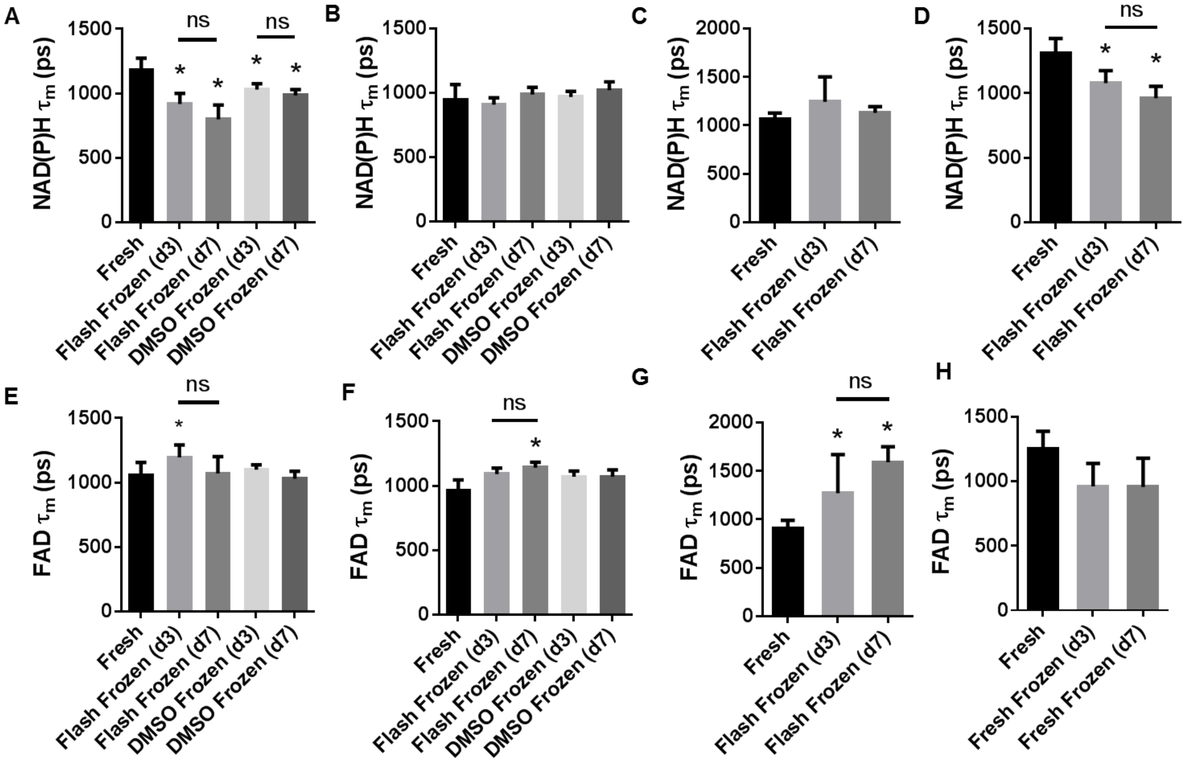

Figure E.9 Mean NAD(P)H and FAD fluorescence lifetimes of organoids derived from frozen/thawed tissue. NAD(P)H τ_m of (A) BT474, (B) HR6, (C) Patient Sample 1, and (D) Patient Sample 2 organoids grown from fresh and frozen tissue. FAD τ_m of (E) BT474, (F) HR6, (G) Patient Sample 1, and (H) Patient Sample 2 organoids grown from fresh and frozen tissue. d3/d7 represents organoids grown for 3 or 7 days after generation. * $p<0.05$ vs. Fresh; ns = not significant

In order to investigate whether cells required a recovery growth period following freeze/thaw protocols, all experiments were repeated on organoids grown for 3 or 7 days. No significant differences were observed in cellular morphology, rates of proliferation or apoptosis, NAD(P)H τ_m, or FAD τ_m values of control organoids for any sample between the organoids generated from flash frozen tissue grown for 3 versus 7 days (Fig. E.1, 2, 5, and Fig. E.9). This observation held for organoids generated from DMSO frozen tissues as well, and suggests the effects of the freezing processes on cellular metabolism persist for at least a week of growth. A slight, but significant, increase in the number of cells per organoid was observed on day 7 versus day 3 in the organoids derived from the flash-frozen BT747 tumor and Patient Sample 1 (Fig.

E.2D, Fig. E.5F). OMI drug response studies of organoids grown for either 3 or 7 days from frozen/thawed tissues yielded similar results; however, additional response (12.5% fewer inconsistencies) was detected in organoids grown for 7 days (Table E.1), suggesting a longer recovery time yields better response data. The lack of response observed in organoids grown for only 3 days and then treated with anti-cancer drugs may suggest inherent selectivity of non-responsive cells which are more suited to surviving the freeze/thaw process, or that the freeze/thaw process induces a survival response within the cells which enable them to also survive the cancer drugs.

The xenograft studies investigated the differences in organoids grown from flash-frozen tissues and slow, DMSO frozen tissues. No significant differences were observed in cell proliferation, apoptosis, or morphology between organoids derived from tissues frozen by either method (Fig. E.1, 2). A significantly greater number of cells per organoid were grown from the BT474 DMSO frozen tissues than the flash frozen tissues (Fig. E.2D). However, this was not observed in the HR6 tumors. The mean NAD(P)H lifetime of BT474 organoids derived from DMSO frozen tissue and the mean FAD lifetime of HR6 organoids derived from DMSO frozen tissue were closer to the values of organoids derived from fresh tissue than organoids derived from flash frozen tissue, suggesting that slow, DMSO freezing of tissues may yield organoids with metabolic behaviors more similar to the metabolic behaviors of organoids derived from fresh tissues than flash-frozen tissues. Furthermore, OMI-measured drug response revealed more consistent OMI drug response behavior of the organoids derived from DMSO frozen tissues then organoids derived from flash frozen tissues (Table E.1).

Recent studies have demonstrated the wealth of knowledge that can be gained from primary tumor organoid research (2, 9, 10, 22). Furthermore, as we have demonstrated, OMI drug response studies of organoids reflect *in vivo* drug response (9). However, organoid generation protocols require immediate processing of fresh tissue into organoids. This limits the application of organoid-based experiments and drug-response studies to medical centers with both operating rooms and research facilities. The purpose of this study was to investigate tissue-freezing methods that would enable preservation of tissues for subsequent organoid generation. This opens up the applicability of clinical organoid drug screens and organoid research by enabling shipment of tissues to centralized testing sites and research labs. Primary tissue samples are routinely flash frozen for storage in tissue banks. Therefore, this study evaluated flash-frozen primary human breast cancer samples, to determine if organoids could be grown from these samples. Furthermore, this study compared the viability and drug response of organoids derived from flash frozen tissue to organoids derived from DMSO freezing protocols, which is the standard method of cell preservation used in cell culture. Our results show that organoids can be grown from flash-frozen or slow, DMSO frozen tissues and these organoids have similar morphologies and rates of proliferation and apoptosis as organoids derived from fresh tissues. Furthermore, while the freezing process effects the basal metabolic rate of the cells, OMI can be used to detect drug response of organoids derived from frozen-thawed tissues. Altogether these results suggest that when possible, slow freezing bulk tissues in DMSO supplemented media induces fewer changes in organoid cellular metabolism and yields drug-response more similar to that of organoids derived from fresh tissues. However, viable organoids can be grown from flash-frozen tissues and present an alternative tissue source if fresh or DMSO frozen tissues are not available, as in current tissue banks.

E.6 Acknowledgements

This work was supported by funding sources that include the NCI SPORE in Breast Cancer (P50 CA098131), ASLMS Student Research Grant (AJW), NSF Graduate Research Fellowship (DGE-0909667; AJW), DOD Breast Cancer Research Program (DOD-BC121998), NIH (NCI R01 CA185747), and Mary Kay Foundation (067-14).

E.7 References

1. Debnath J, Brugge JS. Modelling glandular epithelial cancers in three-dimensional cultures. Nature reviews Cancer. 2005;5(9):675-88.
2. Griffith LG, Swartz MA. Capturing complex 3D tissue physiology in vitro. Nature reviews Molecular cell biology. 2006;7(3):211-24.
3. Gudjonsson T, Ronnov-Jessen L, Villadsen R, Bissell MJ, Petersen OW. To create the correct microenvironment: three-dimensional heterotypic collagen assays for human breast epithelial morphogenesis and neoplasia. Methods. 2003;30(3):247-55.
4. Kamb A. What's wrong with our cancer models? Nature reviews Drug discovery. 2005;4(2):161-5.
5. Voskoglou-Nomikos T, Pater JL, Seymour L. Clinical predictive value of the in vitro cell line, human xenograft, and mouse allograft preclinical cancer models. Clin Cancer Res. 2003;9(11):4227-39.
6. Beck JN, Singh A, Rothenberg AR, Elisseeff JH, Ewald AJ. The independent roles of mechanical, structural and adhesion characteristics of 3D hydrogels on the regulation of cancer invasion and dissemination. Biomaterials. 2013;34(37):9486-95.
7. Cheung KJ, Ewald AJ. Illuminating breast cancer invasion: diverse roles for cell-cell interactions. Current opinion in cell biology. 2014;30:99-111.
8. Nguyen-Ngoc KV, Shamir ER, Huebner RJ, Beck JN, Cheung KJ, Ewald AJ. 3D culture assays of murine mammary branching morphogenesis and epithelial invasion. Methods in molecular biology. 2015;1189:135-62.
9. Walsh AJ, Cook RS, Sanders ME, Aurisicchio L, Ciliberto G, Arteaga CL, Skala MC. Quantitative optical imaging of primary tumor organoid metabolism predicts drug response in breast cancer. Cancer Res. 2014;74(18):5184-94.
10. Campbell JJ, Davidenko N, Caffarel MM, Cameron RE, Watson CJ. A multifunctional 3D co-culture system for studies of mammary tissue morphogenesis and stem cell biology. PLoS One. 2011;6(9):e25661.

11. Ritter CA, Perez-Torres M, Rinehart C, Guix M, Dugger T, Engelman JA, Arteaga CL. Human breast cancer cells selected for resistance to trastuzumab in vivo overexpress epidermal growth factor receptor and ErbB ligands and remain dependent on the ErbB receptor network. Clin Cancer Res. 2007;13(16):4909-19.

12. Walsh AJ, Cook RS, Manning HC, Hicks DJ, Lafontant A, Arteaga CL, Skala MC. Optical metabolic imaging identifies glycolytic levels, subtypes, and early-treatment response in breast cancer. Cancer Res. 2013;73(20):6164-74.

13. Walsh AJ, Poole KM, Duvall CL, Skala MC. Ex vivo optical metabolic measurements from cultured tissue reflect in vivo tissue status. Journal of biomedical optics. 2012;17(11):116015.

14. Skala MC, Riching KM, Bird DK, Gendron-Fitzpatrick A, Eickhoff J, Eliceiri KW, Keely PJ, Ramanujam N. In vivo multiphoton fluorescence lifetime imaging of protein-bound and free nicotinamide adenine dinucleotide in normal and precancerous epithelia. Journal of biomedical optics. 2007;12(2):024014.

15. Skala MC, Riching KM, Gendron-Fitzpatrick A, Eickhoff J, Eliceiri KW, White JG, Ramanujam N. In vivo multiphoton microscopy of NADH and FAD redox states, fluorescence lifetimes, and cellular morphology in precancerous epithelia. Proc Natl Acad Sci U S A. 2007;104(49):19494-9.

16. Walsh AJ, Skala MC. An automated image processing routine for segmentation of cell cytoplasms in high-resolution autofluorescence images. SPIE Proceedings. 2014;8948(56).

17. Lakowicz JR, Szmacinski H, Nowaczyk K, Johnson ML. Fluorescence Lifetime Imaging of Free and Protein-Bound Nadh. Proc Natl Acad Sci U S A. 1992;89(4):1271-5.

18. Nakashima N, Yoshihara K, Tanaka F, Yagi K. Picosecond fluorescence lifetime of the coenzyme of D-amino acid oxidase. J Biol Chem. 1980;255(11):5261-3.

19. Lakowicz J. Principles of fluorescence spectroscopy. New York: Plenum Publishers; 1999.

20. Wozniak MA, Keely PJ. Use of three-dimensional collagen gels to study mechanotransduction in T47D breast epithelial cells. Biol Proced Online. 2005;7:144-61.

21. Nelson CM, Vanduijn MM, Inman JL, Fletcher DA, Bissell MJ. Tissue geometry determines sites of mammary branching morphogenesis in organotypic cultures. Science. 2006;314(5797):298-300.

22. Nguyen-Ngoc KV, Cheung KJ, Brenot A, Shamir ER, Gray RS, Hines WC, Yaswen P, Werb Z, Ewald AJ. ECM microenvironment regulates collective migration and local dissemination in normal and malignant mammary epithelium. Proc Natl Acad Sci U S A. 2012;109(39):E2595-604.

23. Mazur P. Manifestations of injury in yeast cells exposed to subzero temperatures. I. Morphological changes in freeze-substituted and in "frozen-thawed" cells. Journal of bacteriology. 1961;82:662-72.

24. Carpenter JF, Crowe JH. The Mechanism of Cryoprotection of Proteins by Solutes. Cryobiology. 1988;25(3):244-55.

APPENDIX F

Collagen Density and Alignment in Responsive and Resistant Trastuzumab-Treated Breast Cancer Xenografts

Walsh AJ, Cook RS, Lee JH, Arteaga CL, Skala MC, "Collagen density and alignment of responsive and resistant trastuzumab-treated breast cancer xenografts" *Journal of Biomedical Optics,* 2015; 20(2):026004.

F.1 Abstract

Tumor collagen characteristics influence tumor malignancy, invasion, and metastasis. This study investigates the effects of trastuzumab (Tz) on the collagen of Tz-responsive (BT474), and Tz-resistant (HR6) breast cancer xenografts. Collagen content was assessed by *in vivo* second harmonic generation (SHG) imaging and histological trichrome staining of tumor sections. Collagen SHG imaging of control BT474 and HR6 tumors demonstrated increased collagen density after 14 days of treatment ($p<0.05$). Trichrome staining revealed decreased collagen in Tz-treated BT474 and HR6 tumors at 2, 5 and 14 days of treatment, suggesting that Tz affects the tumor microenvironment independent of epithelial cell response. Additionally, collagen alignment analysis revealed significantly less aligned collagen in the Tz-treated BT474 tumors at day 14 compared with control BT474 tumors. There was no correlation between SHG endpoints (collagen density and alignment) and trichrome staining ($p>0.05$), consistent with the physically distinctive nature of these measurements. There was also no correlation between tumor size and collagen endpoints ($p>0.05$). These results identify changes within the collagen compartment of the tumor microenvironment following Tz treatment that are independent from tumor cell response to Tz, and demonstrate that intravital collagen SHG imaging is capable of measuring dynamic changes in tumor microenvironment following treatment that complement trichrome staining.

F.2 Introduction

Collagen is an important protein within the extracellular matrix (ECM) of normal and malignant tissues. In normal breast tissue, increased collagen is associated with increased risk of developing breast cancer and increased disease aggressiveness (1). Recent studies of intra-tumoral collagen demonstrate that collagen fiber alignment and density associate with aggressive disease and increased invasion (1-3). Furthermore, a high density of interconnected collagen fibers within the extracellular matrix of tumors can block the diffusion of drugs into the tumor (4). These studies highlight the importance of collagen within the tumor microenvironment (TME), particularly with respect to tumor invasion and drug response. They also demonstrate a need for studies that monitor dynamic changes in collagen during breast tumor progression, and elucidate how intra-tumoral collagen may change in response to anti-cancer treatments.

Breast cancers are divided into three clinical subtypes: estrogen receptor (ER) positive, human epidermal growth factor receptor 2 (HER2) positive, and triple negative breast cancer (TNBC, lacking expression of ER, HER2, and progesterone receptor, or PR). HER2 is overexpressed in approximately 20% of breast cancers, correlating with poor clinical outcome and increased tumor malignancy (5). Fortunately, several drugs are approved for direct targeting of HER2, including trastuzumab (a monoclonal antibody) and lapatinib (a tyrosine kinase inhibitor). HER2 inhibitors increase the survival of patients when used alone and in combination with standard chemotherapies (6-9). Unfortunately, many patients do not initially respond to HER2 inhibitors, or develop acquired resistance to these targeted agents (9).

Trastuzumab (Tz) specifically binds to the extracellular domain of HER2 and prevents activation of the intracellular HER2 tyrosine kinase. Tz has other mechanisms of action, including blockade of HER2 dimerization, increased HER2 endocytosis and degradation, and induction of antibody-dependent cellular cytotoxicity (ADCC) (10, 11). Tz induces cytostatic effects by arresting the cell cycle in the G1 phase and inhibits signaling involved in cell survival (12, 13). Additionally, Tz has been shown to inhibit angiogenesis and reduce the expression of growth factors such as VEGF and TGF-β. However, additional changes that occur in the TME, particularly changes in collagen content and organization, following Tz treatment are poorly understood.

Images of collagen within the TME can be obtained from second harmonic generation (SHG) microscopy. SHG is a non-linear optical phenomenon in which two photons of the same wavelength are combined through a material to yield one photon with twice the energy (one-half the wavelength) of the incident photon. Collagen SHG imaging probes the fibrillar collagen content of tissues and generates photon intensity images of collagen fibers within the tissue, which can be analyzed to assess collagen density and alignment (14-18). Collagen fibers, such as type I, II, III, V, and XI, exhibit a strong SHG signal. In particular, increased amounts of collagen types I, III, and V have been found within breast cancers (19, 20). SHG imaging of breast cancer samples has revealed distinct collagen alignment configurations that correlate with increased tumor aggressiveness and invasion (1-3, 21). SHG images can be assessed for collagen density and relative alignment of collagen fibers. Additionally, tumor collagen can be assessed by trichrome staining of histological slides. Trichrome stains all types of collagen non-discriminately and provides information complementary to that quantified from SHG images of fibrillar collagen. In contrast to trichrome stains, SHG microscopy can be performed *in vivo*.

Few studies have characterized changes in the TME following chemotherapy or targeted therapy. Therefore, this study investigates changes in collagen content of HER2+ tumors following treatment with Tz. Two isogenic HER2+ breast cancer cell lines, one Tz-responsive (BT474) and the other selected for Tz resistance (HR6), were established as xenografts in athymic mice. Tumor-bearing mice treated with Tz or with a control IgG were used to assess collagen content from SHG images *in vivo* at three time points (2, 5, and 14 days of treatment) and in histological trichrome-stained tumor sections harvested at days 2, 5, and 14. These studies tested the hypothesis that Tz treatment affects collagen in the TME, independent of the effect of Tz on the tumor cells themselves.

F.3 Materials and Methods

F.3.1 Xenograft Model

This study was approved by the Vanderbilt University Animal Care and Use Committee and meets the NIH guidelines for animal welfare. A total of 36 mice were used. BT474 (10^8; ATCC) and HR6 cells (10^8; (22)) in 100 μL Matrigel (Corning) were injected in the inguinal mammary fat pads of 6 week old female athymic nude mice (J:NU; Jackson Laboratories). Each mouse was injected in two locations, on the right and left of the lower portion of the mammary fat pad and two tumors grew in all mice except three, which only had one tumor (tumor take rate of 96%). BT474 and HR6 cells are ER+/HER2+ isogenic cell lines. The HR6 cell line was derived from a BT474 tumor that developed resistance to Tz treatment (22). These two cell lines were chosen because both overexpress HER2, the target protein of Tz, but only the BT474 tumors shrink in response to Tz treatment. Tumors were allowed to grow to approximately 150 mm^3; then the mice were randomized into control or trastuzumab treatment groups, with nine mice in each group. Tumor-bearing mice were treated intraperitoneal with control human immunoglobulin, 10 mg/kg (IgG; R&D Systems) or Tz, 10 mg/kg (Genentech), twice weekly for two weeks (on days 0, 3, 7, and 10). This dose of Tz was chosen to mimic the therapeutic dose in patients (23). To minimize tumor variance, age-matched mice were used, a single batch of cells for each tumor type was generated and injected, the same number of cells per tumor was injected, and treatment was initiated when the tumors were approximately the same size (~150 mm^3).

For intravital imaging, the mice were anesthetized with isofluorane and the skin overlaying the tumor was removed. The tumor was covered with a coverslip and the mouse was positioned on the microscope stage. Three locations of each tumor were imaged. Each tumor type (BT474, HR6) and group (control, Tz) at each time point (2, 5, and 14 days of treatment) consisted of 3 mice (6 tumors). One mouse from the control and Tz-treated BT474 groups on day 2 and the Tz-treated HR6 day 2 group only grew 1 tumor and therefore, those groups consisted of 5 tumors. Mice were humanly euthanized after imaging while under anesthesia. Tumors were collected *post-mortem* for tissue fixation. The time points (2, 5, and 14 days) were chosen based on previous studies of these mouse tumors, which found metabolic and vascular changes within 2 and 5 days, respectively of Tz treatment, and significant changes in tumor volume within 14 days of Tz treatment (24, 25).

F.3.2 Collagen SHG Imaging

Collagen SHG imaging was performed on a custom built, commercial multiphoton microscope (Bruker). A 40X oil-immersion objective (1.3 NA) coupled the illumination and emission light through an inverted microscope (TiE, Nikon). A titanium:sapphire laser (Coherent Inc.) tuned to 890 nm, with an average power of 8.4 to 8.6 mW, provided the illumination light. The incident light was attenuated by a Pockel cell to vary the power of the illumination light which results in an elliptically polarized beam. A PMT (Hamamatsu) detected the emitted photons through a 450/35 nm notch filter. A pixel dwell time of 4.8 μs was used to collect 256x256 pixel images. Single frame images for three different locations for each tumor were acquired. Each image frame was averaged 8 times to reduce noise. Sequential images were separated laterally by at least one field of view, 270 μm. Images were acquired of tumor tissue approximately 20-60 μm in depth into the tumor.

F.3.3 Collagen SHG Image Analysis

Collagen alignment was quantified from the SHG images using the curvelet-based alignment analysis software, CurveAlign (http://loci.wisc.edu/software/). CurveAlign uses a fast discrete curvelet transform to find the location and edges of collagen fibers and returns orientation data and descriptive statistics. For our images, collagen alignment was assessed relative to the horizontal plane of the image. An alignment coefficient of 1 indicates parallel fibers while 0 indicates perpendicular fibers. Collagen density was quantified by image thresholding. The histogram of pixel intensities for most images was bimodal, with one mode representing the background pixels and one mode representing the collagen fibers. Each pixel was assigned a value of 0 or 1, depending on if the intensity value of that pixel was above (value = 1) or below (value = 0) the optimal threshold value computed for the image using Otsu's method (Matlab). Collagen density was quantified as the sum of the thresholded image, which represents the portion of collagen positive pixels. The collagen alignment and density outputs from the three fields of view interrogated for each tumor were averaged for a single collagen profile of each tumor.

F.3.4 Trichrome Staining and Analysis

Tumors were collected and placed in buffered formalin, paraffin embedded, sliced, and stained with trichrome. Trichrome stains multiple cellular structures including collagen, cell cytoplasms, and cell nuclei. All types of collagen are stained with trichrome, and the resulting sections can be qualitatively analyzed. Collagen staining was quantified from 3 tumors per group by expert (RSC) analysis of intra- and extra- tumoral collagen content. Tumor collagen content was scored based on presence and intensity of staining, with an increased score indicative of increased collagen staining. The trichrome score represents the sum of four measures, selected between 0-2 for each field of view analyzed: intra dense strands, intra diffuse strands, extra dense strands, and extra diffuse strands.

F.3.5 Statistics

Independence of observations between tumors was confirmed using logistic regression. Differences in collagen alignment, density, and trichrome staining were assessed between control and Tz-treated tumors within each time point and within control or Tz-treated tumors over time using non-parametric rank sum tests. We used an alpha significance level of 0.05. Correlation analysis was performed using Spearman's Rank Correlation Coefficient.

F.4 Results

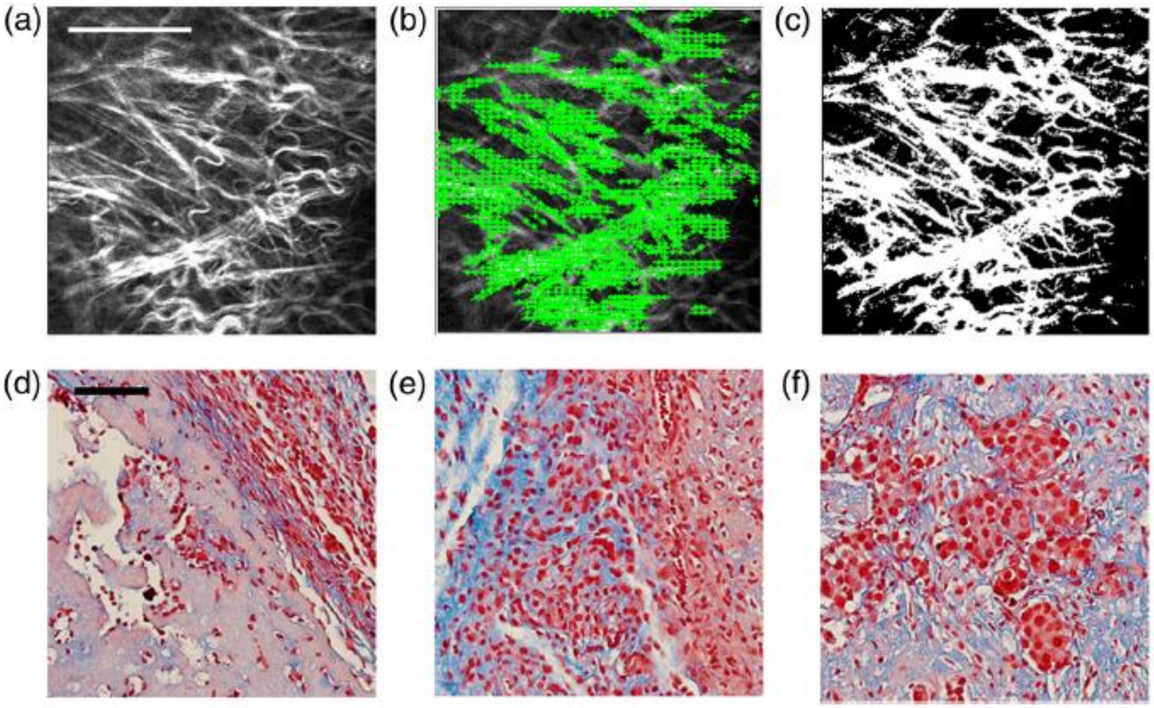

Figure F.1. Collagen SHG images and representative trichrome images. (a) Original collagen SHG image. **(b)** Overlay image of identified collagen fiber angles (green arrows). **(c)** Collagen density is obtained from a thresholded image. (**d-f**) Representative trichrome images obtained at 400X to demonstrate a low (**d**; score of 2), medium (**e**; score of 5), and high (**f**, score of 8) score. Scale bars are 100 μm.

The collagen content of Tz-responsive (BT474) and Tz-resistant (HR6) tumors was examined by *in vivo* collagen SHG imaging and trichrome staining over a 14 day time course of control-IgG or Tz treatment. BT474 tumors respond to Tz with increased cell death and decreased tumor volume, while Tz does not induce cell death or decrease growth in HR6 tumors (22, 24, 25). Collagen SHG images were analyzed using CurveAlign to extract relative fiber alignment and density of collagen positive pixels (Fig. F.1). Figure F.1c shows the thresholded intensity mask image of collagen density, where all collagen positive pixels have a value of 1 and all negative pixels have a value of 0. Trichrome stained tumor sections were scored from 0-8 based on the presence and intensity of the intra- and extra-tumor collagen. Representative images of trichrome stained tumor sections demonstrate trichrome scoring heterogeneity (Fig. F.1d-f).

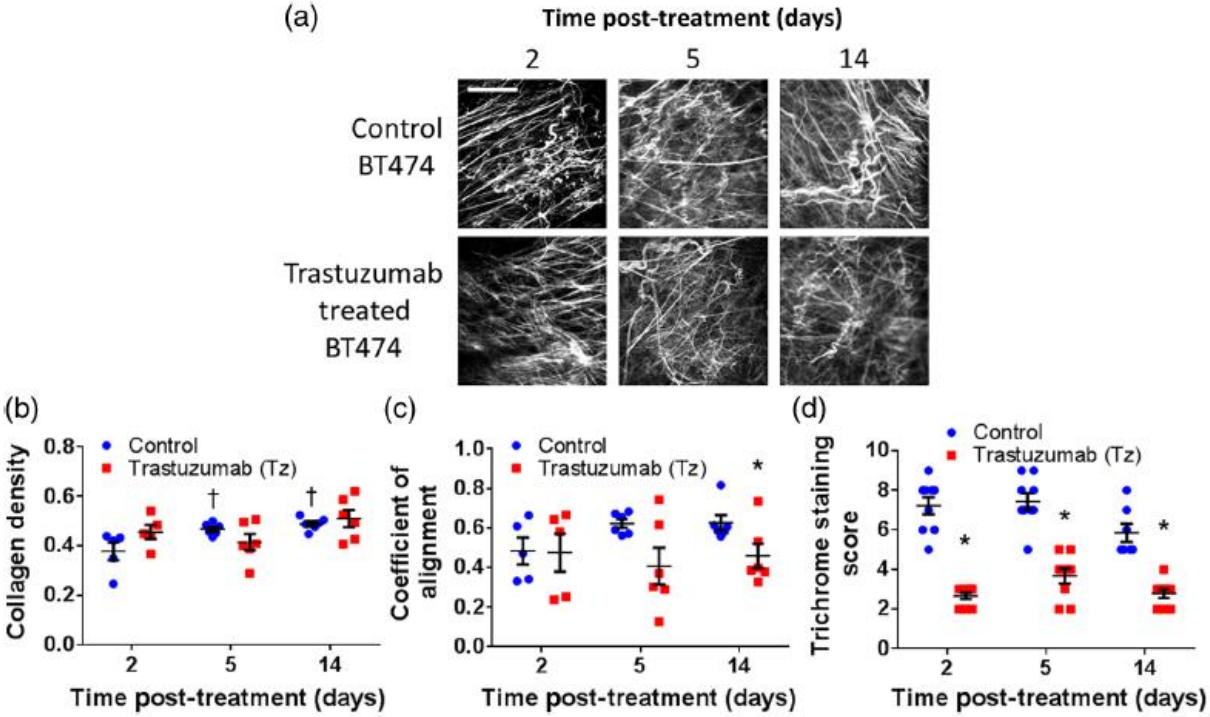

Figure F.2. Collagen changes in BT474 tumors treated with trastuzumab. (a) Representative collagen SHG images from BT474 tumors. Scale bar is 100 μm. **(b)** Collagen density of SHG images for control and Tz-treated BT474 tumors. **(c)** Coefficient of alignment of SHG images for control and Tz-treated BT474 tumors. **(d)** Trichrome staining score for control and Tz-treated BT474 tumors. † ($p<0.05$) vs. day 2. * ($p<0.05$) vs. control.

Collagen analysis revealed significant differences as a result of tumor growth and treatment with Tz in BT474 xenografts. Representative collagen SHG images demonstrate the typical size, density, and alignment of collagen fibers within control and Tz-treated BT474 tumors over the time course (Fig. F.2a). Collagen density was obtained from collagen SHG images as the portion of collagen positive pixels. Control BT474 tumors initially had a collagen density of 0.38 on day 2, which significantly ($p<0.05$) increased to 0.47 on day 5 and was maintained at 0.49 on day 14 (Fig. F.2b). No significant differences in collagen density were detected between control and Tz-treated BT474 tumors. Likewise, no differences in collagen alignment were detected in BT474 tumors treated with Tz for 2 or 5 days. On day 14, however, there was a significant reduction in the collagen alignment of Tz-treated BT474 tumors compared with control BT474 tumors ($p<0.05$; Fig. F.2c). The intra-tumor variance for the density of the BT474 tumors was 0.002 while the inter-group variance was 0.004, suggesting greater differences between tumors within a time point and treatment group, than within individual tumors. The intra-tumor variance for the coefficient of alignment of collagen fibers within BT474 tumors was 0.008 while the inter-group variance was 0.02 ($p<0.05$), again indicating greater heterogeneity between individual tumors rather than within a tumor.

Trichrome staining of collagen revealed significant differences in collagen between control and Tz-treated BT474 tumors. A trichrome staining score was assigned to each histology section based on visual analysis of the intra- and extra- tumoral collagen, both dense and diffuse. An increased score indicates increased collagen content. Significant reductions in collagen trichrome scores were detected on 2, 5, and 14 days ($p<0.05$) of treatment in the BT474 tumors (Fig. F.2d).

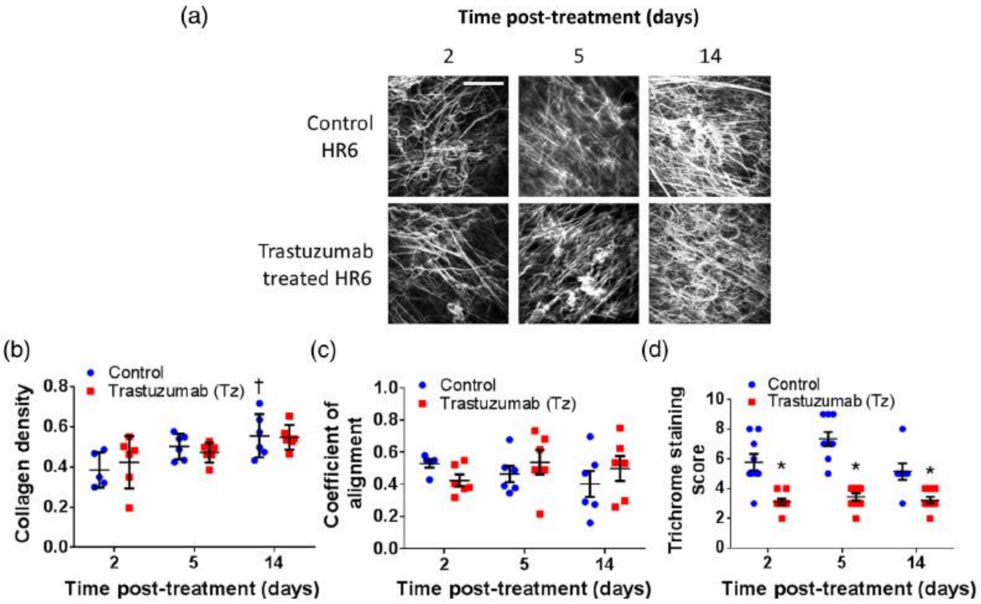

Figure F.3. Collagen changes in HR6 tumors treated with trastuzumab. (a) Representative collagen SHG images from HR6 tumors, scale bar is 100 μm. **(b)** Collagen density of SHG images for control and Tz-treated HR6 tumors. **(c)** Coefficient of alignment of SHG images for control and Tz-treated HR6 tumors. **(d)** Trichrome staining score for control and Tz-treated HR6 tumors. † ($p<0.05$) vs. day 2. * ($p<0.05$) vs. control.

Representative collagen SHG images from control and Tz-treated HR6 tumors are shown in Fig. 3a. Control HR6 tumors showed an increase in collagen density over time, from 0.38 on day 2 to 0.55 on day 14 ($p<0.05$; Fig. F.3b), similar to the increase in collagen density observed in the control BT474 tumors over time (Fig. F.2b). Tz resulted in stable collagen SHG density in both the BT474 and HR6 tumors across all time points (Fig. F.2b, F.3b). No significant differences in collagen density between the Tz-responsive and Tz-resistant tumors (within control and Tz-treated groups) were observed at any time point ($p>0.05$). The intra-tumor variance for the collagen density of the HR6 tumors was less than the variance between HR6 tumor groups (0.003 and 0.007, respectively; $p<0.05$). Likewise, the intra-tumor variance for the collagen coefficient of alignment of the HR6 tumors was less than the variance between HR6 tumor groups (0.01 and 0.02, respectively; $p<0.05$). Tz failed to induce a decreased collagen alignment in HR6 tumors over time or between control and trastuzumab-treated tumors (Fig. F.3c). A significant reduction in collagen alignment ($p<0.05$) was detected in control HR6 tumors compared with control BT474 tumors on days 5 and 14. A significant reduction in the trichrome score was detected in Tz-treated HR6 tumors compared to control tumors at every time point (Fig. F.3d).

Correlation analysis was performed between collagen endpoints from control BT474 and HR6 tumors using matched tumor data to investigate relationships between SHG imaging endpoints and trichrome scores. Neither the collagen density nor the coefficient of alignment determined from SHG images (Fig. F.4a) correlated with trichrome score. Furthermore, none of the endpoints, trichrome score, SHG density, or SHG coefficient of alignment, correlated with tumor volume (Fig. F.4b-d). The SHG density did not correlate with the coefficient of alignment (Fig. F.4e). However, a significant correlation was detected between SHG density and the age of the tumor (Fig. F.4f).

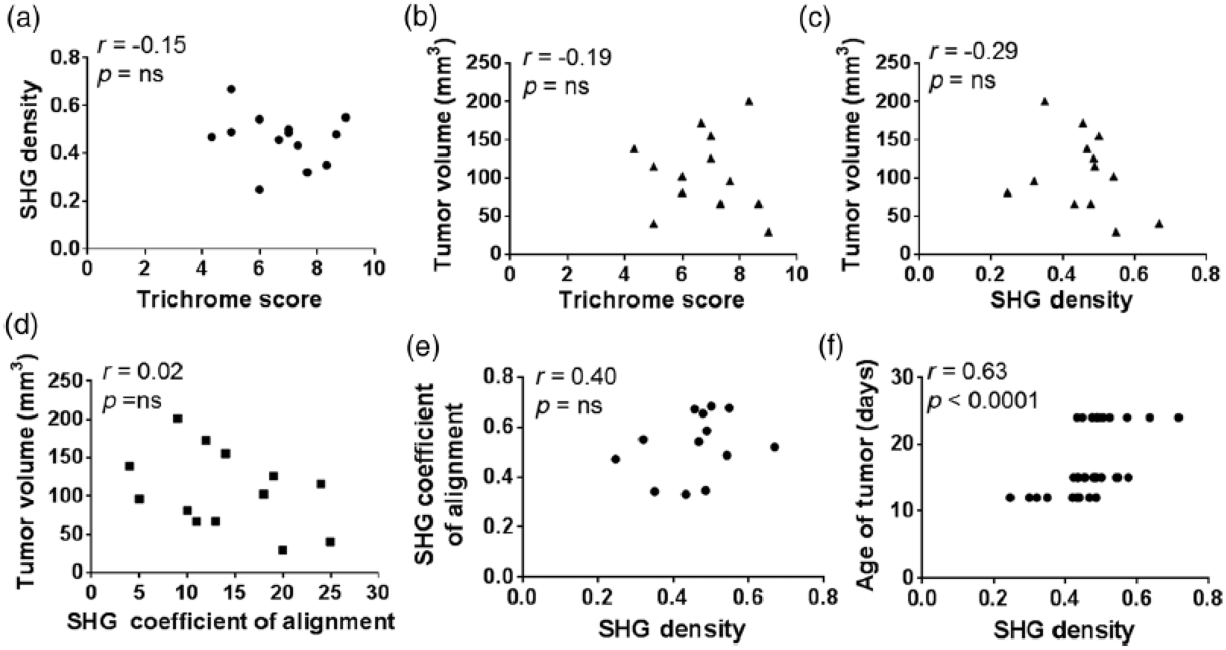

Figure F.4. Correlations between SHG endpoints and trichrome. (a) Correlation between trichrome score and SHG density. (**b**) Correlation between trichrome score and tumor volume. **(c)** Correlation between SHG density and tumor volume. **(d)** Correlation between SHG coefficient of alignment and tumor volume. **(e)** Correlation between SHG density and SHG coefficient of alignment. (**f**) Correlation between SHG density and age of tumor. r is Spearman’s correlation coefficient. ns = not significant. Tumor volume measurements were obtained from paraffin embedded tumors which results in tissue shrinkage.

F.5 Discussion

Tz is a HER2-targeted antibody prescribed clinically for treatment of breast cancers that overexpress HER2. While many studies have characterized the effects of Tz on the tumor epithelium, few studies have investigated the effects of Tz on the tumor microenvironment. This study investigated the effects of Tz on breast tumor collagen in both Tz-responsive and Tz-resistant tumors.

Representative collagen SHG images demonstrate the typical size, alignment, and density of collagen fibers within the tumors over time and with treatment (Figs. F.1a, F.2a, F.3a). These images were acquired from a microscope system designed for multiphoton fluorescence imaging and fluorescence lifetime imaging. The only modifications necessary to image collagen SHG was the addition of a narrow emission filter at one-half the wavelength of the incident near infrared light. Collagen SHG imaging is sensitive to the polarization of the incident light. The incident light in our experimental set-up is attenuated by a Pockel cell to vary the power of the illumination light, which results in an elliptically polarized beam. Therefore, we should capture collagen fibers at all angles, but the intensity of the fibers may be direction-dependent due to the polarization of the incident beam. In order to account for this bias in intensity with fiber orientation, we applied an intensity threshold to our images for further analysis so that our endpoints are independent of absolute pixel intensity. Collagen SHG images were analyzed to extract collagen density and relative fiber alignment (Figs. F.2b-c, F.3b-c).

Analysis of the collagen SHG images revealed a statistically significant increase in the density of collagen in control BT474 and HR6 tumors over time (Figs. F.2b, F.3b). Correlation analysis (Fig. F.4) does not show a correlation between larger tumors and collagen density. However, there is a significant correlation between SHG density and tumor age. These results suggest increased fibrillar collagen within aging tumors, which is consistent with previous reports of increased collagen content in malignant and progressing tumors (1). Upon treatment with Tz, the BT474 tumors shrink over 14 days (25), and the collagen density within these tumors showed no significant change over the time course (Fig. F.2b). This suggests that Tz decreases the amount of fibrillar collagen in parallel with decreases in tumor volume in responsive tumors, thus maintaining constant collagen density over time.

The relative alignment of collagen fibers is associated with tumor invasion and progression, with radially aligned fibers characteristic of aggressive disease (1-3). To assess collagen fiber alignment, a coefficient of alignment was determined for each image using CurveAlign. Images with perfectly parallel fibers would have an alignment coefficient of 1 while images with perpendicular fibers, a value of 0. The Tz-treated BT474 tumors showed a significant decrease in coefficient of collagen alignment compared to control BT474 tumors on day 14 (Fig. F.2c), suggesting less aggressive characteristics upon treatment with the therapeutic antibody. No change in collagen alignment was detected in the HR6 tumors treated with Tz, suggesting no significant effect of Tz on the collagen fiber alignment of these non-responding tumors. A significant reduction in collagen alignment was detected in control HR6 tumors compared with control BT474 tumors on days 5 and 14. This may be due to differences in the characteristics and behavior of these two tumors. The HR6 tumors grow at a faster rate than the BT474 tumors which may influence microenvironment composition (25). HR6 cells also express higher levels of EGFR and P-EGRF compared to the BT474 cells (22), which may influence tumor behavior and microenvironment composition (26, 27).

Histological analysis of collagen stained with trichrome dye revealed significant reductions in collagen content in BT474 tumors treated with trastuzumab at all time-points (Fig. F.2d). The trichrome staining score is a sum four measures, diffuse and dense collagen both intra and extra tumoral, and all four individually show similar trends. Trichrome stains all forms of collagen, including fibrillar collagen. Tumors contain multiple types of collagen, including type I, II, III, and IV. Collage type IV is particularly important within tumors because it composes the basal membrane and is involved in tumor invasion (28, 29).

The HR6 SHG and trichrome results suggest that Tz may have direct effects on the tumor microenvironment. The Tz-treated HR6 tumors did not show an increase in SHG density over the 14 day study, consistent with the Tz-treated BT474 tumors and contrary to the control HR6 and BT474 tumors (Fig. F.2b, F.3b). Furthermore, the trichrome scores revealed significantly reduced scores at all time points for the Tz-treated HR6 tumors compared to the control HR6 tumors (Fig.

F.3d). Few studies have investigated the effects of Tz treatment on non-responsive tumor cells and tumor microenvironment. In a study of a novel glaucoma surgical intervention, Tz was tested as an anti-scar agent (30), revealing that Tz suppressed fibroblast proliferation and reduced tissue levels of TGF-β, FGF- β, and PDGF (30). This and the HR6 results suggest that Tz may affect the collagen content of tumors by directly modifying fibroblasts behavior or by modulating paracrine growth factors secreted by tumor cells. Furthermore, our previous studies of Tz effects on the tumor vasculature of BT474 and HR6 tumors revealed significant decreases in vessel oxygen saturation with 5 days of Tz-treatment in both tumor models (24). Our studies and these previous results suggest that Tz treatment may affect the tumor microenvironment independent of its effects on the tumor cells.

The correlation analysis (Fig. F.4) indicates that the SHG endpoints, collagen density and coefficient of alignment, do not correlate with the trichrome staining score or with each other. These results agree with findings of Strupler et al, who directly compared sequential slides of collagen SHG and trichrome strain and reported that trichrome is less specific at identifying fibrillar collagen and difficult to score and compare with SHG (31). This suggests that SHG density, SHG coefficient of alignment, and trichrome score are different measurements. The inconsistencies between trichrome staining and SHG may be due to the source of contrast. Trichrome stains all collagen, including fibrillar and non-fibrrillar collagen as well as other components of the extracellular matrix, while only certain fibrillar collagen strands will exhibit SHG (31). Tumors can have increased content of non-fibrillar collagens, in particular, collagen IV (28, 29), which does not exhibit SHG (31). Additionally, discrepancies between SHG density and trichrome staining may be due to sampling error in either the SHG measurements or trichrome imaging, both of which are limited to a small fields of view and are thus only probing a small portion of the tumor. Imaging additional trichrome stained histological slices of the tumor or obtaining 3D stacks of SHG images may provide increased representation of the tumor and more accurate measurements.

The results of this study highlight several changes in the collagen content and organization of the tumor microenvironment both in growing tumors and with Tz-treatment. However, there may be confounding factors that influence the composition of the tumor microenvironment and the effectiveness of Tz. The tumor extracellular matrix can affect drug diffusion (18, 32, 33) and extracellular proteins such as laminin can co-localize with HER2 and limit the efficacy of Tz (34). Therefore, the initial composition of the tumor extracellular matrix may influence Tz treatment. Furthermore, variability in tumor growth rates may cause variable vascular instability, which may affect the tumor microenvironment, collagen measurements, and Tz-delivery and effectiveness (35). In this study, variability across tumors was controlled by the use of a single batch of cells to initiate tumors, the use of age-matched mice, injection of the same number of cells per tumor, and the use of mouse weight to determine Tz dose. However, some variability occurred between tumors within groups due to experimental error and biological variance. This inherent variability may mask some effects of Tz on the tumor microenvironment and may limit the effectiveness of Tz inhibition of HER2.

In conclusion, these studies suggest that Tz treatment may affect the tumor microenvironment independent of its effects on the tumor cells. We have also demonstrated that collagen SHG and histological trichrome staining analysis of collagen provide complementary endpoints of tumor collagen content and morphology. Collagen SHG imaging can be performed *in vivo* through window chambers for longitudinal studies (24, 36) while trichrome staining is inherently *post-mortem*, potentially limiting the number of time points and increasing animal burden and expense. Trichrome staining revealed decreased collagen content in both Tz-responsive and non-responsive tumors treated with Tz. Furthermore, collagen SHG imaging revealed similar trends in collagen density in both Tz-responsive and non-responsive tumors treated with Tz, suggesting consistent effects of Tz on the tumor microenvironment irrespective of Tz-induced tumor size reduction. However, there was a decrease in the alignment of collagen fibers of Tz-treated responsive tumors only after 14 days of treatment. These results highlight the changes occurring within the collagen compartment of the tumor microenvironment following systemic Tz treatment.

F.6 Acknowledgements

This work was supported by funding sources that include the NCI SPORE in Breast Cancer (P50 CA098131), ASLMS Student Research Grant (AJW), NSF Graduate Research Fellowship (DGE-0909667; AJW), DOD Breast Cancer Research Program (DOD-BC121998), NIH (NCI R01 CA185747), and Mary Kay Foundation (067-14).

F.7 References

1. Provenzano PP, Inman DR, Eliceiri KW, Knittel JG, Yan L, Rueden CT, White JG, Keely PJ. Collagen density promotes mammary tumor initiation and progression. BMC Med. 2008;6:11.

2. Provenzano PP, Eliceiri KW, Campbell JM, Inman DR, White JG, Keely PJ. Collagen reorganization at the tumor-stromal interface facilitates local invasion. BMC Med. 2006;4(1):38.

3. Provenzano PP, Eliceiri KW, Keely PJ. Multiphoton microscopy and fluorescence lifetime imaging microscopy (FLIM) to monitor metastasis and the tumor microenvironment. Clin Exp Metastasis. 2009;26(4):357-70.

4. Jain RK, Stylianopoulos T. Delivering nanomedicine to solid tumors. Nat Rev Clin Oncol. 2010;7(11):653-64.

5. Ross JS, Fletcher JA. The HER-2/neu oncogene in breast cancer: prognostic factor, predictive factor, and target for therapy. Stem Cells. 1998;16(6):413-28.

6. Burris HA, 3rd, Hurwitz HI, Dees EC, Dowlati A, Blackwell KL, O'Neil B, Marcom PK, Ellis MJ, Overmoyer B, Jones SF, Harris JL, Smith DA, Koch KM, Stead A, Mangum S, Spector NL. Phase I safety, pharmacokinetics, and clinical activity study of lapatinib (GW572016), a reversible dual inhibitor of epidermal growth factor receptor tyrosine kinases, in heavily pretreated patients with metastatic carcinomas. J Clin Oncol. 2005;23(23):5305-13.

7. Storniolo AM, Pegram MD, Overmoyer B, Silverman P, Peacock NW, Jones SF, Loftiss J, Arya N, Koch KM, Paul E, Pandite L, Fleming RA, Lebowitz PF, Ho PT, Burris HA, 3rd. Phase I dose escalation and pharmacokinetic study of lapatinib in combination with trastuzumab in patients with advanced ErbB2-positive breast cancer. Journal of clinical oncology : official journal of the American Society of Clinical Oncology. 2008;26(20):3317-23.

8. Piccart-Gebhart MJ, Procter M, Leyland-Jones B, Goldhirsch A, Untch M, Smith I, Gianni L, Baselga J, Bell R, Jackisch C, Cameron D, Dowsett M, Barrios CH, Steger G, Huang CS, Andersson M, Inbar M, Lichinitser M, Lang I, Nitz U, Iwata H, Thomssen C, Lohrisch C, Suter TM, Ruschoff J, Suto T, Greatorex V, Ward C, Straehle C, McFadden E, Dolci MS, Gelber RD. Trastuzumab after adjuvant chemotherapy in HER2-positive breast cancer. The New England journal of medicine. 2005;353(16):1659-72.

9. Vogel CL, Cobleigh MA, Tripathy D, Gutheil JC, Harris LN, Fehrenbacher L, Slamon DJ, Murphy M, Novotny WF, Burchmore M, Shak S, Stewart SJ, Press M. Efficacy and safety of trastuzumab as a single agent in first-line treatment of HER2-overexpressing metastatic breast cancer. Journal of Clinical Oncology. 2002;20(3):719-26.

10. Valabrega G, Montemurro F, Aglietta M. Trastuzumab: mechanism of action, resistance and future perspectives in HER2-overexpressing breast cancer. Annals of oncology : official journal of the European Society for Medical Oncology / ESMO. 2007;18(6):977-84.

11. Hudis CA. Trastuzumab--mechanism of action and use in clinical practice. The New England journal of medicine. 2007;357(1):39-51.

12. Mayfield S, Vaughn JP, Kute TE. DNA strand breaks and cell cycle perturbation in herceptin treated breast cancer cell lines. Breast cancer research and treatment. 2001;70(2):123-9.

13. Cuello M, Ettenberg SA, Clark AS, Keane MM, Posner RH, Nau MM, Dennis PA, Lipkowitz S. Down-regulation of the erbB-2 receptor by trastuzumab (herceptin) enhances tumor necrosis factor-related apoptosis-inducing ligand-mediated apoptosis in breast and ovarian cancer cell lines that overexpress erbB-2. Cancer Res. 2001;61(12):4892-900.

14. Chen XY, Nadiarynkh O, Plotnikov S, Campagnola PJ. Second harmonic generation microscopy for quantitative analysis of collagen fibrillar structure. Nat Protoc. 2012;7(4):654-69.

15. Campagnola PJ, Millard AC, Terasaki M, Hoppe PE, Malone CJ, Mohler WA. Three-dimensional high-resolution second-harmonic generation imaging of endogenous structural proteins in biological tissues. Biophys J. 2002;82(1 Pt 1):493-508.

16. Zipfel WR, Williams RM, Christie R, Nikitin AY, Hyman BT, Webb WW. Live tissue intrinsic emission microscopy using multiphoton-excited native fluorescence and second harmonic generation. Proc Natl Acad Sci U S A. 2003;100(12):7075-80.

17. Cox G, Kable E, Jones A, Fraser IK, Manconi F, Gorrell MD. 3-dimensional imaging of collagen using second harmonic generation. J Struct Biol. 2003;141(1):53-62.

18. Brown E, McKee T, diTomaso E, Pluen A, Seed B, Boucher Y, Jain RK. Dynamic imaging of collagen and its modulation in tumors in vivo using second-harmonic generation. Nature medicine. 2003;9(6):796-800.

19. Kauppila S, Stenback F, Risteli J, Jukkola A, Risteli L. Aberrant type I and type III collagen gene expression in human breast cancer in vivo. Journal of Pathology. 1998;186(3):262-8.

20. Barsky SH, Rao CN, Grotendorst GR, Liotta LA. Increased Content of Type-V Collagen in Desmoplasia of Human-Breast Carcinoma. Am J Pathol. 1982;108(3):276-83.

21. Provenzano PP, Rueden CT, Trier SM, Yan L, Ponik SM, Inman DR, Keely PJ, Eliceiri KW. Nonlinear optical imaging and spectral-lifetime computational analysis of endogenous and exogenous fluorophores in breast cancer. Journal of biomedical optics. 2008;13(3):031220.

22. Ritter CA, Perez-Torres M, Rinehart C, Guix M, Dugger T, Engelman JA, Arteaga CL. Human breast cancer cells selected for resistance to trastuzumab in vivo overexpress epidermal growth factor receptor and ErbB ligands and remain dependent on the ErbB receptor network. Clin Cancer Res. 2007;13(16):4909-19.

23. Gee MS, Upadhyay R, Bergquist H, Alencar H, Reynolds F, Maricevich M, Weissleder R, Josephson L, Mahmood U. Human breast cancer tumor models: molecular imaging of drug susceptibility and dosing during HER2/neu-targeted therapy. Radiology. 2008;248(3):925-35.

24. McCormack DR, Walsh AJ, Sit W, Arteaga CL, Chen J, Cook RS, Skala MC. In vivo hyperspectral imaging of microvessel response to trastuzumab treatment in breast cancer xenografts. Biomedical optics express. 2014;5(7):2247-61.

25. Walsh AJ, Cook RS, Manning HC, Hicks DJ, Lafontant A, Arteaga CL, Skala MC. Optical metabolic imaging identifies glycolytic levels, subtypes, and early-treatment response in breast cancer. Cancer Res. 2013;73(20):6164-74.

26. Laato M, Kahari VM, Niinikoski J, Vuorio E. Epidermal growth factor increases collagen production in granulation tissue by stimulation of fibroblast proliferation and not by activation of procollagen genes. The Biochemical journal. 1987;247(2):385-8.

27. Buckley A, Davidson JM, Kamerath CD, Wolt TB, Woodward SC. Sustained release of epidermal growth factor accelerates wound repair. Proc Natl Acad Sci U S A. 1985;82(21):7340-4.

28. Ioachim E, Charchanti A, Briasoulis E, Karavasilis V, Tsanou H, Arvanitis DL, Agnantis NJ, Pavlidis N. Immunohistochemical expression of extracellular matrix components tenascin, fibronectin, collagen type IV and laminin in breast cancer: their prognostic value and role in tumour invasion and progression. European journal of cancer. 2002;38(18):2362-70.

29. Kim JP, Chen JD, Wilke MS, Schall TJ, Woodley DT. Human Keratinocyte Migration on Type-Iv Collagen - Roles of Heparin-Binding Site and Alpha-2-Beta-1 Integrin. Lab Invest. 1994;71(3):401-8.

30. Turgut B, Eren K, Akin MM, Bilir Can N, Demir T. Impact of trastuzumab on wound healing in experimental glaucoma surgery. Clinical & experimental ophthalmology. 2014.

31. Strupler M, Pena AM, Hernest M, Tharaux PL, Martin JL, Beaurepaire E, Schanne-Klein MC. Second harmonic imaging and scoring of collagen in fibrotic tissues. Optics express. 2007;15(7):4054-65.

32. Netti PA, Berk DA, Swartz MA, Grodzinsky AJ, Jain RK. Role of extracellular matrix assembly in interstitial transport in solid tumors. Cancer Res. 2000;60(9):2497-503.

33. Davies Cde L, Berk DA, Pluen A, Jain RK. Comparison of IgG diffusion and extracellular matrix composition in rhabdomyosarcomas grown in mice versus in vitro as spheroids reveals the role of host stromal cells. British journal of cancer. 2002;86(10):1639-44.

34. Beyer I, Li Z, Persson J, Liu Y, van Rensburg R, Yumul R, Zhang XB, Hung MC, Lieber A. Controlled extracellular matrix degradation in breast cancer tumors improves therapy by trastuzumab. Molecular therapy : the journal of the American Society of Gene Therapy. 2011;19(3):479-89.

35. Less JR, Skalak TC, Sevick EM, Jain RK. Microvascular architecture in a mammary carcinoma: branching patterns and vessel dimensions. Cancer Res. 1991;51(1):265-73.

36. Shan SQ, Sorg B, Dewhirst MW. A novel rodent mammary window of orthotopic breast cancer for intravital microscopy. Microvasc Res. 2003;65(2):109-17.